折展多面体机构设计及其过约束消减方法

Design of Deployable Polyhedral Mechanisms and Analysis of Constraint Reduction

一级学科：机械工程

研究方向：折展结构

作者姓名：顾元庆

指导教师：陈焱　　教授

天津大学机械工程学院

二〇二四年一月

摘要

折展多面体作为一类特殊的三维折展结构，在航空航天、模块化建筑和机器人等工程领域拥有巨大应用潜力。折展多面体的设计融合了机构运动学和立体几何学的巧妙灵感，但通过运动学策略来实现两种规则多面体之间的单自由度变换依然面临挑战。此外，大多数多面体机构都为空间多环路过约束机构，该机构本质阻碍了其工程化发展，在运动学等价基础上的过约束消减方法则成为了亟待解决的运动学理论难题。本文聚焦于机构运动学理论，建立了基于对称性与不同类型机构单元的折展多面体设计准则，获得了一系列单自由度径向折展多面体的创新设计，并提出了多环路过约束多面体机构的过约束消减方法。本文的研究重点如下：

首先，将球面四杆机构嵌入至空间九杆机构以提供运动约束，提出了一种具有三重对称运动的球面四杆同步机构。将此同步机构作为构建单元，设计了一系列单自由度径向折展多面体，并基于几何缩短操作揭示了九种多面体单自由度变换方案。此外，通过解析运动约束条件，实现了多面体机构的局部过约束消减，并证明了去除冗余约束后的运动等价特性。

其次，将 Sarrus 连杆机构嵌入至扩展后的柏拉图多面体，构建了一系列基于 Sarrus 连杆机构的单自由度折展多面体。基于旋量理论与等效移动副概念，实现了复杂多面体机构自由度的简化分析。此外，本文引入哈密尔顿路径这一数学概念，提出了多环路过约束多面体机构的过约束消减方法，在运动学等价的基础上大幅降低了机构过约束度。

最后，将多重对称的空间七杆机构网格作为构建单元，按照相应的空间对称性嵌入至阿基米德多面体表面，提出了一系列基于空间七杆机构的径向折展多面体。本文用机构学的方法实现了几何学中丰富的多面体对称变换，拓宽了可变换多面体的设计空间。在所提出的哈密尔顿路径过约束消减方法基础上，通过去除路径边缘冗余约束，实现了此类多面体机构冗余约束的进一步去除。

本文基于空间对称性建立了新型折展多面体的设计准则，提出了多环路过约束多面体机构的过约束消减方法。不仅为折展多面体机构的创新研究奠定强有力的理论基础，也为其工程化发展提供有效的技术支撑。

关键词：机构运动学，折展多面体，多面体变换，对称性，同步径向运动，过约束消减，运动学等价

ABSTRACT

Deployable polyhedrons, a special type of 3D deployable structure, have great potential in engineering fields such as aerospace, modular construction and robotics. The design of deployable polyhedral mechanisms (DPMs) combines the ingenious inspirations of mechanism kinematics and solid geometry, yet it remains challenging to realise one-degree-of-freedom (DOF) transformations between two regular polyhedrons with a kinematic strategy. Moreover, most of these transformations involve spatial, multiloop, and overconstrained mechanisms that have limited their application potential. Thus, overconstraint reduction based on kinematic equivalence has become a problem that needs to be solved. This dissertation focuses on mechanism kinematics, establishes a design criterion for deployable polyhedrons based on spatial symmetries and different types of mechanism units. Herein, a family of DPMs with 1-DOF synchronized radial motion is constructed, the overconstraint reduction strategy for multiloop overconstrained mechanisms is proposed. The highlights of this dissertation are as follows.

First, a synchronized mechanism with a threefold-symmetric motion feature is proposed by integrating a spatial 9*R* linkage and three pairs of spherical 4*R* (S4*R*) linkages. Subsequently, by embedding the proposed S4*R*-synchronized mechanism cells into the polyhedral surface, a group of S4*R*-based polyhedrons is constructed, and a total of nine paired transformations are realized by means of dimensional shortening operations. Furthermore, overconstraint reduction of the S4*R*-based polyhedral mechanisms is achieved by analyzing the constraint conditions, and the kinematic equivalence after removing redundant constraints is demonstrated and verified.

Next, a family of Sarrus-based deployable polyhedral mechanisms is proposed by carrying out the expansion operation of Platonic polyhedrons and implanting Sarrus linkages. Subsequently, based on screw theory and equivalent prismatic joints, an equivalent analysis of multiloop polyhedral mechanisms is proposed to significantly simplify the calculation process. Moreover, a systematic method for the overconstraint reduction of multiloop overconstrained mechanisms is proposed by introducing the Hamiltonian path to topological graphs of DPMs, in which the degrees of overconstraint in each Sarrus-based DPM are greatly reduced without affecting the original kinematics.

Finally, considering the multi-symmetric spatial 7*R* assembly as the construction cell, a series of 1-DOF 7*R*-based polyhedrons is obtained by embedding the 7*R* assembly into polyhedral surfaces following the corresponding symmetries. The rich polyhedral geometric transformations are realized with a kinematic method, which widens the design of transformable polyhedrons. Moreover, based on the proposed Hamiltonian-path reduction strategy, further removal of redundant constraints in 7*R*-based polyhedral mechanisms is achieved by removing path-contour redundant constraints.

Therefore, this dissertation establishes an approach for the design of novel DPMs based on spatial symmetries and proposes the overconstraint reduction strategy based on the Hamiltonian path. This dissertation establishes a strong theoretical foundation for the innovative research of DPMs and provides effective technical support for their engineering applications.

KEY WORDS: Mechanism kinematics, Deployable polyhedral mechanism, Polyhedral transformation, Symmetry, Synchronized radial motion, Overconstraint reduction, Kinematic equivalence

Contents

List of Figures

List of Tables

Notation

Nomenclature

a	Edge length of regular polyhedrons
$a_{i(i+1)}$	Link lengths of linkages between joint i and joint i+1
c	Degree of overconstraint
c_{e}	Equivalent degree of overconstraint
h	Length of inclined sides in an octagon
l	Length of horizontal or vertical sides in an octagon
m	Number of degrees of freedom
r	Inscribed sphere radius of polyhedral mechanisms
x_i, y_i, z_i	x, y, z coordinate axis of system i
R	Circumscribed sphere radius of polyhedral mechanism
R_i	Offset of joint i
V	Volume of polyhedral mechanism
$\boldsymbol{S}_i$	Motion screws
$\boldsymbol{M}_i$	Constraint matrix
$\boldsymbol{Q}_{(i+1)i}$	3×3 transformation matrix from the i th coordinate system to the $i+1$th coordinate system
$\boldsymbol{T}_{(i+1)i}$	4×4 transformation matrix from the i th coordinate system to the $i+1$th coordinate system

Greek Alphabets

α	Angle between the revolute axes and platform edge in a Sarrus linkage
$\alpha_{i(i+1)}$	Twist angle of link $i(i+1)$ between joints i and i+1 o
β	Angle of the bottom in the polyhedral platform
γ	Angle between axes in two limbs in a Sarrus linkage
θ_i	Angle of rotation from x_i to x_{i+1} about axis z_i in joint i
φ_i	Dihedral angle for the i-th crease in the mechanical study

Abbreviations

2D	Two dimensional
3D	Three dimensional
DOF	Degree of freedom
DPM	Deployable polyhedral mechanism
D-H	Denavit-Hartenberg
G-K	Grübler-Kutzbach
T_d	Tetrahedral symmetry
O_h	Octahedral symmetry
I_h	Icosahedral symmetry
TP	Transformation path

Chapter 1 Introduction

1.1 Background and Significance

Deployable mechanisms[1], due to their extraordinary ability to fold a large structure into a compact size, have interested researchers over the past decades in the fields of civil engineering[2-7], aerospace exploration[8-16], robotics[17-22] and more. Some example engineering applications are shown in Fig. 1-1. Three-dimensional (3D) deployable mechanisms with a large volume deployment ratio[23, 24] offer several advantages, e.g., they enable various spatial shapes and sizes and can be deployed into larger structures with more functions[25]. Because of their low degrees of freedom (DOFs) and superiorly foldable properties, they have recently attracted increasing attention.

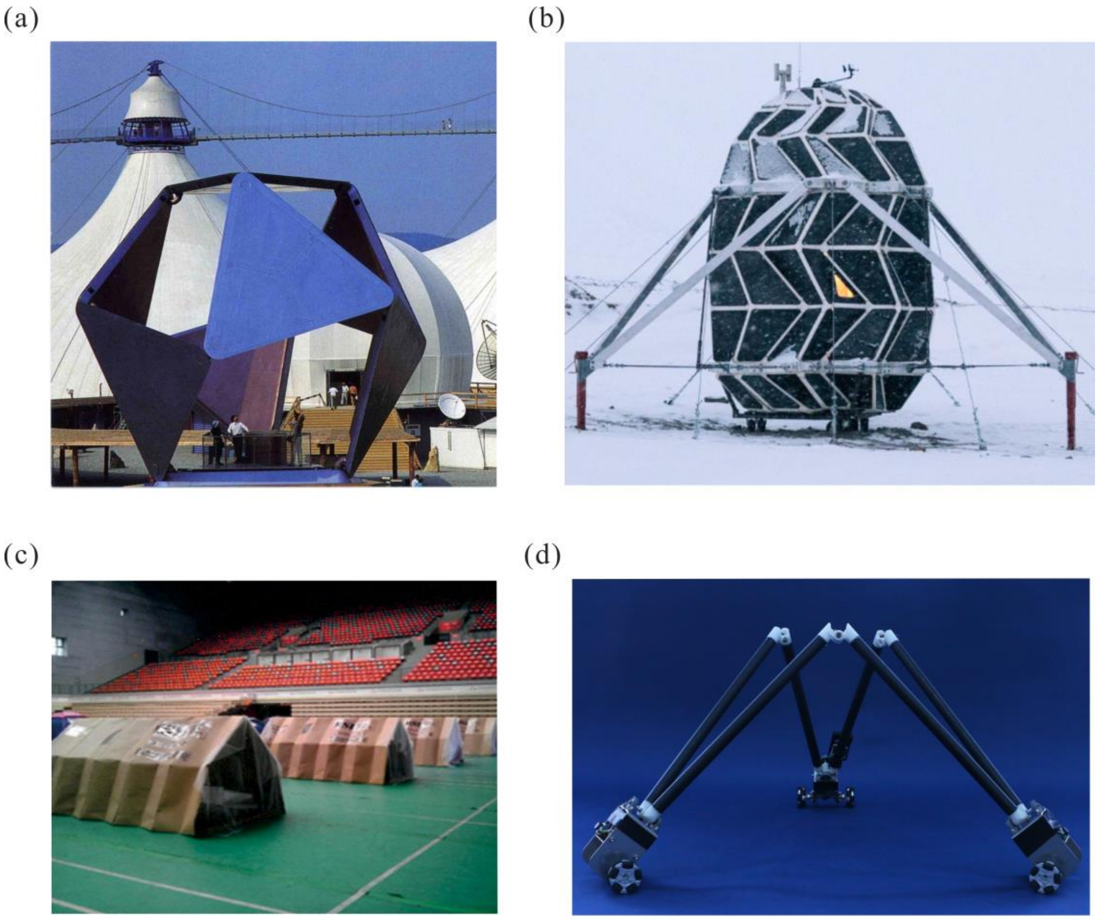

Fig. 1-1 Engineering applications of deployable mechanisms. (a) Heureka-polyhedron showpiece[7]; (b) lunar habitat[15]; (c) origami tent[16]; (d) Bricard-based deployable robot[22].

Deployable polyhedral mechanisms (DPMs) have been developed with various design strategies[26] by combining the ingenious inspirations of mechanism kinematics and solid geometry. Recent studies of DPMs have focused on embedding linkages and their mobile chains into vertices, faces and edges of regular convex polyhedrons[27], in which the design and assembly strategies of basic mechanism units play a key role in their constructions. Moreover, this may be beneficial for practical applications because the deploying or folding of DPMs can be more easily controlled owing to their lower degrees of freedom[28]. Compared to other deployable mechanisms, deployable polyhedral mechanisms have regular geometric configurations and higher volume folding ratios. Thus, they could attract the attention of both scientists and engineers, due to their potential applications in the fields of manufacturing, architecture and space exploration, such as human habitats on Mars that need to be folded neatly for launch. However, there is little work describing how to construct deployable polyhedrons and transformable polyhedrons by symmetrically synthesizing S4*R* linkages[29], overconstrained Sarrus linkages[30] and spatial 7*R* linkages[31]. Furthermore, DPMs with 1-DOF synchronized radial motion and symmetric transformability can enhance the development of 3D deployable mechanisms with modular and customizable potential[32], yet it remains challenging to determine a novel and systemic construction method for synchronized radial DPMs.

On the other hand, typical DPMs have multiloop overconstrained mechanisms[33-35] because the interconnection of each mechanistic units often results in a large number of redundant constraints. Due to the harsh working environment and the errors in fabrication, the overconstraints bring additional internal loads that can render those mechanisms immobile and reduce the reliability, which cannot be completely overcome simply by improving the manufacturing accuracy[36-38]. Therefore, it is useful to reduce or even eliminate the redundant constraints of the original overconstrained mechanism while maintaining their equivalent kinematic behaviors[39, 40]. In previous works, overconstraint reduction strategies were mainly based on replacement of hinge types and the removal of redundant hinges[41]. However, there remains a lack of a systematic guiding ideology for overconstraint reduction due to the complex topology relations of multiloop mechanisms, which is still a greatly challenging issue in kinematics. Nevertheless, the mathematics-inspired method could be explored to propose a reduction strategy for multiloop mechanisms and enhance their practical applications.

Therefore, the study of symmetric construction methods and overconstraint reduction strategies can pave the way for the development of deployable and transformable polyhedrons, which not only are valuable in theoretical investigation but also facilitate their applications in various engineering fields, such as deployable mechanisms for aerospace exploration and architecture, as well as metamaterials.

1.2 Literature Review

1.2.1 Kinematic Theory in Mechanism

Kinematics are an essential part of the study of mechanisms, which focuses on the geometric properties of the mechanism motion, including the positions, velocities and accelerations of links and joints without considering the forces that drive the motion. In the past, a number of kinematic methods have been proposed, including the matrix method[42-44], quaternion and duel quaternion method[45-51], bond theory[52-56], screw theory[57, 58], Lie group and Lie algebra[59-62], some of which are advantageous to analyze articular types of mechanisms and to identify specific mechanism parameters. For the design of mobile mechanism assemblies, it is vital to identify the positions and angular relations of the links in motion, while the other physical quantities are of less interest[63]. Here, some essential kinematic analysis methods, including the matrix method, screw theory and truss method, are used to reveal the kinematics of DPMs.

In kinematics, a mechanism is any linkage connected by kinematic joints, and the degree of freedom is the number of independent parameters required to determine the configuration of the mechanism[64]. Based on the Grübler-Kutzbach (G-K) formula[58], the expected mechanism mobility $M=d(n-g-1)+\Sigma f_i$, where d is the mobility coefficient that can be obtained from the motion screw system, n is the number of rigid links, g is the number of kinematic joints, and f_i is the degree of freedom of the ith kinematic joint.

The G-K criterion only considers the influence of mechanism topology on degrees of freedom. However, in practice, there are many special cases where the G-K criterion is inaccurate, and various correction formulas have been proposed to better calculate the degrees of freedom of all types of mechanisms using only one formula[65], yet with few favorable outcomes, because the influence of specific geometric parameters for the mechanism have not been completely considered. Moreover, a mechanism can realize a full periodic range of motion even though the G-K criterion indicates otherwise. This type of mechanism is called the overconstrained mechanism with greater mobility than that predicted by the mobility criterion due to the strict geometry conditions that are known as overconstrained conditions[66]. Thus, the degrees of overconstraint c [35] in one overconstrained mechanism can be derived as $c = m - M$, in which m represents the actual degrees of freedom. However, many deployable mechanisms are multiloop overconstrained mechanisms that increase the stiffness of the entire deployable system yet reduce the reliability due to the overconstrained conditions.

1.2.2 Spherical Linkages and Spatial Linkages

1.2.2.1 Spherical Linkages and Rigid Origami

With the rapid development of origami engineering in this century[67], many origami-inspired foldable structures have been widely adopted in the fields of aerospace devices[68], civil engineering[69], robotics[70], metamaterials[71] and so on. Rigid origami, as a branch of origami, paves the way for widespread engineering applications of origami mechanisms due to the advantage of folding rigid materials without any deformation[72]. In mechanism theory, the sheets and creases of rigid origami can be modelled as equivalent rigid links and revolute joints[73], respectively, where an origami vertex at the intersection of creases is regarded as a spherical linkage[74], such as the typical four-crease origami vertex, which can be kinematically modelled as a spherical 4*R* linkage (S4*R*), see Fig. 1-2. Thus, a rigid origami pattern is kinematically equivalent to an assembly of spherical linkages[75]. Many known origami patterns have been investigated with mechanism kinematics to reveal their specific folding characteristics, e.g., Miura pattern[76], square-twist pattern[71], diamond pattern[77] and waterbomb pattern[78].

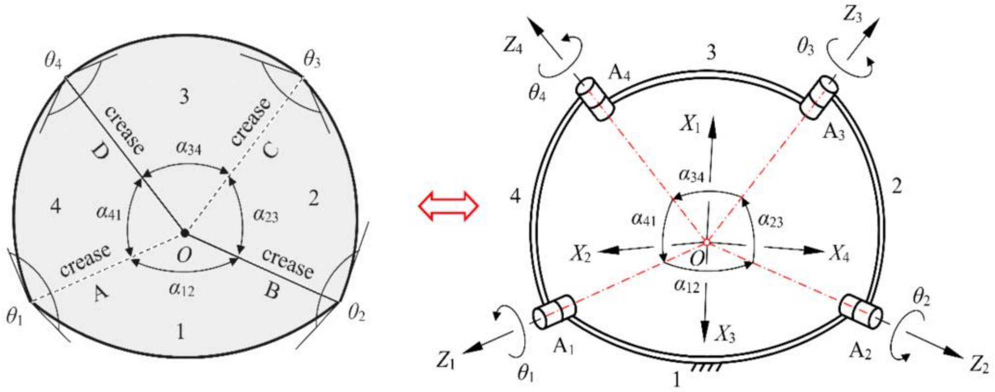

Fig. 1-2 A four-crease origami vertex and its equivalent S4*R* linkage[75].

In addition to the mentioned 2D typical patterns that can be folded and unfolded into flat surfaces, several 3D origami mechanisms can also be folded flat with novel crease patterns, including origami tubes, cartons and cubes. Inspired by the cylindrical origami tubes devised by Tachi[79], Liu et al.[16] presented a family of origami prismatic mechanisms by solving the compatibility of the assembly of spherical 4R linkages, and Chen et al.[80] provided a more flexible design for origami tubes by combining several tubes with parallelograms or kite cross sections. In addition, as demonstrated in Fig. 1-3(a), Wu and You[81] presented a new solution for rigid and flat foldable tall bags without considering the top surface. Wei and Dai[74] investigated the geometry and kinematics of equivalent mechanisms evolved from a crash-lock origami carton, as shown in Fig. 1-3(b). Gu and Chen[82] proposed a new approach for constructing rigid origami boxes with various geometries and shapes by using spherical linkage loops. Furthermore, Gu and Chen[23] developed a total of four crease patterns that enable origami cubes with rigid and flat foldability and a single degree of freedom, for which an example with a spherical 4R-5R-4R-5R loop is shown in Fig. 1-3(c).

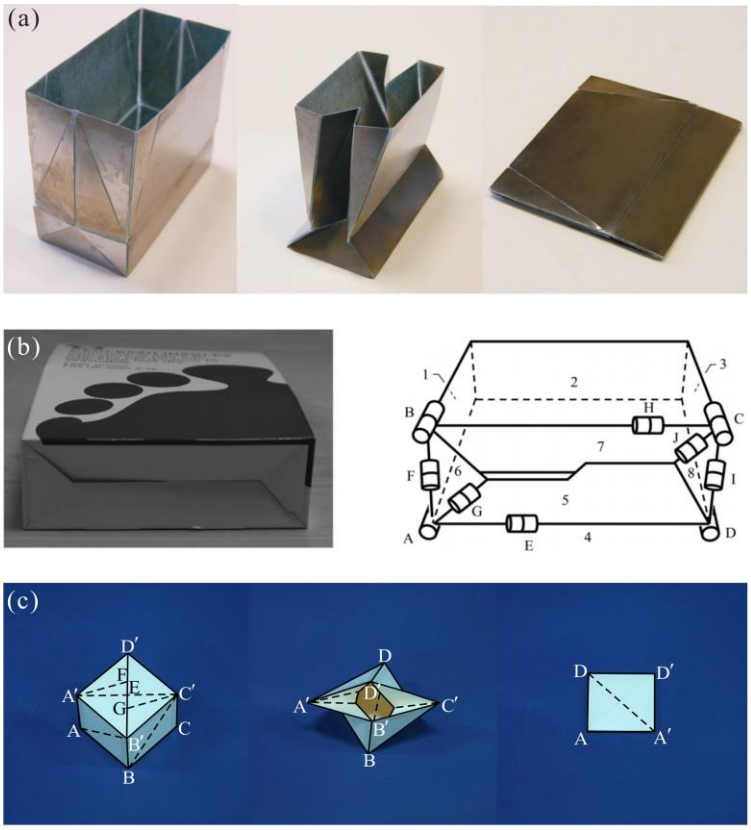

Fig. 1-3 3D origami and kirigami mechanisms. (a) Rigid origami shopping bag[81]; (b) crash-lock base origami carton[74]; (c) rigid ang flat foldable origami cube[23].

Thus, prior research shows that it is impossible to rigidly fold the 3D sealed structures, in which hollows and slits should be introduced to fold such spatial structures[83]. Furthermore, due to the geometric complexity and limitations of these structures, the layout and arrangement of creases and slits are still challenging for the design of spatially deployable mechanisms, especially for regular deployable polyhedrons.

1.2.2.2 Spatially Overconstrained Linkages

Overconstrained linkage is a unique type of spatial mechanism with greater mobility than that predicted by the mobility criterion[66]. The first published research on spatial overconstrained linkages can be traced back to the Sarrus linkage[30], as shown in Fig. 1-4, which is capable of exact straight-line motion between platforms A and B. Thereafter, more overconstrained mechanisms were developed with more attention from mathematicians, scientists and engineers, such as, to mention but a few, the Bennett linkage[84], Bricard[85, 86], Wohlhart[87] and Waldron linkages[88].

Furthermore, various multiloop overconstrained mechanisms with high expansion ratios can be constructed through the synthesis of the above single-loop overconstrained linkages. Zhang and Chen[89] proposed mobile assemblies of Bennett linkages from four-crease thick origami patterns. Qi et al.[90] developed two types of large spatial deployable networks based on Myard linkages with different twist angles. Based on Bricard linkages, a mobile assembly with a threefold-symmetric configuration was presented by connecting any two adjacent linkages with a scissor [91], and integrated networks of plane-symmetric Bricard linkages were discovered referring to diamond thick-panel origami[92]. and a new family of Bricard-derived deployable mechanisms was derived with a large volume[93]. However, there is little work reported on the assembly of Sarrus linkages.

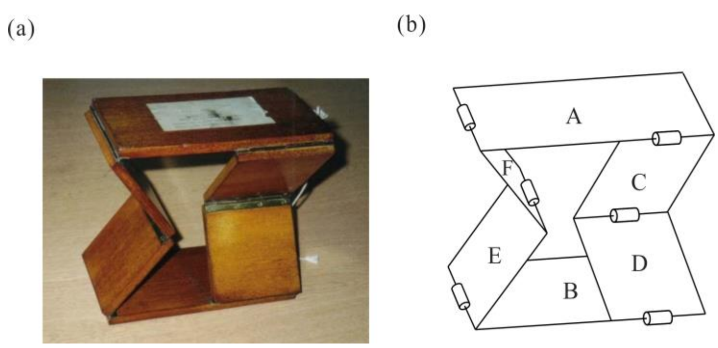

Fig. 1-4 Sarrus linkage[30]. (a) A physical model; (b) a mechanism diagram.

1.2.2.3 Spatial 7*R* and 8*R* Linkages

Referring to the G-K formula[58], a spatial 7*R* linkage is generally 1-DOF, in which plane-symmetric 7*R* linkages are preferred to design the spatial deployable mechanisms. Xu et al.[94] proposed a deployable tetrahedron unit mechanism to design truss antennas, i.e., a 3*RR*-3*RRR* multiloop coupled mechanism[95], which is actually an assembly of plane-symmetric 7*R* linkages. Similarly, the plane-symmetric 7*R* linkage shown in Fig. 1-5(a) is used to construct a two-layer and two-loop spatial deployable mechanism, which is capable of accurate straight-line motion[96]. Furthermore, Zhou et al.[97] developed a general plane-symmetric 7*R* linkage, as shown in Fig. 1-5(b), to fold a triangular frustum into a bundle, as well as various polygons and polyhedrons. Recently, a systematic synthesis method based on a symmetric 7*R* single-loop mechanism was presented to address the structural design of two-dimensional truss-shaped deployable aerospace platforms with 1-DOF synchronized motion[98]. In contrast, Kong[99, 100] proposed a variable-DOF single-loop 7*R* spatial mechanism with five motion modes, which is based on the combination of a general variable-DOF single-loop 7*R* spatial mechanism and a plane-symmetric Bennett 6*R* mechanism.

However, an 8*R* linkage without overconstrained conditions has two DOFs. As shown in Fig. 1-5(c), Wei and Dai[33] proposed a two-DOF single-loop dual-plane-symmetric spatial 8*R* linkage that performed exact straight-line motion, in which a geared 8*R* linkage is then incorporated to generate a 1-DOF exact straight-line motion. Furthermore, a reconfigurable 8*R* linkage constructed by using a variable revolute joint was introduced by Wei and Dai[101]. Then, a Sarrus-like overconstrained spatial 8*R* linkage has been reported that can be treated as a two-limb parallel mechanism (see Fig. 1-5(d)), in which straight-line motion between two platforms can also be obtained even though this overconstrained linkage has three DOFs[102] due to two groups of four parallel joints. In their work, in addition to the Sarrus linkage, those two nonoverconstrained spatial 8*R* linkages can also generate the exact straight-line motion. Furthermore, Chai et al.[103] proposed an 8*R* square mechanism based on two alternative Bennett mechanisms. Several 8*R* linkages can be found in metamorphic mechanisms, such as a reconfigurable 8*R* mechanism proposed by Wang et al.[104] can realize a square shape.

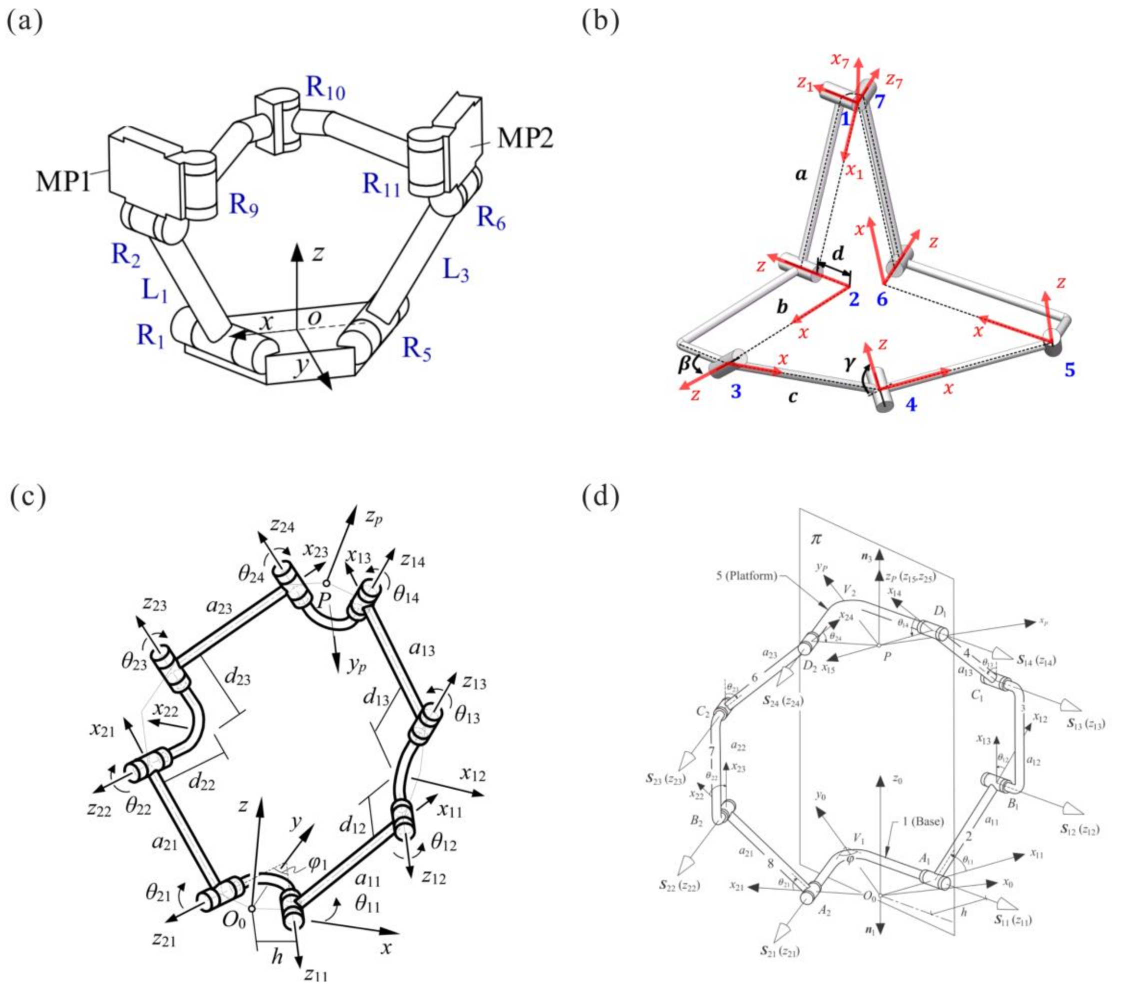

Fig. 1-5 Spatial 7*R* and 8*R* linkages. (a) A 7*R* linkage with linear motion[96]; (b) A plane-symmetric 7*R* linkage[97]. (c) An 8*R* linkage with straight-line motion[33]; (d) an overconstrained 8*R* linkage[102].

1.2.3 Polyhedral Transformations in Geometry

A polyhedron is a three-dimensional shape with flat polygonal faces, straight edges and sharp corners or vertices, in which a polyhedron that bounds a convex set is called a convex polyhedron. For the convex regular polyhedrons in 3D Euclidean space, their faces are congruent regular polygons and are assembled in the same way around each vertex, in which two classic groups are Platonic polyhedrons (five types) and Archimedean polyhedrons (thirteen types)[105] (see Figs. 1-6). The five Platonic polyhedrons in Fig. 1-6(a) are tetrahedron, hexahedron (cube), octahedron, dodecahedron and icosahedron, and the thirteen Archimedean polyhedrons in Fig. 1-6(b) are truncated tetrahedron, cuboctahedron, truncated cube, truncated octahedron, rhombicuboctahedron, truncated cuboctahedron, icosidodecahedron, truncated dodecahedron, truncated icosahedron, rhombicosidodecahedron, truncated icosidodecahedron, snub cube and snub dodecahedron.

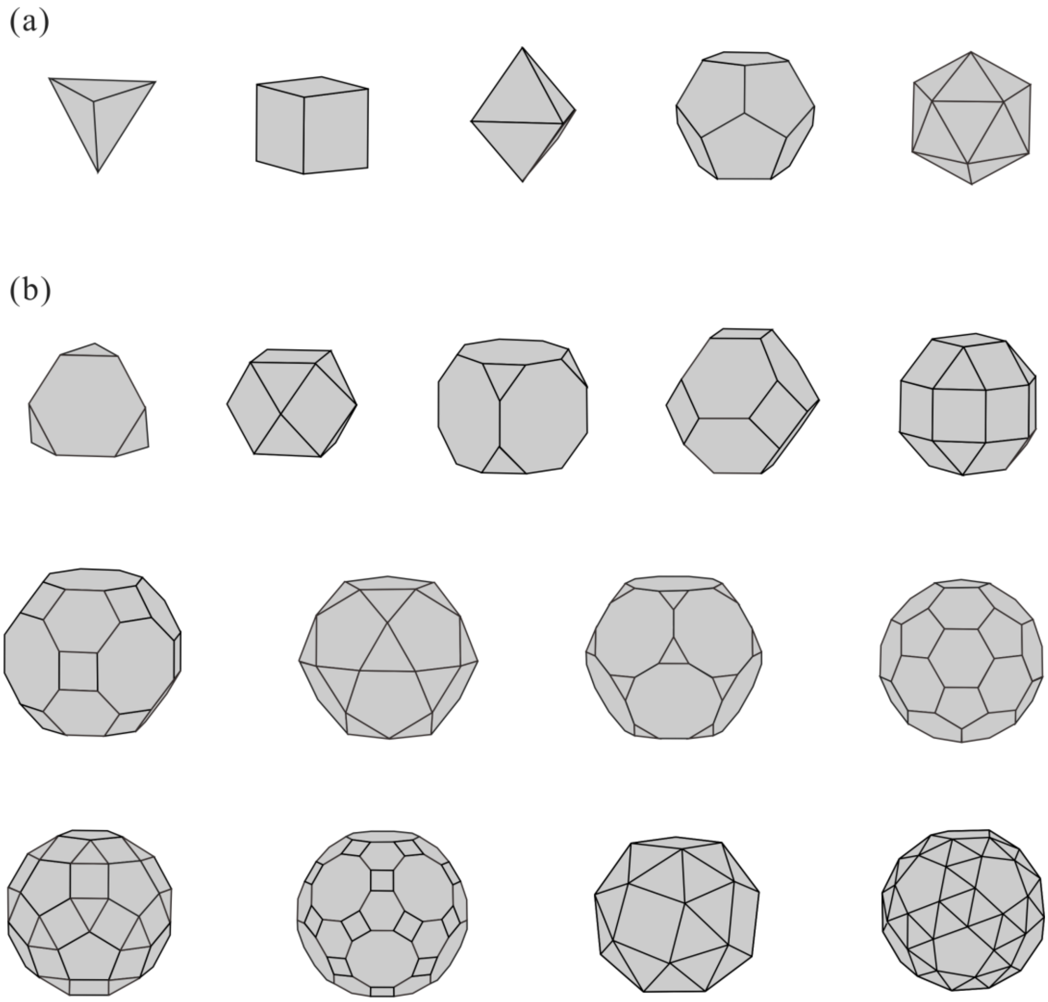

Fig. 1-6 Two classic groups of regular polyhedrons. (a) Five Platonic polyhedrons and (b) thirteen Archimedean polyhedrons.

Moreover, we find some interesting polyhedral pairs among Archimedean and Platonic polyhedrons through mathematical transformations, which are demonstrated following tetrahedral (T_d), octahedral (O_h), and icosahedral (I_h) symmetries[106].

First, considering a truncated tetratetrahedron with T_d symmetry in Fig. 1-7 as an example, three types of edge lengths in a truncated tetratetrahedron are defined as *a*, *b* and *c*, in which each length is related to two adjacent facets in two different colours. Based on this, for instance, if we only shorten the edge length *a* to zero while *b* and *c* are retained in transformation path 1 (TP1), then all yellow hexagon facets will become triangles, and the cyan squares will vanish, yet the blue hexagons remain intact. As a result, the polyhedral geometric transformation from a truncated tetratetrahedron to a truncated tetrahedron is obtained in TP 1. Subsequently, if edge length b is shortened to zero while a and c are reserved in TP 2, i.e., all yellow hexagon facets are reserved, leading to the same transformation as given in TP1 due to the duality of the tetrahedron. Next, a transformation from a truncated tetratetrahedron to a rhombitetratetrahedron is shown in TP 3 by only shortening the edge length c to zero and reserving all cyan squares.

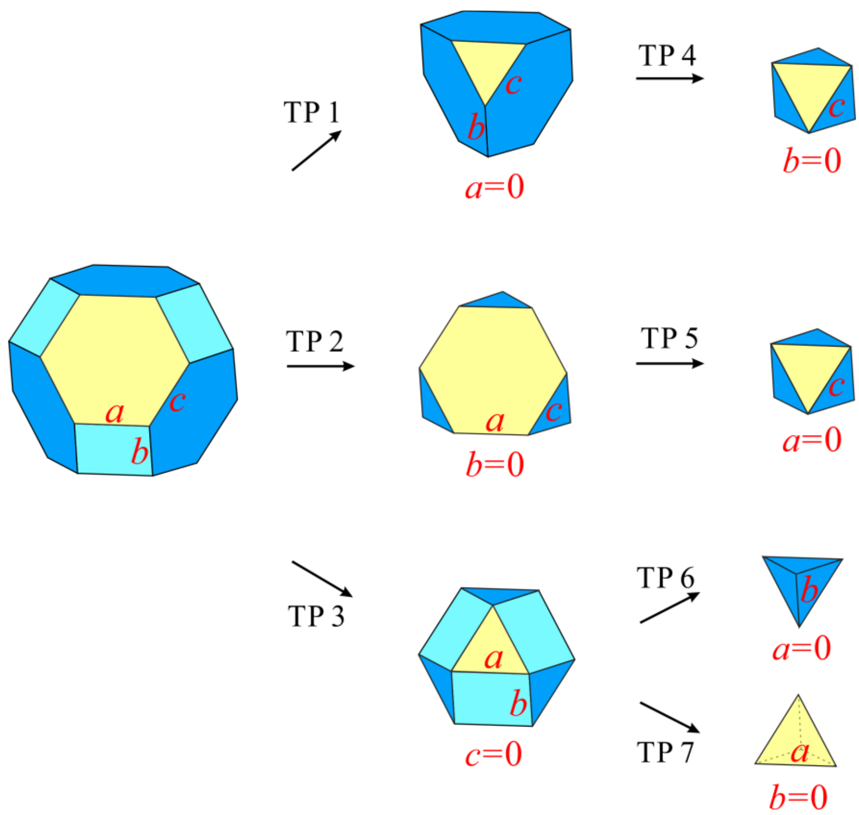

Fig. 1-7 Transformations of polyhedrons with the same T_d symmetry. TP 1 and TP 2: transformation from a truncated tetratetrahedron to a truncated tetrahedron. TP 3: transformation from truncated a tetratetrahedron to a rhombitetratetrahedron. TP 4 and TP 5: transformations from a truncated tetrahedron to a tetratetrahedron. TP 6 and TP 7: transformations from rhombitetratetrahedron to tetrahedron.

On the other hand, further transformations based on the results of TP 1 to TP 3 in Fig. 1-8 can also be demonstrated by shortening the remaining edge length. In TP 4, a truncated tetrahedron becomes a tetratetrahedron when the edge length b shortens to zero, as well as the same transformation in TP5. Finally, taking similar operations for a rhombitetratetrahedron, two dual tetrahedrons occur along TP 6 and TP 7. Regardless of which transformation, T_d symmetry is always reserved in each paired case.

These geometric transformations can be immediately applied to the other Archimedean polyhedrons with O_h and I_h symmetries. As shown in Fig. 1-9, three types of edge lengths a, b and c are defined in a truncated cuboctahedron. If edge length a is shortened to zero while b and c are retained in TP1, then all the blue octagons are still reserved, leading to the transformation from a truncated cuboctahedron to a truncated cube. Subsequently, if the edge length b is shortened to zero in TP 2, a transformation from an original truncated cuboctahedron to a truncated octahedron is realized. Similarly, a transformation from an original truncated cuboctahedron to a rhombicuboctahedron is shown in TP 3 by only shortening the edge length c to zero; thus, all cyan squares are reserved.

Next, in TP 4, a truncated cube becomes a cuboctahedron when the edge length b shortens to zero, and shortening the edge length a of a truncated octahedron results in a cuboctahedron in TP 5. Finally, referring to TP 6 and TP 7, we can obtain a cube and an octahedron by making edge lengths a and b in a rhombicuboctahedron equal to zero, respectively. Due to the synchronized geometry operations for edge length, O_h symmetry is always reserved in each paired transformation. Compared with the transformations with T_d symmetry in Fig. 1-8, this family of O_h transformations can realize all seven distinct solutions due to its O_h duality between a cube and an octahedron.

In addition, similar to the cases in Figs. 1-8, we can obtain seven different transformations from TP1 to TP7 beginning from a truncated icosidodecahedron with I_h symmetry; the details can be found in Figs. 1-9. Here, in TP 1 to TP 3, all deployable configurations are truncated icosidodecahedrons, similarly leading to three different folded configurations. In particular, dodecahedrons and icosahedrons occur along TP 6 and TP 7, respectively. Additionally, regardless of the transformation, I_h symmetry is always preserved in each paired case. Thus far, all five Platonic polyhedrons are demonstrated in Figs. 1-7 to 1-9.

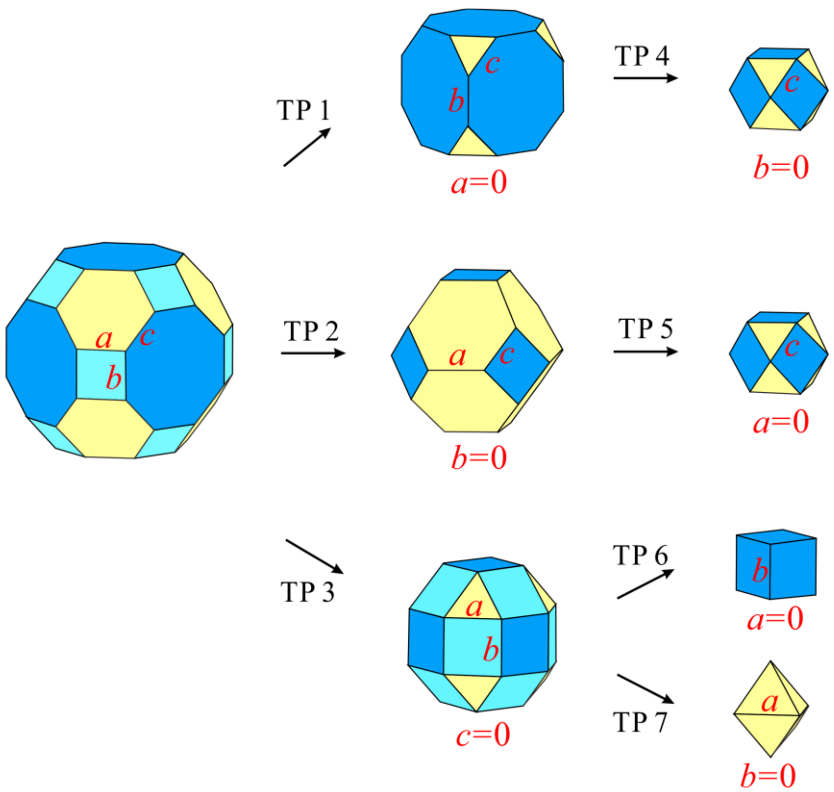

Fig. 1-8 Transformations of polyhedrons with the same O_h symmetry. TP 1: transformation from a truncated icosidodecahedron to a truncated dodecahedron. TP 2: transformation from a truncated icosidodecahedron to a truncated icosahedron. TP 3: transformation from truncated icosidodecahedron to rhombicosidodecahedron. TP 4: transformation from a truncated dodecahedron to an icosidodecahedron. TP 5: transformation from a truncated icosahedron to an icosidodecahedron. TP 6: transformation from rhombicosidodecahedron to dodecahedron. TP 7: transformation from rhombicosidodecahedron to icosahedron.

Thus far, in addition to two special Archimedean polyhedrons without symmetry, i.e., the snub cube and snub dodecahedron in Fig. 1-6 (last two polyhedrons), the geometric transformations among the remaining eleven Archimedean and all five Platonic polyhedrons have been demonstrated following T_d, O_h and I_h symmetries, respectively. Among these transformations, a total of eighteen transformations are identified without duplicate cases, of which four, seven and seven cases are respectively shown in Figs. 1-7 to 1-9. The richer geometric transformations have been identified following different symmetries, yet it is challenging to realize these structures using a kinematic strategy due to the design of novel mechanism units and their coordinated tessellations. Here, it is shown that this objective can be achieved by the introduction of 1-DOF transformable and deployable polyhedral mechanisms.

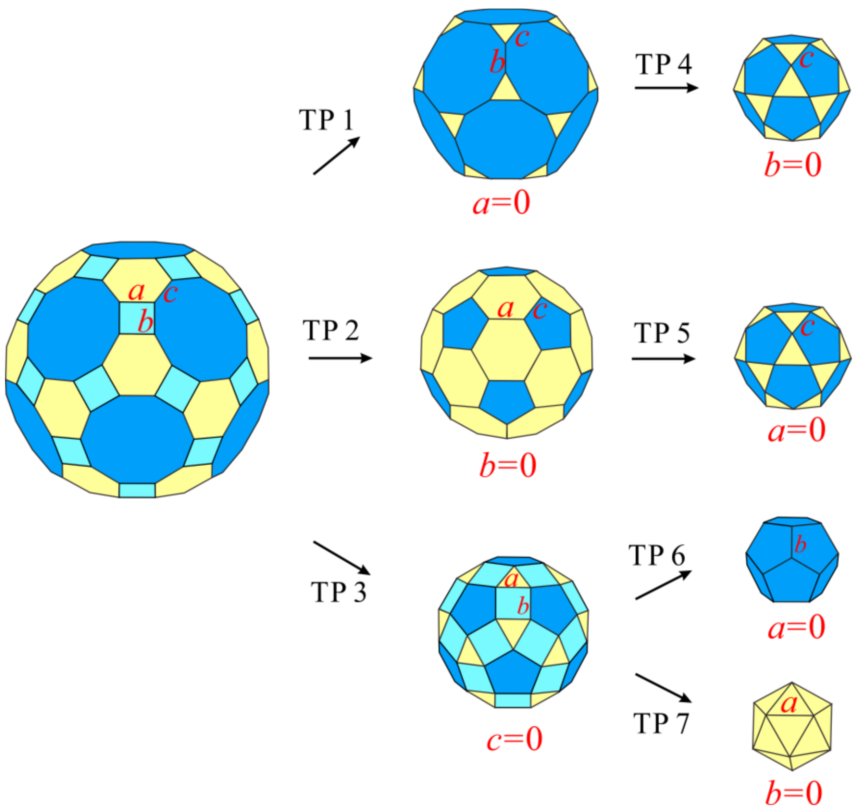

Fig. 1-9 Transformations of polyhedrons with the same I_h symmetry. TP 1: transformation from a truncated icosidodecahedron to a truncated dodecahedron. TP 2: transformation from a truncated icosidodecahedron to a truncated icosahedron. TP 3: transformation from truncated icosidodecahedron to rhombicosidodecahedron. TP 4: transformation from a truncated dodecahedron to an icosidodecahedron. TP 5: transformation from a truncated icosahedron to an icosidodecahedron. TP 6: transformation from rhombicosidodecahedron to dodecahedron. TP 7: transformation from rhombicosidodecahedron to icosahedron.

1.2.4 Deployable Polyhedral Mechanisms

Deployable polyhedral mechanisms and transformable polyhedral mechanisms have been developed with various design strategies, in which the design of deployable polyhedrons combines the ingenious inspirations of solid geometry and mechanism kinematics[29]. Verheyen[107] reported pioneering work on expandable polyhedral mechanism known as Jitterbug transformers (see Fig. 1-10(a)). Similarly, it was the well-known showpiece of a mobile octahedron named “Heureka-polyhedron”[7] built at the Heureka Exposition in Zurich in 1991[108], which was obtained from Fuller’s Jitterbug by replacing spherical joints with two-DOF Hooke’s joints. Furthermore, based on the Fulleroid[109], the construction methods of Fulleroid-like polyhedral mechanisms were proposed by Wohlhart[110], Kiper[111] and Röschel[112]. Furthermore, several overconstrained linkages were adopted for the synthesis of DPMs. As shown in Fig. 1-10(b), Kiper and Söylemez[113] introduced a deployable tetrahedral polyhedron by integrating multiple loops of equilateral Bennett linkages, yet with a rather small expansion ratio. Wang and Kong[114, 115] demonstrated a family of overconstrained multiloop DPMs by connecting orthogonal single-loop linkages, including the orthogonal Bricard linkage, as shown in Fig. 1-10(c), using *S*-joints. Moreover, taking the four-sided antiprism mechanism constructed by asymmetric eight-bar linkage as an example[116], see Fig. 1-10(d), various DPMs based on prisms and antiprisms have been developed following prismatic geometry[116-120].

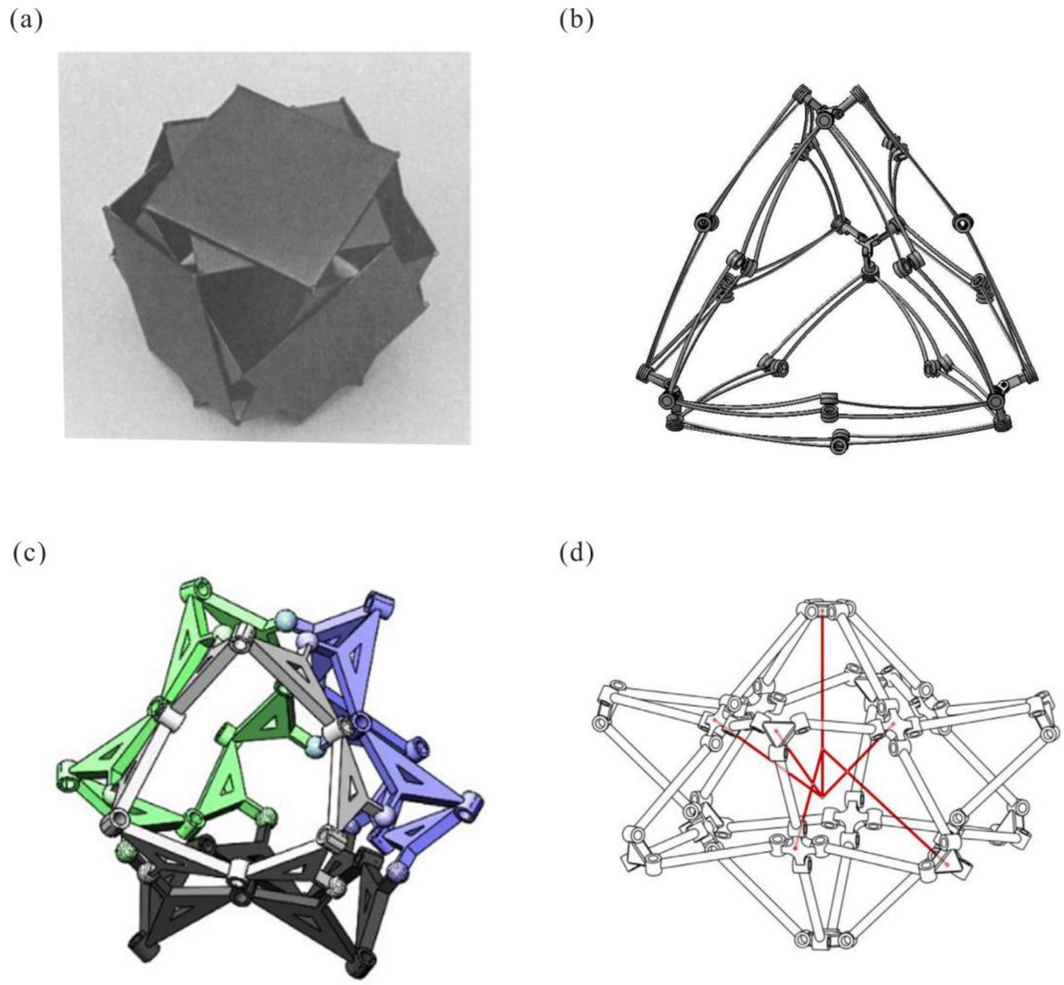

Fig. 1-10 Deployable polyhedral mechanisms. (a) Jitterbug transformers[107]; (b) Bennett-based DPM[113]; (c) Bricard-based DPM[114]; (d) four-sided antiprism DPM with asymmetric eight-bar linkage[116].

1.2.4.1 Polyhedral Mechanisms with Deployable Transformability

The interesting polyhedral transformations among Archimedean and Platonic polyhedrons through mathematical operations are shown in Figs. 1-7 to 1-9. Transformable polyhedrons are mathematically interesting yet kinematically challenging. However, some existing designs introduce many constraints that make control of the conversion process extremely difficult and cumbersome, thus limiting the practical application of these mechanisms. Thus, to facilitate the control of transformations, transformable polyhedrons with a kinematic strategy require few DOFs, and the internal space must not be occupied by complex joints.

Yang et al.[121] realized a 1-DOF transformation between cuboctahedron and octahedron based on a spatial multiloop mechanism, which was constructed by two Bennett linkages and four *RSRS* linkages, as shown in Fig. 1-11(a). Then, as shown in Fig. 1-11(b), they constructed a 1-DOF polyhedral transformation between a truncated octahedron and cube by setting up two threefold-symmetric Bricard linkages with the same parameters, while other related vertices were set with *R* or *S* joints[122]. Similarly, a 1-DOF transformation between the truncated tetrahedron and tetrahedron was achieved and constructed with one threefold-symmetric Bricard 6*R* linkage and three *RSRRSR* linkages with a large volume deployable ratio of 23[123]. Furthermore, various transformable polyhedrons have been constructed to mechanically transform cyclic polyhedrons into their corresponding dual forms[124-127]. Wohlhart[128] proposed a variety of new twisting towers that can be derived on the basis of three special Archimedean polyhedrons, i.e., cuboctahedron, rhombicuboctahedron and rhombicosidodecahedron, by omitting square side facets and setting up 2*R*-joints at the vertices, in which the 1-DOF transformation from a rhombicuboctahedron to a cuboctahedron is identified and illustrated in Fig. 1-11(c). In addition, the concept of transformable polyhedrons with articulated faces was proposed by Laliberté and Gosselin[129], which was described as polyhedral frameworks with faces that were constrained to remain planar, for which the mechanical assembly of a cube with articulated planar faces is given in Fig. 1-11(d). Nevertheless, this type of DPM had more DOFs and could generate more shape transformations, which offered potential applications in fields such as reconfigurable deployable mechanisms.

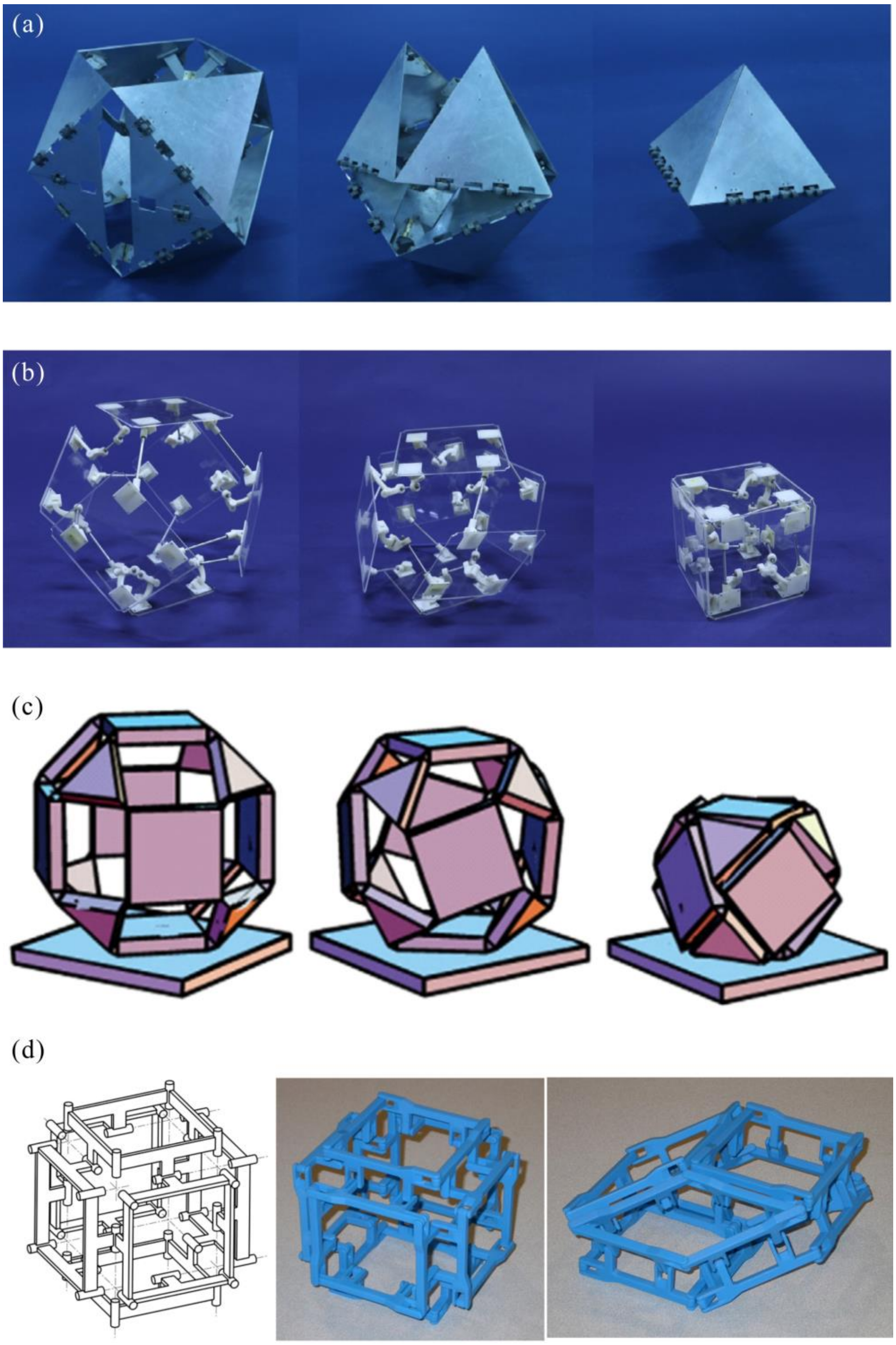

Fig. 1-11 Transformable polyhedral mechanisms. (a) Transformation of cuboctahedron and octahedron[121]; (b) transformation between truncated octahedron and cube[122]; (c) transformation between rhombicuboctahedron and cuboctahedron[128]; (d) transformation of cube and its general configuration[129].

1.2.4.2 Polyhedral Mechanisms with Synchronized Radial Motion

In addition to the above investigations, there is a special type of DPM that is capable of performing radial motions with shape-keeping capability. As shown in Fig. 1-12(a), a popular toy named Hoberman Sphere[130] with 1-DOF radial motion was produced by combining Sarrus linkages and scissor-like elements. To retain the exterior shape during deployment, Agrawal et al.[131] set up radially expanding polyhedrons by introducing prismatic joints to polyhedral edges. Based on 1-DOF regular polygon-shaped planar linkages, Gosselin and Gagnon-Lachance[132] developed a family of expandable polyhedral mechanisms by assembling planar linkages with spherical joints to retain the shape; as an example, a cubic mechanism is demonstrated in Fig. 1-12(b). Similar polyhedral mechanisms were synthesized by integrating the assembly of planar mechanisms into the edges[133, 134] and faces[135, 136] of various polyhedrons.

In addition, based on plane-symmetric spatial eight-bar linkage and a virtual-axis-based method, Wei and Dai [35] proposed a synthesis mothed for constructing a family of overconstrained regular and semiregular DPMs possessing 1-DOF radially reciprocating motion, in which the prototype hexahedral mechanism is presented in Fig. 1-12(c). Furthermore, reconfigurable DPMs constructed by using a variable revolute joint were introduced by Wei and Dai[101]. Furthermore, Xiu et al.[137] developed a synthesis approach for generating Fulleroid-like Platonic and Archimedean DPMs by integrating the mentioned overconstrained eight-bar linkages into the Archimedean polyhedron bases, in which a Fulleroid-like deployable cuboctahedral mechanism is given in Fig. 1-12(d). Recently, taking 1-DOF polygonal prisms as basic units, group DPMs with radially reciprocating motion were proposed based on an additive-then-subtractive design strategy, where a deployable regular-tetrahedron mechanism was selected as a design example to show the procedure of their synthesis method[26].

Various deployable polyhedral mechanisms have been proposed in the past two decades, yet there is little work on how to construct DPMs together with radial motion and shape transformation, in which it is challenging to design the basic mechanism units with synchronized motion and obtain their assembly strategy. Although the prismatic joints, planar scissor-like linkages and eight-bar linkage were adopted in the reported works, other new radial mechanism units have not been proposed as well as their novel spatial tessellations following polyhedral symmetries.

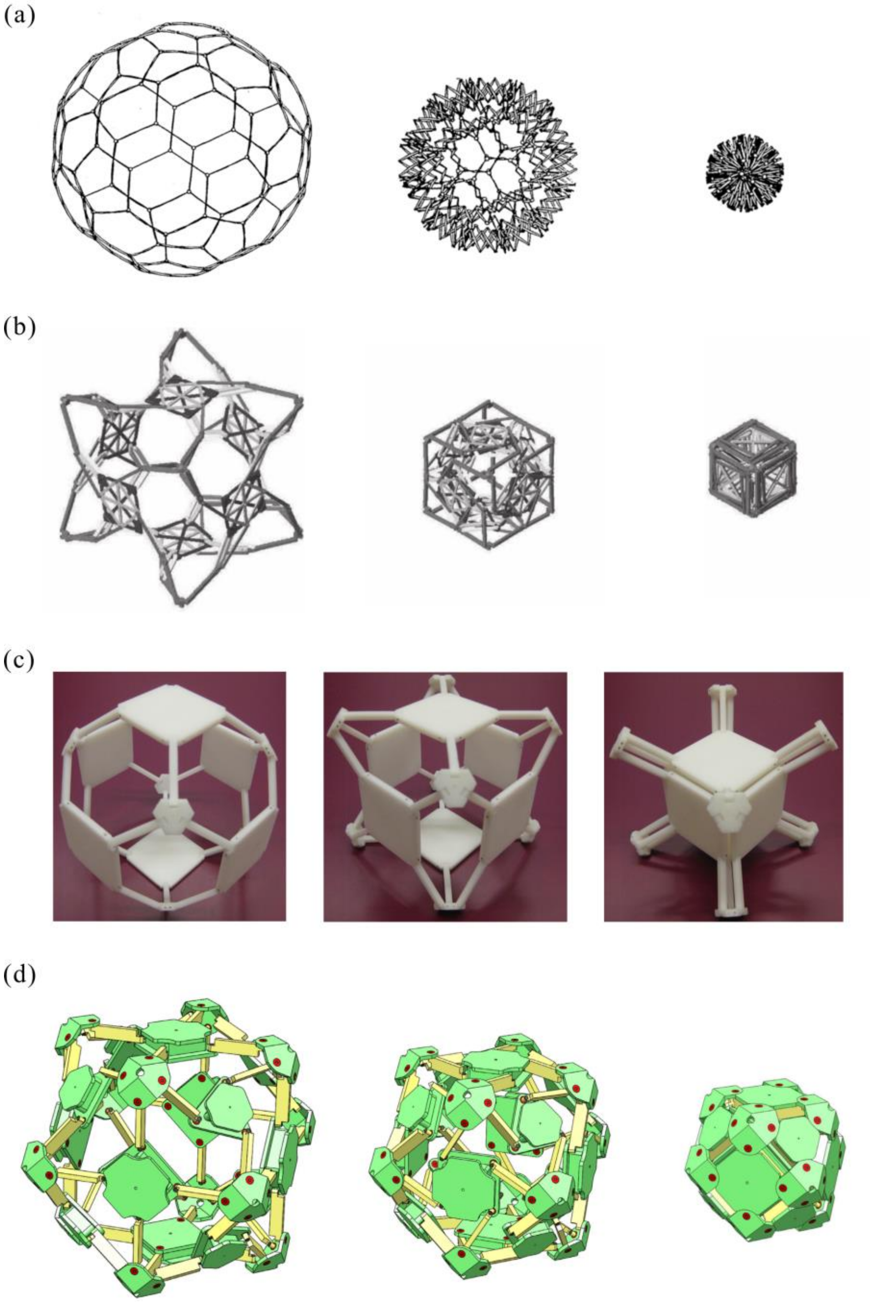

Fig. 1-12 Polyhedral mechanisms with synchronized radial motion. (a) Hoberman Sphere[130]; (b) a cubic mechanism constructed by planar linkages with spherical joints[132]; (c) hexahedral mechanism based on plane-symmetric spatial eight-bar linkages[35]; (d) Fulleroid-like deployable cuboctahedral mechanism based on overconstrained eight-bar linkages[137].

1.2.5 Overconstraint reduction Strategy

The aforementioned 3D deployable mechanisms, especially DPMs, offer great potential in deployable mechanisms for space exploration[138, 139]. However, the interconnection of these overconstrained linkages often results in a large number of redundant constraints in deployable mechanisms[140]. Moreover, most deployable polyhedral mechanisms are overconstrained multiloop mechanisms[28]. To ensure the motion of the overconstrained mechanisms, the strict overconstrained geometric conditions of links and joints must be satisfied. Nevertheless, due to the harsh working environment of those deployable mechanisms and the errors in fabrication, the overconstraints bring additional internal loads that can render those mechanisms immobile and reduce the reliability in the operation of the deployable mechanisms, which cannot be completely overcome by simply improving the manufacturing accuracy[38, 141]. Therefore, it is important to reduce or even eliminate the redundant constraints of the original overconstrained mechanism by designing a less-overconstrained or nonoverconstrained form while maintaining their equivalent kinematic behaviours.

Several overconstraint reduction strategies for single-loop and 2D multiloop mechanisms have been developed. To reduce the degree of overconstraint in a Bennett linkage, an *RRRS* linkage with kinematic equivalence was reported by using a spherical joint to replace a revolute joint[142, 143], yet overconstraints still exist in this linkage. Furthermore, Yang et al.[25] proposed a truss method based on Maxwell's rule[144] to obtain a nonoverconstrained form of the Bennett linkage as the *RSSR* linkage, as well as that of the Myard linkage as the *RRSRR* linkage. Recently, several methods to address the overconstraint reduction of origami mechanisms have been developed. Based on joint removal with kinematic equivalence, Brown et al. proposed certain reduction methods to reduce the redundant constraints of zero-thickness origami-based mechanisms, such as connected 1-DOF sections and end-to-end chains[145], for which the reduced hexagonal pattern is shown in Fig. 1-13(a). Similar reduction approaches have been applied in Miura-ori-based deployable arrays[146]. In addition, the hinge-removing technique[41] was presented for thick-panel origami based on the construction of a Waldron hybrid 6*R* linkage from two Bennett linkages, as demonstrated in Fig. 1-13(b), which facilitates the engineering application of thick-panel origami, as it can create a flat working surface in the deployed state. Furthermore, a novel folding method of uniform-thickness panels was proposed, as shown in Fig. 1-13(c), which can be treated as a modified Miura-ori where slits are introduced along the diagonals of some facets to reduce constraint[147]. The two triangular panels separated by a slit move apart during deployment, yet they are always parallel, which mimics the motion of the original Miura-ori pattern.

However, few works have reported on how to reduce the overconstraints of 3D multiloop DPMs while preserving their motion behaviour. The novel reduction strategy for complex multiloop overconstrained mechanisms should be further explored, in which mathematics could provide special inspirations to address this problem.

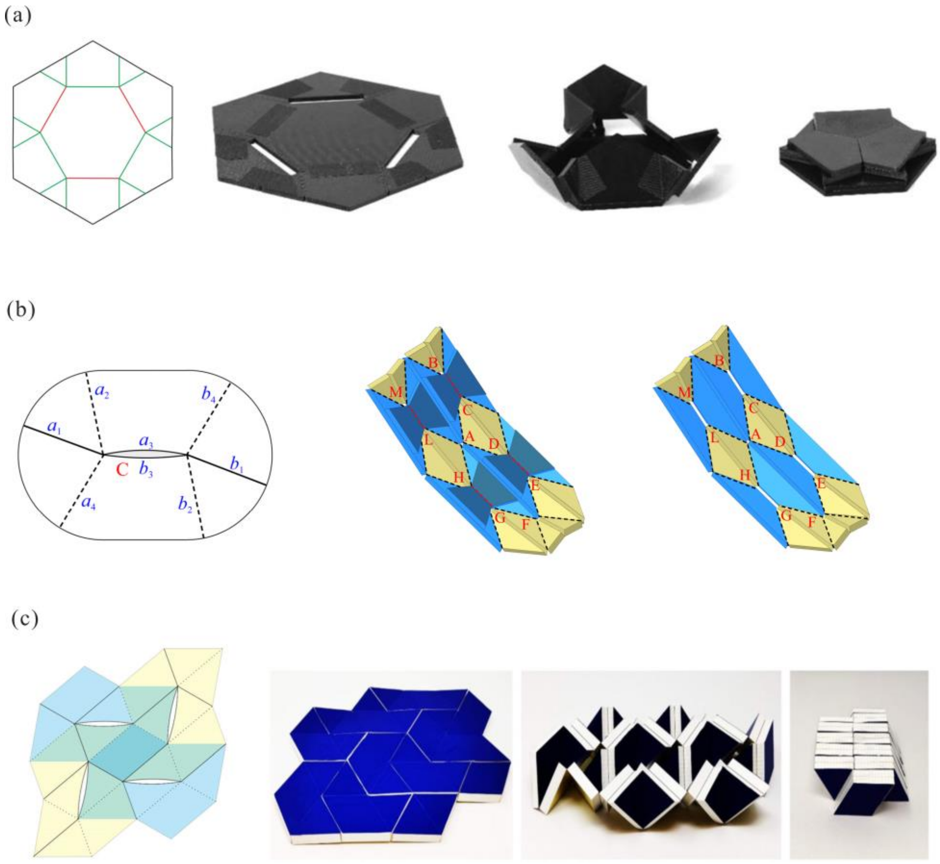

Fig. 1-13 Joint removal of 2D origami mechanisms. (a) Joint removal in hexagonal patterns[145]; (b) joint removal in thick-panel origami with four- and six-creased vertices[41]; (c) a modified Miura-ori pattern with slits[147].

1.3 Aim and Scope

This dissertation proposes a construction method of novel DPMs with 1-DOF synchronized radial motion, accomplishes richer polyhedral transformations with a mechanism kinematic strategy, investigates the mechanism topology following polyhedral symmetry, and proposes a novel overconstraint reduction strategy for multiloop overconstrained DPMs by combining kinematics and mathematics.

In this process, by introducing S4*R* linkages to provide symmetric motion, the approach to construct S4*R*-based polyhedrons with 1-DOF radial motion is first investigated. Based on the S4*R*-synchronized mechanism, a construction method of nine transformable polyhedral mechanisms with distinct symmetries is presented by embedding the S4*R*-synchronized mechanism cells into the surface of Archimedean polyhedrons. Then, the synthesis method, kinematic analysis and constraint reduction of Sarrus-based deployable polyhedral mechanisms are investigated. The Hamiltonian paths of 3D topological graphs are introduced for removing redundant constraints. Finally, considering spatial 7*R* linkages as the basic construction units as well as their multi-symmetric loops, the design of deployable Archimedean polyhedrons is presented, and their richer polyhedral transformations are revealed following tetrahedral, octahedral and icosahedral symmetries. Therefore, this dissertation aims to propose a novel and systemic construction method of radial DPMs by using S4*R* linkages, Sarrus linkages and spatial 7*R* linkages as the radial mechanism units, respectively.

1.4 Main Contents

This dissertation consists of five chapters, which are described as follows.

Chapter 1 presents a review of the previous works mainly on 3D deployable mechanisms and polyhedral mechanisms.

Chapter 2 proposes a method to create a novel S4*R*-synchronized mechanism with threefold-symmetric motion, which is constructed by integrating three pairs of S4*R* linkages to a spatial 9*R* linkage. Then, the synthesis of three 1-DOF radial S4*R*-based polyhedrons is proposed by properly embedding S4*R*-synchronized mechanism cells into the surface of polyhedrons, as well as structural variations with mechanism topology isomorphism by introducing shortening operations. Overconstraint reduction of the proposed S4*R*-based polyhedrons is investigated with constraint space.

Chapter 3 constructs Sarrus-based tetrahedral, cubic and dodecahedral mechanisms by implanting Sarrus linkages. Three paired transformations with synchronized radial motion are revealed. Moreover, the overconstraint reduction of multiloop overconstrained DPMs is proposed by introducing the Hamiltonian path to 3D topological graphs. Through topological reduction operations based on their corresponding Hamiltonian paths, the simplest constraint forms of those polyhedral mechanisms are proposed with kinematic equivalence.

Chapter 4 discusses to the design of a family of deployable Archimedean polyhedrons by means of spatial 7*R* linkages. Various 7*R*-based DPMs are demonstrated following tetrahedral, octahedral and icosahedral symmetries, respectively, in which the symmetry is always reserved in the folding process of each 7*R*-based polyhedron. Finally, the overconstraint reduction of those DPMs is further investigated through a topology reduction operation, which is an extension of the Hamiltonian-path reduction strategy proposed in Chapter 3.

As the conclusion of this dissertation, Chapter 5 summarizes main achievements and future works. This dissertation establishes a rational design principle of DPMs using three mechanism types as the basic mechanism units following polyhedral symmetries, and conducts the overconstraint reduction of the proposed DPMs. Finally, a logic diagram of the main research works shown here is shown in Fig. 1-14.

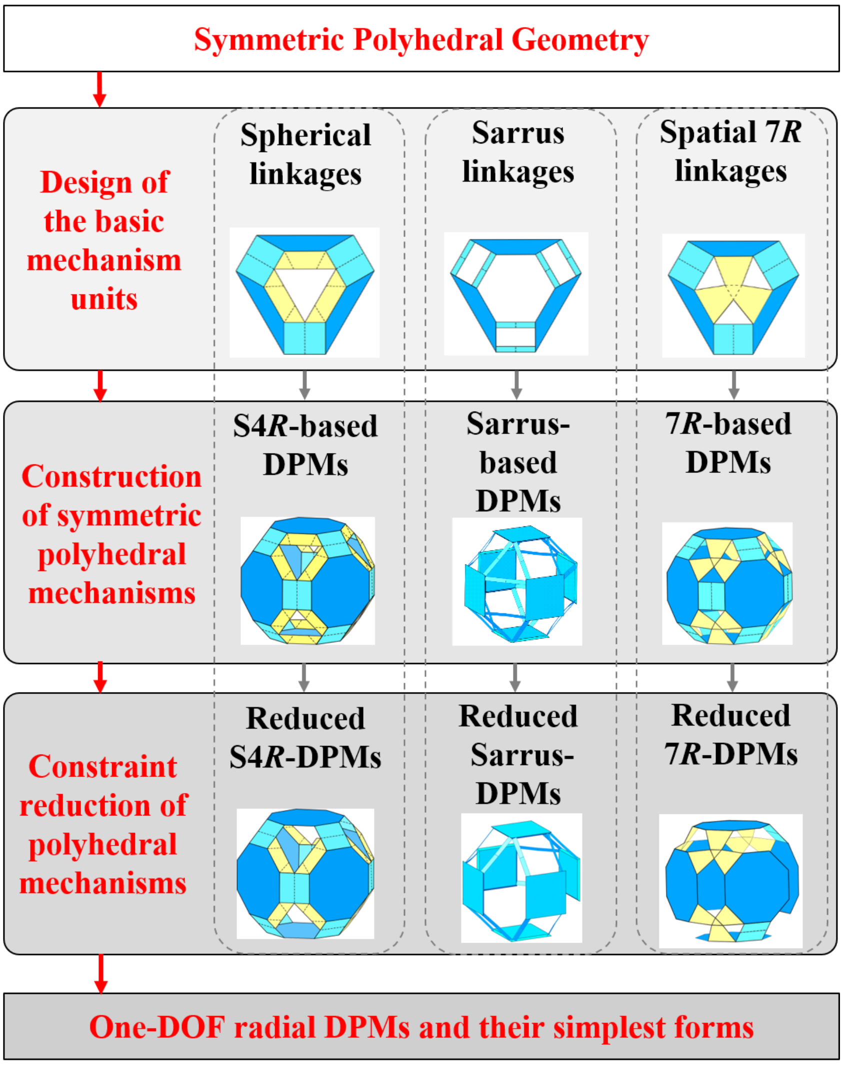

Fig. 1-14 Logic diagram of the main contents in this dissertation.

Chapter 2 1-DOF Deployable S4*R*-based Polyhedrons

2.1 Introduction

Deployable polyhedral mechanisms are generally constructed by embedding linkages and their mobile chains into the vertices, faces and edges of regular convex polyhedrons. However, there is little work on how to construct deployable polyhedrons using origami mechanisms, especially for the most typical S4*R* linkages, which are not only interesting in solid mathematical geometry but also challenging in the kinematics of mechanism science. The difficulty of research is how to arrange new crease patterns on polyhedrons.

Thus, the objective of this chapter is to construct S4*R*-based DPMs with 1-DOF radial motion and achieve paired polyhedral transformations among Archimedean polyhedrons. For this purpose, three paired polyhedrons are identified in Fig. 2-1, and each pair possesses the same polyhedral symmetry, which are tetrahedral symmetry, octahedral symmetry and icosahedral symmetry. In each deployed polyhedron, any hexagon yellow facet is alternately surrounded by three cyan squares and three blue polygons, in which each vertex is intersected by three different facets. For instance, to transform a truncated cuboctahedron to a truncated cube, as shown in Fig. 2-1(b), the identical octagonal faces in blue move radially towards the centroid during the transformation, while the faces in other colours are folded.

The outline of this chapter is as follows. In Section 2.2, a novel S4*R*-synchronized mechanism with threefold-symmetric motion characteristics is constructed by integrating three pairs of S4*R* linkages into a spatial 9*R* linkage. Section 2.3 presents the synthesis of three 1-DOF S4*R*-based polyhedrons by properly embedding S4*R*-synchronized mechanism cells into the surface of polyhedrons, as well as the structural variations with mechanism topology isomorphism by introducing the shortening operations. In Section 2.4, overconstraint reduction of the proposed S4*R*-based polyhedrons is investigated by removing redundant links and joints to reduce overconstraint in the polyhedral mechanism. Finally, the main findings of the research are summarized in Section 2.5.

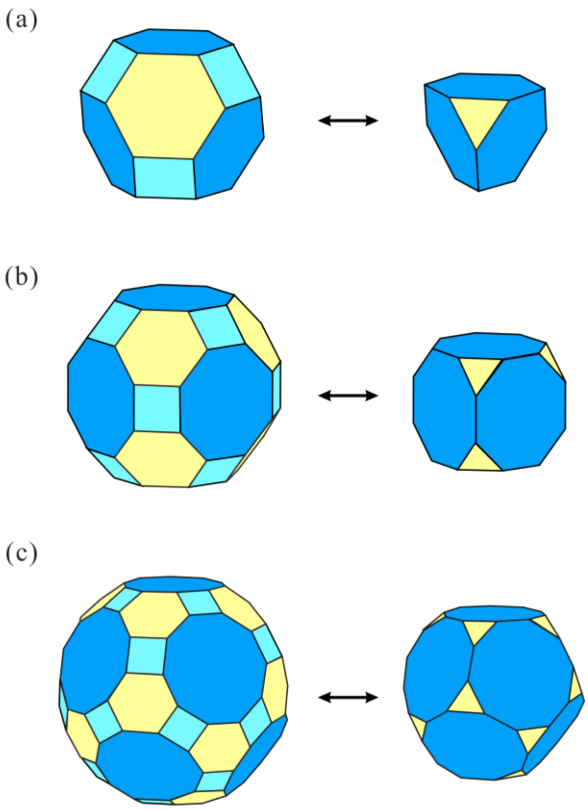

Fig. 2-1 Three paired Archimedean polyhedrons. (a) Truncated tetratetrahedron and truncated tetrahedron; (b) truncated cuboctahedron and truncated cube; (c) truncated icosidodecahedron and truncated dodecahedron. Their volumetric expansion ratios are 4.17, 3.07, and 2.43, respectively.

2.2 S4*R*-synchronized Mechanism

Considering the truncated cuboctahedron in Fig. 2-2(a) as an example, to realize the transformation illustrated in Fig. 2-1(b), the blue facets move synchronously and radially with respect to the polyhedral centroid, while the facets in cyan and yellow are folded. The highlighted red line area in Fig. 2-2(a) is adopted as a cell of the truncated cuboctahedron, which is centred around a yellow facet and has a threefold-symmetric facet arrangement. A crease pattern is identified in Fig. 2-2(b) by removing the yellow facet and embedding three valley creases into three cyan sheets. Thus, sheets p_1 to p_9 are connected sequentially to deliver a spatial 9*R* linkage, where solid lines between two adjacent sheets denote mountain creases and dashed lines stand for valley creases.

To reveal the motion characteristics of this spatial 9*R* linkage, kinematic analysis can be conducted based on the D-H matrix method, in which its D-H coordinate frames are established in Fig. 2-2(c). There exists $z_2 // z_3 // z_4$, $z_5 // z_6 // z_7$ and $z_8 // z_9 // z_1$

based on the polyhedral geometry, and the D-H parameters of the spatial 9*R* linkage can be obtained as

$$\begin{aligned}&\alpha_{12}=\alpha_{45}=\alpha_{78}=\beta,\ \alpha_{23}=\alpha_{34}=\alpha_{56}=\alpha_{67}=\alpha_{89}=\alpha_{91}=0\\&a_{12}=a_{45}=a_{78}=0,\ a_{23}=a_{34}=a_{56}=a_{67}=a_{89}=a_{91}=a/2\\&R_1=R_4=R_7=-R,\ R_2=R_5=R_8=R,\ R_3=R_6=R_9=0\end{aligned} \tag{2-1}$$

where link length $a/2$ represents half of the polyhedral edge length, and β can be determined by the corresponding polyhedral geometry.

The closure equation in the D-H method can be rewritten as

$$\boldsymbol{T}_{21}\boldsymbol{T}_{32}\boldsymbol{T}_{43}=\boldsymbol{T}_{91}\boldsymbol{T}_{89}\boldsymbol{T}_{78}\boldsymbol{T}_{67}\boldsymbol{T}_{56}\boldsymbol{T}_{45} \tag{2-2}$$

Substituting the above D-H parameters into this closure equation (2-2) and referring to the relations between dihedral angles and kinematic joint angles, the kinematic relations of dihedral angles φ_i in spatial 9*R* linkage can be derived as

$$\cos\left(\varphi_5-\varphi_6+\varphi_7\right)=\frac{\cos\beta}{1+\cos\beta} \tag{2-3a}$$

$$\sin\left(\varphi_2-\varphi_3\right)=\sin\left(\varphi_5-\varphi_6+\varphi_7-\varphi_4\right) \tag{2-3b}$$

$$\cos\left(\varphi_2-\varphi_3\right)=\cos\left(\varphi_5-\varphi_6+\varphi_7-\varphi_4\right) \tag{2-3c}$$

$$\cos\left(\varphi_2\right)-\cos\left(\varphi_2-\varphi_3\right)=\cos\left(\varphi_7\right)-\cos\left(\varphi_7-\varphi_6\right) \tag{2-3d}$$

Adjusting the order of the transformation matrix in the closure equation,

$$\boldsymbol{T}_{54}\boldsymbol{T}_{65}\boldsymbol{T}_{76}=\boldsymbol{T}_{34}\boldsymbol{T}_{23}\boldsymbol{T}_{12}\boldsymbol{T}_{91}\boldsymbol{T}_{89}\boldsymbol{T}_{78} \tag{2-4}$$

drives the corresponding kinematic relationships

$$\cos\left(\varphi_8-\varphi_9+\varphi_1\right)=\frac{\cos\beta}{1+\cos\beta} \tag{2-5a}$$

$$\sin\left(\varphi_5-\varphi_6\right)=\sin\left(\varphi_8-\varphi_9+\varphi_1-\varphi_7\right) \tag{2-5b}$$

$$\cos\left(\varphi_5-\varphi_6\right)=\cos\left(\varphi_8-\varphi_9+\varphi_1-\varphi_7\right) \tag{2-5c}$$

$$\cos\left(\varphi_5\right)-\cos\left(\varphi_5-\varphi_6\right)=\cos\left(\varphi_1\right)-\cos\left(\varphi_1-\varphi_9\right) \tag{2-5d}$$

And, taking a similar matrix operation,

$$\boldsymbol{T}_{87}\boldsymbol{T}_{98}\boldsymbol{T}_{19}=\boldsymbol{T}_{67}\boldsymbol{T}_{56}\boldsymbol{T}_{45}\boldsymbol{T}_{34}\boldsymbol{T}_{23}\boldsymbol{T}_{12} \tag{2-6}$$

yields

$$\cos\left(\varphi_2-\varphi_3+\varphi_4\right)=\frac{\cos\beta}{1+\cos\beta} \tag{2-7a}$$

$$\sin\left(\varphi_8-\varphi_9\right)=\sin\left(\varphi_2-\varphi_3+\varphi_4-\varphi_1\right) \tag{2-7b}$$

$$\cos\left(\varphi_8-\varphi_9\right)=\cos\left(\varphi_2-\varphi_3+\varphi_4-\varphi_1\right) \tag{2-7c}$$

$$\cos(\varphi_8)-\cos(\varphi_8-\varphi_9)=\cos(\varphi_4)-\cos(\varphi_4-\varphi_3) \tag{2-7d}$$

Hence, the associated dihedral angles in this spatial 9*R* linkage can be identified as

$$\varphi_2-\varphi_3+\varphi_4=\varphi_5-\varphi_6+\varphi_7=\varphi_8-\varphi_9+\varphi_1=\arccos\left(\frac{\cos\beta}{1+\cos\beta}\right) \tag{2-8}$$

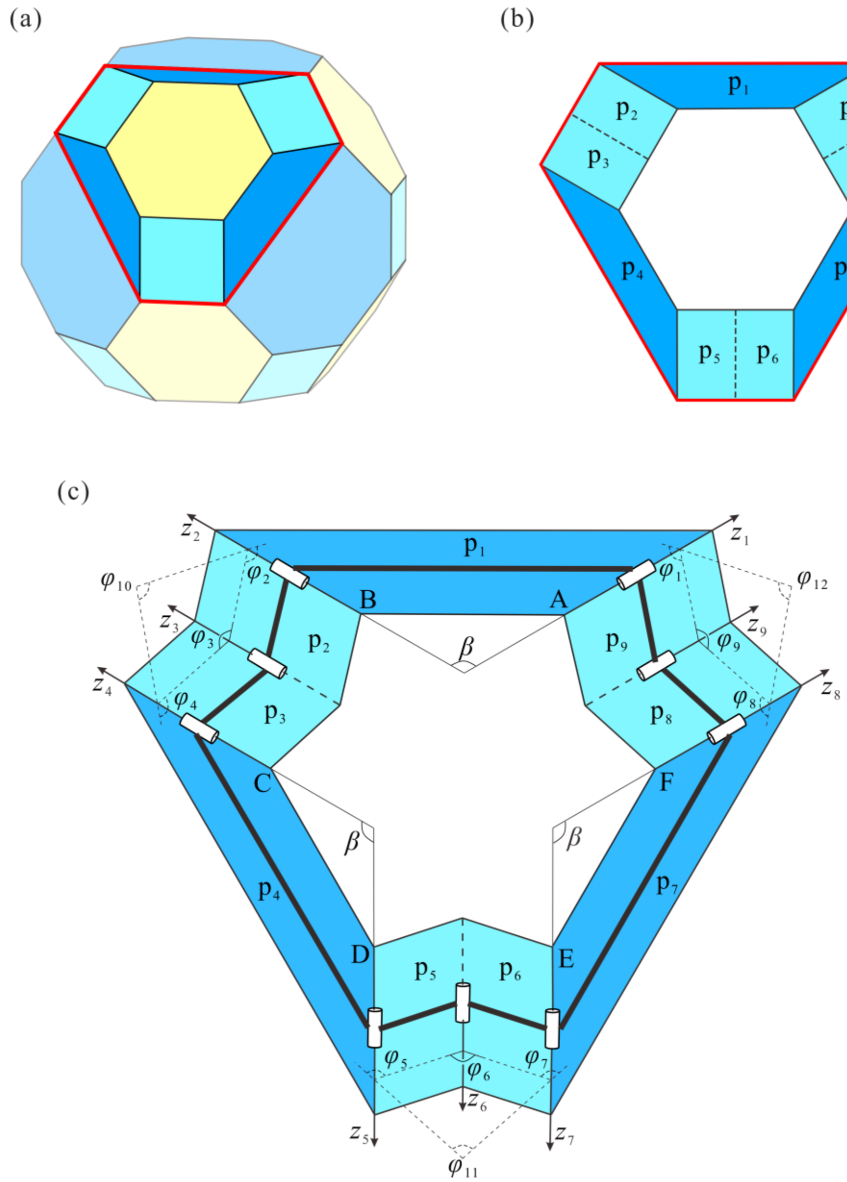

Fig. 2-2 Spatial 9*R* linkage. (a) A cell of the truncated cuboctahedron illustrated in the red line area; (b) a crease pattern with the connection of nine sheets p_1 to p_9; (c) D-H coordinate frames of its corresponding spatial 9*R* linkage.

If three independent dihedral angles, e.g., φ_2, φ_3 and φ_5, are given as the kinematic inputs, the rest of the dihedral angles can be determined by Eqs. (2-3), (2-5), (2-7) and (2-8); hence, this spatial 9*R* linkage has three DOFs, which is consistent with the calculation result of the G-K formula.

In addition, referring to Fig. 2-2(c), φ_{10} is a virtual dihedral angle between platforms p_1 and p_4, so do φ_{11} between p_4 and p_7, and φ_{12} between p_7 and p_1, there exist further relations that

$$\varphi_{10}=\varphi_2-\varphi_3+\varphi_4,\ \varphi_{11}=\varphi_5-\varphi_6+\varphi_7,\ \varphi_{12}=\varphi_8-\varphi_9+\varphi_1 \tag{2-9}$$

Combining Eq. (2-8) and Eq. (2-9) yields

$$\varphi_{10}=\varphi_{11}=\varphi_{12}=\arccos\left(\frac{\cos\beta}{1+\cos\beta}\right) \tag{2-10}$$

which reveals that the spatial angles between any two platforms are identical in each folding configuration of the proposed spatial 9*R* linkage even though it is 3-DOF.

To achieve 1-DOF synchronized radial motion, extra motion constraints are needed. Here, two additional sheets are introduced to form an S4*R* linkage at vertex A to constrain the motion between p_1 and p_9. Moreover, the same operation is applied to vertices B to F, which forms a modified crease pattern, as shown in Fig. 2-3(a). Taking two paired S4*R* linkages A and B sharing a common crease AB as an example, as shown in Fig. 2-3(b), to obtain an associated symmetric motion between sheets p_2 and p_9, the symmetrically identical design parameters of two S4*R* linkages are set as

$$\alpha_{12}=(\beta+180°)/2,\ \alpha_{23}+\alpha_{34}=120°,\ \alpha_{41}=90° \tag{2-11}$$

in which α_{12} is associated with polyhedral geometry, while α_{23} and α_{34} are the variable design parameters.

Substituting Eq. (2-11) into the closure equation, the kinematic relationships of dihedral angles ϕ_1^i to ϕ_4^i in S4*R* linkages A and B are

$$\begin{gathered}\cos\phi_1^i(\sin\alpha_{12}\cos\alpha_{23}-\cos\alpha_{12}\sin\alpha_{23}\cos\phi_2^i)+\sin\alpha_{23}\sin\phi_1^i\sin\phi_2^i-\cos(120°-\alpha_{23})=0\\ \sin(120°-\alpha_{23})\sin\phi_3^i=\sin\phi_1^i\cos\phi_2^i+\cos\alpha_{12}\cos\phi_1^i\sin\phi_2^i\\ \sin(120°-\alpha_{23})\cos\phi_4^i=\cos\alpha_{12}\cos\alpha_{23}+\sin\alpha_{12}\sin\alpha_{23}\cos\phi_2^i\end{gathered} \tag{2-12}$$

where i =A, B.

Moreover, the inverse kinematics of the S4*R* linkages can be revealed to avoid physical interference during the entire folding. The range of the dihedral angle ϕ_1^i can be obtained based on the polyhedral geometry; thus, the minimum design parameter α_{23} can be derived from Eq. (2-12) when $\phi_2^i=0$ as

$$\sin(\alpha_{12}-\alpha_{23\min})\cos\phi_1^i-\cos(120°-\alpha_{23\min})=0 \tag{2-13}$$

When $\phi_4^i = 0$, the maximum of α_{23} can be calculated with

$$\sin\alpha_{12}\sin\left(\alpha_{23\max}-30°\right)\cos\phi_1^i+\cos\alpha_{12}\cos\left(\alpha_{23\max}-30°\right)-\cos\left(\alpha_{23\max}\right)=0. \quad (2\text{-}14)$$

With the above deduction and the structural geometry of polyhedrons given in Fig. 2-1, the configuration parameters and design parameters are listed in Table 2-1.

Table 2-1 Configuration parameters and design parameters of the four-crease vertex.

The paired polyhedrons	ϕ_{1d}^i	ϕ_{1f}^i	β	α_{12}	$\alpha_{23\min}$	$\alpha_{23\max}$
Truncated tetratetrahedron and truncated tetrahedron	125.26°	35.26°	60°	120°	69.23°	78.53°
Truncated cuboctahedron and truncated cube	135°	45°	90°	135°	69.90°	87.56°
Truncated icosidodecahedron and truncated dodecahedron	148.28°	58.28°	108°	144°	61.42°	94.22°

Furthermore, the adjacent S4*R* linkages A and B share a common revolute joint, referring to Fig. 2-3(b), i.e.,

$$\phi_2^{\mathrm{A}} = \phi_2^{\mathrm{B}} \quad (2\text{-}15)$$

thus,

$$\phi_j^{\mathrm{A}} = \phi_j^{\mathrm{B}}\ (j = 1, 2, 3, 4) \quad (2\text{-}16)$$

Therefore, the associated symmetric motion between sheets p_2 and p_9 in the paired S4*R* linkages is realized and is not affected by geometric parameters.

Similarly, the above geometric parameters and kinematic relationships can be readily applied to the paired S4*R* linkages C and D, as well as E and F, as illustrated in the synthesized S4*R*-synthesized mechanism in Fig. 2-3(c), thus the further assembly conditions can be expressed as

$$\phi_j^{\mathrm{A}} = \phi_j^{\mathrm{B}},\ \phi_j^{\mathrm{C}} = \phi_j^{\mathrm{D}},\ \phi_j^{\mathrm{E}} = \phi_j^{\mathrm{F}}\ (j = 1, 2, 3, 4) \quad (2\text{-}17)$$

Thus far, considering the common panels and joints in Fig. 2-3(c) among the spatial 9*R* linkage and six S4*R* linkages A to F, we can establish the transmission relationships in the entire S4*R*-based mechanism,

$$\varphi_1 = \phi_1^{\mathrm{A}},\ \varphi_2 = \phi_1^{\mathrm{B}},\ \varphi_4 = \phi_1^{\mathrm{C}},\ \varphi_5 = \phi_1^{\mathrm{D}},\ \varphi_7 = \phi_1^{\mathrm{E}},\ \varphi_8 = \phi_1^{\mathrm{F}} \quad (2\text{-}18)$$

Referring to Eqs. (2-17) and (2-18), we have

$$\varphi_1 = \varphi_2,\ \varphi_4 = \varphi_5,\ \varphi_7 = \varphi_8 \quad (2\text{-}19)$$

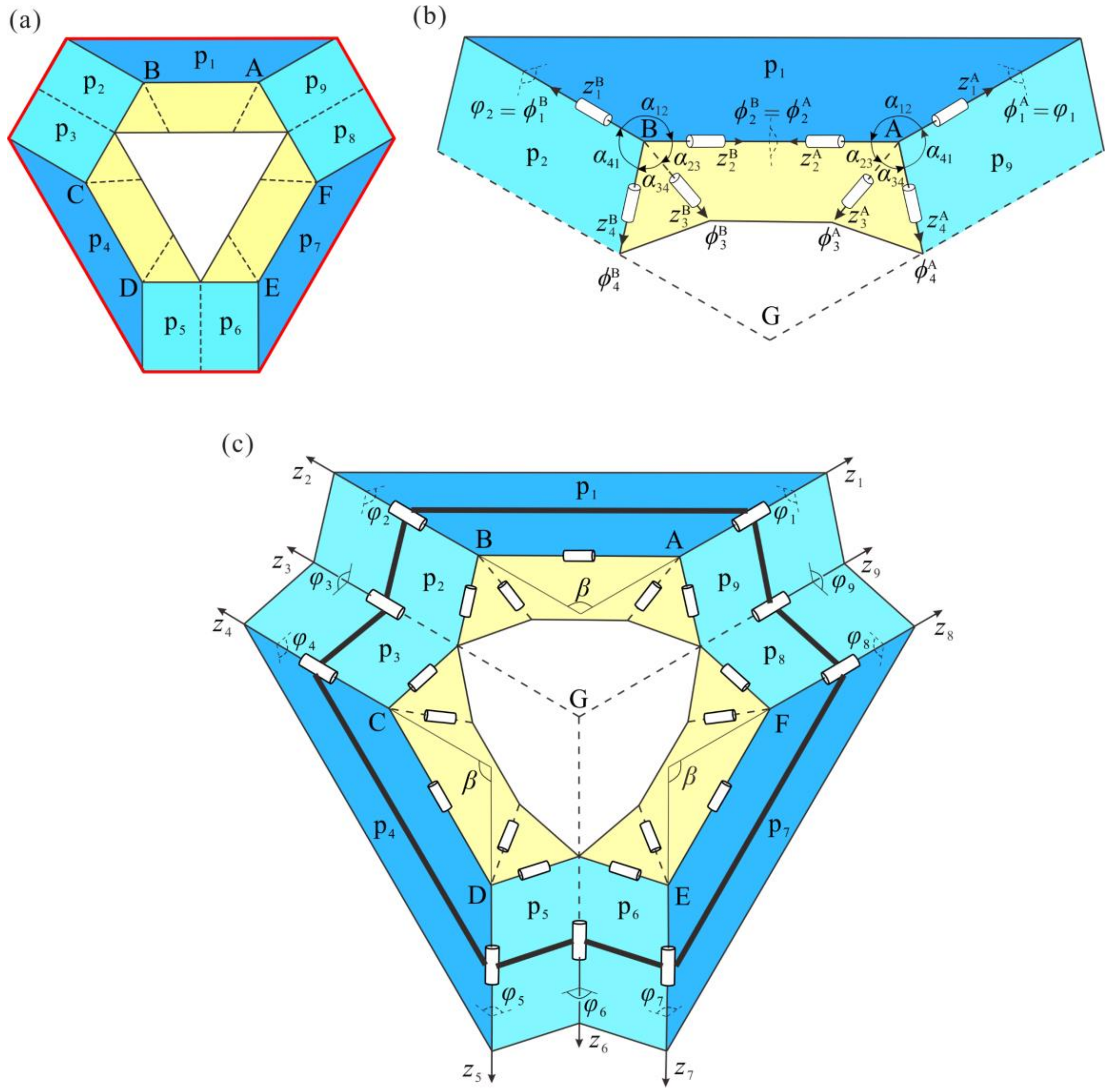

Fig. 2-3 S4*R*-synthesized mechanism. (a) A modified crease pattern by introducing six four-crease vertices A to F; (b) D-H coordinate frames of the paired S4*R* linkages A and B; (c) the S4*R*-synthesized mechanism based on the modified pattern.

Subsequently, for the spatial 9*R* linkage, substituting Eq. (2-19) into kinematic relationships obtained in Eqs. (2-3), (2-5) and (2-7) yields

$$\varphi_1 = \varphi_2 = \varphi_4 = \varphi_5 = \varphi_7 = \varphi_8 \tag{2-20a}$$

$$\varphi_3 = \varphi_6 = \varphi_9 = 2\varphi_1 - \arccos\left(\frac{\cos\beta}{1+\cos\beta}\right) \tag{2-20b}$$

for S4*R* linkages A to F,

$$\phi_j^{\mathrm{A}} = \phi_j^{\mathrm{B}} = \phi_j^{\mathrm{C}} = \phi_j^{\mathrm{D}} = \phi_j^{\mathrm{E}} = \phi_j^{\mathrm{F}} \quad (j = 1, 2, 3, 4) \tag{2-21}$$

Furthermore, by assigning $\beta=90°$, α_{12}=135° and $\alpha_{23\min}$=69.90° in the case of a truncated cuboctahedron, as given in Table 2-1, the input–output curves of the dihedral angles in the entire S4R-synchronized mechanism are illustrated in Fig. 2-4. In the unfolded process, φ_i in the spatial 9R linkage are linearly dependent; for the six S4R linkages, in addition to $\phi_1^i=\varphi_1$, ϕ_2^i increases from 0° to 125.26°, ϕ_3^i is from 67.16° to 180°, and ϕ_4^i is from 56.71° to 144.74°, where i =A, B,…, F.

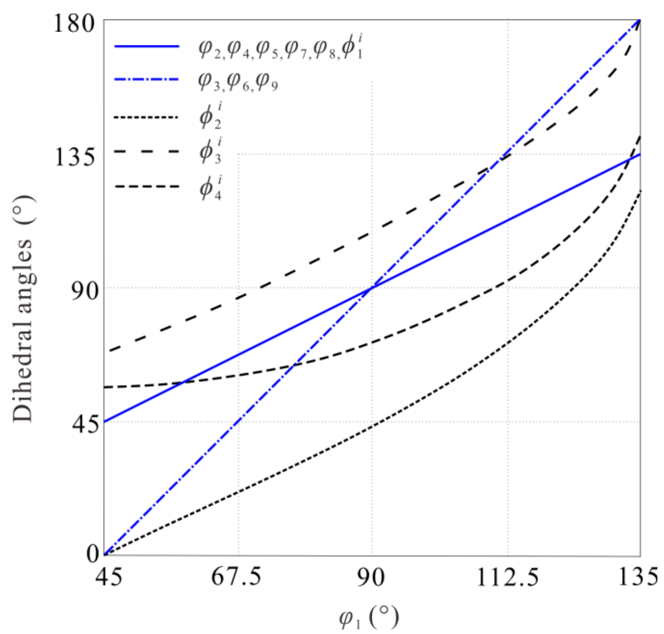

Fig. 2-4 Input–output curves of dihedral angles in the S4R-synchronized mechanism with $\beta=90°$, $\alpha_{12}=135°$, $\alpha_{23\min}=69.90°$ and i =A, B,…, F.

The above analysis shows that if φ_1 is given as the only kinematic input, the rest of the dihedral angles in the entire S4R-synchronized mechanism can be determined. Moreover, the synchronized radial motion of this mechanism can be revealed and proven by means of the direction and position vectors. Referring to the kinematic deductions of the 1-DOF S4R-synchronized mechanism with $\beta=90°$ and $\alpha_{12}=135°$, the direction vectors of the joint axes of z_1 to z_9 are shown in Figs. 2-5, in which z_3, z_6 and z_9 are vertical to each other and intersect at the origin of the global coordinate frame in every configuration. The direction vectors of z_1 to z_9 and the position vectors of points A to F′ can be derived as

$$\boldsymbol{z}_1=\begin{bmatrix}1 & 0 & 0\end{bmatrix}^{\mathrm{T}},\ \boldsymbol{A}=\begin{bmatrix}d & -\dfrac{a\cos\varphi_1}{2} & \dfrac{a\sin\varphi_1}{2}\end{bmatrix}^{\mathrm{T}}$$

$$\begin{aligned}
&\boldsymbol{z}_2=\begin{bmatrix}0 & 1 & 0\end{bmatrix}^{\mathrm{T}},\ \boldsymbol{B}=\begin{bmatrix}-\dfrac{a\cos\varphi_1}{2} & d & \dfrac{a\sin\varphi_1}{2}\end{bmatrix}^{\mathrm{T}}\\
&\boldsymbol{z}_3=\begin{bmatrix}0 & 1 & 0\end{bmatrix}^{\mathrm{T}},\ \boldsymbol{B}'=\begin{bmatrix}0 & d & 0\end{bmatrix}^{\mathrm{T}}\\
&\boldsymbol{z}_4=\begin{bmatrix}0 & 1 & 0\end{bmatrix}^{\mathrm{T}},\ \boldsymbol{C}=\begin{bmatrix}-\dfrac{a\sin\varphi_1}{2} & d & \dfrac{a\cos\varphi_1}{2}\end{bmatrix}^{\mathrm{T}}\\
&\boldsymbol{z}_5=\begin{bmatrix}0 & 0 & -1\end{bmatrix}^{\mathrm{T}},\ \boldsymbol{D}=\begin{bmatrix}-\dfrac{a\sin\varphi_1}{2} & -\dfrac{a\cos\varphi_1}{2} & -d\end{bmatrix}^{\mathrm{T}}\\
&\boldsymbol{z}_6=\begin{bmatrix}0 & 0 & -1\end{bmatrix}^{\mathrm{T}},\ \boldsymbol{D}'=\begin{bmatrix}0 & 0 & -d\end{bmatrix}^{\mathrm{T}},\\
&\boldsymbol{z}_7=\begin{bmatrix}0 & 0 & -1\end{bmatrix}^{\mathrm{T}},\ \boldsymbol{E}=\begin{bmatrix}-\dfrac{a\cos\varphi_1}{2} & -\dfrac{a\sin\varphi_1}{2} & -d\end{bmatrix}^{\mathrm{T}}\\
&\boldsymbol{z}_8=\begin{bmatrix}1 & 0 & 0\end{bmatrix}^{\mathrm{T}},\ \boldsymbol{F}=\begin{bmatrix}d & -\dfrac{a\sin\varphi_1}{2} & \dfrac{a\cos\varphi_1}{2}\end{bmatrix}^{\mathrm{T}}\\
&\boldsymbol{z}_9=\begin{bmatrix}1 & 0 & 0\end{bmatrix}^{\mathrm{T}},\ \boldsymbol{F}'=\begin{bmatrix}d & 0 & 0\end{bmatrix}^{\mathrm{T}}
\end{aligned}\tag{2-22}$$

in which $d=a\left(\sqrt{2}-\cos\varphi_1\right)/2$.

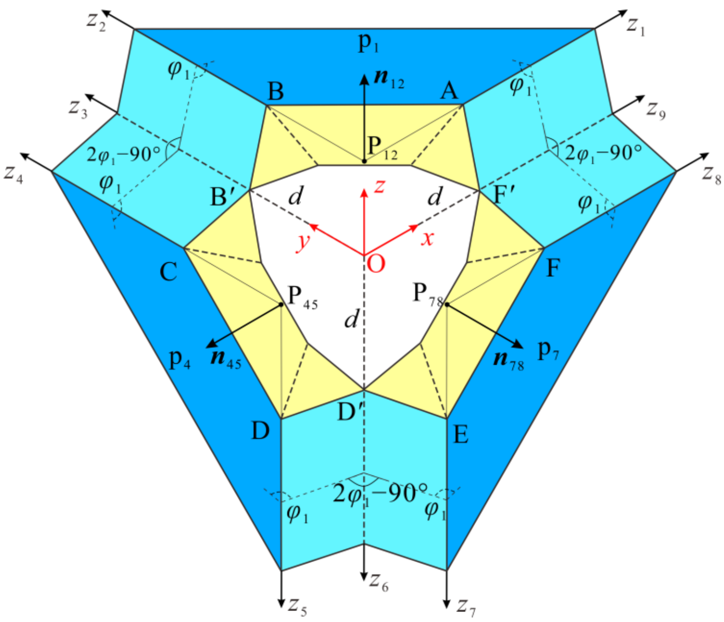

Fig. 2-5 Direction vectors of joint axes of z_1 to z_9 in the S4*R*-based mechanism.

The direction vector $\boldsymbol{n}_{12}$ in platform p_1 is the normal vector of z_1 and z_2 passing the common point $\boldsymbol{P}_{12}$, as do the normal vector $\boldsymbol{n}_{45}$ for z_4 and z_5 passing $\boldsymbol{P}_{45}$ and the normal vector $\boldsymbol{n}_{78}$ for z_7 and z_8 passing $\boldsymbol{P}_{78}$, which can be obtained as

$$\boldsymbol{n}_{12}=\begin{bmatrix}0 & 0 & 1\end{bmatrix}^{\mathrm{T}},\quad \boldsymbol{P}_{12}=\begin{bmatrix}-\dfrac{a\cos\varphi_1}{2} & -\dfrac{a\cos\varphi_1}{2} & \dfrac{a\sin\varphi_1}{2}\end{bmatrix}^{\mathrm{T}}$$

$$\boldsymbol{n}_{45}=\begin{bmatrix}-1 & 0 & 0\end{bmatrix}^{\mathrm{T}},\ \boldsymbol{P}_{45}=\begin{bmatrix}-\dfrac{a\sin\varphi_1}{2} & -\dfrac{a\cos\varphi_1}{2} & \dfrac{a\cos\varphi_1}{2}\end{bmatrix}^{\mathrm{T}}$$

$$\boldsymbol{n}_{78}=\begin{bmatrix}0 & -1 & 0\end{bmatrix}^{\mathrm{T}},\ \boldsymbol{P}_{78}=\begin{bmatrix}-\dfrac{a\cos\varphi_1}{2} & -\dfrac{a\sin\varphi_1}{2} & \dfrac{a\cos\varphi_1}{2}\end{bmatrix}^{\mathrm{T}} \tag{2-23}$$

Thus far, the motion directions of the three platforms illustrated in blue are invariable, and the distances of the three points $\boldsymbol{P}_{12}$, $\boldsymbol{P}_{45}$ and $\boldsymbol{P}_{78}$ with respect to the origin O are always identical. Hence, this S4*R*-based mechanism presents a 1-DOF synchronized radial motion. Hence, as illustrated in Fig. 2-6, this S4*R*-synchronized mechanism performs a 1-DOF threefold-symmetric radial motion.

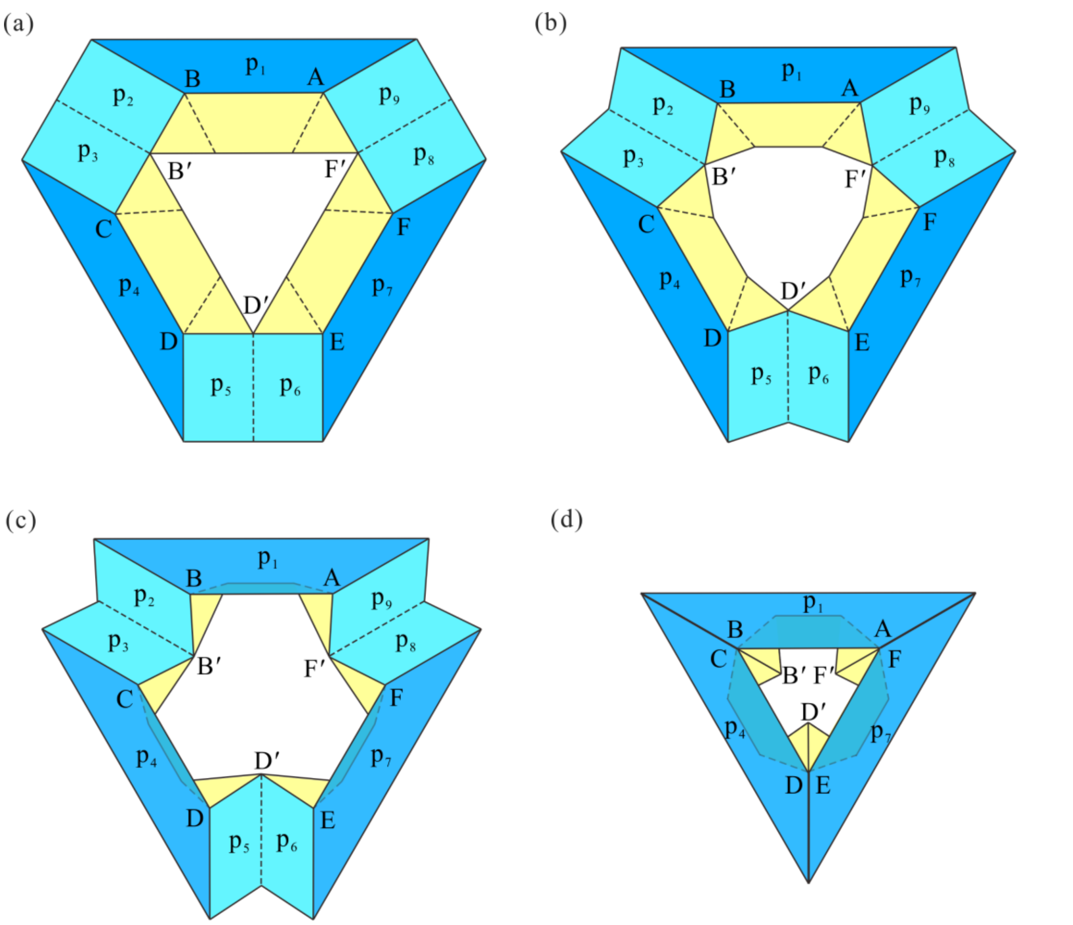

Fig. 2-6 Folding process of the S4*R*-synchronized mechanism, from (a) the deployed configuration, via (b) and (c) two intermediate configurations, to (d) the folded configuration.

Based on kinematic equivalence, the double-spherical Bennett 6*R* linkage can also be adopted by removing the common revolute joint of each pair of S4*R* linkages. Therefore, a novel S4*R*-synchronized mechanism is constructed in this section by integrating three pairs of S4*R* linkages into a spatial 9*R* linkage. The proposed 1-DOF S4*R*-synchronized mechanism can be utilized as a mechanism cell to construct a series of novel S4*R*-based polyhedrons with synchronized radial motion, as is presented in the next section.

2.3 Construction and Variations of a Series of S4*R*-based Polyhedrons

2.3.1 Symmetric Construction of S4*R*-based Polyhedrons

The truncated cuboctahedron with octahedral symmetry is selected from Fig. 2-1 to demonstrate the construction process of the S4*R*-based polyhedron. As shown in Fig. 2-7(a), a one-eighth portion of the entire polyhedral surface is symmetrically highlighted by grey dotted lines. Referring to Fig. 2-7(b), we then embed the 1-DOF crease pattern proposed in Fig. 2-3(a) into this one-eighth surface, which can be regarded as the S4*R*-based mechanism cell. Ultimately, following O_h tessellation, the complete S4*R*-based truncated cuboctahedron is constructed in Fig. 2-7(c) by embedding and merging eight mechanism cells. With the 1-DOF radial motion of mechanism cells and the symmetric property, it is straightforward to show that the entire motion of the proposed S4*R*-based truncated cuboctahedron is 1-DOF, coordinated and radially synchronized. A corresponding prototype is fabricated, as shown in Fig. 2-7(d), in which the sheets at each four-crease vertex have been expanded along the valley creases until the red lines to cover the maximum yellow surface in a deployed polyhedron.

During the 1-DOF synchronous radial motion, the inscribed sphere radius r, circumscribed sphere radius R and the Volume V of the S4*R*-based truncated cuboctahedron as illustrated in Fig.2-7(c) are

$$r = (\sqrt{2}\sin(\varphi_1 - 45°) + \sqrt{2} + 1)a/2 \tag{2-24a}$$

$$R = \sqrt{(8 + 4\sin(\varphi_1 - 45°))/(2 - \sqrt{2}) - 2\sin\varphi_1}\; a/2 \tag{2-24b}$$

$$V = \begin{pmatrix} 102 + 68\sqrt{2} + 3(48 + 29\sqrt{2})\sin(\varphi_1 - 45°) \\ -(18 + 12\sqrt{2})\sin(2\varphi_1) + \sqrt{2}\sin(3\varphi_1 + 45°) \end{pmatrix} a^3/12 \tag{2-24c}$$

where a is the edge length of a regular truncated cuboctahedron.

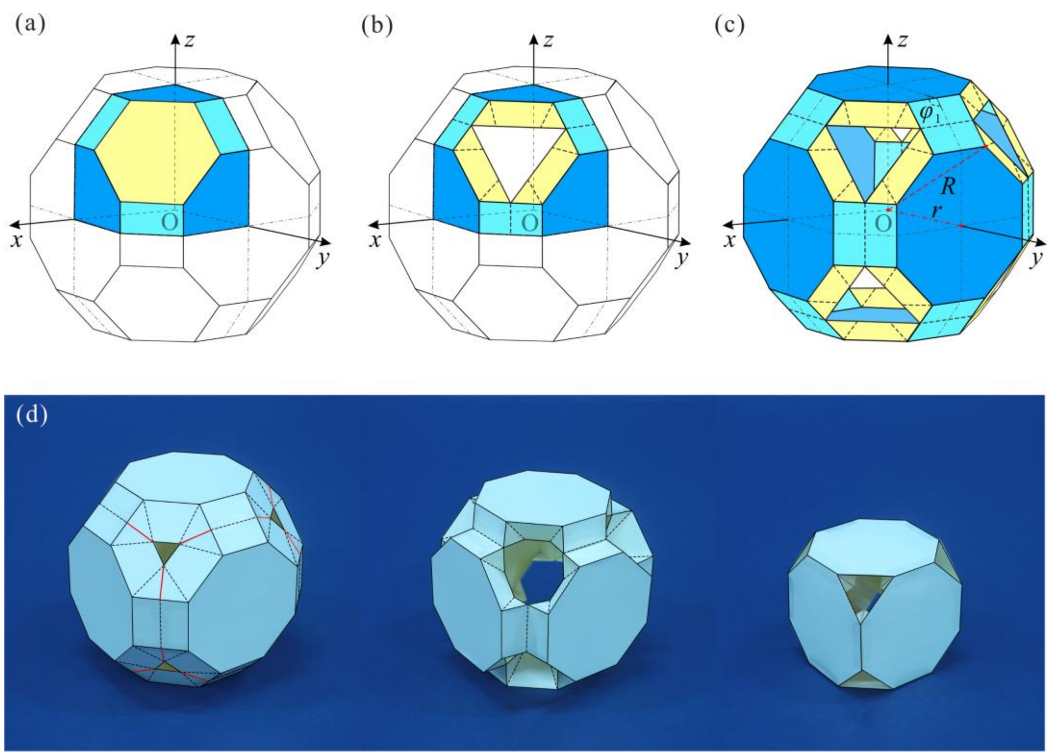

Fig. 2-7 Construction of S4*R*-based truncated cuboctahedron. (a) A one-eighth of the entire polyhedral surface in a truncated cuboctahedron; (b) the embedding of one S4*R*-synchronized mechanism cell; (c) construction of the entire S4*R*-based truncated cuboctahedron; (d) the transformation sequence of a cardboard prototype from a truncated cuboctahedron (left) to a truncated cube (right), in which the red lines stand for slits.

Thus, taking φ_1 as the only input dihedral angle, the curves for the deployable radius *r* and *R* and the volume *V* can be obtained and illustrated in Fig. 2-8.

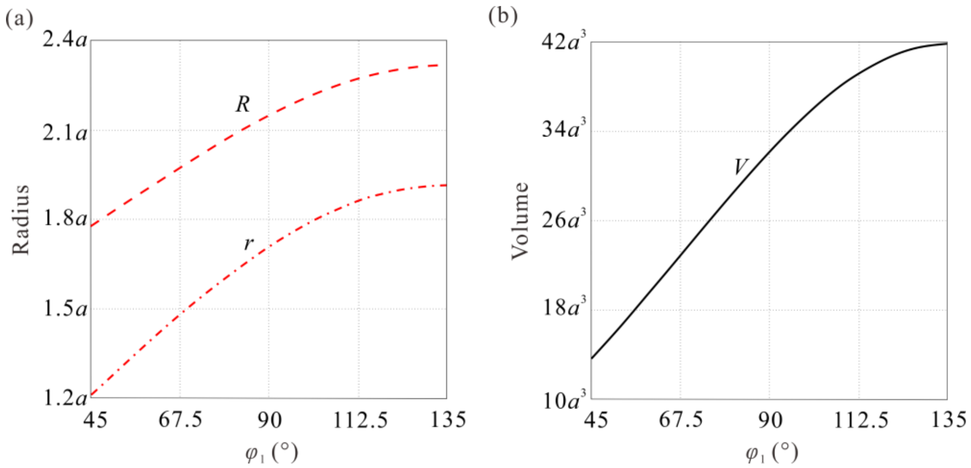

Fig. 2-8 The curves of (a) inscribed sphere radius *r* and circumscribed sphere radius *R* and (b) the Volume *V* vs. folding angle φ_1.

Furthermore, the proposed construction method can be readily extended to the other two cases, as shown in Fig. 2-1. Based on tetrahedral symmetry, one S4*R*-based mechanism cell is embedded into a quarter surface of the truncated tetratetrahedron, as shown in Fig. 2-9(a). Then, a prototype S4*R*-based truncated tetratetrahedron is created and fabricated, as illustrated in Fig. 2-9(b). Following icosahedral symmetry, the tessellation of one mechanism cell on the one-twentieth surface in Fig. 2-9(c) results in an S4*R*-based truncated icosidodecahedron in Fig. 2-9(d). The transformation sequences of the two prototypes show that both can realise 1-DOF synchronized radial motion.

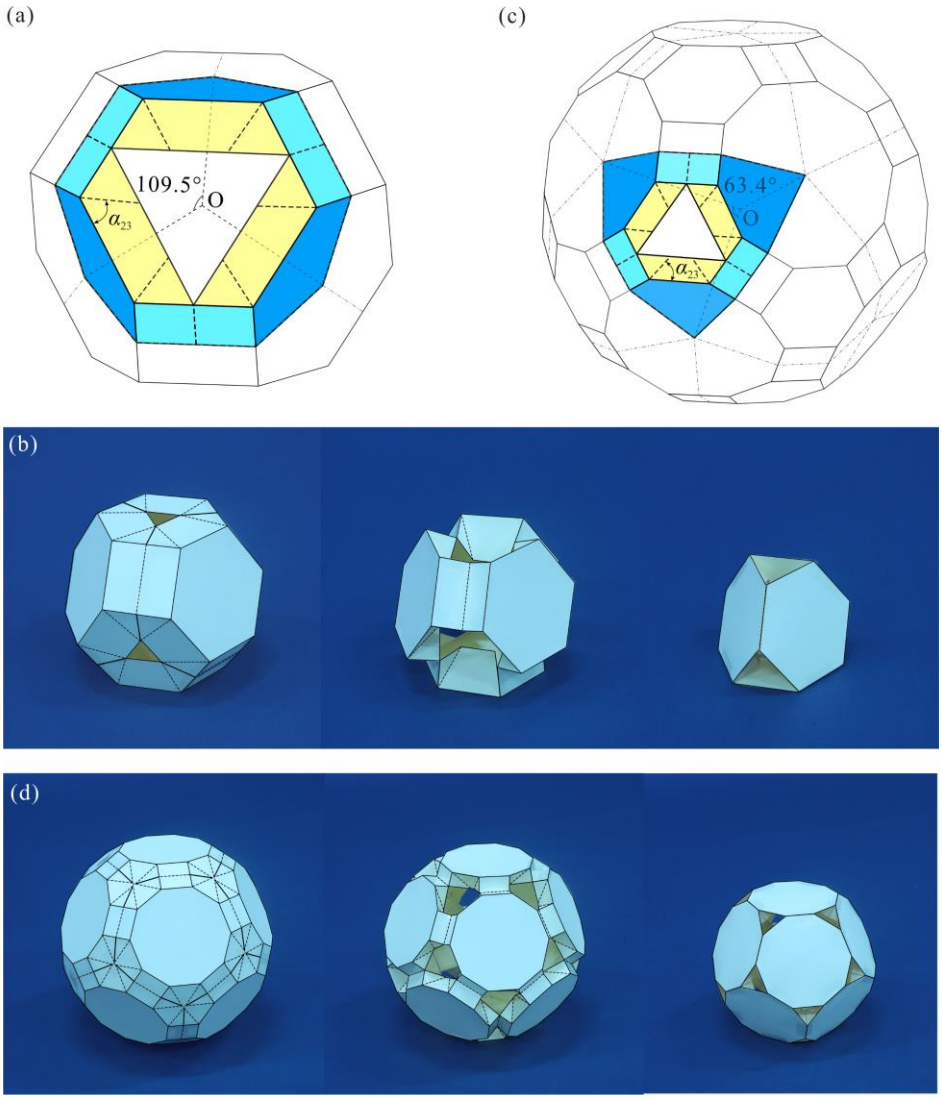

Fig. 2-9 Tessellation with T_d and I_h symmetries. (a) One mechanism cell of the S4*R*-based truncated tetratetrahedron and (b) its transformation sequences of the cardboard prototype; (c) one mechanism cell in the S4*R*-based truncated icosidodecahedron and (d) its cardboard prototype.

In summary, the procedure of constructing such S4*R*-based polyhedrons can be summarized as follows. Step 1: Divide a threefold-symmetric portion centred around a yellow facet on a polyhedral surface according to the corresponding symmetry. Step 2: embed the 1-DOF S4*R*-synchronized mechanism cell into this portion surface. Step 3: synthesize the entire polyhedral mechanism following symmetric tessellation of mechanism cells. Step 4: Verify the kinematic characteristics, i.e., one DOF, radial synchronized motion and the symmetry reserved in the continuous motion. If the threefold-symmetric portion cannot be divided out from a polyhedral surface in Step 1, then the objective polyhedron should be reconsidered. Moreover, the synthesis process of mechanism cells in Step 3 should satisfy the kinematic compatibility.

2.3.2 Structural Variations with Mechanism Topology Isomorphism

To date, three paired transformations have been realized by symmetrically embedding S4*R*-synchronized mechanism cells into the surface of polyhedrons. Next, we aim to create a wider range of polyhedral transformations using dimensional shortening operations, in which the related mechanism topology remains isomorphic.

First, an octagon with two types of sides lies in the middle of the first row in Fig. 2-10, in which the length of the horizontal or vertical sides is l and the inclined side is h. Following the leftward path I, l is gradually shortened until it is reduced to zero while h is retained, which ultimately leads to an inclined square with side length h. On the other hand, shortening h to zero along the rightward path II results in a square with side length l. Subsequently, referring to the planar shortening operations of an octagon, the second row demonstrates the corresponding polyhedral assemblies. As a result, based on the original truncated cuboctahedron, a rhombicuboctahedron and a truncated octahedron eventually reach along path I and path II, respectively, where the rhombicuboctahedron′ in path I and truncated octahedron′ in path II represent the intermediate shortening results. Furthermore, following the polyhedral transformation principle indicated in Fig. 2-1, the third row in Fig. 2-10 shows the corresponding folded polyhedrons in geometric dimensions.

Together with the shortening operations in Fig. 2-10 and the proposed construction method of the S4*R*-based polyhedral mechanism, structural variations of polyhedrons are presented as follows with mechanism topology isomorphism.

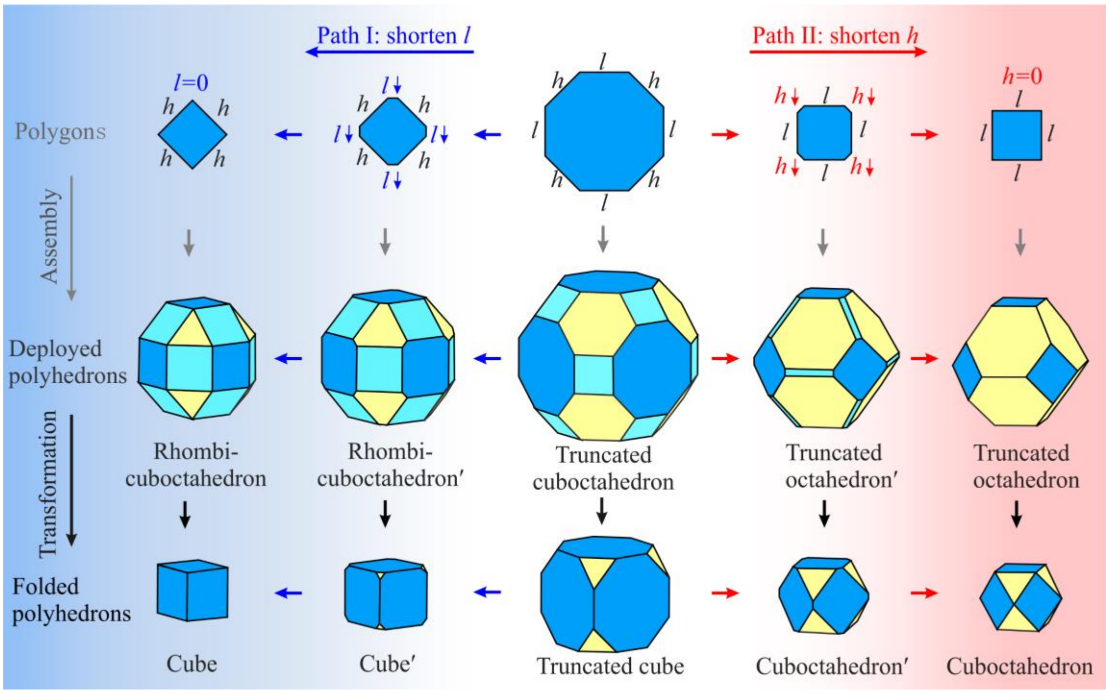

Fig. 2-10 Dimensional shortening operations. The first row: the leftward path I to shorten side length l and the rightward path II to shorten side length h in an octagon; the second row: the corresponding polyhedral assemblies; the third row: the corresponding transformation results.

Here, the original mechanism cell is taken as the middle one in the first row of Fig. 2-11. Combined with the proposed shortening operations along paths I and II, the S-l-cell and S-h-cell both possess the same mechanism topology as the original cell due to the paired S4*R* linkages at the corners.

Next, in terms of the construction of the entire polyhedral mechanism, the second row in Fig. 2-11 depicts the proposed S4*R*-based polyhedrons in the deployed state. Similarly, the third row displays the corresponding folded configurations of the above S4*R*-based polyhedrons. The S4*R*-based rhombicuboctahedron′ in path I can perform 1-DOF radial motion due to the same mechanism topology as the original truncated cuboctahedron mechanism, as well as the S4*R*-based truncated octahedron′ in path II. In the extremal cases l=0 and h=0, the dimension of the S4*R* linkage pairs is shortened to zero, which is only theoretically possible but rather difficult to make a physical prototype without special design on the joints.

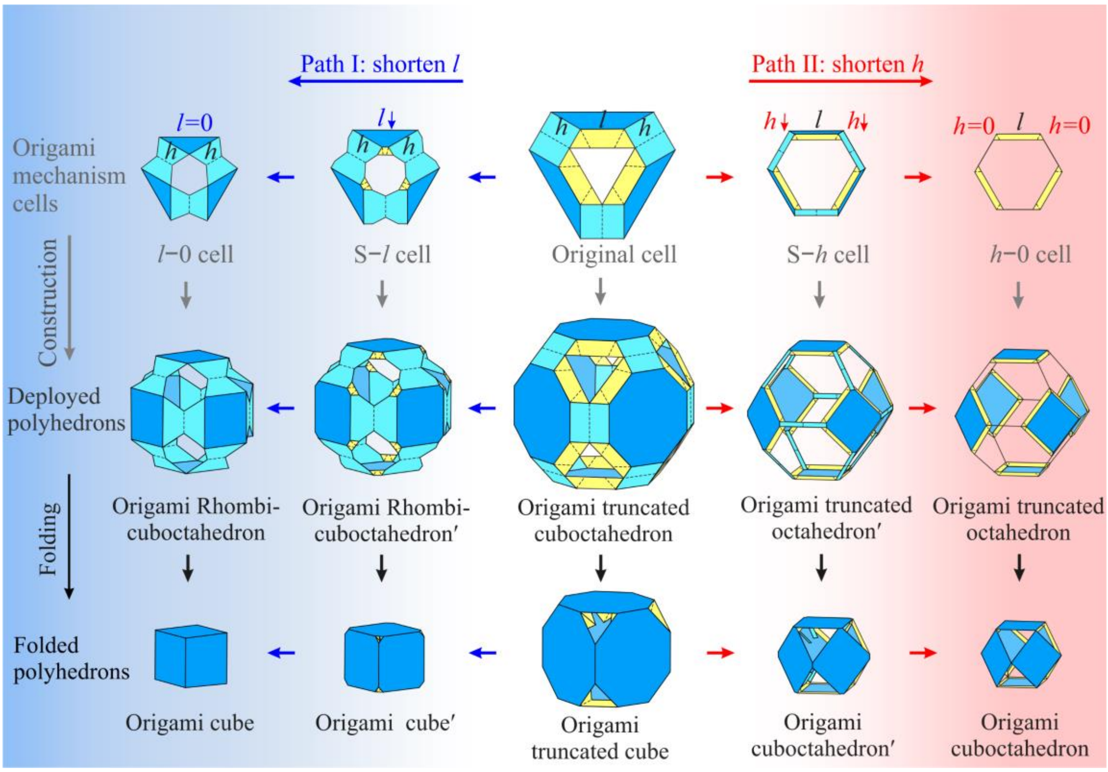

Fig. 2-11 Variations of S4*R*-based polyhedrons with shortening operations. The first row: leftward path I to shorten side length *l* and path II to shorten side length *h* in an original mechanism cell. the second row: the folded configurations of the deployable polyhedrons; the third row: the folded configurations.

Therefore, the S4*R*-based rhombicuboctahedron′ and truncated octahedron′ in Fig. 2-11 are identified and constructed along path I and path II to achieve the other two 1-DOF radial transformations with O_h symmetry, respectively. Moreover, the proposed structural variations can be directly extended to the other two original S4*R*-based polyhedrons (see Fig. 2-9) with T_d and I_h symmetries. In summary, based on the three original cases given in Fig. 2-1, a total of six transformations with structural variations are demonstrated in Fig. 2-12, all of which can perform 1-DOF synchronized radial motion.

Based on the polyhedral geometry, the specific design parameters of the cyan and yellow sheets of the S-*l*-cell and S-*h*-cell are presented as follows to avoid physical interference during folding, especially in the folded configuration.

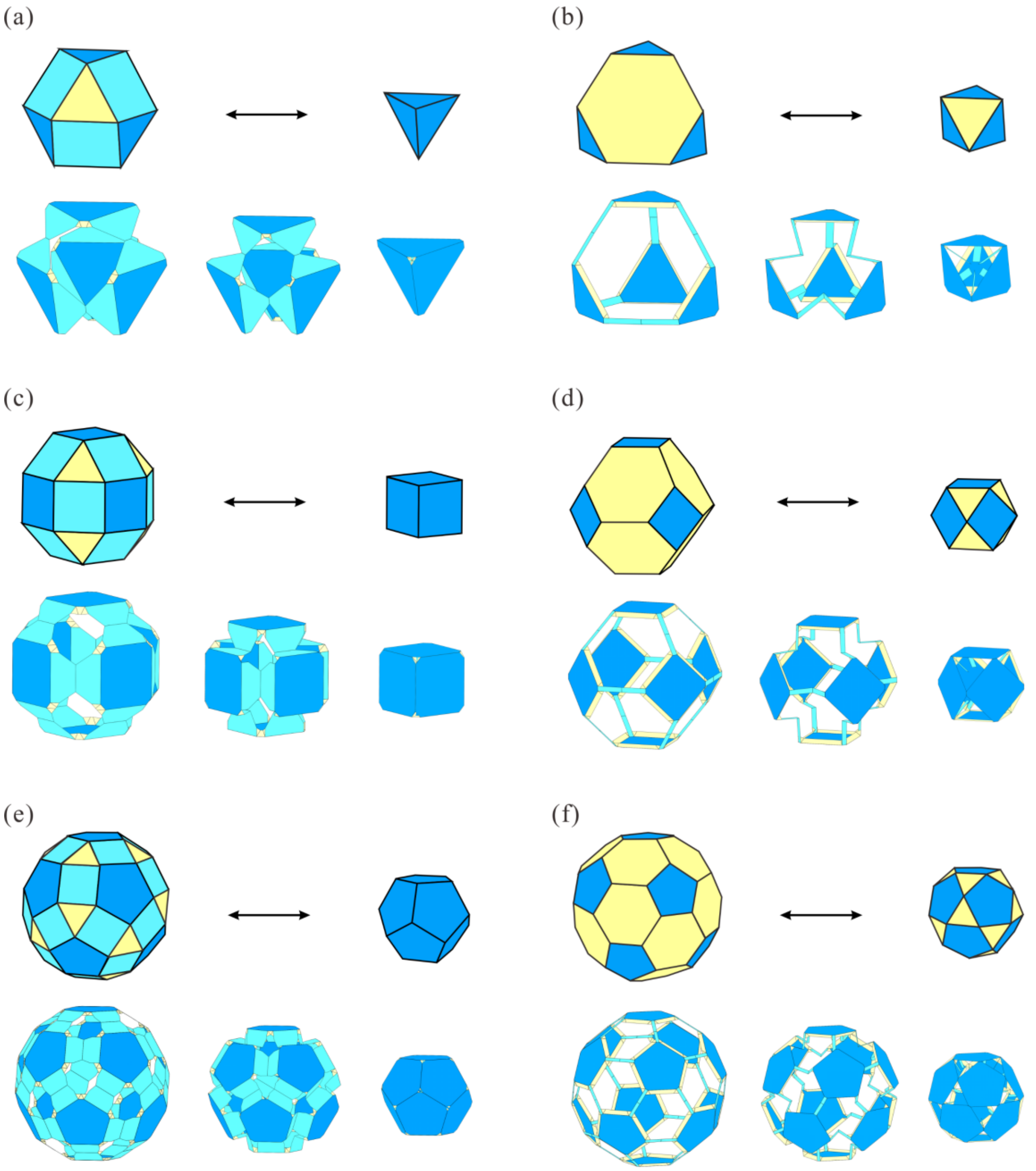

Fig. 2-12 The paired polyhedrons and their transformation solutions. (a) Rhombitetratetrahedron and tetrahedron (VDR=20); (b) truncated tetrahedron and tetratetrahedron (VDR=5.75); (c) rhombicuboctahedron and cube (VDR=8.71); (d) truncated octahedron and cuboctahedron (VDR=4.80); (e) rhombicosidodecahedron and dodecahedron (VDR=5.43); (f) truncated icosahedron and icosidodecahedron (VDR=4.00). (VDR=Volumetric Deployable Ratio).

Based on threefold symmetry of the S-l-cell in Fig. 2-11, a one-third portion of the S-l-cell is shown in Fig. 2-13(a). Theoretically, l can be shortened to an infinitesimal one; here, we assign $l' = 0.1l$ that facilitates manufacturing and presentation.

Then, the length b without interference can be derived as

$$b_{\max} = \frac{l' \tan\gamma}{2\sin(\beta/2)} \tag{2-25}$$

in which γ can be obtained from the polyhedral geometry in the completely folded state as 35.26°, 54.74° and 69.09° in the rhombitetratetrahedron, rhombicuboctahedron and rhombicosidodecahedron, respectively.

On the other hand, one-third of the S-h-cell is illustrated in Fig. 2-13 (b), in which we set up $h' = 0.1h$, and the length c of the valley crease between two yellow sheets can be obtained as

$$c_{\max} = \frac{h'}{2\cos(90°+\beta/2-\alpha_{23})} \tag{2-26}$$

Other geometric parameters and shapes of these sheets can also be properly adjusted without physical interference and with mechanism isomorphism.

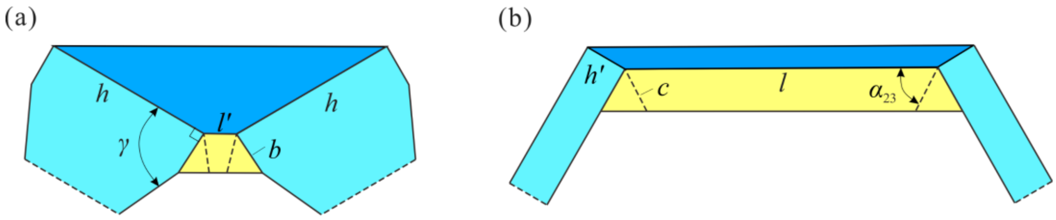

Fig. 2-13 Design parameters in (a) one-third of the S-l-cell and (b) one-third of the S-h-cell.

2.4 Overconstraint reduction of S4*R*-based Polyhedrons

To achieve 1-DOF synchronized radial motion, we add extra motion constraints of the original S4R-synchronized mechanism into the depiction of Fig. 2-3, i.e., three paired S4R linkages are introduced into a spatial 9R linkage. However, we can further reduce the motion constraints by arbitrarily removing one pair of S4R linkages, in which two pairs of S4R linkages still need to be reserved. As shown in Fig. 2-14, we remove the paired S4R linkages A and B, meaning that the motion constraint between sheets p_2 and p_9 vanishes. Thus, the original constraint relationships in Eq. (2-19) are reduced as

$$\varphi_4 = \varphi_5, \varphi_7 = \varphi_8 \tag{2-27}$$

in which $\varphi_1 = \varphi_2$ in Eq. (2-19) vanishes.

Substituting Eq. (2-27) into Eqs. (2-3) and (2-5), we have

$$\varphi_1 = \varphi_4 = \varphi_5,\ \varphi_2 = \varphi_7 = \varphi_8,\ \varphi_3 = \varphi_6 = \varphi_9 \tag{2-28}$$

referring to Eq. (2-7d),

$$\cos(\varphi_2)-\cos(\varphi_2-\varphi_3)=\cos(\varphi_1)-\cos(\varphi_1-\varphi_3) \tag{2-29}$$

Combining Eq. (2-28) and Eq. (2-3d) yields

$$\varphi_1=\varphi_2 \tag{2-30}$$

Therefore, the kinematic relationships about dihedral angles can also be obtained as

$$\varphi_1=\varphi_2=\varphi_4=\varphi_5=\varphi_7=\varphi_8 \tag{2-31a}$$

$$\varphi_3=\varphi_6=\varphi_9=2\varphi_1-\arccos\left(\frac{\cos\beta}{1+\cos\beta}\right) \tag{2-31b}$$

Thus far, the reserved two paired S4*R* linkages, C and D and E and F, can also provide the necessary constraint for the 1-DOF S4*R*-synchronized mechanism. Based on the above derivation, the yellow sheets and the relative joints at S4*R* linkages A and B can be removed without affecting the original kinematics. The simplified S4*R*-synchronized mechanism can also perform a 1-DOF threefold-symmetric synchronized radial motion as the original mechanism (see Fig. 2-15). In addition, the yellow sheets at S4*R* linkages C to F cannot be further removed because that will increase the DOF of the S4*R*-synchronized mechanism.

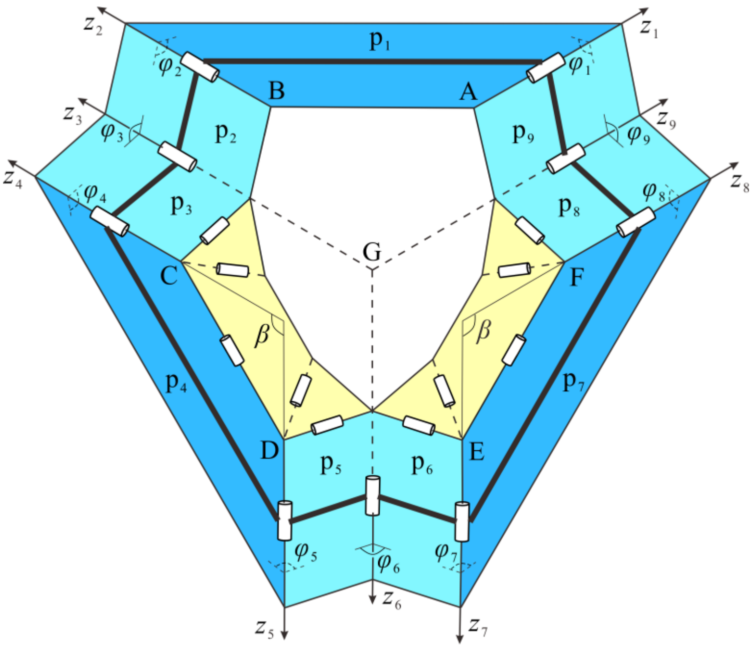

Fig. 2-14 Reduction of S4*R*-synchronized mechanism.

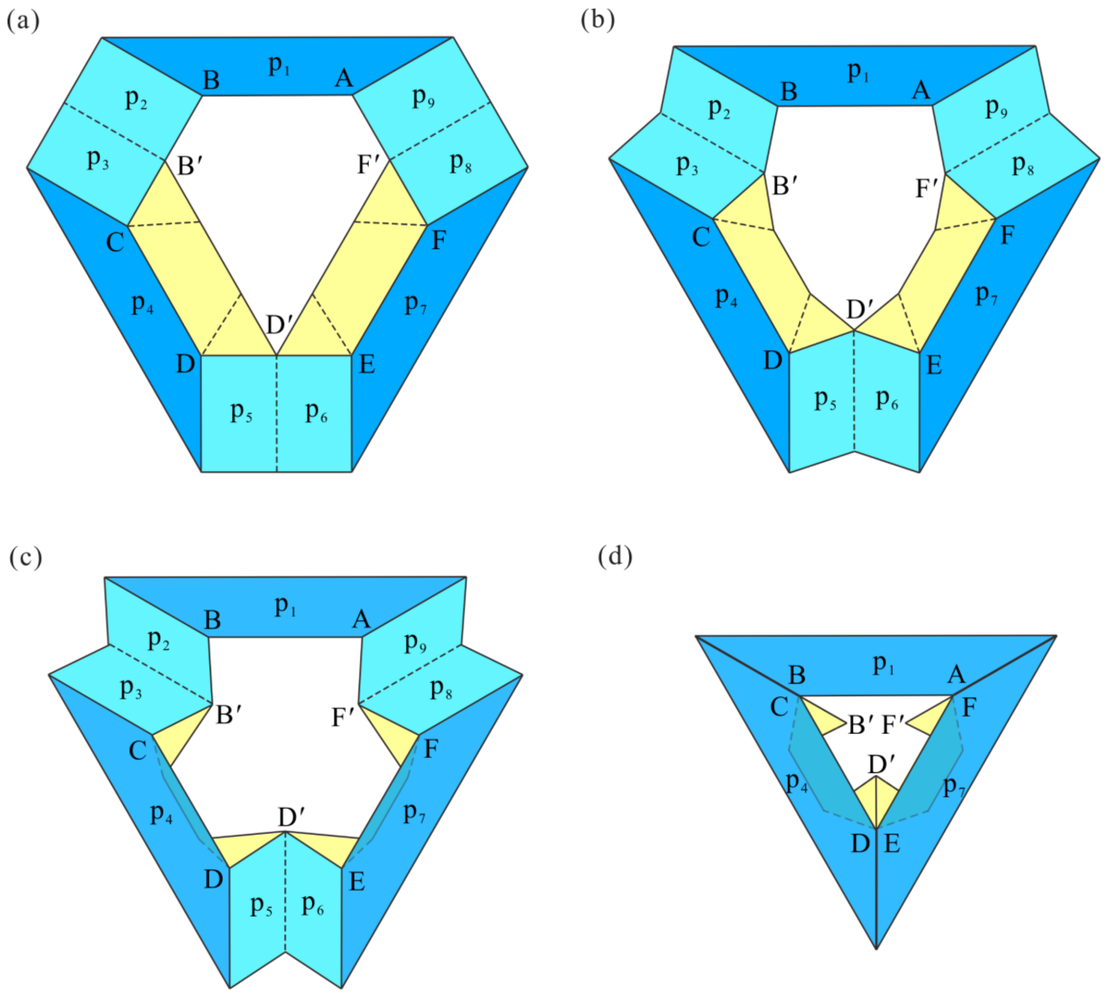

Fig. 2-15 Folding process of the simplified S4*R*-synchronized mechanism, from (a) the deployed configuration, via (b) and (c) two intermediate configurations, to (d) the folded configuration.

Considering the three S4*R*-based polyhedrons with O_h symmetry in Fig. 2-11 as examples, following the O_h tessellation of the simplified S4*R*-synchronized mechanism, simplified S4*R*-based truncated cuboctahedron, rhombicuboctahedron and truncated octahedron are proposed. The folding progresses are illustrated in Fig. 2-16, and it can be seen that the original 1-DOF synchronized radial motion is reserved in each simplified S4*R*-based polyhedron, as well as the O_h symmetry in each configuration. The original truncated cuboctahedron mechanism consists of 102 links and 156 joints with overconstraints of 175. After removing the redundant constraint, there are 78 links and 116 joints with overconstraints of 119, which indicates a significant reduction in overconstraints.

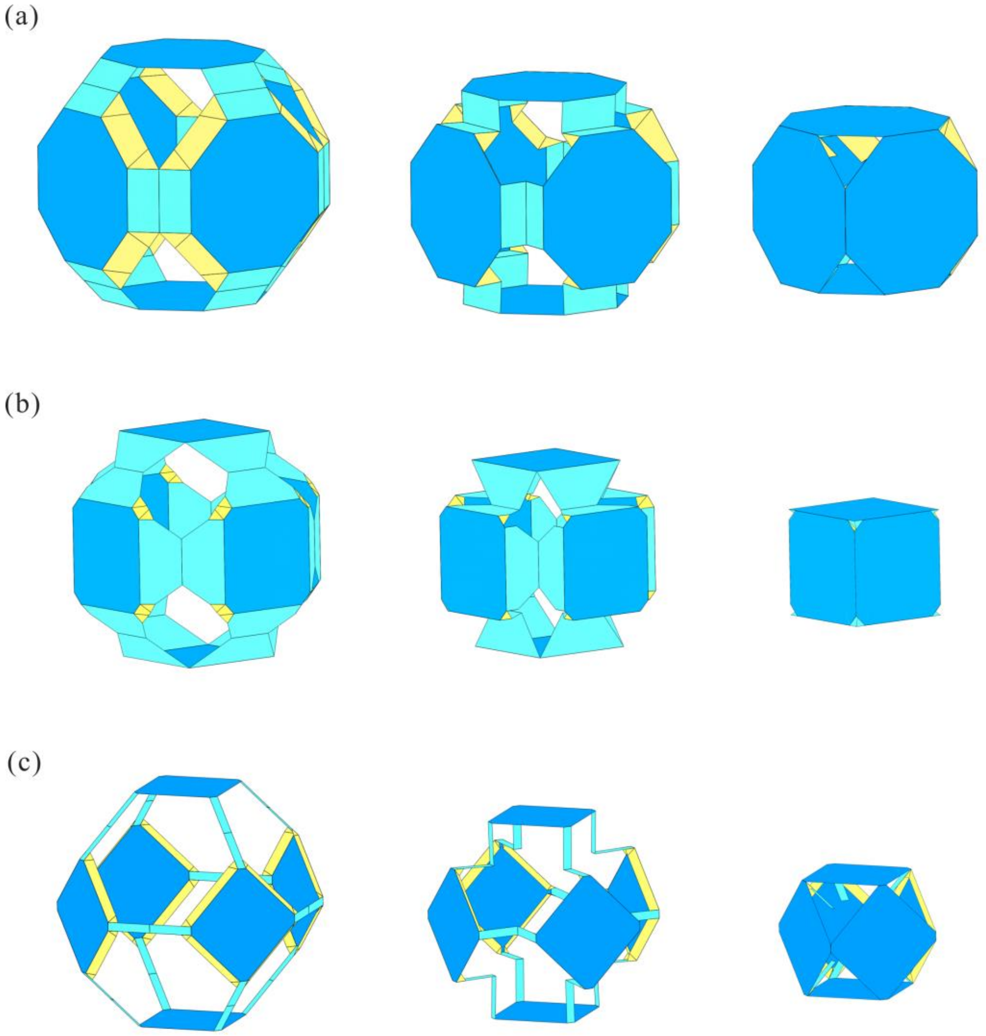

Fig. 2-16 Simplified deployable S4*R*-based polyhedrons based on (a) truncated cuboctahedron, (b) rhombicuboctahedron and (c) truncated octahedron.

2.5 Conclusions and Discussion

In this chapter, we proposed an innovative approach for constructing a family of S4*R*-based DPMs with 1-DOF radial motion and deployable transformability among Archimedean polyhedrons. As construction cell DPMs, a 1-DOF S4*R*-synchronized mechanism is constructed by embedding three pairs of spherical 4*R* linkages into a spatial 9*R* linkage to provide kinematic constraints. Three 1-DOF transformable S4*R*-based polyhedrons are obtained by assembling 1-DOF mechanism cells following T_d, O_h and I_h symmetries. Furthermore, dimensional structural variations with mechanism topology isomorphism are demonstrated to realize various transformable solutions. Ultimately, a total of nine transformable polyhedrons with 1-DOF radial motion were obtained. In addition, the overconstraint reduction of the proposed DPMs was proposed by removing redundant links and joints.

Although only Archimedean solids are studied in this chapter due to their interesting transformability, such construction methods can be adapted to explore the design of other 1-DOF deployable polyhedrons, such as Johnson solids. Note that to realize such polyhedral construction, three blue platforms in an S4R-based mechanism cell should surround a hexagonal facet (or triangular facet after shortening operations) and separate from each other to derive a threefold-symmetric feature. The tessellation of mechanism cells should follow the original symmetry of a polyhedron. Furthermore, the dimensional shortening operations should ensure the symmetry of the platforms and the radial motion towards the centroid, as well as mechanism topology isomorphism.

Due to the synchronized radial motion of S4R-based polyhedrons, their corresponding symmetric properties are preserved in all configurations, i.e., they are isotropic. Regarding an S4R-based polyhedron as a construction cell, the work in this chapter potentially provides a new kinematic strategy to create three-dimensional metamaterials with enriched properties, such as a large deformation range, Poisson's ratios of -1 and negative thermal expansion. Furthermore, in the kinematics of the S4R-based polyhedral mechanism, the focus is on the 1-DOF mechanism topology. In addition to the structural variations reported in this chapter, relative geometric conditions can also be properly adjusted to meet specific engineering requirements. We expect the proposed S4R-based DPMs and their tessellation to enhance their applications in various engineering fields, such as deployable mechanisms for architectures as well as space exploration.

Chapter 3 Sarrus-based Deployable Polyhedral Mechanisms

3.1 Introduction

Deployable polyhedrons with transformability are concerned with solid geometry and mechanism science, which present geometric inspirations and kinematic challenges. In this chapter, we focus on three paired transformations between Platonic and Archimedean polyhedrons, as shown in Fig. 3-1, referring to polyhedral expansion in solid geometry. The blue facets in a Platonic polyhedron are separated and moved apart radially, and new facets in beige are formed among separated elements to form a corresponding Archimedean polyhedron. Due to this expansion operation, the two polyhedrons in each transformation have identical polyhedral symmetry properties; Figs. 3-1(a) to (c) show tetrahedral symmetry, octahedral symmetry and icosahedral symmetry, respectively. However, it is challenging to accomplish such transformation from a mechanistic point of view.

Moreover, most deployable polyhedral mechanisms are highly overconstrained multiloop mechanisms, which will hinder their practical applications. To ensure the motion of the heavily overconstrained mechanism, the strict geometric conditions of links and joints should be satisfied. Nevertheless, due to the harsh working environment of those deployable mechanisms and the errors in fabrication, the ideal geometric constraints are difficult to meet. Moreover, the overconstraints bring additional internal loads that can render those mechanisms immobile, reducing the reliability of the deployable mechanisms. Therefore, it is important yet difficult to reduce or even eliminate the redundant constraints for the original overconstrained mechanism by designing a less-overconstrained or nonoverconstrained form while maintaining their equivalent kinematic behaviours. Hence, the other objective of the chapter is to investigate the overconstraint reduction of the multiloop DPMs.

The outline of this chapter is as follows. In Section 3.2, we first construct the deployable tetrahedral, cubic and dodecahedral mechanisms by implanting Sarrus linkages along the straight-line motion path. Three paired transformations with synchronized radial motion between Platonic and Archimedean polyhedrons are revealed, and their significant symmetric properties perfectly remain in each work configuration. Moreover, with the assistance of equivalent prismatic joints, an equivalent analysis strategy for the mobility of multiloop polyhedral mechanisms is proposed to significantly simplify the calculation process. In Section 3.3, combining kinematics and mathematics, the overconstraint reduction of multiloop overconstrained DPMs is proposed by introducing the Hamiltonian path to 3D topological graphs. Through the removal of redundant joints based on their corresponding Hamiltonian paths, the simplest constraint forms of those polyhedral mechanisms are proposed with kinematic equivalence. Furthermore, nonsimplest constraint forms of Sarrus-based with rotational symmetries. Finally, a conclusion is given in Section 3.4.

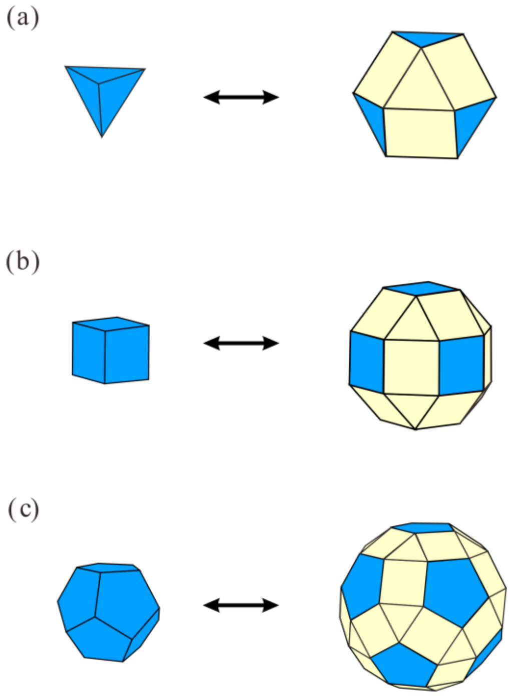

Fig. 3-1 Three paired Platonic and Archimedean polyhedrons. (a) A tetrahedron and a rhombitetratetrahedron with tetrahedral symmetry; (b) a cube and a rhombicuboctahedron with octahedral symmetry; (c) a dodecahedron and a rhombicosidodecahedron with icosahedral symmetry. The volumetric expansion ratios are 20, 8.71, and 5.43, respectively.

3.2 Construction and Equivalent Analysis of Sarrus-based DPMs

3.2.1 Deployable Tetrahedral Mechanism

3.2.1.1 Construction of a Deployable Tetrahedral Mechanism

A hollow tetrahedron with four congruous prismoid platforms A, B, C and D is shown in Fig. 3-2(a). Its four vertices are denoted by a to d, six edges are ab, ac, ad, bc, cd and bd with the x-axis passing through midpoints of edges ad and bc, as do the y-

axis for edges *ac* and *bd*, and the *z*-axis for edges *ab* and *cd*. Here, the coordinate origin O is the centroid of this tetrahedron, and the perpendiculars of the four platforms intersecting at the centroid O are denoted by red dashed-dotted lines. Subsequently, by carrying out the expansion operation, four platforms are separated synchronously and moved radially along the corresponding perpendiculars, and each pair of adjacent triangular prismoid platforms undergoes a straight-line motion, as shown in Fig. 3-2(b). Based on tetrahedral geometry, the angle between the bottom and side facets of each triangular prismoid is β=35.26°, i.e., half of the dihedral angle (70.53°) between prismoids A and B. Moreover, any edge of the tetrahedron is divided into two edges, such as ab into a_1b_1 and a_2b_2. At this moment, the trends of straight-line motion occur between any two adjacent platforms while they are away from the centroid, which are represented by red solid lines. For instance, virtual straight-line motion path p_1 between platforms A and B is parallel to line a_1a_2, or b_1b_2. To enable this motion, the Sarrus linkage is adopted in this chapter because it can generate the exact straight-line motion between two platforms. As shown in Fig. 3-2(c), one Sarrus linkage between platforms A and B consists of six rigid bodies connected by six revolute joints. Three parallel joints with axes z_1, z_2 and z_3 are implanted along line a_1a_2, as are the other three joints with axes z_4, z_5 and z_6 along b_1b_2. Here, the angle between the revolute axes in two limbs in a Sarrus linkage is γ. To avoid physical interference in the fully folded configuration and consider the tetrahedral geometry, $\gamma \in (0, 70.53°]$ should be satisfied. Moreover, due to the radial decomposition of triangular prismoids, for instance, the side facet of platform A is coplanar with a virtual plane of axes z_3 and z_6. Thus, the straight-line motion along p_1 between platforms A and B is obtained.

Furthermore, we can take a similar implantation and integrate five extra Sarrus linkages into each pair of two adjacent platforms along paths p_2 to p_6 following the procedure along p_1, in which the geometric relations of all integrated Sarrus linkages are identical to demonstrate consistency. Thus, a novel deployable tetrahedral mechanism is obtained, as shown in Fig. 3-2(d), which consequently leads to a transformation from a rhombitetratetrahedron (the deployed configuration) to a tetrahedron (the folded configuration). Moreover, we set γ_{max}=70.53° to obtain a planar triangle in a fully deployed configuration among three different platform vertices (such as a_1, a_2 and a_3), which are composed of three limbs of three adjacent Sarrus linkages. Based on such a construction, Sarrus-based deployable tetrahedron performs synchronized radial motion. These four platforms have straight-line motion along their respective perpendiculars relative to the centroid O while separating from each other, which mechanically presents the expansion operation in geometry. It should be noted that the four platforms A to D are located on the faces of a virtual tetrahedron during the continuous motion process, in which the T_d symmetry of this deployable tetrahedron is completely reserved.

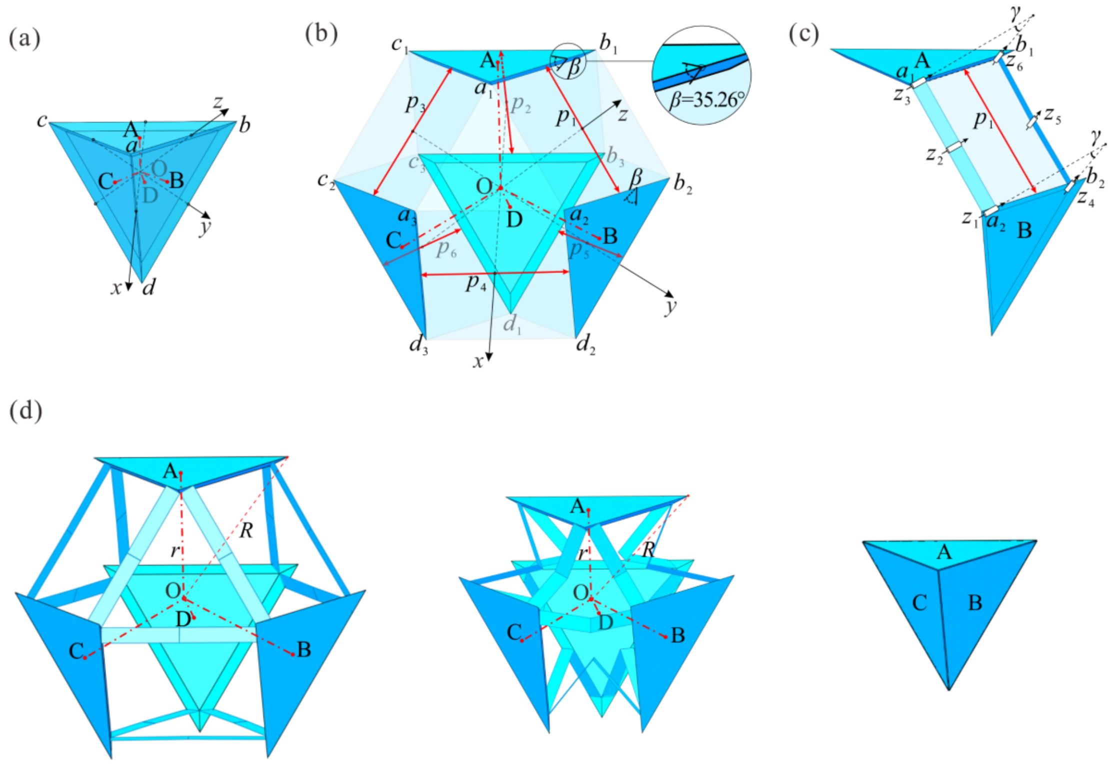

Fig. 3-2 Construction of a deployable tetrahedral mechanism. (a) A tetrahedron and the Cartesian coordinate system; (b) the expansion of four triangular platforms of a tetrahedron; (c) the Sarrus linkage with platforms A and B; (d) the motion sequence (transformation) from a rhombitetratetrahedron (the deployed configuration) to a tetrahedron (the folded configuration).

3.2.1.2 Mobility Analysis and Equivalent Strategy

The mobility of the proposed deployable tetrahedral mechanisms can be investigated with screw theory. First, as the foundational element of polyhedral construction, a Sarrus linkage in an arbitrary configuration is given in Fig. 3-3(a) with a local coordinate frame $\{x_i, y_i, z_i\}$, where origin O_i is located at the centre of the virtual plane between two mobile platforms, the y_i-axis is aligned with the straight-line motion direction and the z_i-axis is perpendicular to the virtual plane. It is well known that this linkage consists of two limbs, and the motion-screw system of limb 1 can be calculated in the associated local coordinate system as

$$\mathbb{S}_{l1}=\begin{cases}\boldsymbol{S}_{i1}=\begin{bmatrix}\sin\alpha & 0 & \cos\alpha & -b\cos\alpha\sin\varphi & l\cos\alpha & b\sin\alpha\sin\varphi\end{bmatrix}^{\mathrm{T}}\\ \boldsymbol{S}_{i2}=\begin{bmatrix}\sin\alpha & 0 & \cos\alpha & 0 & l\cos\alpha-b\cos\varphi & 0\end{bmatrix}^{\mathrm{T}}\\ \boldsymbol{S}_{i3}=\begin{bmatrix}\sin\alpha & 0 & \cos\alpha & b\cos\alpha\sin\varphi & l\cos\alpha & -b\sin\alpha\sin\varphi\end{bmatrix}^{\mathrm{T}}\end{cases} \tag{3-1}$$

for limb 2,

$$\mathbb{S}_{l2}=\begin{cases}\boldsymbol{S}_{i4}=\begin{bmatrix}-\sin\alpha & 0 & \cos\alpha & -b\cos\alpha\sin\varphi & -l\cos\alpha & -b\sin\alpha\sin\varphi\end{bmatrix}^{\mathrm{T}}\\ \boldsymbol{S}_{i5}=\begin{bmatrix}-\sin\alpha & 0 & \cos\alpha & 0 & b\cos\varphi-l\cos\alpha & 0\end{bmatrix}^{\mathrm{T}}\\ \boldsymbol{S}_{i6}=\begin{bmatrix}-\sin\alpha & 0 & \cos\alpha & b\cos\alpha\sin\varphi & -l\cos\alpha & b\sin\alpha\sin\varphi\end{bmatrix}^{\mathrm{T}}\end{cases} \tag{3-2}$$

where subscript i indicates the number of Sarrus linkages involved in the integration of the proposed deployable polyhedral mechanisms, φ is the folding angle between half of the limb and platform, b is half of the edge length of a regular rhombitetratetrahedron, and $l=a/2$ and $\alpha=\gamma/2$.

The reference coordinate frame $\{x, y, z\}$ in the deployed configuration of the tetrahedral mechanism is established in Fig. 3-3(b), in which its reference origin O is located at the centroid of the rhombitetratetrahedron and six local origins O_i (i =1, 2, …, 6) are the centres of virtual planes expanded by any two adjacent platforms. Conceivably, the four platforms A, B, C and D are located at the vertices of a virtual dual tetrahedron during the continuous motion process; thus, a dual tetrahedron is introduced in Fig. 3-3(c) to conveniently describe the directions of axes y_i, i.e., the direction of straight-line motion between two adjacent platforms.

The motion screws of a Sarrus linkage element in Fig. 3-3(a) is transformed with respect to the reference coordinate system in Fig. 3-3(b) using the adjoint transformation matrix $\mathbf{Ad}_T$, in which $\boldsymbol{R}_i$ is the 3×3 rotation transformation matrix and $\boldsymbol{p}_i$ is the skew-symmetric matrix of vector $\boldsymbol{p}_i$ that presents the displacements of origin O_i relative to origin O. Referring to tetrahedral geometric conditions and $\mathrm{T_d}$ symmetry in Figs. 3-3(b) and (c), $\boldsymbol{R}_i$ and $\boldsymbol{p}_i$ (i =1, 2, …, 6) in the deployable tetrahedral mechanism can be obtained as

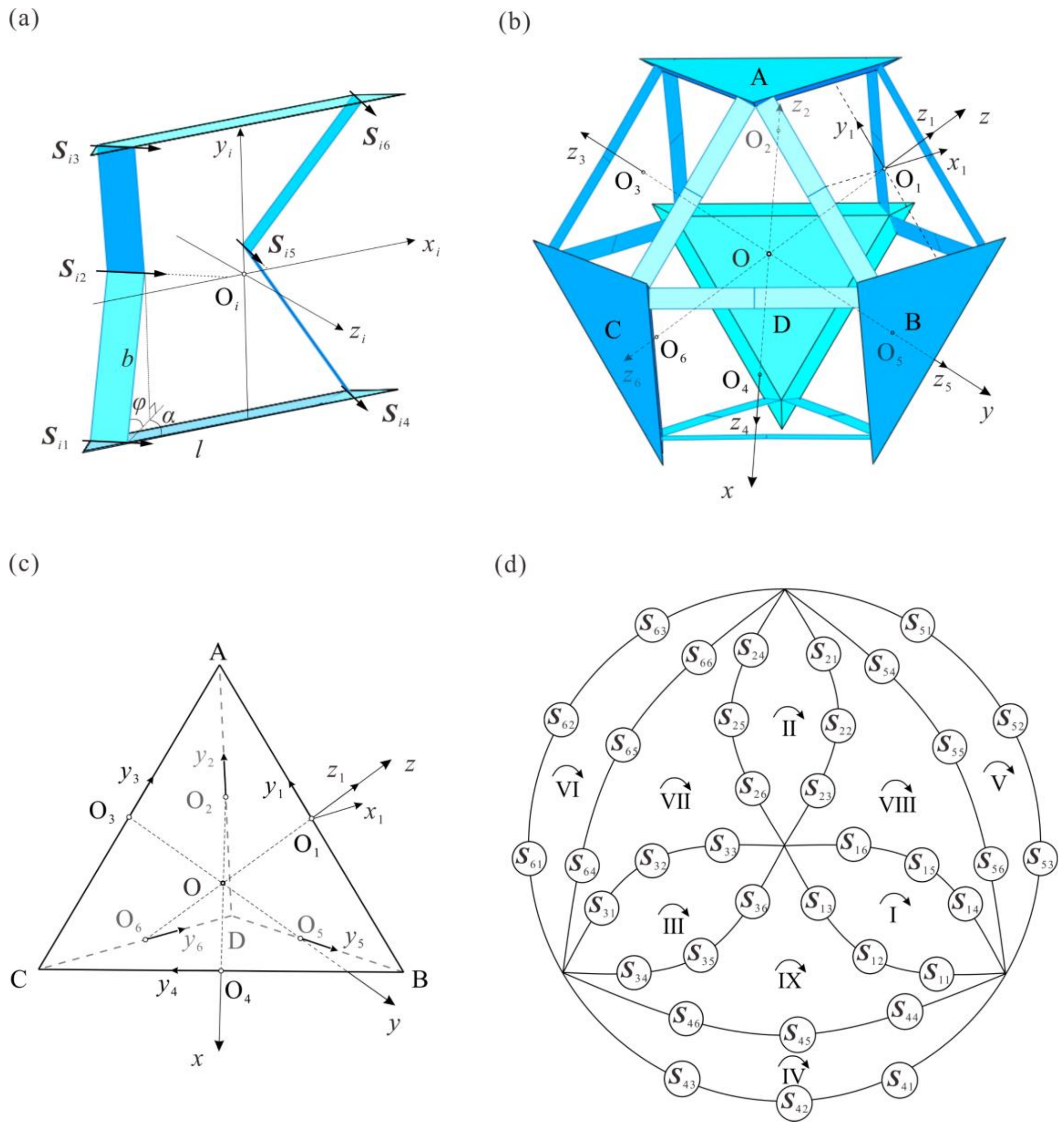

Fig. 3-3 Mobility analysis of deployable tetrahedral mechanism. (a) Joint screws in a Sarrus linkage; coordinate systems in (b) deployed configuration of the tetrahedral mechanism and (c) its dual tetrahedron; (d) constraint graph of this mechanism.

$$\boldsymbol{R}_1 = \begin{bmatrix} -\sqrt{2}/2 & -\sqrt{2}/2 & 0 \\ \sqrt{2}/2 & -\sqrt{2}/2 & 0 \\ 0 & 0 & 1 \end{bmatrix},\ \boldsymbol{p}_1 = d_1\begin{bmatrix} 0 & 0 & 1 \end{bmatrix}^{\mathrm{T}}$$

$$\boldsymbol{R}_2 = \begin{bmatrix} 0 & 0 & -1 \\ -\sqrt{2}/2 & -\sqrt{2}/2 & 0 \\ -\sqrt{2}/2 & \sqrt{2}/2 & 0 \end{bmatrix},\ \boldsymbol{p}_2 = d_1\begin{bmatrix} -1 & 0 & 0 \end{bmatrix}^{\mathrm{T}}$$

$$\boldsymbol{R}_3=\begin{bmatrix}\sqrt{2}/2 & -\sqrt{2}/2 & 0\\ 0 & 0 & -1\\ \sqrt{2}/2 & \sqrt{2}/2 & 0\end{bmatrix},\ \boldsymbol{p}_3=d_1\begin{bmatrix}0 & -1 & 0\end{bmatrix}^{\mathrm{T}}$$

$$\boldsymbol{R}_4=\begin{bmatrix}0 & 0 & 1\\ -\sqrt{2}/2 & -\sqrt{2}/2 & 0\\ \sqrt{2}/2 & -\sqrt{2}/2 & 0\end{bmatrix},\ \boldsymbol{p}_4=d_1\begin{bmatrix}1 & 0 & 0\end{bmatrix}^{\mathrm{T}}$$

$$\boldsymbol{R}_5=\begin{bmatrix}-\sqrt{2}/2 & \sqrt{2}/2 & 0\\ 0 & 0 & 1\\ \sqrt{2}/2 & \sqrt{2}/2 & 0\end{bmatrix},\ \boldsymbol{p}_5=d_1\begin{bmatrix}0 & 1 & 0\end{bmatrix}^{\mathrm{T}}$$

$$\boldsymbol{R}_6=\begin{bmatrix}-\sqrt{2}/2 & -\sqrt{2}/2 & 0\\ -\sqrt{2}/2 & \sqrt{2}/2 & 0\\ 0 & 0 & -1\end{bmatrix},\ \boldsymbol{p}_6=d_1\begin{bmatrix}0 & 0 & -1\end{bmatrix}^{\mathrm{T}} \tag{3-3}$$

Furthermore, the number of links and joints involved in the deployable tetrahedral mechanism are 28 and 36, respectively. Using the Euler formula in the multiloop mechanism, the number of independent loops in this mechanism can be obtained as $36-28+1=9$, and the associated constraint graph is sketched in Fig. 3-3(d). According to Kirchhoff's circulation law for independent loops shown in the constraint graph, the constraint matrix of the deployable tetrahedral mechanism is organized as

$$\boldsymbol{M}_1=\begin{bmatrix}\boldsymbol{S}_1 & \mathbf{0}_6 & \mathbf{0}_6 & \mathbf{0}_6 & \mathbf{0}_6 & \mathbf{0}_6\\ \mathbf{0}_6 & \boldsymbol{S}_2 & \mathbf{0}_6 & \mathbf{0}_6 & \mathbf{0}_6 & \mathbf{0}_6\\ \mathbf{0}_6 & \mathbf{0}_6 & \boldsymbol{S}_3 & \mathbf{0}_6 & \mathbf{0}_6 & \mathbf{0}_6\\ \mathbf{0}_6 & \mathbf{0}_6 & \mathbf{0}_6 & \boldsymbol{S}_4 & \mathbf{0}_6 & \mathbf{0}_6\\ \mathbf{0}_6 & \mathbf{0}_6 & \mathbf{0}_6 & \mathbf{0}_6 & \boldsymbol{S}_5 & \mathbf{0}_6\\ \mathbf{0}_6 & \mathbf{0}_6 & \mathbf{0}_6 & \mathbf{0}_6 & \mathbf{0}_6 & \boldsymbol{S}_6\\ \mathbf{0}_6 & -\boldsymbol{S}_2'' & -\boldsymbol{S}_3' & \mathbf{0}_6 & \mathbf{0}_6 & -\boldsymbol{S}_6''\\ -\boldsymbol{S}_1'' & -\boldsymbol{S}_2' & \mathbf{0}_6 & \mathbf{0}_6 & -\boldsymbol{S}_5'' & \mathbf{0}_6\\ -\boldsymbol{S}_1' & \mathbf{0}_6 & -\boldsymbol{S}_3'' & -\boldsymbol{S}_4'' & \mathbf{0}_6 & \mathbf{0}_6\end{bmatrix} \tag{3-4}$$

where $\boldsymbol{S}_i=\begin{bmatrix}\boldsymbol{S}_{i1} & \boldsymbol{S}_{i2} & \boldsymbol{S}_{i3} & \boldsymbol{S}_{i4} & \boldsymbol{S}_{i5} & \boldsymbol{S}_{i6}\end{bmatrix}$, $\boldsymbol{S}_i'=\begin{bmatrix}\boldsymbol{S}_{i1} & \boldsymbol{S}_{i2} & \boldsymbol{S}_{i3} & \mathbf{0} & \mathbf{0} & \mathbf{0}\end{bmatrix}$, $\boldsymbol{S}_i''=\begin{bmatrix}\mathbf{0} & \mathbf{0} & \mathbf{0} & \boldsymbol{S}_{i4} & \boldsymbol{S}_{i5} & \boldsymbol{S}_{i6}\end{bmatrix}$ and $\mathbf{0}_6=\begin{bmatrix}\mathbf{0} & \mathbf{0} & \mathbf{0} & \mathbf{0} & \mathbf{0} & \mathbf{0}\end{bmatrix}$ with $\mathbf{0}=\begin{bmatrix}0 & 0 & 0 & 0 & 0 & 0\end{bmatrix}^{\mathrm{T}}$.

The mobility of this mechanism can be determined with the 54×36 constraint matrix as

$$m = n - \text{rank}(\boldsymbol{M}_1) = 36 - 35 = 1 \tag{3-5}$$

in which m represents the actual mobility of this mechanism and n is the number of joints. Moreover, all six involved Sarrus linkages have identical kinematic behaviour to generate the synchronized radial motion of the entire mechanism, which is revealed and proven as follows.

As shown in Fig. 3-4, considering the Sarrus linkage between platforms A and B as an example, φ_1 and φ_1' are two related kinematic variables, as shown in Fig. 3-3(a), and $\varphi_1'=2\varphi_1$ can be easily obtained. Moreover, for all six involved Sarrus linkages, $\varphi_i'=2\varphi_i$ (i =1 to 6). Next, among platforms A, B and C, a spatial 9R linkage can be identified as an assembly of three limbs of three corresponding Sarrus linkages, in which the revolute axes z_1 to z_9 are highlighted in red. Similarly, a general kinematic solution of this spatial 9R linkage is revealed in Section 2.2, including the matrix operation process based on the D-H matrix method.

In this tetrahedral mechanism, for the spatial 9R linkage among platforms A, B and C, we have the motion constraint relationships as

$$\varphi_1'=2\varphi_1,\ \varphi_3'=2\varphi_3, \varphi_4'=2\varphi_4 \tag{3-6}$$

Substituting this constraint condition into kinematic solution of this 9R linkage yields

$$\varphi_1=\varphi_3=\varphi_4,\ \varphi_1'=\varphi_3'=\varphi_4' \tag{3-7}$$

Conducting a similar calculation procedure, other constraint conditions for the remaining three 9R linkages are

$$\begin{aligned} &\varphi_1'=2\varphi_1,\ \varphi_2'=2\varphi_2,\ \varphi_5'=2\varphi_5 \\ &\varphi_2'=2\varphi_2,\ \varphi_3'=2\varphi_3,\ \varphi_6'=2\varphi_6 \\ &\varphi_4'=2\varphi_4,\ \varphi_5'=2\varphi_5,\ \varphi_6'=2\varphi_6 \end{aligned} \tag{3-8}$$

Furthermore, we can obtain the kinematic relationships in the entire tetrahedral mechanism as

$$\varphi_1=\varphi_2=\varphi_3=\varphi_4=\varphi_5=\varphi_6,\ \varphi_1'=\varphi_2'=\varphi_3'=\varphi_4'=\varphi_5'=\varphi_6' \tag{3-9}$$

Therefore, all the six involved Sarrus linkages have the identical kinematic behaviour that can generate the 1-DOF synchronized radial motion of the entire tetrahedral mechanism.

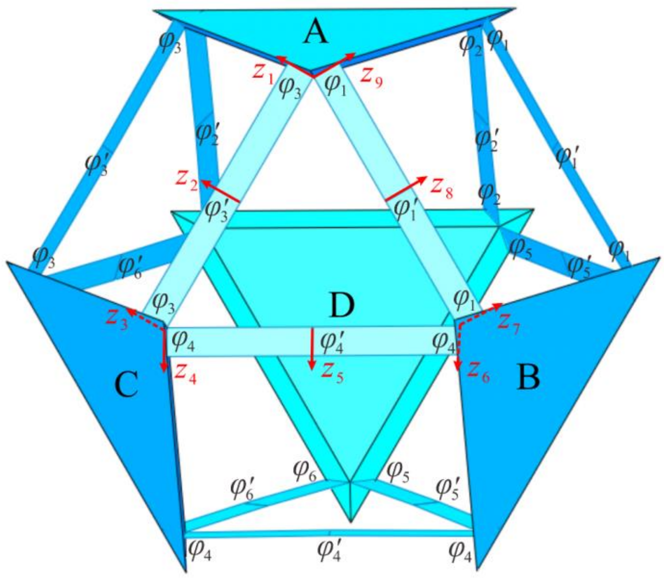

Fig. 3-4 Analysis of kinematic variables in the tetrahedral mechanism.

Based on the above derivation, we prove that the tetrahedral mechanism has a mobility of one. However, the calculation and solution of the constraint matrix are complicated due to the complexity of the polyhedral geometry and the significantly large number of links and joints in the proposed polyhedral mechanism. To find a simple and effective analysis method for the mobility of deployable polyhedrons, we present the equivalent analysis strategy as follows by solving the equivalent motion screws.

Additionally, beginning with the construction element, the constraint screw system of limb 1 in Sarrus linkage can be obtained by solving the reciprocal screws of $\mathbb{S}_{l1}$ as

$$\mathbb{S}_{l1}^{r}=\begin{cases}\boldsymbol{S}_{i1}^{r}=\begin{bmatrix}\tan\alpha & 0 & 1 & 0 & 0 & 0\end{bmatrix}^{\mathrm{T}}\\ \boldsymbol{S}_{i2}^{r}=\begin{bmatrix}0 & 0 & 0 & 0 & 1 & 0\end{bmatrix}^{\mathrm{T}}\\ \boldsymbol{S}_{i3}^{r}=\begin{bmatrix}0 & 0 & 0 & -\cot\alpha & 0 & 1\end{bmatrix}^{\mathrm{T}}\end{cases} \tag{3-10}$$

for limb 2,

$$\mathbb{S}_{l2}^{r}=\begin{cases}\boldsymbol{S}_{i4}^{r}=\begin{bmatrix}-\tan\alpha & 0 & 1 & 0 & 0 & 0\end{bmatrix}^{\mathrm{T}}\\ \boldsymbol{S}_{i5}^{r}=\begin{bmatrix}0 & 0 & 0 & 0 & 1 & 0\end{bmatrix}^{\mathrm{T}}\\ \boldsymbol{S}_{i6}^{r}=\begin{bmatrix}0 & 0 & 0 & \cot\alpha & 0 & 1\end{bmatrix}^{\mathrm{T}}\end{cases} \tag{3-11}$$

The platform constraint-screw multiset is the combination of the above two constraint screw systems, which contains five linearly independent screws. A nonunique basis for the subspace of the constraint screw multiset can be selected as

$$\mathbb{S}_i^r = \begin{cases} \boldsymbol{S}_{i1}^r = \begin{bmatrix} 1 & 0 & 1 & 0 & 0 & 0 \end{bmatrix}^{\mathrm{T}} \\ \boldsymbol{S}_{i2}^r = \begin{bmatrix} 0 & 0 & 0 & 0 & 1 & 0 \end{bmatrix}^{\mathrm{T}} \\ \boldsymbol{S}_{i3}^r = \begin{bmatrix} 0 & 0 & 0 & -1 & 0 & 1 \end{bmatrix}^{\mathrm{T}} \\ \boldsymbol{S}_{i4}^r = \begin{bmatrix} -1 & 0 & 1 & 0 & 0 & 0 \end{bmatrix}^{\mathrm{T}} \\ \boldsymbol{S}_{i5}^r = \begin{bmatrix} 0 & 0 & 0 & 1 & 0 & 1 \end{bmatrix}^{\mathrm{T}} \end{cases} \tag{3-12}$$

By considering the reciprocal screw of $\mathbb{S}_i^r$, the equivalent motion screw between two platforms in a Sarrus linkage is

$$\boldsymbol{S}_{fi} = \begin{bmatrix} 0 & 0 & 0 & 0 & 1 & 0 \end{bmatrix}^{\mathrm{T}} \tag{3-13}$$

which indicates the straight-line motion between two platforms along the y_i-axis.

Therefore, we regard a Sarrus linkage as a prismatic joint, and the tetrahedral mechanism obtained in Fig. 3-2 can be simplified as an equivalent mechanism with six prismatic joints denoted by P_1 to P_6 (see Fig. 3-5(a)). The original six motion screws in Eqs. (3-1) and (3-2) can be equivalently replaced by a single motion screw in Eq. (3-13); thus, the equivalent topological graph is given in Fig. 3-5(b). Furthermore, the simplified mobility analysis of the tetrahedral mechanism can be conducted by redrawing the constraint graph in Fig. 3-5(c) with equivalent motion screws $\boldsymbol{S}_{f1}$ to $\boldsymbol{S}_{f6}$, which can also be obtained in the reference coordinate system through adjoint transformation matrices. According to Fig. 3-5(c), the constraint matrix $\boldsymbol{M}_{e1}$ can be rewritten as

$$\boldsymbol{M}_{e1} = \begin{bmatrix} \boldsymbol{S}_{f1} & \boldsymbol{S}_{f2} & \mathbf{0} & \mathbf{0} & \boldsymbol{S}_{f5} & \mathbf{0} \\ \mathbf{0} & -\boldsymbol{S}_{f2} & \boldsymbol{S}_{f3} & \mathbf{0} & \mathbf{0} & \boldsymbol{S}_{f6} \\ -\boldsymbol{S}_{f1} & \mathbf{0} & -\boldsymbol{S}_{f3} & \boldsymbol{S}_{f4} & \mathbf{0} & \mathbf{0} \end{bmatrix} \tag{3-14}$$

which is a 18×6 one.

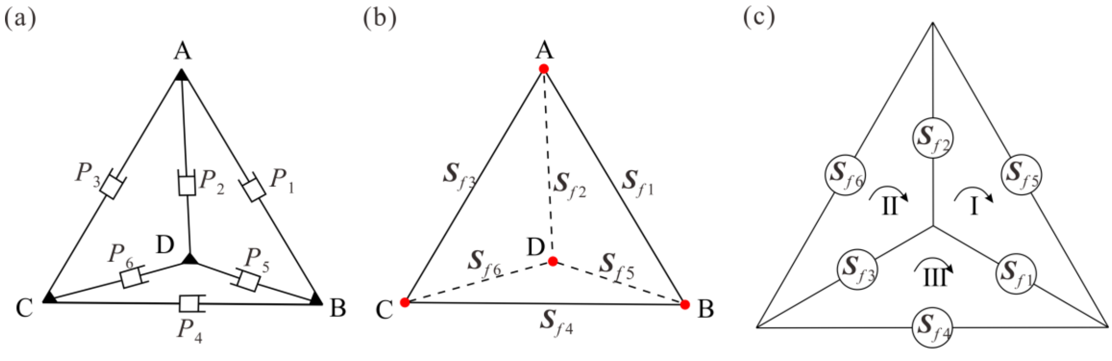

Fig. 3-5 Equivalent tetrahedral mechanism. (a) Schematic diagram of the equivalent mechanism with prismatic joints, (b) its three-dimensional equivalent topological graph and (c) constraint graph.

Therefore, referring to this equivalent constraint matrix, the identical conclusion that the deployable tetrahedral mechanism has mobility one can be verified as

$$m = n_e - \mathrm{rank}(\boldsymbol{M}_{\mathrm{e1}}) = 6 - 5 = 1 \tag{3-15}$$

in which n_e is the number of equivalent prismatic joints.

Due to the 1-DOF synchronized radial motion with unchanged T_d symmetry of this tetrahedral mechanism, both the inscribed sphere and circumscribed sphere related to the four platforms are regular spheres. When φ=0 (the folding angle in a Sarrus linkage), referring to a tetrahedron in a fully folded configuration, the inscribed sphere radius (r) and circumscribed sphere radius (R) in this mechanism are $\sqrt{6}a/12$ and $\sqrt{6}a/4$, respectively. Following deployed motion until φ=90°, i.e., a completely deployable configuration, r increases to $\sqrt{6}a/3$, and R becomes a.

Thus, together with the kinematic and geometric calculations, the relationships between the polyhedral geometry and kinematic angle are $r = \sqrt{6}a(3\sin\varphi + 1)/12$ and $R = a\sqrt{(3\sin^2\varphi + 2\sin\varphi + 3)/8}$. Next, for the volume ($V$) of the deployable tetrahedron during continuous motion, $V = \sqrt{2}a^3(\sin^3\varphi + 9\sin^2\varphi + 9\sin\varphi + 1)/12$, in which a is the edge length of a regular tetrahedron. Hence, the input–output curves between the polyhedral geometry and kinematic angle are illustrated in Fig. 3-6.

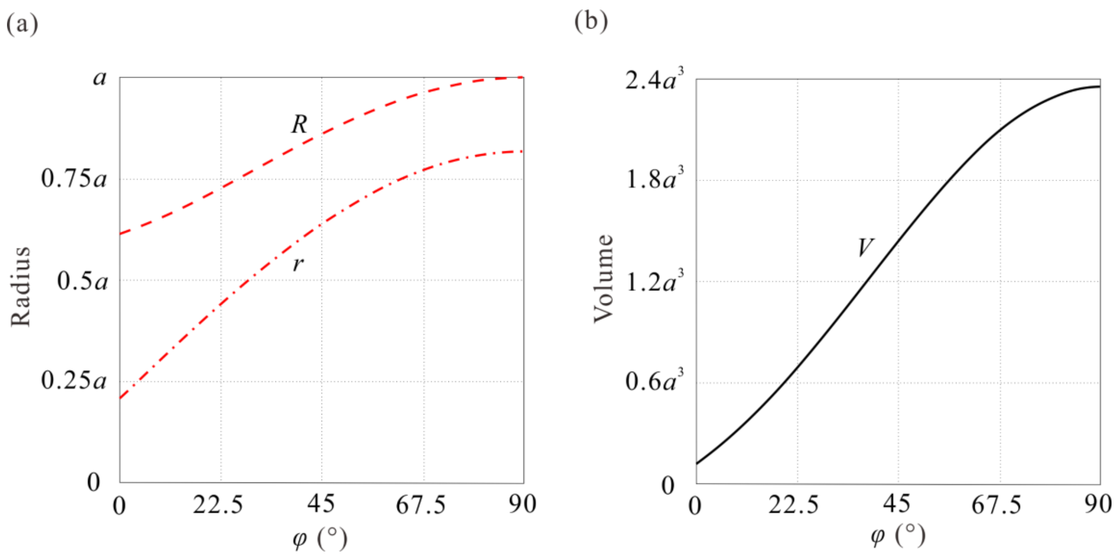

Fig. 3-6 Kinematic curves of (a) inscribed sphere radius r and circumscribed sphere radius R and (b) the volume V vs. folding angle φ.

Therefore, a novel synthesis mothed based on the expansion operation and Sarrus linkages is presented to construct the 1-DOF deployable tetrahedral mechanism, and its significant symmetry property perfectly remains in each work configuration, whose corresponding prototype is fabricated (see Fig. 3-7). The kinematic strategy of construction and mobility analysis can be readily extended to deployable cubic and dodecahedral mechanisms with distinct symmetries, as shown below.

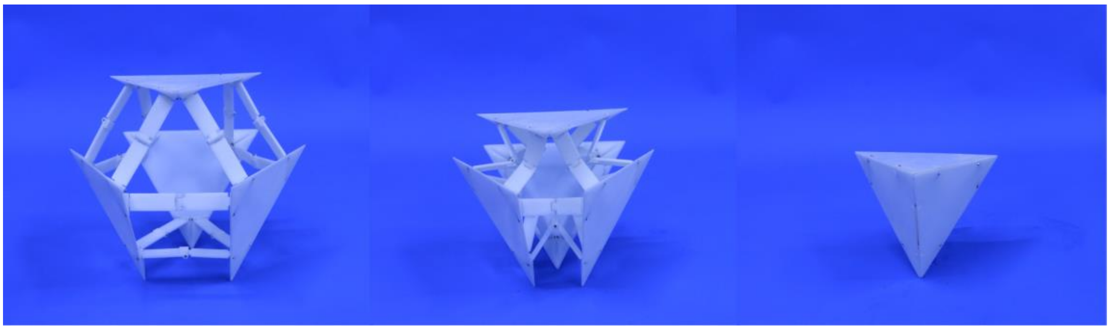

Fig. 3-7 Motion sequence of the tetrahedral mechanism.

3.2.2 Deployable Cubic Mechanism

A cube with six congruous square prismoid platforms A to F and twelve edges is shown in Fig. 3-8(a), in which the axes in a global coordinate system are perpendicular to the platforms. Following the expansion operation, Fig. 3-8(b) presents all separated platforms along red dash-dot perpendiculars, and a total of twelve virtual motion paths (indicated in red lines) between each pair of adjacent platforms are generated in Fig. 3-8(c). In this case, the angle between the bottom and side facets of each square prismoid is β=45°. As a result, twelve Sarrus linkages need to be involved to construct a deployable cubic mechanism, in which the geometry and kinematics of each identical Sarrus linkage are the same as those in Fig. 3-2(c). Moreover, $\gamma \in \left(0, 109.47°\right]$ should be satisfied in this case to avoid interference, and the angle between the virtual plane (Sarrus translational platform) and polyhedral platform is also β=45°. Therefore, the transformation from a rhombicuboctahedron to a cube with synchronized radial motion is obtained and shown in Fig. 3-8(d).

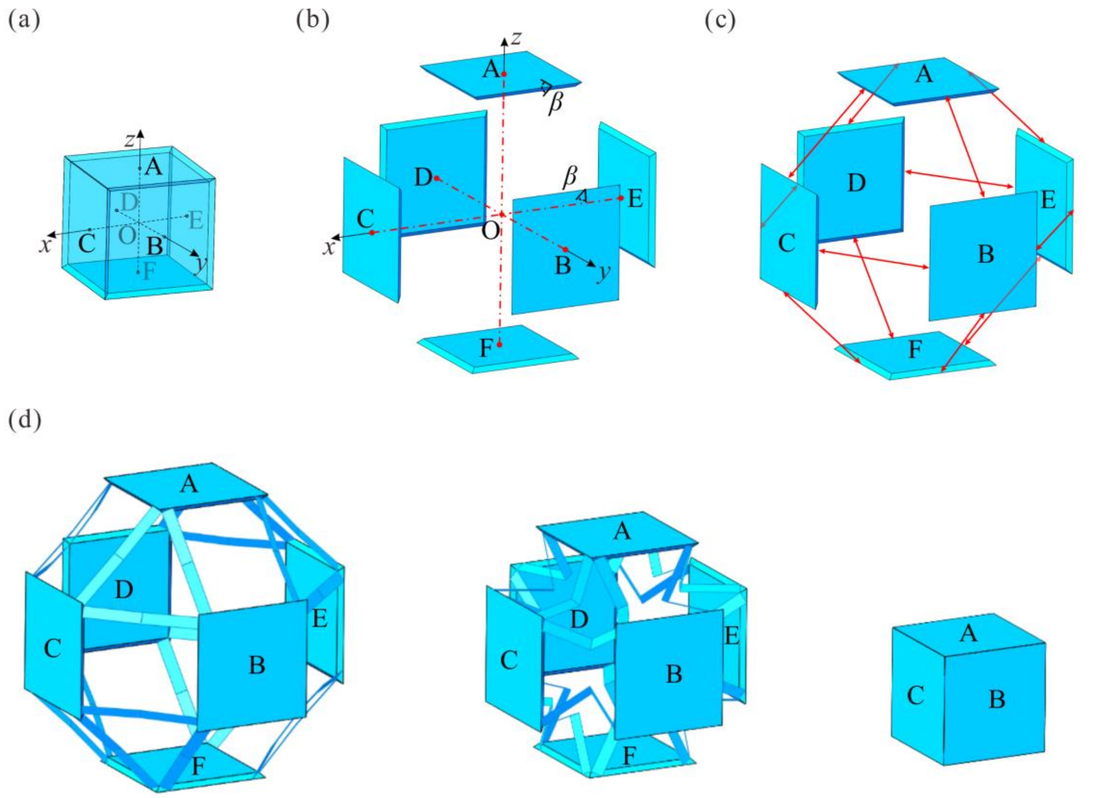

Fig. 3-8 Construction of the deployable cubic mechanism. (a) A cube and the Cartesian coordinate system; (b) the expansion of six square platforms of a cube; (c) straight-line motion paths between two adjacent platforms; (d) the motion sequence from a rhombicuboctahedron (the deployed configuration) to a cube (the folded configuration).

Without loss of generality, the equivalent mobility analysis method can be effectively applied to this deployable cubic mechanism involving twelve Sarrus linkages. Similarly, by regarding a Sarrus linkage as a prismatic joint, the equivalent motion screws can be calculated based on the reference coordinate frame in Fig. 3-9(a) and its dual octahedron in Fig. 3-9(b), in which the details of adjoint transformation matrices are provided in Appendix A. Thus, the equivalent mechanism of the proposed cubic mechanism can be obtained in Fig. 3-9(c) with prismatic joints P_1 to P_{12}, which has a base of its dual octahedron. Inspired by the Schlegel diagram for polyhedral representation, i.e., a planar projection of a polyhedron, Fig. 3-9(d) illustrates the constraint graph of the equivalent mechanism with $\boldsymbol{S}_{f1}$ to $\boldsymbol{S}_{f12}$; then, the constraint matrix can be derived as

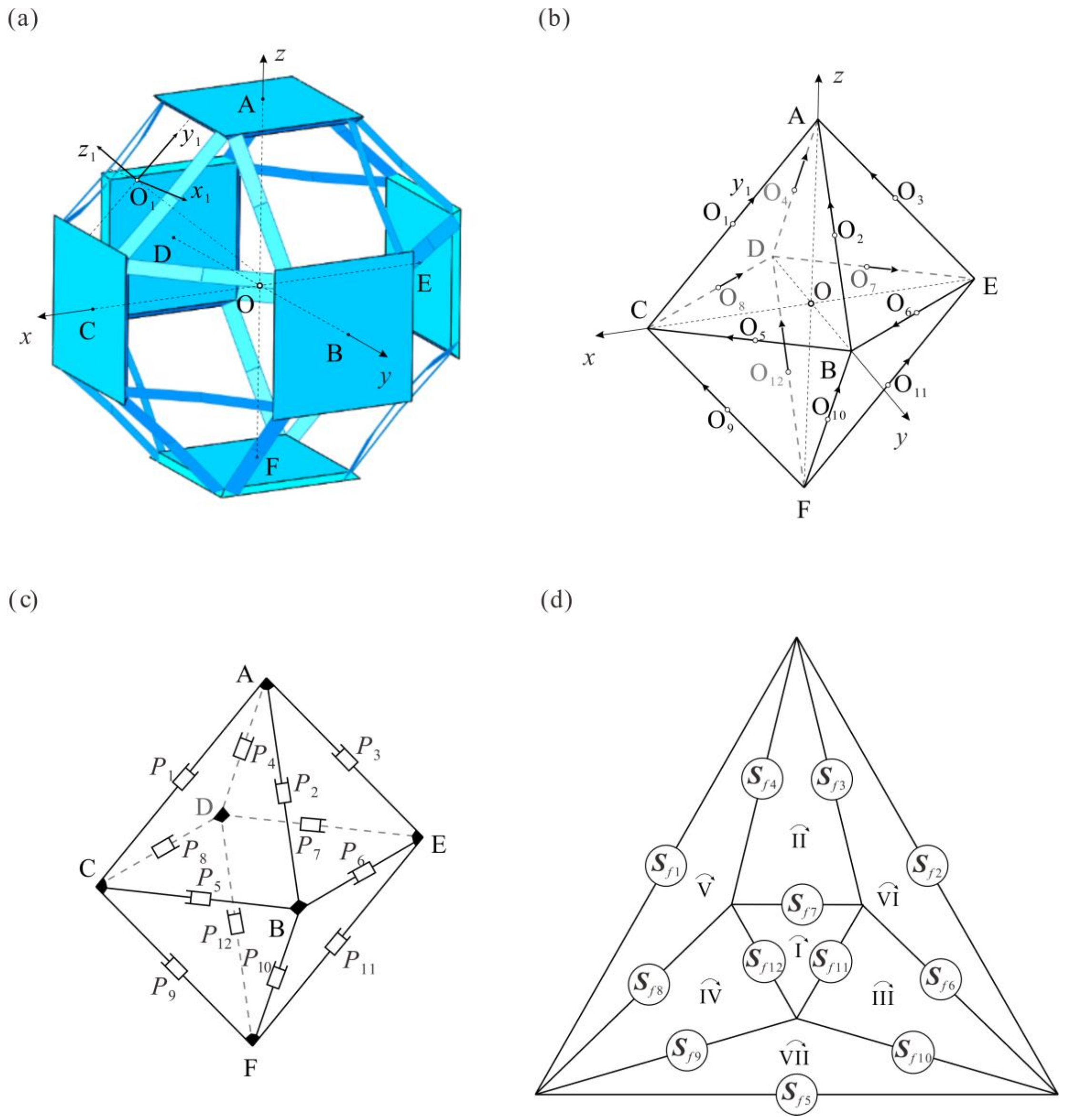

Fig. 3-9 Mobility analysis of deployable cubic mechanism. Coordinate system in (a) deployed configuration of cubic mechanism (rhombicuboctahedron) and (b) its dual octahedron (y_i presents the direction of straight-line motion); (c) the equivalent mechanism with twelve prismatic joints and (d) its constraint graph.

$$
\boldsymbol{M}_{e2}=\begin{bmatrix}
\mathbf{0}&\mathbf{0}&\mathbf{0}&\mathbf{0}&\mathbf{0}&\mathbf{0}&\boldsymbol{S}_{f7}&\mathbf{0}&\mathbf{0}&\mathbf{0}&\boldsymbol{S}_{f11}&\boldsymbol{S}_{f12}\\
\mathbf{0}&\mathbf{0}&\boldsymbol{S}_{f3}&\boldsymbol{S}_{f4}&\mathbf{0}&\mathbf{0}&-\boldsymbol{S}_{f7}&\mathbf{0}&\mathbf{0}&\mathbf{0}&\mathbf{0}&\mathbf{0}\\
\mathbf{0}&\mathbf{0}&\mathbf{0}&\mathbf{0}&\mathbf{0}&\boldsymbol{S}_{f6}&\mathbf{0}&\mathbf{0}&\mathbf{0}&\boldsymbol{S}_{f10}&-\boldsymbol{S}_{f11}&\mathbf{0}\\
\mathbf{0}&\mathbf{0}&\mathbf{0}&\mathbf{0}&\mathbf{0}&\mathbf{0}&\mathbf{0}&\boldsymbol{S}_{f8}&\boldsymbol{S}_{f9}&\mathbf{0}&\mathbf{0}&-\boldsymbol{S}_{f12}\\
\boldsymbol{S}_{f1}&\mathbf{0}&\mathbf{0}&-\boldsymbol{S}_{f4}&\mathbf{0}&\mathbf{0}&\mathbf{0}&-\boldsymbol{S}_{f8}&\mathbf{0}&\mathbf{0}&\mathbf{0}&\mathbf{0}\\
\mathbf{0}&\boldsymbol{S}_{f2}&-\boldsymbol{S}_{f3}&\mathbf{0}&\mathbf{0}&-\boldsymbol{S}_{f6}&\mathbf{0}&\mathbf{0}&\mathbf{0}&\mathbf{0}&\mathbf{0}&\mathbf{0}\\
\mathbf{0}&\mathbf{0}&\mathbf{0}&\mathbf{0}&\boldsymbol{S}_{f5}&\mathbf{0}&\mathbf{0}&\mathbf{0}&-\boldsymbol{S}_{f9}&-\boldsymbol{S}_{f10}&\mathbf{0}&\mathbf{0}
\end{bmatrix} \tag{3-16}
$$

The rank of this constraint matrix is 11, thus $m = n_e - \text{rank}(\boldsymbol{M}_{e2}) = 12 - 11 = 1$, which indicates that the deployable cubic mechanism has mobility. To verify the equivalent analysis result, the original constraint graph and a 114×72 original constraint matrix $\boldsymbol{M}_2$ are given in Appendix A, which confirms that the Sarrus-based deployable cubic mechanism has a mobility of one.

3.2.3 Deployable Dodecahedral Mechanism

Furthermore, we can also create a deployable dodecahedral mechanism following I_h symmetry with the proposed construction strategy. A dodecahedron with twelve congruous pentagonal platforms and thirty edges is given in Fig. 3-10(a). After the expansion operation of pentagonal prismoids with β=58.28° (a half of the dihedral angle between two adjacent pentagonal platforms), thirty red straight-line motion paths are illustrated in Fig. 3-10(b). Considering the similar implantation of Sarrus linkages as given in Fig. 3-2(c), the deployable dodecahedron based on thirty identical Sarrus linkages is constructed in Fig. 3-10(c), in which $\gamma \in \left(0, 138.19°\right]$ should be considered. Moreover, the radial transformation from a rhombicosidodecahedron to a dodecahedron is obtained.

By following the equivalent analysis approach, the coordinate systems of the deployable dodecahedral mechanism are established in Figs. 3-11(a) and (b), and thirty motion screws can be derived referring to the details listed in Appendix B. Hence, we obtain an equivalent mechanism with thirty prismatic joints on the basis of a dual icosahedron, as shown in Fig. 3-11(c). Together with the Schlegel diagram of its dual icosahedron, the equivalent constraint graph with thirty motion screws $\boldsymbol{S}_{f1}$ to $\boldsymbol{S}_{f30}$ is sketched in Fig. 3-11(d); then, a 114×30 equivalent constraint matrix $\boldsymbol{M}_{e3}$ can be organized as

$$\boldsymbol{M}_{e3} = \begin{bmatrix} \mathbf{0}_{6\times6} & \mathbf{0}_{6\times6} & \boldsymbol{M}_{13} & \boldsymbol{M}_{14} & \boldsymbol{M}_{15} \\ \mathbf{0}_{6\times6} & \boldsymbol{M}_{22} & \boldsymbol{M}_{23} & \boldsymbol{M}_{24} & \boldsymbol{M}_{25} \\ \boldsymbol{M}_{31} & \boldsymbol{M}_{32} & \boldsymbol{M}_{33} & \mathbf{0}_{7\times6} & \mathbf{0}_{7\times6} \end{bmatrix} \tag{3-17}$$

in which its submatrices are given in Appendix B.

The rank of this constraint matrix can be calculated as 29. Therefore, the mobility of the deployable dodecahedral mechanism is $m = n_e - \text{rank}(\boldsymbol{M}_{e3}) = 30 - 29 = 1$. Furthermore, the original constraint graph and the 114×30 original constraint matrix

$\boldsymbol{M}_3$ of this mechanism can be found in Appendix B, as well as the same conclusion about the mobility of one.

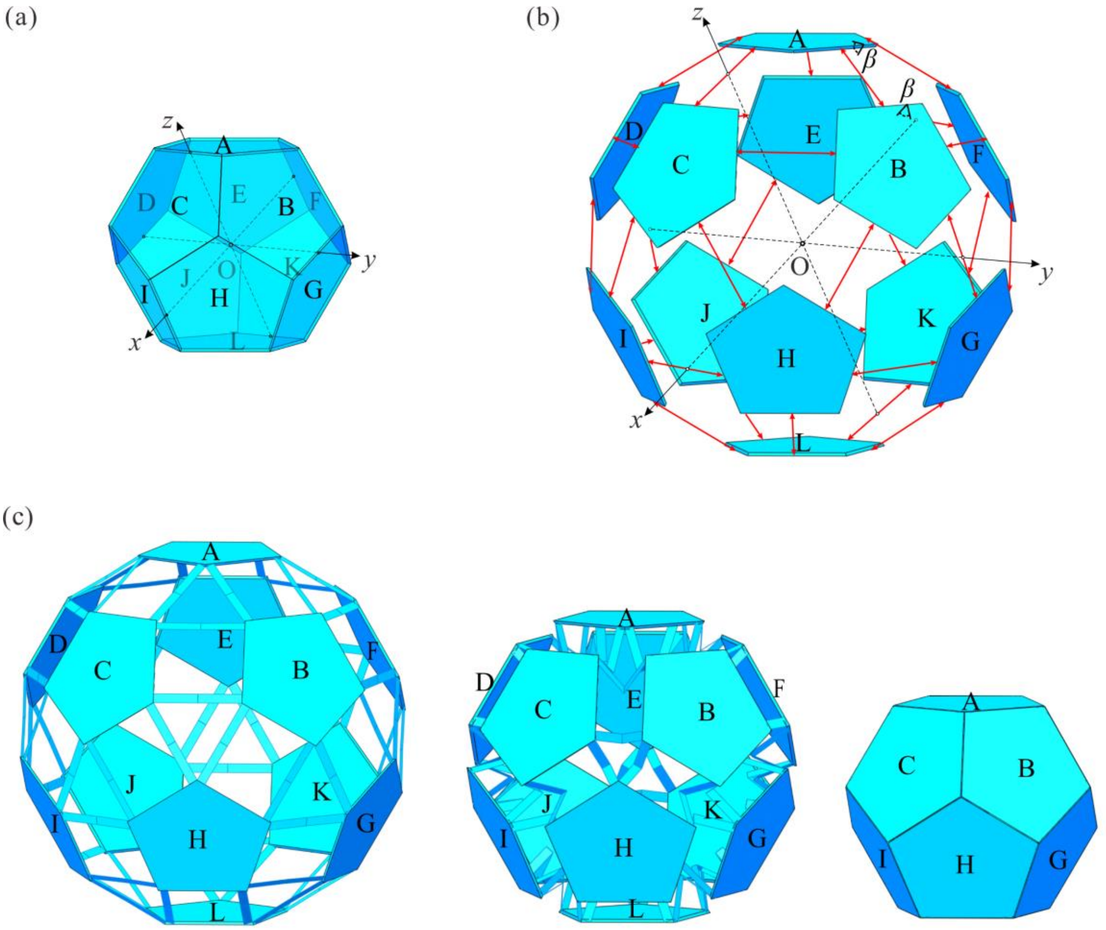

Fig. 3-10 Construction of the deployable dodecahedral mechanism. (a) A dodecahedron and the Cartesian coordinate system; (b) straight-line motion paths between two adjacent pentagonal platforms; (c) the motion sequence from a rhombicosidodecahedron (the deployed configuration) to a dodecahedron (the folded configuration).

Although only three platonic polyhedrons are investigated in this chapter (due to their regular transformability), these construction methods can be adapted to explore the design of other 1-DOF deployable polyhedrons, such as Archimedean and prismatic polyhedrons. The details of Sarrus-based DPMs that can be constructed with the proposed method are listed in Table 3-1, including the number of Sarrus linkages (N_{Sarrus}), links (N_{link}), joints (N_{joint}) and the angle $\beta_{(M,N)}$ for radially decomposed prismoids and the angle γ_{max} to avoid interference. To realize such polyhedral construction, three adjacent platforms in a polyhedron should surround at a common vertex, similar to the synthesis principle of the proposed tetrahedral, cubic and dodecahedral mechanisms.

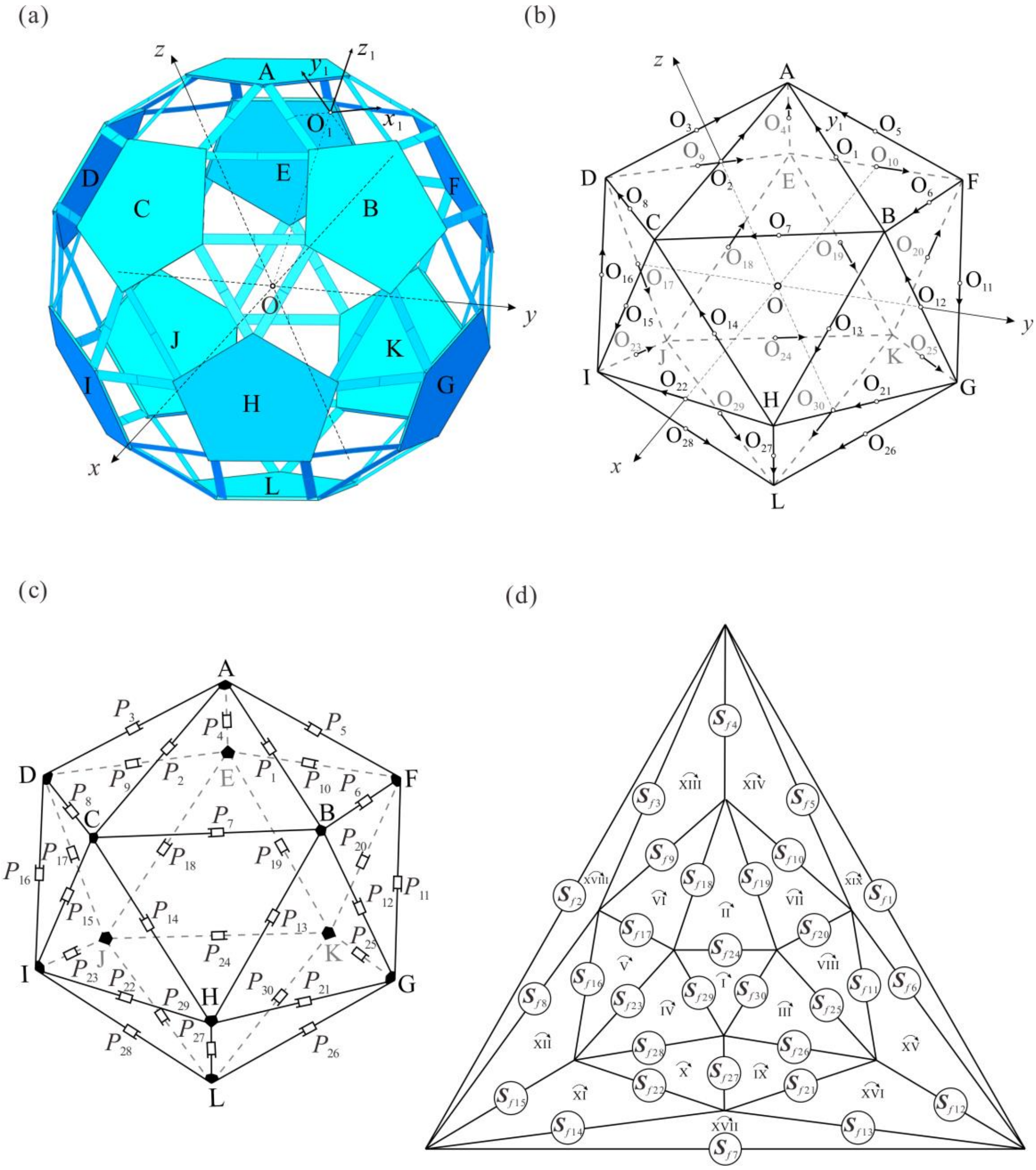

Fig. 3-11 Mobility analysis of the deployable dodecahedral mechanism. Coordinate system in (a) deployed configuration of the dodecahedron (rhombicosidodecahedron) and (b) its dual icosahedron y_i present the direction of straight-line motion); (c) the equivalent mechanism with thirty prismatic joints and (d) its constraint graph.

Table 3-1 Sarrus-based DPMs in different polyhedral groups

Polyhedral groups	Deployable mechanisms	N_{Sarrus}	N_{link}	N_{joint}	$\beta_{(M,N)}$ (°)	γ_{max} (°)
Platonic polyhedrons	Tetrahedron	6	28	36	35.26 $_{(3,3)}$	70.53
	Cube	12	54	72	45 $_{(4,4)}$	109.47
	Dodecahedron	30	132	180	58.28 $_{(5,5)}$	139.18
Archimedean polyhedrons	Truncated tetrahedron	18	80	108	54.74 $_{(3,6)}$ 35.26 $_{(6,6)}$	129.52
	Truncated cube	36	158	216	62.63 $_{(3,8)}$ 45 $_{(8,8)}$	147.35
	Truncated octahedron	36	158	216	62.63 $_{(4,6)}$ 54.74 $_{(6,6)}$	143.13
	Truncated cuboctahedron	72	314	432	72.37 $_{(4,6)}$ 67.5 $_{(4,8)}$ 62.63 $_{(6,8)}$	155.09
	Truncated dodecahedron	90	392	540	71.31 $_{(3,10)}$ 58.28 $_{(10,10)}$	160.61
	Truncated icosahedron	90	392	540	69.09 $_{(6,6)}$ 71.31 $_{(5,6)}$	156.72
	Truncated icosidodecahedron	180	782	1080	79.55 $_{(4,6)}$ 74.14 $_{(4,10)}$ 71.31 $_{(6,10)}$	164.89
Prisms	N-prism ($N \geq 3$)	$3N$	$13N+2$	$18N$	$90(N-2)/N$ $_{(4,4)}$ 45 $_{(4,N)}$	$2\arccos(1+\csc^2(\pi/N))^{-1/2}$

3.3 Overconstraint reduction Inspired by Hamiltonian Paths

3.3.1 Reduction of the Tetrahedral Mechanism

The proposed tetrahedral mechanism is illustrated in Fig. 3-12, as is its equivalent mechanism with six prismatic joints and the corresponding three-dimensional topological graphs, which is the basis of the dual tetrahedron. Based on the Grübler-Kutzbach formula, the mobility of one mechanism can be described as

$$M = d(n - g - 1) + \sum_{i=1}^{g} f_i \tag{3-18}$$

where M is the expected mobility, d is the mobility coefficient and can be obtained from the motion screw system, n is the number of rigid links, g is the number of kinematic joints, and f_i is the degree of freedom of the i-th kinematic joint.

Taking the proposed 1-DOF deployable tetrahedral mechanism in Fig. 3-12(a) with 28 links and 36 revolute joints as an example, its expected mobility $M = 6(28-36-1)+36 = -18$; hence, it is a highly overconstrained mechanism. Thus, the original degree of overconstraints c in this mechanism can be derived as

$$c = m - M = 1-(-18) = 19 \tag{3-19}$$

in which m represents the actual mobility of the mechanism.

Referring to the equivalent strategy, the equivalent tetrahedral mechanism with six prismatic joints is shown in Fig. 3-12(b). Thus, combining Eqs. (3-18) and (3-19), the equivalent overconstraints c_e in this equivalent mechanism are

$$c_e = m - M = 1-(-3) = 4 \tag{3-20}$$

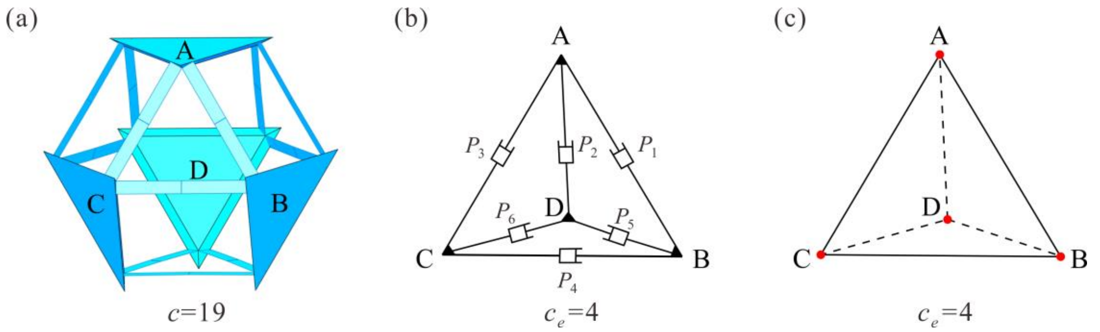

Fig. 3-12 Sarrus-based deployable tetrahedral mechanism. (a) Original mechanism constructed by Sarrus linkages; (b) the equivalent mechanism with prismatic joints; (c) the corresponding three-dimensional topological graph.

However, overconstraints still exist. To reduce or even eliminate the overconstraints in the multiloop mechanism and find the effective constraint space for polyhedral platforms, we clarify the reduction process as follows by utilizing the topology operation.

The essential premise of reduction is that each platform requires at least two equivalent prismatic joints to maintain the closed-loop mechanism, i.e., each vertex is related to at least two edges in the topological graph, and then the original kinematic properties, including mobility and radial motion, should be reserved among polyhedral platforms. It is mathematically surprising to find that the Hamiltonian path (or Hamiltonian cycle) matches the premise of the reduction process. There are two significant characteristics of the Hamiltonian path: first, it is a closed-loop path with a sequence of edges that visits all the vertices of a graph; second, each vertex between two edges is only accessed exactly once along the path. For demonstration purposes, the generation process of the Hamiltonian path in a tetrahedron is taken as an example, as shown in Fig. 3-13. First, starting from vertex A, any edge among AB, AC and AD is identical due to tetrahedral symmetry; here, edge AB in Fig. 3-13(a) is selected. Subsequently, edges BD and BC are also identical in tetrahedral symmetry, so edge BD is selected in Fig. 3-13(b). Next, edge DC can only be selected to connect vertex C instead of edge DA, as shown in Fig. 3-13(c). Finally, the closed-loop path is obtained in Fig. 3-13(d) by connecting the initial vertex A through the edge CA. Due to the tetrahedral symmetry, there is only one Hamiltonian path in a tetrahedron.

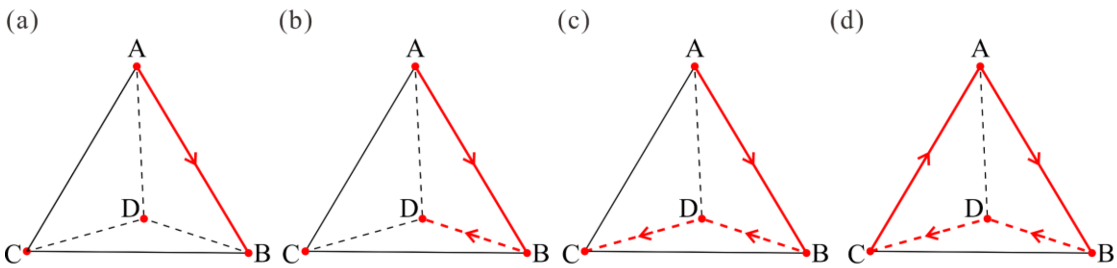

Fig. 3-13 Only one Hamiltonian path in a tetrahedron.

Next, the obtained Hamiltonian path, also given in Fig. 3-14(a), can split the tetrahedron into two half shells, as shown in Figs. 3-14(b) and (e). The half shell in Fig. 3-14(b) is an assembly of two 1-DOF triangular units ADC and ADB connected by one common edge AD. The constraint matrix in this two-loop equivalent mechanism can be directly derived as

$$\boldsymbol{M}'_{e1}=\begin{bmatrix}\boldsymbol{S}_{f1} & \boldsymbol{S}_{f2} & \mathbf{0} & \boldsymbol{S}_{f5} & \mathbf{0}\\ \mathbf{0} & -\boldsymbol{S}_{f2} & \boldsymbol{S}_{f3} & \mathbf{0} & \boldsymbol{S}_{f6}\end{bmatrix} \tag{3-21}$$

The true mobility of the two-loop mechanism shown in Fig. 3-14(b) is $m = n_e - \text{rank}(\boldsymbol{M}'_{e1}) = 5 - 4 = 1$. However, the overconstraints of this two-loop equivalent mechanism are $c_e = m - M = 1 - (-3) = 2$, and for the original Sarrus-based mechanism, $c = m - M = 1 - (-12) = 13$. Furthermore, to explore the possibility of the simplest constraint path based on Fig. 3-14(b), we can only remove edge AD under the mentioned reduction premise. Thus, a skew quadrilateral (nonplanar quadrilateral) ABDC is obtained in Fig. 3-14(c). The constraint matrix of this single-loop equivalent mechanism with four equivalent prismatic joints P_1, P_3, P_6 and P_5 in Fig. 3-14(d) is

$$\boldsymbol{M}''_{e1} = \begin{bmatrix} \boldsymbol{S}_{f1} & \boldsymbol{S}_{f3} & \boldsymbol{S}_{f6} & \boldsymbol{S}_{f5} \end{bmatrix} \tag{3-22}$$

The mobility of this single-loop mechanism is $m = n_e - \text{rank}(\boldsymbol{M}''_{e1}) = 4 - 3 = 1$ and its degree of overconstraint is $c_e = m - M = 1 - 1 = 0$. Therefore, we can regard a skew quadrilateral as the simplest topological graph, i.e., the single-loop mechanism in Fig. 3-14(d) can be obtained as the simplest constraint form with four equivalent prismatic joints.

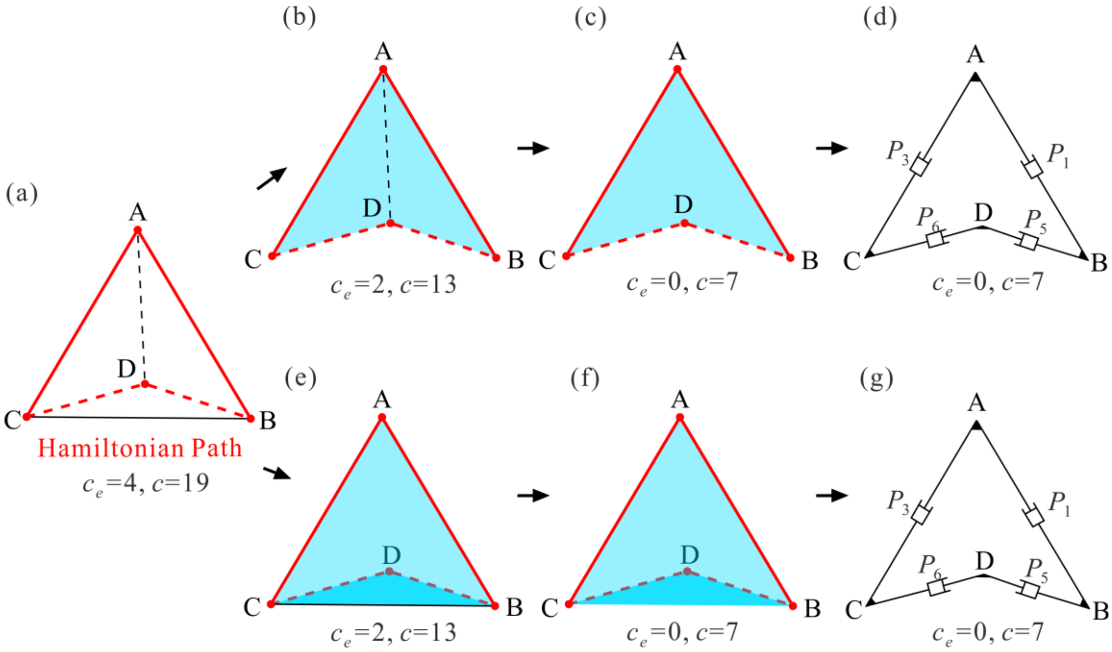

Fig. 3-14 Reduction process of the equivalent tetrahedral mechanism. (a) The only one 3D Hamiltonian path (illustrated in red line); (b) one half shell split by Hamiltonian path, and (c) the simplest topological graph and (d) its corresponding simplest equivalent mechanism; (e) the other half shell and (f) its simplest topological graph and (g) equivalent mechanism.

On the other hand, the other half shell in Fig. 3-14(e) is also a 1-DOF assembly of two triangular units ABC and BCD connected by edge BC, which is congruent with the one in Fig. 3-14(b) due to symmetry. Thus, the same reduction process can be conducted to obtain the simplest topological graph in Fig. 3-14(f) and the simplest equivalent mechanism in Fig. 3-14(g), which are the same as Figs. 3-14(c) and (d), respectively.

According to the original tetrahedral mechanism and its kinematic solution based on the D-H matrix method, as shown in Fig. 3-4, referring to Figs. 3-14(b) and (c), the simplified tetrahedral mechanism and the simplest form are illustrated in Figs. 3-15(a) and (b), respectively. Moreover, $\varphi_i'=2\varphi_i$ still exists in all involved Sarrus linkages, yet some original 9*R* linkages vanish after reduction. First, a spatial 12*R* linkage with revolute axes z_1 to z_{12} can be identified in Fig. 3-15(a) after removing the Sarrus linkage between platforms B and C. Its motion constraint conditions can be obtained as follows: among platforms A, D and B,

$$\varphi_1=\varphi_2=\varphi_5\,,\ \ \varphi_1'=\varphi_2'=\varphi_5' \tag{3-23}$$

among platforms A, D and C,

$$\varphi_3=\varphi_2=\varphi_6\,,\ \ \varphi_3'=\varphi_2'=\varphi_6' \tag{3-24}$$

Substituting these constraint conditions into matrix calculations of this 12*R* linkage yields

$$\varphi_1=\varphi_2=\varphi_3=\varphi_5=\varphi_6\,,\ \ \varphi_1'=\varphi_2'=\varphi_3'=\varphi_5'=\varphi_6' \tag{3-25}$$

Thus, the identical kinematic behaviour of five involved Sarrus linkages and the equivalent kinematics of the entire simplified tetrahedral mechanism are revealed.

However, there are no original 9*R* linkages reserved in the simplest mechanism in Fig. 3-15(b); thus, the constraint conditions in Eqs. (3-23) and (3-24) no longer exist, and we can only utilize the fundamental conditions in each Sarrus linkage, i.e.,

$$\varphi_1'=2\varphi_1\,,\ \ \varphi_3'=2\varphi_3\,,\ \ \varphi_5'=2\varphi_5\,,\ \ \varphi_6'=2\varphi_6 \tag{3-26}$$

After the matrix calculations of this 12*R* linkage, we have

$$\varphi_1=\varphi_3=\varphi_5=\varphi_6\,,\ \ \varphi_1'=\varphi_3'=\varphi_5'=\varphi_6' \tag{3-27}$$

Therefore, the equivalent kinematics of the four involved Sarrus linkages and the entire simplest tetrahedron can also be obtained. Hence, the edges BC and AD are redundant in their mechanism topology and can be removed without affecting the motion behaviour of the polyhedral platforms.

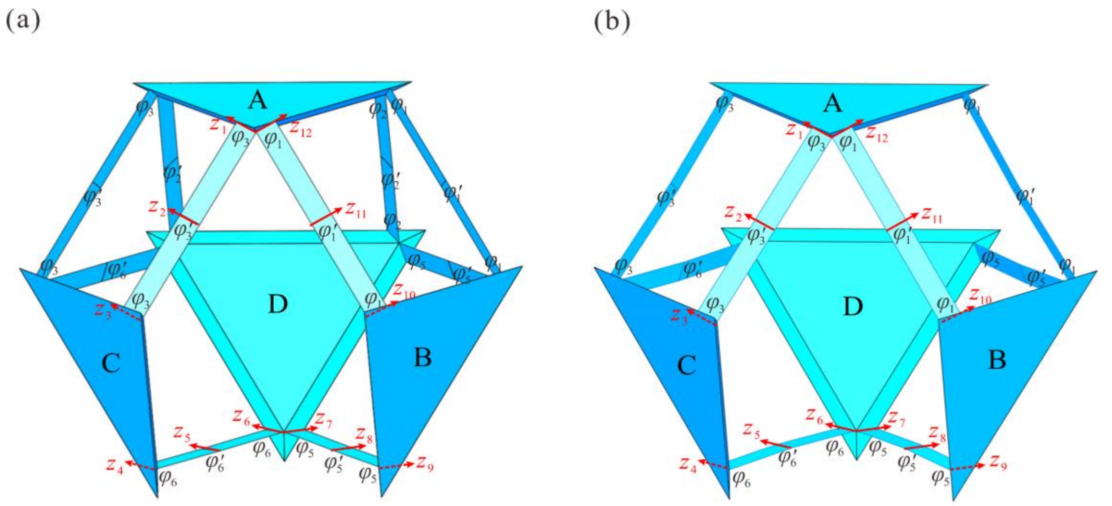

Fig. 3-15 Analysis of kinematic variables in (a) the simplified tetrahedral mechanism and (b) its simplest mechanism.

Ultimately, by mapping the proposed simplest equivalent mechanism in Fig. 3-14(d) or (g) back to the original Sarrus-based mechanism, Fig. 3-16(a) shows the simplest tetrahedral mechanism integrated by four Sarrus linkages, in which the 1-DOF synchronized radial motion is preserved, whose prototype is shown in Fig. 3-16(b).

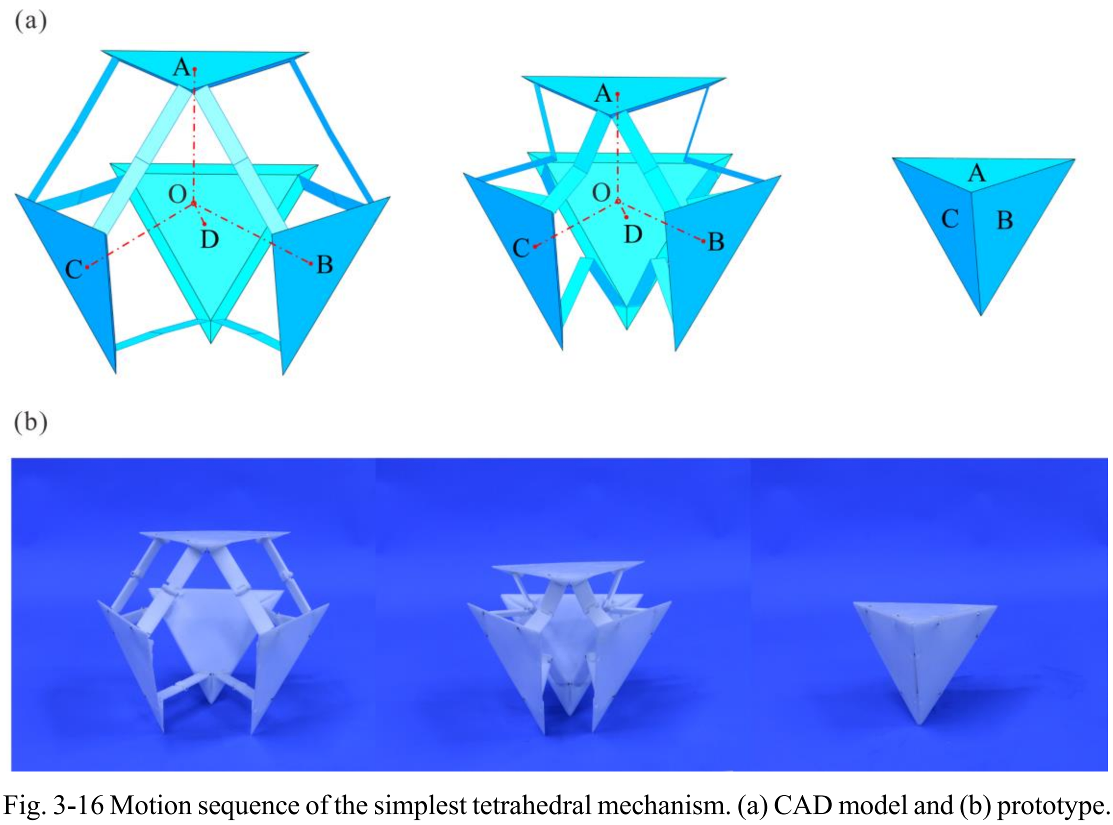

Fig. 3-16 Motion sequence of the simplest tetrahedral mechanism. (a) CAD model and (b) prototype.

Nevertheless, the actual overconstraint of this simplified Sarrus-based mechanism is $c = m - M = 1 - (-6) = 7$ based on the four involved overconstrained Sarrus linkages. Compared with the original mechanism in Fig. 3-12, the actual overconstraint is greatly reduced from 19 to 7. Furthermore, if we arbitrarily remove one of eight limbs among four platforms, i.e., remove two links with three revolute joints in a Sarrus linkage, the mobility of this tetrahedral mechanism will become two; hence, the simplified tetrahedral mechanism in Fig. 3-16 can be regarded as the simplest constraint form.

Furthermore, the skew quadrilateral topological graph in Fig. 3-14(c) will be taken as the basic unit with $c_e = 0$ to conduct the overconstraint reduction in complex Hamiltonian paths for other polyhedral mechanisms.

3.3.2 Reduction of the Cubic Mechanism

Inspired by the characteristic of the Hamiltonian path that matches the premise of the reduction process, a similar topology operation can be conducted to demonstrate the reduction of the deployable cubic mechanism given in Fig. 3-17, in which the original and equivalent overconstraints are $c_e = 10$ and $c = 43$, respectively. The 3D topological graph of the equivalent cubic mechanism in Fig. 3-17, with a basis of dual octahedron, possesses a total of two distinct Hamiltonian paths.

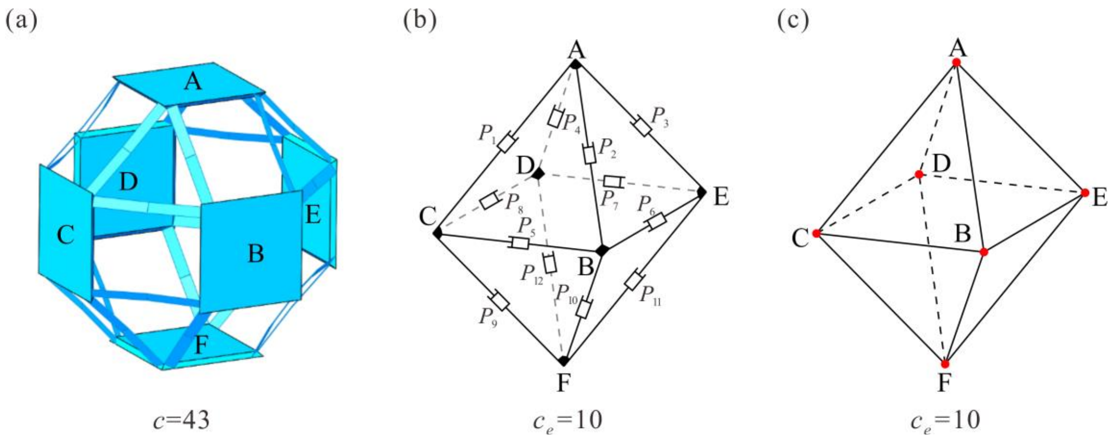

Fig. 3-17 Sarrus-based deployable cubic mechanism. (a) Original mechanism constructed by Sarrus linkages; (b) the equivalent mechanism with prismatic joints; (c) the corresponding three-dimensional topological graph.

First, Hamiltonian path 1 of a double-Z shape in an octahedron is shown in Fig. 3-18(a) in red lines; it splits this octahedron into two congruent half shells due to the octahedral symmetry, see Figs. 3-18(b) and (d). Taking Fig. 3-18(b) as an example, this half shell is an assembly of four 1-DOF triangular units FBC, BCA, CAD and ADE with equivalent kinematics, and the mobility in its corresponding mechanism can be calculated as one with $c_e = 4$ and $c = 25$, which proves that the edges DF, EF and EB are redundant. Subsequently, we can arrange the proposed skew quadrilateral basic unit in this half shell generated from path 1 to conduct further reduction. As shown in Fig. 3-18(c), starting from vertex F with a smaller included edge angle, we can arrange a quadrilateral FBAC (highlighted in blue); thus, the next quadrilateral ACDE can be readily arranged in the remaining space. Compared with the reduction result in Fig. 3-18(b), we regard that edges BC and AD are removed, which results in a two-loop 1-DOF mechanism constructed by seven equivalent prismatic joints with $c_e = 0$. Moreover, due to the octahedral symmetry, an identical reduction result based on the other half shell in Fig. 3-18(d) can also be obtained (see Fig. 3-18(e)).

According to the topological graph in Fig. 3-18(c) from path 1, the corresponding equivalent prismatic joints $\boldsymbol{S}_{fi}$ and the constraint graph are given in Fig. 3-19. The resulting constraint matrix $\boldsymbol{M}'_{\mathrm{e2}}$ can be derived as

$$\boldsymbol{M}'_{e2} = \begin{bmatrix} \boldsymbol{S}_{f1} & \mathbf{0} & \boldsymbol{S}_{f3} & \boldsymbol{S}_{f7} & \boldsymbol{S}_{f8} & \mathbf{0} & \mathbf{0} \\ -\boldsymbol{S}_{f1} & \boldsymbol{S}_{f2} & \mathbf{0} & \mathbf{0} & \mathbf{0} & \boldsymbol{S}_{f9} & \boldsymbol{S}_{f10} \end{bmatrix} \tag{3-28}$$

where the rank of this matrix is 6, the mobility of the cubic mechanism in Fig. 3-19 can be verified as $m = n_e - \mathrm{rank}(\boldsymbol{M}'_{\mathrm{e2}}) = 7 - 6 = 1$, and the equivalent kinematics can also be revealed based on similar matrix method as illustrated in Fig. 3-15.

However, the actual overconstraints $c = 13$ still exist in the corresponding Sarrus-based mechanism due to the related seven Sarrus linkages. Furthermore, if we remove the common edge AC in Fig. 3-18(c) or edge EF in Fig. 3-18(e), i.e., $\boldsymbol{S}_{f1}$ in Fig. 3-19, the single-loop equivalent mechanism with six prismatic joints will occur, and then its mobilities will become two, which is contrary to the reduction process. Thus, the topological graph in Fig. 3-18(c) or Fig. 3-18(e) can be identified as the 1-DOF simplest constraint path derived from path 1.

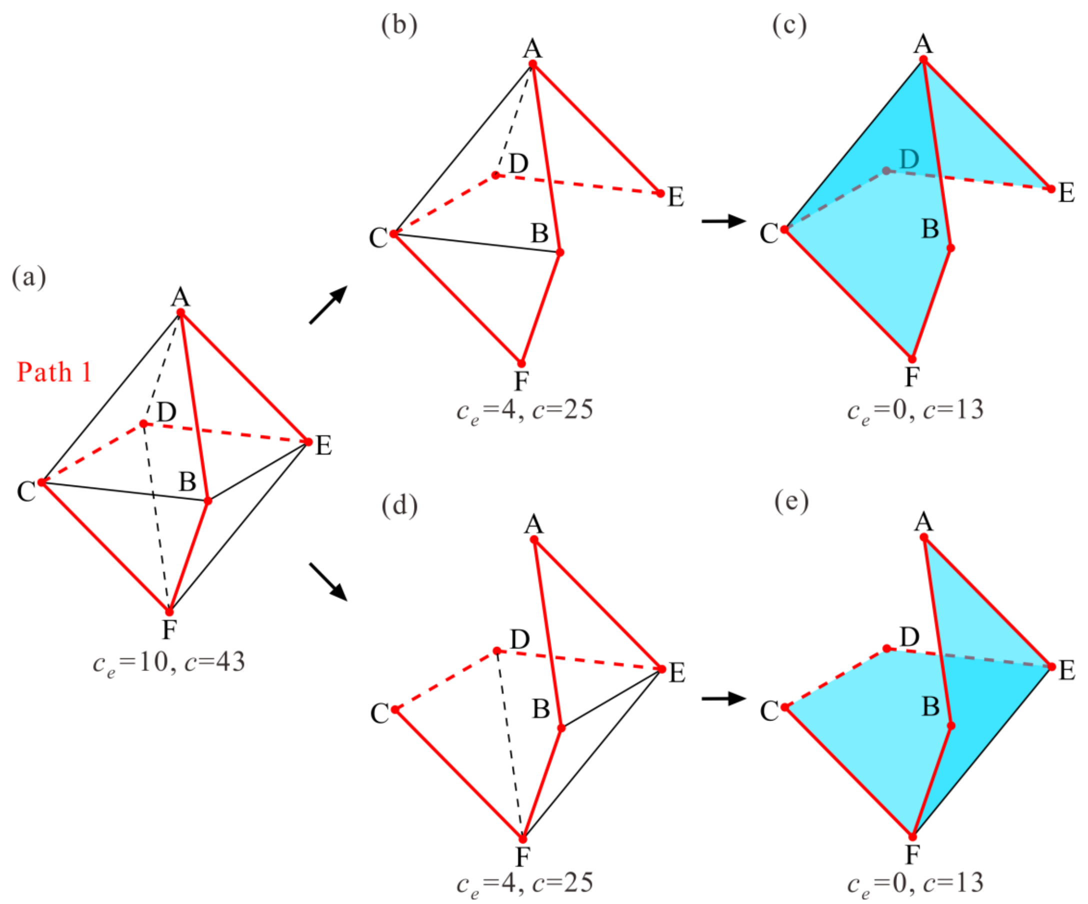

Fig. 3-18 Reduction process of equivalent cubic mechanism using Hamiltonian path 1. (a) Hamiltonian path 1 in the 3D topological graph. (b) One half shell split by path 1, and (c) the simplest topological graph. (d) The other half shell and (e) its simplest topological graph.

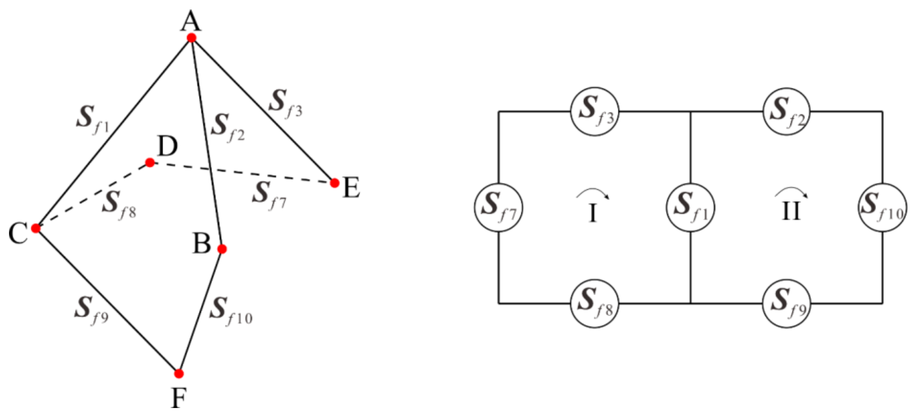

Fig. 3-19 Constraint graphs of the simplest cubic mechanism derived from path 1.

However, Hamiltonian path 2 of a threefold zigzag shape is shown in Fig. 3-20(a), which also splits this octahedron into two congruent half shells due to symmetry (see Figs. 3-20(b) and (d)). For the topological graph in Fig. 3-20(b), three external triangular units are connected to the central unit, leading to a 1-DOF four-loop mechanism with $c_e = 4$ and $c = 25$. Next, due to its threefold symmetry, we can select any one of vertices D, E and F at the beginning to arrange the skew quadrilateral basic unit. For example, a quadrilateral FBAC is generated in Fig. 3-20(c), yet two resulting triangular units ACD and ABE, as illustrated in grey, cannot be merged into a quadrilateral anyway, which also applies to the identical reduction result in Fig. 3-20(e). No matter which arrangement for this case, there are always two triangles that cannot be merged.

Referring to the topological graph in Fig. 3-20(c) from path 2, the corresponding constraint graph is shown in Fig. 3-21, and the corresponding constraint matrix $\boldsymbol{M}''_{e2}$ is

$$\boldsymbol{M}''_{e2} = \begin{bmatrix} \boldsymbol{S}_{f1} & \boldsymbol{0} & \boldsymbol{0} & \boldsymbol{S}_{f4} & \boldsymbol{0} & \boldsymbol{S}_{f8} & \boldsymbol{0} & \boldsymbol{0} \\ -\boldsymbol{S}_{f1} & \boldsymbol{S}_{f2} & \boldsymbol{0} & \boldsymbol{0} & \boldsymbol{0} & \boldsymbol{0} & \boldsymbol{S}_{f9} & \boldsymbol{S}_{f10} \\ \boldsymbol{0} & -\boldsymbol{S}_{f2} & \boldsymbol{S}_{f3} & \boldsymbol{0} & \boldsymbol{S}_{f6} & \boldsymbol{0} & \boldsymbol{0} & \boldsymbol{0} \end{bmatrix} \tag{3-29}$$

where the rank of this matrix is 7, and the mobility of the cubic mechanism in Fig. 3-21 is $m = n_e - \text{rank}(\boldsymbol{M}''_{e2}) = 8 - 7 = 1$. As a result, the topological graph in Fig. 3-20(c) has a mobility of one with $c_e = 2$ and $c = 19$ due to the connection of one skew quadrilateral unit and two triangular units.

However, if edge AB (or AC) is further removed, the mobility will become two. Thus, the constraint path in Fig. 3-20(c) or Fig. 3-20(e) can be regarded as the simplified constraint path derived from path 2. However, compared with the constraint path in Fig. 3-18(c), this constraint path cannot be treated as the simplest of these cubic mechanisms due to its eight associated equivalent prismatic joints among all six platforms. Thus, the only simple topological graph of the cubic mechanism can be identified in Figs. 3-18(c) and (e).

According to the simplest topological graph in Fig. 3-18(c), the simplest 1-DOF deployable cubic mechanism is obtained with the original motion behaviour of its platforms unchanged, whose motion sequences are given in Fig. 3-22. Compared with the original cubic mechanism in Fig. 3-17, the actual overconstraints in this simplest Sarrus-based cubic mechanism are greatly reduced from 43 to 13.

In this section, the 1-DOF simplest topological graph of the cubic mechanism is identified as two 1-DOF skew quadrilaterals connected by one common edge, and the reduction method inspired by the Hamiltonian path can be readily applied to the complex dodecahedral mechanism in the next section.

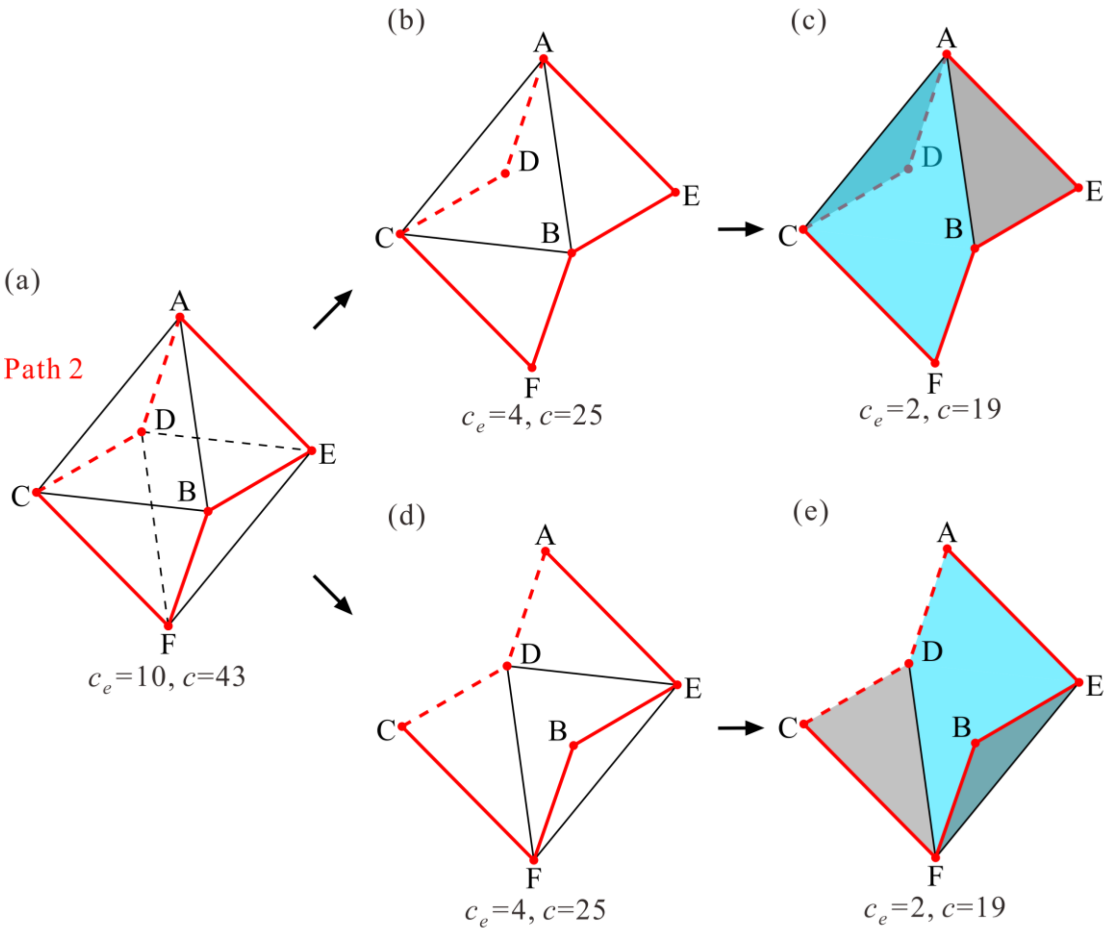

Fig. 3-20 Reduction process of equivalent cubic mechanism using Hamiltonian path 2. (a) Hamiltonian path 2 in the 3D topological graph. (b) One half shell split by path 2, and (c) the simplified topological graph. (d) The other half shell and (e) the simplified topological graph.

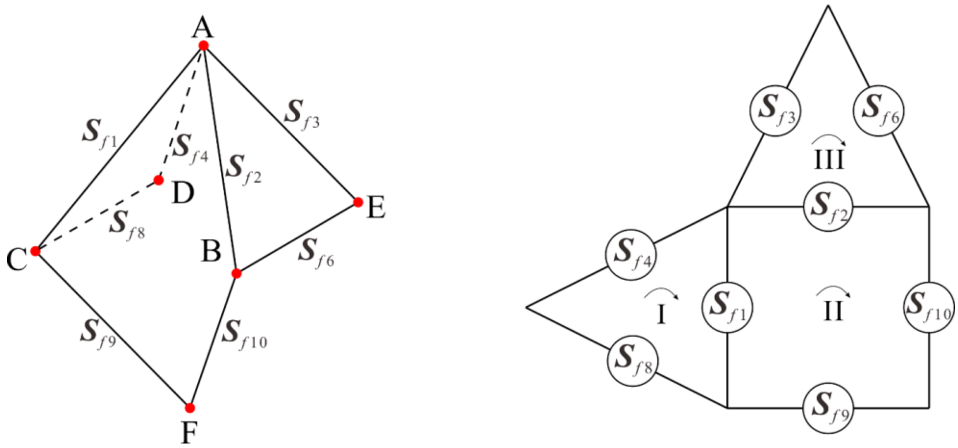

Fig. 3-21 Constraint graphs of the simplified cubic mechanism derived from path 2.

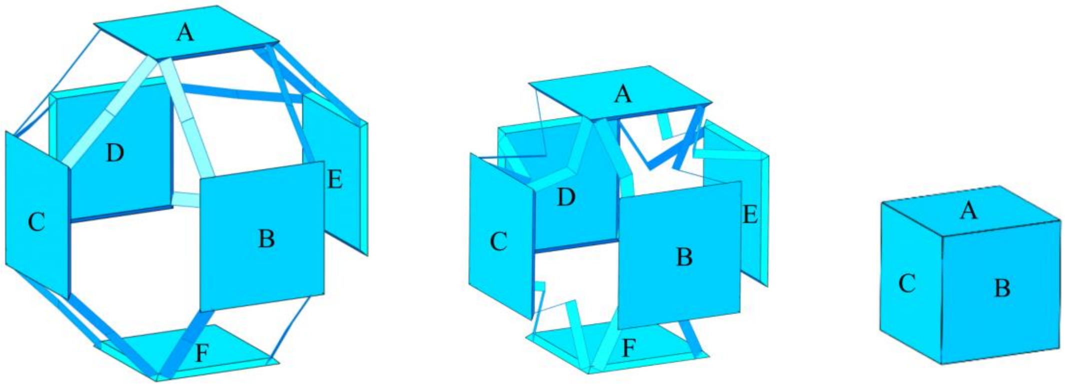

Fig. 3-22 Motion sequence of the simplest cubic mechanism.

3.3.3 Reduction of the Dodecahedral Mechanism

As shown in Fig. 3-23, the original 3D topological graph of the deployable dodecahedral mechanism is related to its dual icosahedron with $c_e = 28$ and $c = 115$. There are a total of 17 distinct Hamiltonian paths on an icosahedron, which presents a different challenge to find all simplest constraint forms for this mechanism. Nevertheless, the proposed reduction method, including arranging the skew quadrilateral into basic units, can still be conducted for dodecahedral mechanisms.

Considering an arbitrary Hamiltonian path as an example, as shown in Fig. 3-24(a) in red lines, which connects all twelve vertices without any symmetry. Next, two distinct half shells split by path 1 are generated in Figs. 3-24(b) and (d), each of which consists of ten 1-DOF triangular units connected in sequence and can be regarded as a 1-DOF assembly. It is intuitive that we only need to repeat the quadrilateral arrangements, as illustrated in Figs. 3-18(b) to (c), to explore the simplest constraint path. Starting from vertex A in Fig. 3-24(b), 1-DOF skew quadrilaterals ADIC, CILH, CHGB, BGKF and FKJE can be sequentially arranged inside the Hamiltonian path, leading to a 1-DOF assembly of these five basic units, as shown in Fig. 3-24(c). Here, the redundant edges CD, IH, BH, FG and EK are alternately removed, such that the two adjacent basic units share one common edge, i.e., edges CI, CH, BG and FK, respectively. Similarly, as shown in Fig. 3-24(d), starting from vertex C, if we further arrange five skew quadrilaterals CBFA, AFED, DEJI, IJKL and LKGH in the other half shell, another different simplest constraint path is obtained in Fig. 3-24(e).

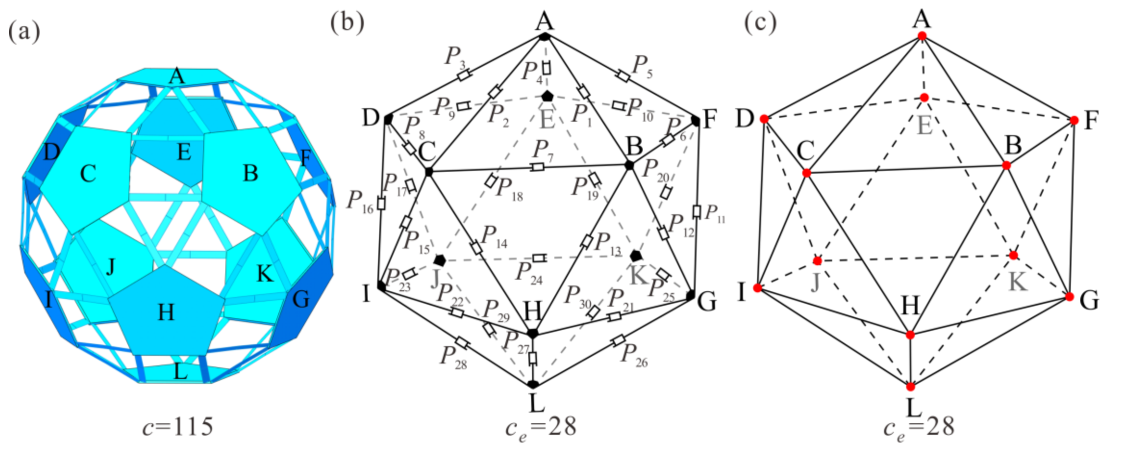

Fig. 3-23 Sarrus-based deployable dodecahedral mechanism. (a) Original mechanism constructed by Sarrus linkages; (b) the equivalent mechanism with prismatic joints; (c) the corresponding three-dimensional topological graph.

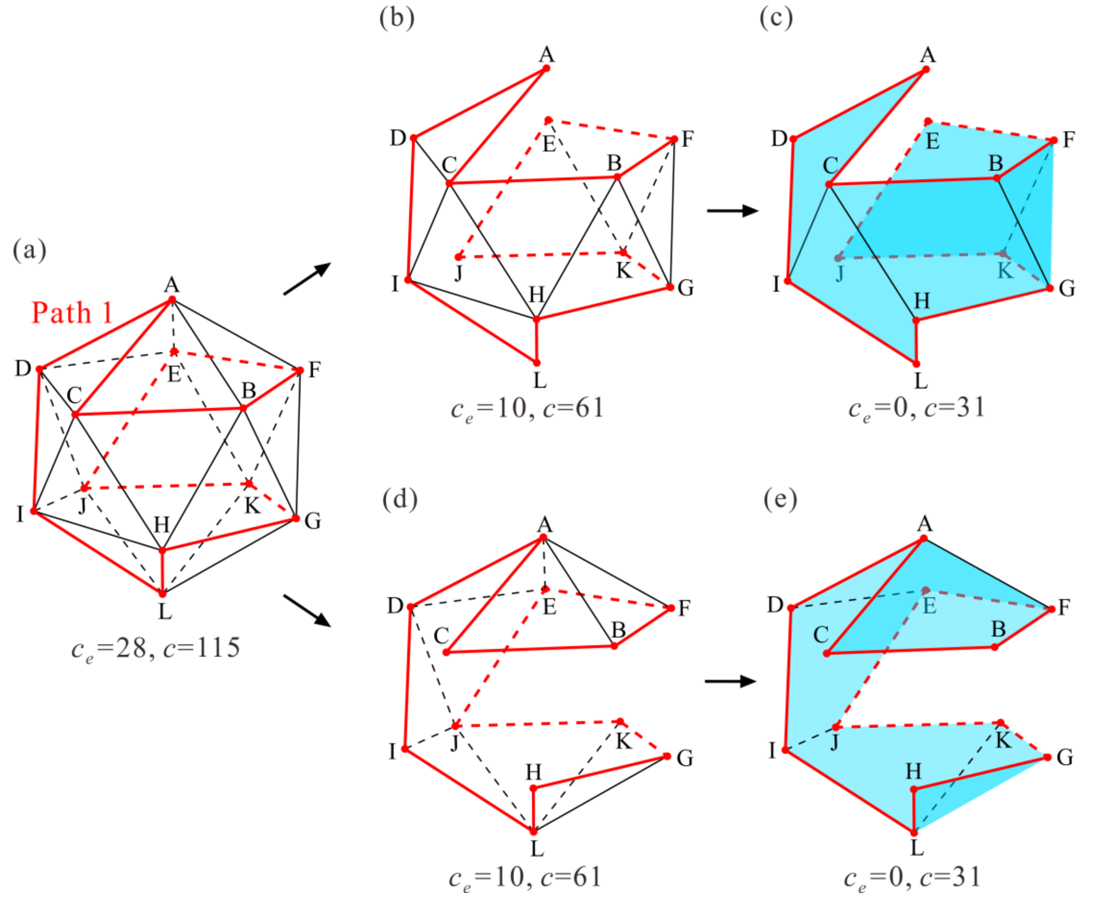

Fig. 3-24 Reduction process of the equivalent dodecahedral mechanism. (a) Hamiltonian path 1 in the 3D topological graph. (b) One half shell split by this path and (c) its simplest constraint path with the removal of redundant edges CD, IH, BH, FG and EK. (d) The other half shell split by this path and (e) its simplest constraint path with the removal of redundant edges AB, AE, DJ, JL and LG.

Referring to the first example of the simplest dodecahedral mechanism represented by Fig. 3-24(c), its mobility can be analysed and verified with a total of 16 associated equivalent kinematic pairs. Based on the corresponding constraint graph in Fig. 3-25(a), its related constraint matrix $\boldsymbol{M}'_{\mathrm{e}3}$ is

$$\boldsymbol{M}'_{e3} = \begin{bmatrix} \boldsymbol{M}'_{11} & \boldsymbol{M}'_{12} \end{bmatrix} \tag{3-30}$$

with

$$\boldsymbol{M}'_{11} = \begin{bmatrix} \boldsymbol{S}_{f2} & \boldsymbol{S}_{f3} & \boldsymbol{0} & \boldsymbol{0} & \boldsymbol{0} & \boldsymbol{0} & \boldsymbol{0} & \boldsymbol{S}_{f15} \\ \boldsymbol{0} & \boldsymbol{0} & \boldsymbol{0} & \boldsymbol{0} & \boldsymbol{0} & \boldsymbol{0} & \boldsymbol{S}_{f14} & -\boldsymbol{S}_{f15} \\ \boldsymbol{0} & \boldsymbol{0} & \boldsymbol{0} & \boldsymbol{S}_{f7} & \boldsymbol{0} & \boldsymbol{S}_{f12} & -\boldsymbol{S}_{f14} & \boldsymbol{0} \\ \boldsymbol{0} & \boldsymbol{0} & \boldsymbol{S}_{f6} & \boldsymbol{0} & \boldsymbol{0} & -\boldsymbol{S}_{f12} & \boldsymbol{0} & \boldsymbol{0} \\ \boldsymbol{0} & \boldsymbol{0} & \boldsymbol{0} & \boldsymbol{0} & \boldsymbol{S}_{f10} & \boldsymbol{0} & \boldsymbol{0} & \boldsymbol{0} \end{bmatrix}$$

$$\boldsymbol{M}'_{12} = \begin{bmatrix} \boldsymbol{S}_{f16} & \boldsymbol{0} & \boldsymbol{0} & \boldsymbol{0} & \boldsymbol{0} & \boldsymbol{0} & \boldsymbol{0} & \boldsymbol{0} \\ \boldsymbol{0} & \boldsymbol{0} & \boldsymbol{0} & \boldsymbol{0} & \boldsymbol{0} & \boldsymbol{0} & \boldsymbol{S}_{f27} & \boldsymbol{S}_{f28} \\ \boldsymbol{0} & \boldsymbol{0} & \boldsymbol{0} & \boldsymbol{S}_{f21} & \boldsymbol{0} & \boldsymbol{0} & \boldsymbol{0} & \boldsymbol{0} \\ \boldsymbol{0} & \boldsymbol{0} & \boldsymbol{S}_{f20} & \boldsymbol{0} & \boldsymbol{0} & \boldsymbol{S}_{f25} & \boldsymbol{0} & \boldsymbol{0} \\ \boldsymbol{0} & \boldsymbol{S}_{f18} & -\boldsymbol{S}_{f20} & \boldsymbol{0} & \boldsymbol{S}_{f24} & \boldsymbol{0} & \boldsymbol{0} & \boldsymbol{0} \end{bmatrix}$$

The rank of constraint matrix $\boldsymbol{M}'_{\mathrm{e}3}$ is 15, and through computation, the mobility of this dodecahedral mechanism can be derived as $m = n_e - \mathrm{rank}(\boldsymbol{M}'_{\mathrm{e}3}) = 16 - 15 = 1$.

Then, using the same approach, the constraint graph derived from another different path in Fig. 3-24(e) is shown in Fig. 3-25(b), and its constraint matrix $\boldsymbol{M}''_{e3}$ is

$$\boldsymbol{M}''_{e3} = \begin{bmatrix} \boldsymbol{M}''_{11} & \boldsymbol{M}''_{12} \end{bmatrix} \tag{3-31}$$

with

$$\boldsymbol{M}''_{11} = \begin{bmatrix} \boldsymbol{S}_{f2} & \boldsymbol{0} & \boldsymbol{S}_{f5} & \boldsymbol{S}_{f6} & \boldsymbol{S}_{f7} & \boldsymbol{0} & \boldsymbol{0} & \boldsymbol{0} \\ \boldsymbol{0} & \boldsymbol{S}_{f3} & -\boldsymbol{S}_{f5} & \boldsymbol{0} & \boldsymbol{0} & \boldsymbol{S}_{f9} & \boldsymbol{S}_{f10} & \boldsymbol{0} \\ \boldsymbol{0} & \boldsymbol{0} & \boldsymbol{0} & \boldsymbol{0} & \boldsymbol{0} & -\boldsymbol{S}_{f9} & \boldsymbol{0} & \boldsymbol{S}_{f16} \\ \boldsymbol{0} & \boldsymbol{0} & \boldsymbol{0} & \boldsymbol{0} & \boldsymbol{0} & \boldsymbol{0} & \boldsymbol{0} & \boldsymbol{0} \\ \boldsymbol{0} & \boldsymbol{0} & \boldsymbol{0} & \boldsymbol{0} & \boldsymbol{0} & \boldsymbol{0} & \boldsymbol{0} & \boldsymbol{0} \end{bmatrix}$$

$$\boldsymbol{M}''_{12} = \begin{bmatrix} \boldsymbol{0} & \boldsymbol{0} & \boldsymbol{0} & \boldsymbol{0} & \boldsymbol{0} & \boldsymbol{0} & \boldsymbol{0} & \boldsymbol{0} \\ \boldsymbol{0} & \boldsymbol{0} & \boldsymbol{0} & \boldsymbol{0} & \boldsymbol{0} & \boldsymbol{0} & \boldsymbol{0} & \boldsymbol{0} \\ \boldsymbol{S}_{f18} & \boldsymbol{0} & \boldsymbol{S}_{f23} & \boldsymbol{0} & \boldsymbol{0} & \boldsymbol{0} & \boldsymbol{0} & \boldsymbol{0} \\ \boldsymbol{0} & \boldsymbol{0} & -\boldsymbol{S}_{f23} & \boldsymbol{S}_{f24} & \boldsymbol{0} & \boldsymbol{0} & \boldsymbol{S}_{f28} & \boldsymbol{S}_{f30} \\ \boldsymbol{0} & \boldsymbol{S}_{f21} & \boldsymbol{0} & \boldsymbol{0} & \boldsymbol{S}_{f25} & \boldsymbol{S}_{f27} & \boldsymbol{0} & -\boldsymbol{S}_{f30} \end{bmatrix}$$

The rank of this constraint matrix $\boldsymbol{M}''_{e3}$ is 15. Thus, the mobility of this simplest dodecahedral mechanism is one.

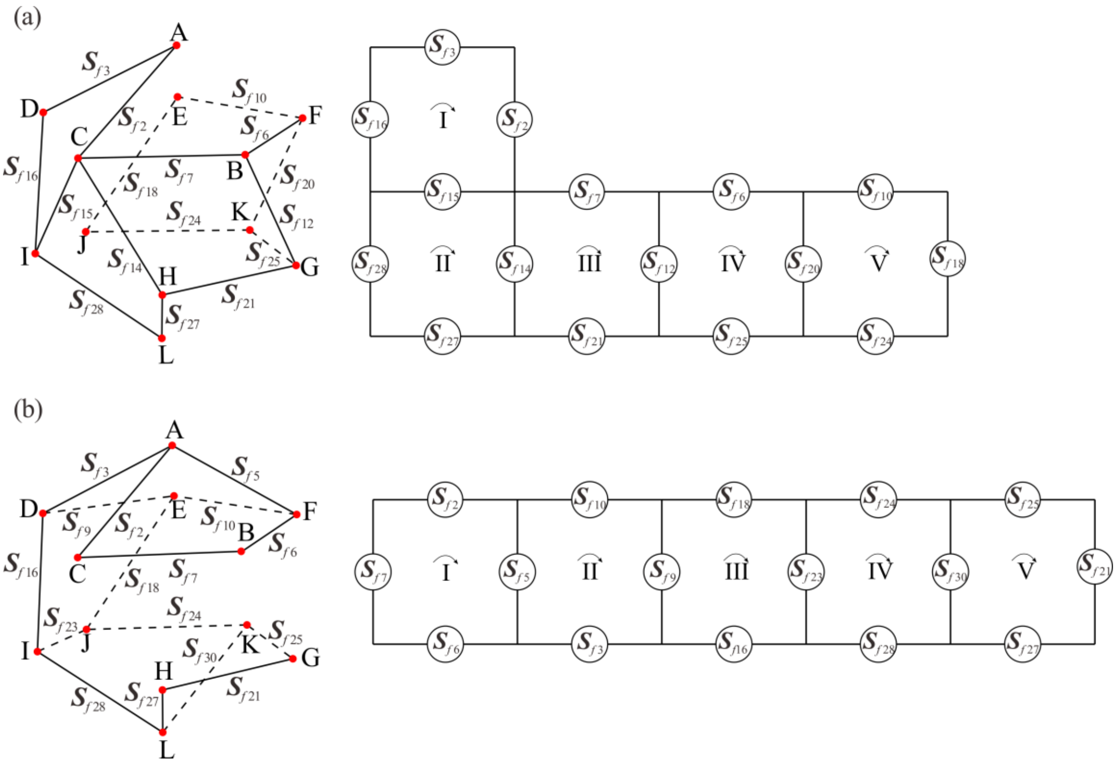

Fig. 3-25 Constraint graphs of the two simplest dodecahedra mechanisms.

Referring to the above mobility analysis, the equivalent mechanism obtained in Fig. 3-24(c) has a mobility of one with an equivalent overconstraint $c_e = 0$, as well as the case in Fig. 3-24(e); hence, both can be regarded as the simplest constraint paths among the twelve polyhedral platforms. Because the two distinct simplest constraint forms are derived from one common Hamiltonian path 1 in Fig. 3-24(a), they have identical outer contour lines, so they can be called complementary simplest paths.

Ultimately, by mapping the simplest topological graphs in Figs. 3-24(c) and (e) to the original Sarrus-based mechanism, the two simplest dodecahedral mechanisms that preserve the original 1-DOF radial motion are generated in Fig. 3-26, in which kinematic equivalence can also be proven based on the matrix method. Compared with the original dodecahedral mechanism in Fig. 3-23, the degrees of overconstraint in these simplest mechanisms are greatly reduced from 115 to 31.

In addition to the mentioned Hamiltonian path as given in Fig. 3-24(a), some other distinct Hamiltonian paths on an icosahedron can also be utilized to identify the simplest dodecahedral mechanisms by following the proposed reduction process, which is organized and listed as follows.

First, similar to path 1 in Fig. 3-24(a), which can generate two complementary paths, as illustrated in Figs. 3-24(c) and (e), Table 3-2 lists five Hamiltonian paths (including path 1), and each can generate two complementary simplest paths, in which five skew quadrilaterals are still arranged in sequence by sharing four common edges.

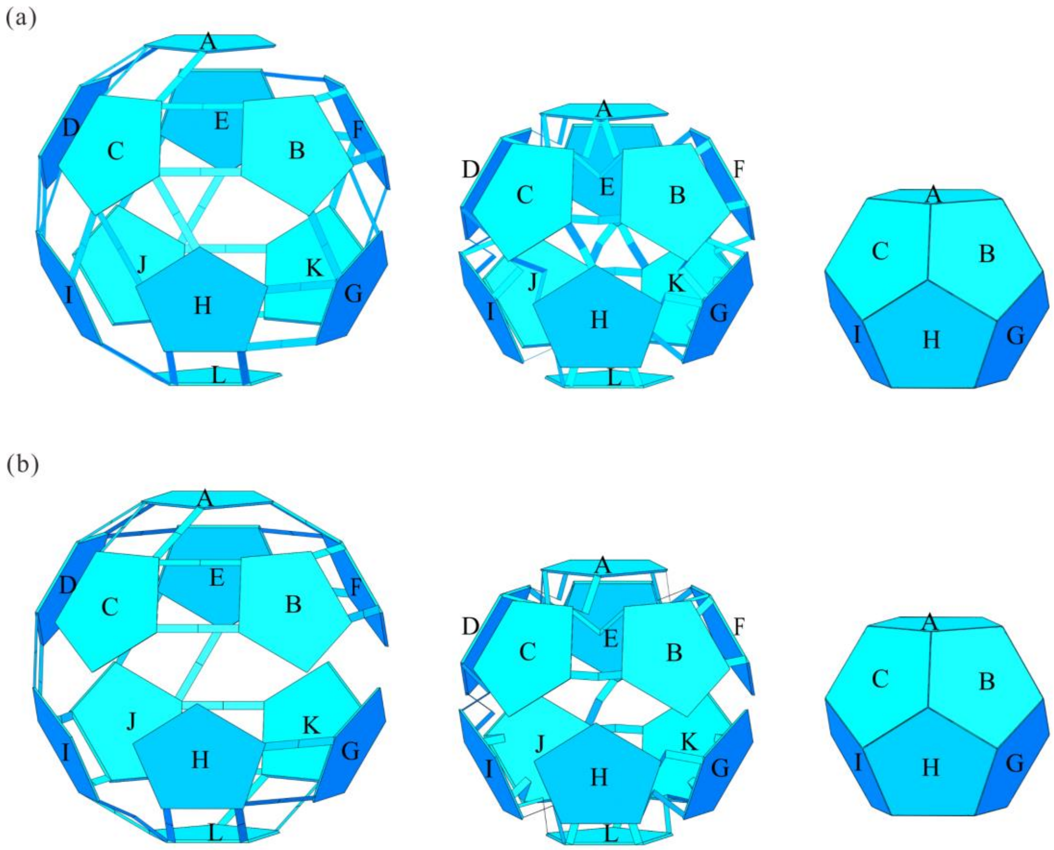

Fig. 3-26 Motion sequence of the simplest dodecahedral mechanisms obtained from (a) one half shell and (b) the other.

Next, each Hamiltonian path in Table 3-3 generates two congruent simplest paths, also as the arrangement of five quadrilaterals due to its C_2-symmetry. In contrast, for two half shells separated from each Hamiltonian path listed in Table 3-4, one shell can be derived into an effective simplest constraint path, as illustrated in blue, and the other shell is unsuccessful due to few unmergeable triangular units, as illustrated in grey, which is similar to the case from Figs. 3-20(b) to (c). The remaining three Hamiltonian paths are given in Table 3-5, yet any effective simplest path can also be obtained as unmergeable grey triangular units.

Table 3-2 Reduction results of dodecahedral mechanism using paths 1 to 5

Hamiltonian paths	Two complementary simplest paths		
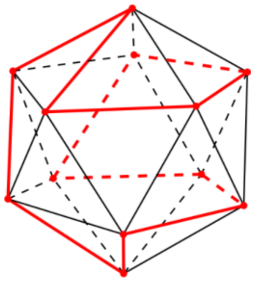 Path 1	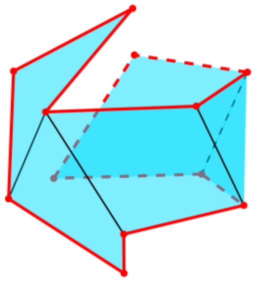 $c_e=0$, $c=31$	+	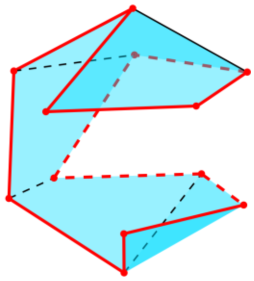 $c_e=0$, $c=31$
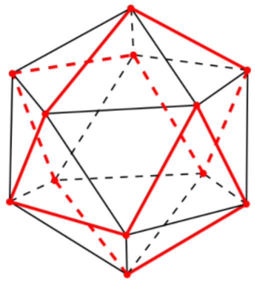 Path 2	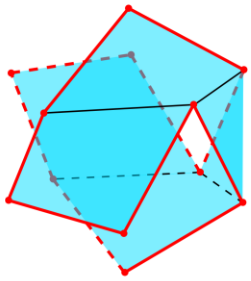 $c_e=0$, $c=31$	+	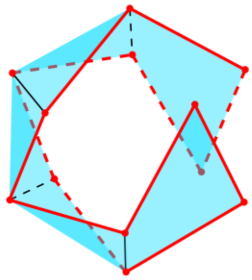 $c_e=0$, $c=31$
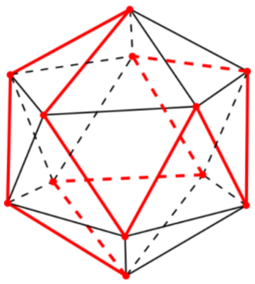 Path 3	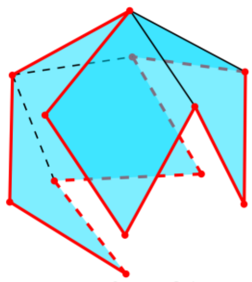 $c_e=0$, $c=31$	+	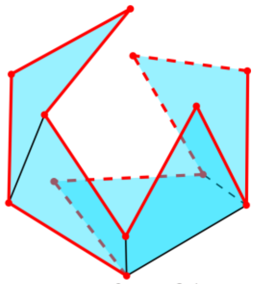 $c_e=0$, $c=31$
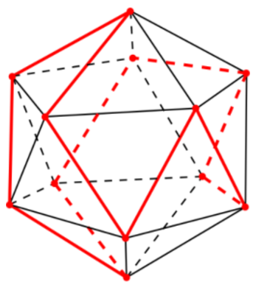 Path 4	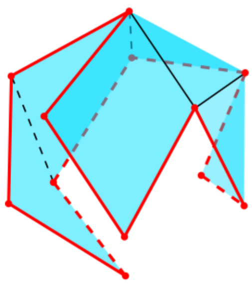 $c_e=0$, $c=31$	+	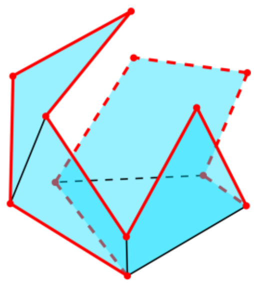 $c_e=0$, $c=31$
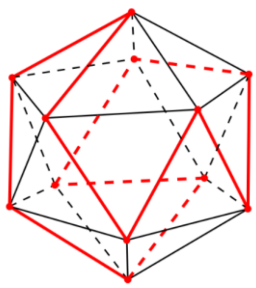 Path 5	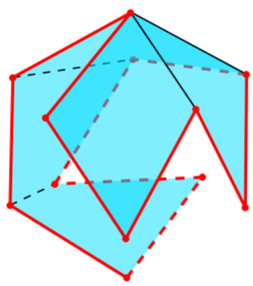 $c_e=0$, $c=31$	+	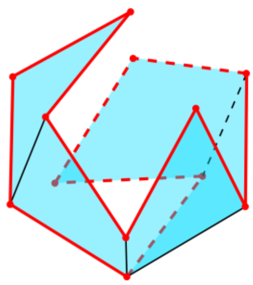 $c_e=0$, $c=31$

Table 3-3 Reduction results of dodecahedral mechanism using paths 6 to 10

Hamiltonian paths	Two congruent simplest paths
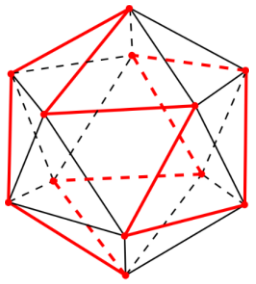 Path 6	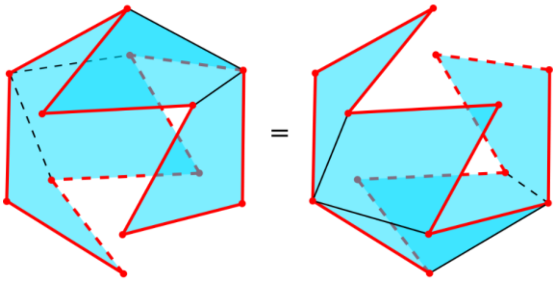 c_e=0, c=31 = c_e=0, c=31
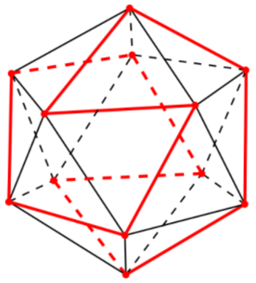 Path 7	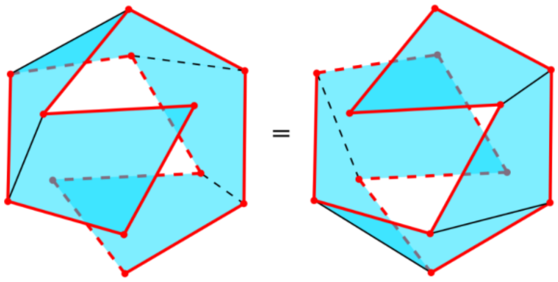 c_e=0, c=31 = c_e=0, c=31
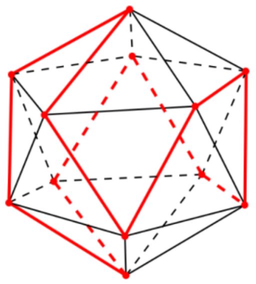 Path 8	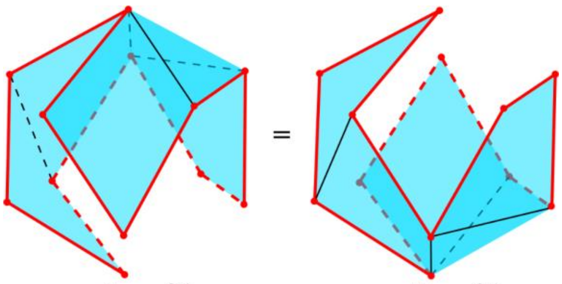 c_e=0, c=31 = c_e=0, c=31
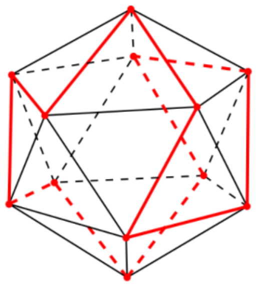 Path 9	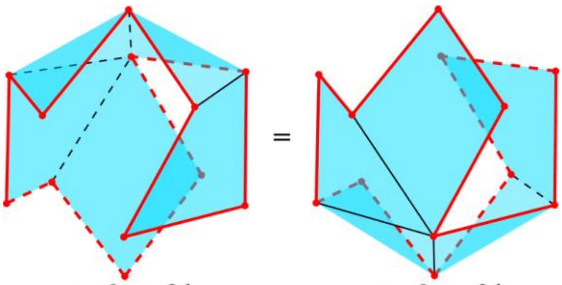 c_e=0, c=31 = c_e=0, c=31
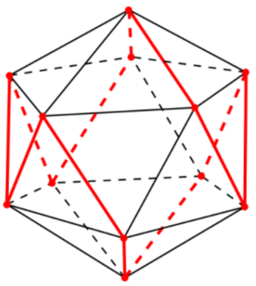 Path 10	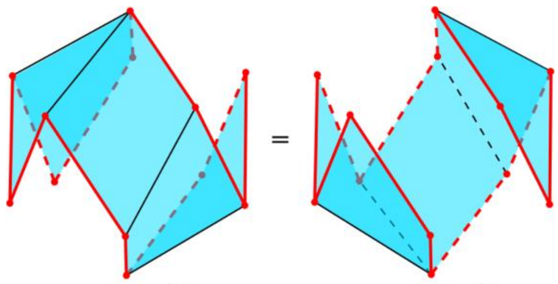 c_e=0, c=31 = c_e=0, c=31

Table 3-4 Reduction results of dodecahedral mechanism using paths 11 to 14

Hamiltonian paths	One simplest path and the other nonsimplest path		
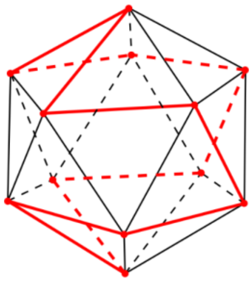 Path 11	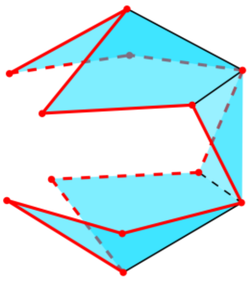 c_e=0, c=31	+	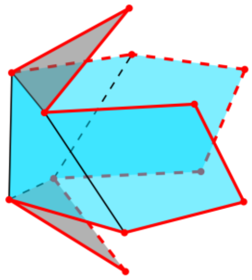 c_e=2, c=37
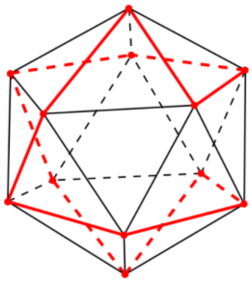 Path 12	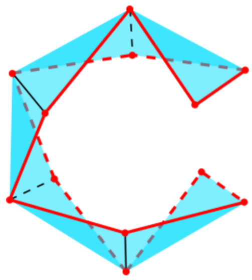 c_e=0, c=31	+	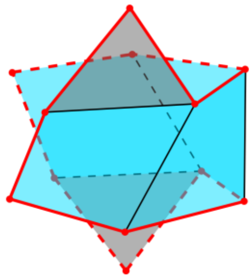 c_e=2, c=37
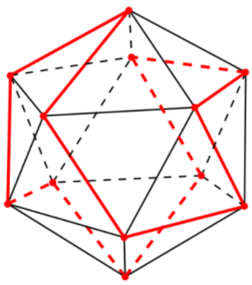 Path 13	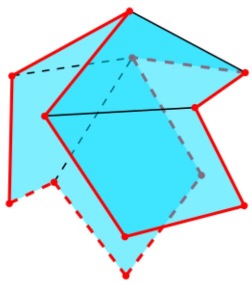 c_e=0, c=31	+	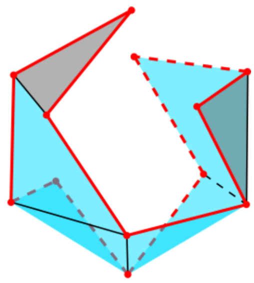 c_e=2, c=37
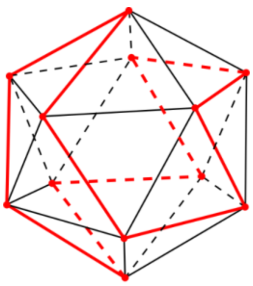 Path 14	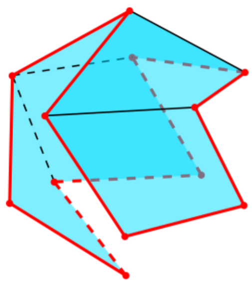 c_e=0, c=31	+	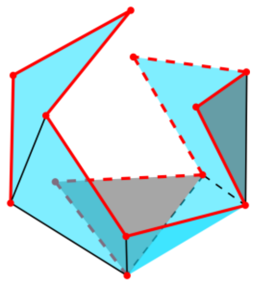 c_e=2, c=37

Table 3-5 Reduction results of dodecahedral mechanism using paths 15 to 17

Hamiltonian paths	Two nonsimplest paths		
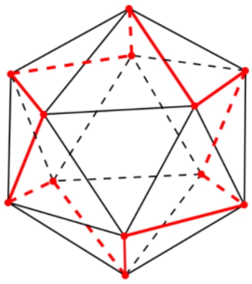 Path 15	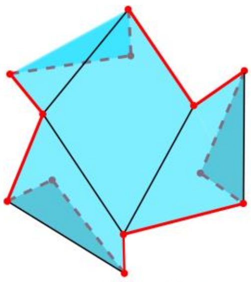 c_e=2, c=37	+	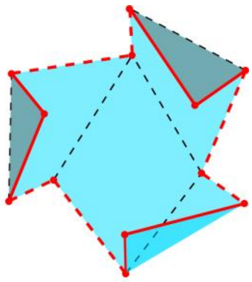 c_e=2, c=37
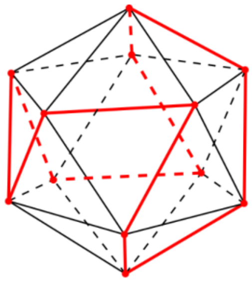 Path 16	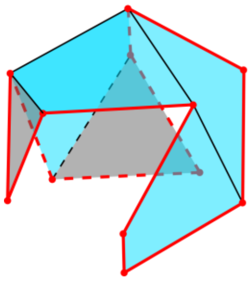 c_e=2, c=37	=	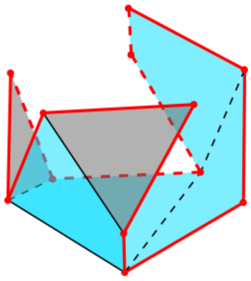 c_e=2, c=37
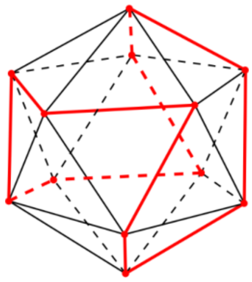 Path 17	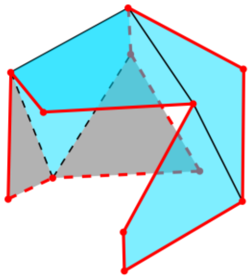 c_e=2, c=37	=	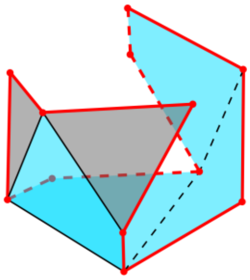 c_e=2, c=37

Therefore, 17 Hamiltonian paths of an icosahedron have been discussed in detail, and a total of 19 simplest constraint paths of this dodecahedral mechanism can be found and identified, each of which is a sequential arrangement of five skew quadrilateral basic units. As a result, each simple dodecahedral mechanism can preserve the original 1-DOF radial motion behaviour, and the degrees of overconstraint are greatly reduced from 115 to 31. It should be noted that in each nonsimplest form, the unmergeable grey triangular units always exist, independent of how the skew quadrilaterals are arranged.

3.4 Nonsimplest Constraint Forms with Rotational Symmetries

By introducing Hamiltonian paths to guide the removal of redundant constraints, the simplest constraint forms of tetrahedral, cubic and dodecahedral mechanisms have been obtained and identified. However, the original polyhedral symmetries vanish in the simplest mechanism due to the irregular and asymmetric arrangement of skew quadrilateral basic units, meaning that the entire symmetry and simplest constraint are contradictory. Here, also based on the skew quadrilateral basic units, some nonsimplest constraint forms of DPMs can be explored combining fewer constraints and rotational symmetry, which could benefit the motion stability under the overconstraint reduction.

For the tetrahedral mechanism, the 1-DOF nonsimplest form is given in Fig. 3-14(b), which has a C_2-symmetry and can also be regarded as plane-symmetry.

Next, referring to the original topological graph of the cubic mechanism given in Fig. 3-27(a), four skew quadrilateral basic units, ABFC, ACFD, ADFE and AEFB, can be set up into its octahedron base following C_4 symmetry (see Fig. 3-27(b)), in which lines BC, CD, DE and EB are removed. Two adjacent basic units share two common topological lines to ensure the original motion. We can identify the mobility of the proposed nonsimplest constraint forms with screw theory. For nonsimplest cubic mechanism with C_4 symmetry as given in Fig. 3-27(b), its constraint matrix can be derived as

$$\boldsymbol{M}_{e2,1} = \begin{bmatrix} \boldsymbol{S}_{f1} & \mathbf{0} & \mathbf{0} & \boldsymbol{S}_{f4} & \boldsymbol{S}_{f9} & \mathbf{0} & \mathbf{0} & \boldsymbol{S}_{f12} \\ \mathbf{0} & \mathbf{0} & \boldsymbol{S}_{f3} & -\boldsymbol{S}_{f4} & \mathbf{0} & \mathbf{0} & \boldsymbol{S}_{f11} & -\boldsymbol{S}_{f12} \\ \mathbf{0} & \boldsymbol{S}_{f2} & -\boldsymbol{S}_{f3} & \mathbf{0} & \mathbf{0} & \boldsymbol{S}_{f10} & -\boldsymbol{S}_{f11} & \mathbf{0} \end{bmatrix} \tag{3-32}$$

The rank of constraint matrix is 7, and through computation, the mobility of this nonsimplest mechanism is $m = n_e - \text{rank}(\boldsymbol{M}_{e2,1}) = 8 - 7 = 1$, compared with the simplest mechanism with $c_e = 0$ and $c = 13$ as given in Fig. 3-18(c), the actual and equivalent overconstraints of this nonsimplest cubic mechanism are $c_e = 2$ and $c = 19$. Thus, the nonsimplest cubic mechanism is obtained following rotational symmetries with the original motion behaviour, whose motion sequences are demonstrated in Fig. 3-27(d).

Furthermore, following the C_2 symmetry to crisscross arrange four skew quadrilateral basic units, AEBC, BCDF, ACDE and DEFB, another nonsimplest topological graph is indicated in Fig. 3-27(c), also see Fig. 3-27(e). The constraint matrix of this nonsimplest cubic mechanism is

$$\boldsymbol{M}_{e2,2} = \begin{bmatrix} \boldsymbol{S}_{f1} & \boldsymbol{S}_{f3} & \mathbf{0} & \mathbf{0} & \boldsymbol{S}_{f7} & \boldsymbol{S}_{f8} & \mathbf{0} & \mathbf{0} \\ \mathbf{0} & \mathbf{0} & \boldsymbol{S}_{f5} & \mathbf{0} & \mathbf{0} & -\boldsymbol{S}_{f8} & \boldsymbol{S}_{f10} & \boldsymbol{S}_{f12} \\ \mathbf{0} & \mathbf{0} & \mathbf{0} & \boldsymbol{S}_{f6} & -\boldsymbol{S}_{f7} & \mathbf{0} & -\boldsymbol{S}_{f10} & -\boldsymbol{S}_{f12} \end{bmatrix} \tag{3-33}$$

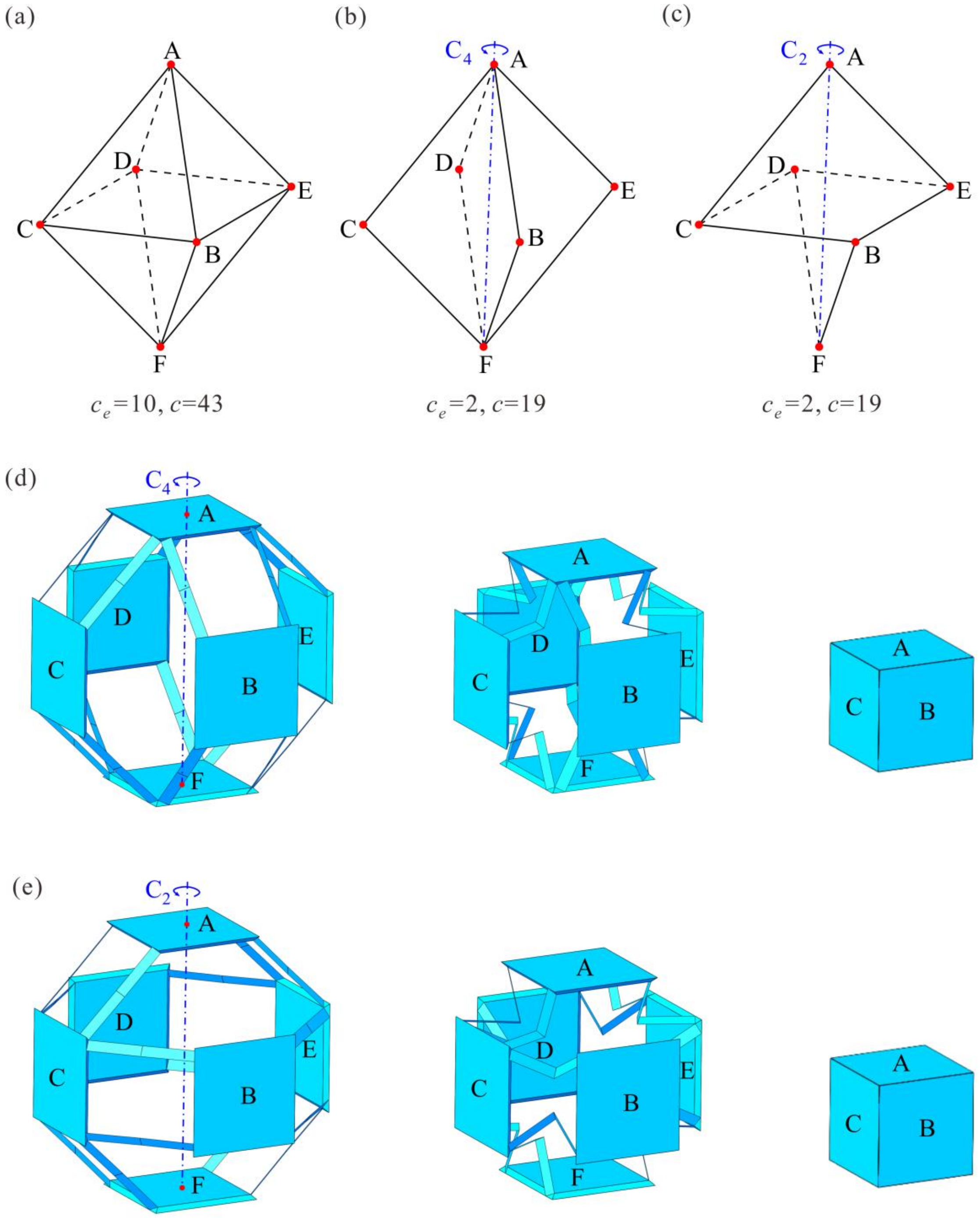

Fig. 3-27 Nonsimplest cubic mechanisms. (a) The original topological graph; (b) the nonsimplest topological graph following C_4 symmetry; (c) the nonsimplest topological graph following C_2 symmetry; (d) motion sequence of the nonsimplest cubic mechanism with C_4 symmetry; (e) motion sequence of the nonsimplest cubic mechanism with C_2 symmetry.

Thus, the mobility can be obtained as $m = n_e - \mathrm{rank}(\boldsymbol{M}_{e2,2}) = 8 - 7 = 1$ also with $c_e = 2$ and $c = 19$. Without loss of generality, all the reduced solutions are given in Appendix C, from the removal of one line in the topological graph to the removal of four lines.

Furthermore, nonsimplest dodecahedral mechanisms can also be obtained using rotational symmetry. Based on the original icosahedral topological graph in Fig. 3-28(a), ten skew quadrilateral basic units, ABHC, CHLI, ACID, DILJ, ADJE, EJLK, AEKF, FKLG, AFGB and BGLH, are crisscross arranged in Fig. 3-28(b) following C_5 symmetry, in which lines BC, CD, DE, EF, FB, HI, IJ, JK, KG and GH are removed, the mobility of this nonsimplest dodecahedral mechanism can be derived with the following constraint matrix

$$\boldsymbol{M}_{e3,1} = \left[\boldsymbol{M}_{11} \;\; \boldsymbol{M}_{12} \right] \tag{3-33}$$

with

$$\boldsymbol{M}_{11} = \begin{bmatrix} \mathbf{0} & \mathbf{0} & \mathbf{0} & \mathbf{0} & \mathbf{0} & \mathbf{0} & \mathbf{0} & \mathbf{0} & \mathbf{0} & \mathbf{0} \\ \mathbf{0} & \mathbf{0} & \mathbf{0} & \mathbf{0} & \mathbf{0} & \boldsymbol{S}_{f11} & \mathbf{0} & \mathbf{0} & \mathbf{0} & \mathbf{0} \\ \mathbf{0} & \mathbf{0} & \mathbf{0} & \mathbf{0} & \mathbf{0} & \mathbf{0} & \mathbf{0} & \mathbf{0} & \mathbf{0} & \mathbf{0} \\ \mathbf{0} & \mathbf{0} & \boldsymbol{S}_{f3} & \boldsymbol{S}_{f4} & \mathbf{0} & \mathbf{0} & \mathbf{0} & \mathbf{0} & \mathbf{0} & \mathbf{0} \\ \mathbf{0} & \mathbf{0} & \mathbf{0} & -\boldsymbol{S}_{f4} & \boldsymbol{S}_{f5} & \mathbf{0} & \mathbf{0} & \mathbf{0} & \mathbf{0} & \mathbf{0} \\ \mathbf{0} & \mathbf{0} & \mathbf{0} & \mathbf{0} & \mathbf{0} & \mathbf{0} & \mathbf{0} & \mathbf{0} & \boldsymbol{S}_{f14} & \boldsymbol{S}_{f15} \\ \mathbf{0} & \mathbf{0} & \mathbf{0} & \mathbf{0} & \mathbf{0} & \mathbf{0} & \boldsymbol{S}_{f12} & \boldsymbol{S}_{f13} & \mathbf{0} & \mathbf{0} \\ \mathbf{0} & \boldsymbol{S}_{f2} & -\boldsymbol{S}_{f3} & \mathbf{0} & \mathbf{0} & \mathbf{0} & \mathbf{0} & \mathbf{0} & \mathbf{0} & -\boldsymbol{S}_{f15} \\ \boldsymbol{S}_{f1} & \mathbf{0} & \mathbf{0} & \mathbf{0} & -\boldsymbol{S}_{f5} & -\boldsymbol{S}_{f11} & -\boldsymbol{S}_{f12} & \mathbf{0} & \mathbf{0} & \mathbf{0} \end{bmatrix}$$

$$\boldsymbol{M}_{12} = \begin{bmatrix} \mathbf{0} & \mathbf{0} & \boldsymbol{S}_{f18} & \boldsymbol{S}_{f19} & \mathbf{0} & \mathbf{0} & \mathbf{0} & \mathbf{0} & \boldsymbol{S}_{f29} & \boldsymbol{S}_{f30} \\ \mathbf{0} & \mathbf{0} & \mathbf{0} & \mathbf{0} & \boldsymbol{S}_{f20} & \boldsymbol{S}_{f26} & \mathbf{0} & \mathbf{0} & \mathbf{0} & -\boldsymbol{S}_{f30} \\ \boldsymbol{S}_{f16} & \boldsymbol{S}_{f17} & \mathbf{0} & \mathbf{0} & \mathbf{0} & \mathbf{0} & \mathbf{0} & \boldsymbol{S}_{f28} & -\boldsymbol{S}_{f29} & \mathbf{0} \\ \mathbf{0} & -\boldsymbol{S}_{f17} & -\boldsymbol{S}_{f18} & \mathbf{0} & \mathbf{0} & \mathbf{0} & \mathbf{0} & \mathbf{0} & \mathbf{0} & \mathbf{0} \\ \mathbf{0} & \mathbf{0} & \mathbf{0} & -\boldsymbol{S}_{f19} & -\boldsymbol{S}_{f20} & \mathbf{0} & \mathbf{0} & \mathbf{0} & \mathbf{0} & \mathbf{0} \\ \mathbf{0} & \mathbf{0} & \mathbf{0} & \mathbf{0} & \mathbf{0} & \mathbf{0} & \boldsymbol{S}_{f27} & -\boldsymbol{S}_{f28} & \mathbf{0} & \mathbf{0} \\ \mathbf{0} & \mathbf{0} & \mathbf{0} & \mathbf{0} & \mathbf{0} & -\boldsymbol{S}_{f26} & -\boldsymbol{S}_{f27} & \mathbf{0} & \mathbf{0} & \mathbf{0} \\ \mathbf{0} & \mathbf{0} & \mathbf{0} & \mathbf{0} & \mathbf{0} & \mathbf{0} & \mathbf{0} & \mathbf{0} & \mathbf{0} & \mathbf{0} \\ \mathbf{0} & \mathbf{0} & \mathbf{0} & \mathbf{0} & \mathbf{0} & \mathbf{0} & \mathbf{0} & \mathbf{0} & \mathbf{0} & \mathbf{0} \end{bmatrix}$$

The mobility of this nonsimplest cubic is $m = n_e - \text{rank}(\boldsymbol{M}_{e3,1}) = 8 - 7 = 1$ also with $c_e = 8$ and $c = 55$, which are obviously more than the simplest results with $c_e = 0$ and $c = 31$ as shown in Fig. 3-24(c).

Moreover, if six skew quadrilateral basic units, ACID, ADEF, AFGB, FKLG, GLIH and LIDJ, are connected end to end following C3 symmetry, the other nonsimplest dodecahedral mechanism is obtained in Fig. 3-28(c), whose motion sequences are demonstrated in Fig. 3-28(e). The corresponding constraint matrix can also be derived as

$$\boldsymbol{M}_{e3,2} = \left[\boldsymbol{M}_{11} \;\; \boldsymbol{M}_{12}\right] \tag{3-34}$$

with

$$\boldsymbol{M}_1 = \begin{bmatrix} \mathbf{0} & \mathbf{0} & \mathbf{0} & \mathbf{0} & \boldsymbol{S}_{f9} & \boldsymbol{S}_{f10} & \mathbf{0} & \mathbf{0} & \mathbf{0} \\ \mathbf{0} & \mathbf{0} & \mathbf{0} & \mathbf{0} & \mathbf{0} & \mathbf{0} & \boldsymbol{S}_{f11} & \mathbf{0} & \mathbf{0} \\ \mathbf{0} & \mathbf{0} & \mathbf{0} & \mathbf{0} & \mathbf{0} & \mathbf{0} & \mathbf{0} & \mathbf{0} & \mathbf{0} \\ \mathbf{0} & \mathbf{0} & \mathbf{0} & \mathbf{0} & \mathbf{0} & \mathbf{0} & \mathbf{0} & \mathbf{0} & \mathbf{0} \\ \mathbf{0} & \boldsymbol{S}_{f2} & \boldsymbol{S}_{f3} & \mathbf{0} & \mathbf{0} & \mathbf{0} & \mathbf{0} & \mathbf{0} & \boldsymbol{S}_{f15} \\ \mathbf{0} & \mathbf{0} & -\boldsymbol{S}_{f3} & \boldsymbol{S}_{f5} & -\boldsymbol{S}_{f9} & -\boldsymbol{S}_{f10} & \mathbf{0} & \mathbf{0} & \mathbf{0} \\ \boldsymbol{S}_{f1} & \mathbf{0} & \mathbf{0} & -\boldsymbol{S}_{f5} & \mathbf{0} & \mathbf{0} & -\boldsymbol{S}_{f11} & \boldsymbol{S}_{f12} & \mathbf{0} \end{bmatrix}$$

$$\boldsymbol{M}_2 = \begin{bmatrix} \mathbf{0} & \boldsymbol{S}_{f17} & \boldsymbol{S}_{f20} & \mathbf{0} & \mathbf{0} & \mathbf{0} & \mathbf{0} & \boldsymbol{S}_{f29} & \boldsymbol{S}_{f30} \\ \mathbf{0} & \mathbf{0} & -\boldsymbol{S}_{f20} & \mathbf{0} & \mathbf{0} & \boldsymbol{S}_{f26} & \mathbf{0} & \mathbf{0} & -\boldsymbol{S}_{f30} \\ \boldsymbol{S}_{f16} & -\boldsymbol{S}_{f17} & \mathbf{0} & \mathbf{0} & \mathbf{0} & \mathbf{0} & \boldsymbol{S}_{f28} & -\boldsymbol{S}_{f29} & \mathbf{0} \\ \mathbf{0} & \mathbf{0} & \mathbf{0} & \boldsymbol{S}_{f21} & \boldsymbol{S}_{f22} & -\boldsymbol{S}_{f26} & -\boldsymbol{S}_{f28} & \mathbf{0} & \mathbf{0} \\ -\boldsymbol{S}_{f16} & \mathbf{0} & \mathbf{0} & \mathbf{0} & \mathbf{0} & \mathbf{0} & \mathbf{0} & \mathbf{0} & \mathbf{0} \\ \mathbf{0} & \mathbf{0} & \mathbf{0} & \mathbf{0} & \mathbf{0} & \mathbf{0} & \mathbf{0} & \mathbf{0} & \mathbf{0} \\ \mathbf{0} & \mathbf{0} & \mathbf{0} & \mathbf{0} & \mathbf{0} & \mathbf{0} & \mathbf{0} & \mathbf{0} & \mathbf{0} \end{bmatrix}$$

which also results in mobility $m = n_e - \text{rank}(\boldsymbol{M}_{e3,2}) = 8 - 7 = 1$ with $c_e = 4$ and $c = 43$.

Therefore, the 1-DOF nonsimplest constraint forms can combine the overconstraint reduction and rotational symmetries, in which other solutions can also be obtain with the proposed combination method.

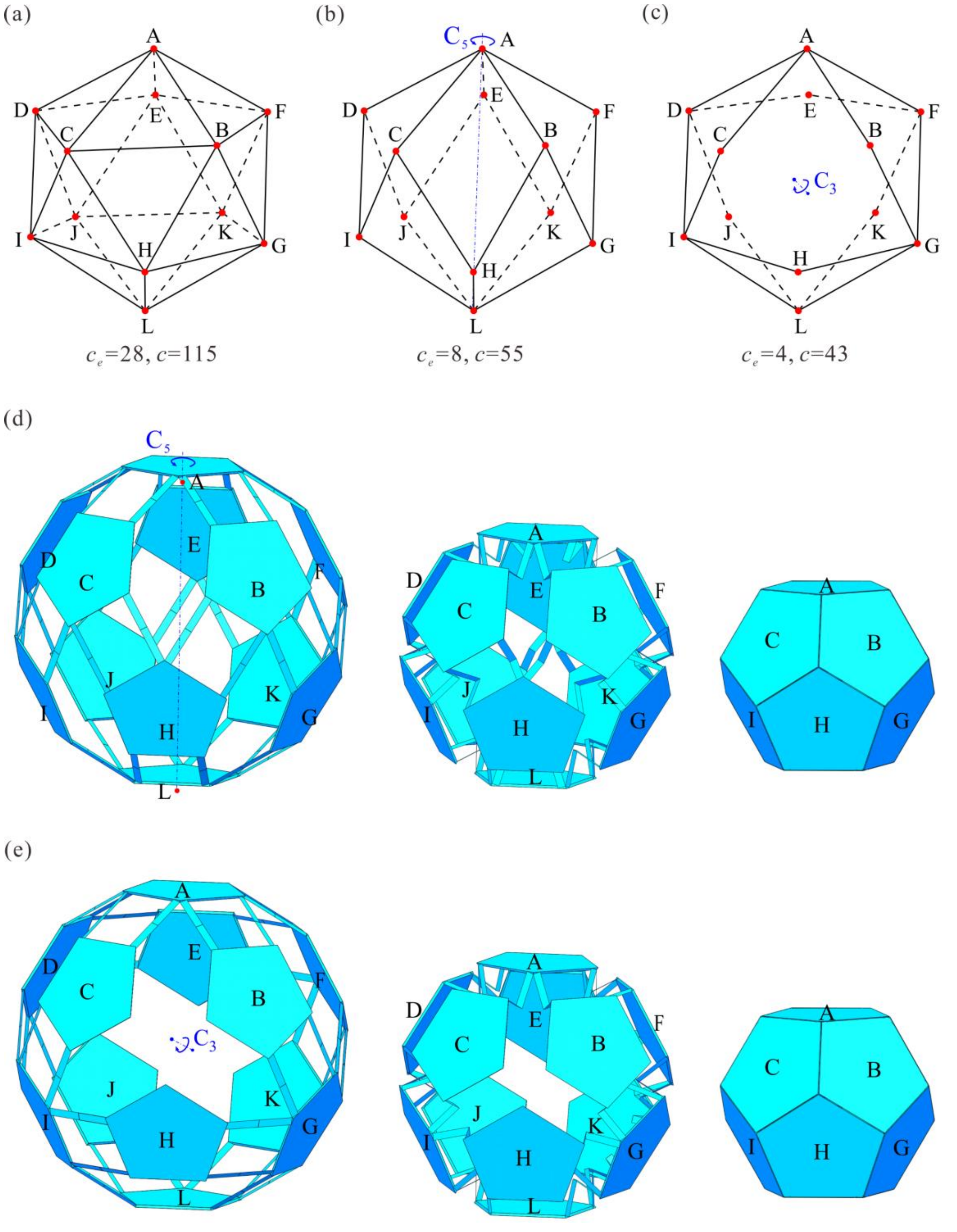

Fig. 3-28 Nonsimplest dodecahedral mechanisms. (a) The original topological graph; (b) the nonsimplest topological graph following C_5 symmetry; (c) the nonsimplest topological graph following C_3 symmetry; (d) motion sequence of the nonsimplest dodecahedral mechanism with C_5 symmetry; (e) motion sequence of the nonsimplest dodecahedral mechanism with C_3 symmetry.

3.5 Conclusions

In this chapter, we have proposed an innovative and intuitive approach for constructing Sarrus-based DPMs based on three Platonic solids. Through integrating the Sarrus linkages into a Platonic solid after the expansion operation, deployable tetrahedral, cubic and dodecahedral mechanisms are synthesized and constructed that enable 1-DOF synchronous radial motion, in which three paired polyhedral transformations between Platonic and Archimedean solids are identified and revealed. The proposed construction technique can be readily extended to the design of deployable semiregular Archimedean polyhedrons, prism polyhedrons and Johnson polyhedrons, which satisfy the geometry condition that only three faces meet at one vertex.

For the mobility analysis of Sarrus-based DPMs, the equivalent analysis strategy for multiloop mechanisms is proposed by regarding each Sarrus linkage as an equivalent prismatic joint. The mobility of each polyhedral mechanism in this chapter has been derived as only one by utilizing the screw-loop equation method with Kirchhoff's circulation law and an associated constraint graph. Subsequently, the calculation process with the conventional analysis method was conducted, revealing the accuracy, simplicity and high efficiency of the proposed equivalent analysis strategy. The proposed construction and analysis strategy can be adapted to design other deployable mechanisms in various regular and irregular polyhedral groups that could facilitate their applications in various engineering fields. Furthermore, based on the construction method, we can also realize all nine paired transformations reported in Chapter 2, where structural variations with mechanism topology isomorphism need to be conducted. This work also paves the way for designing kinematic cells for metastructures and metamaterials, especially in Oh symmetry.

In addition, a novel Hamiltonian-path-based reduction method of 1-DOF Sarrus-based DPMs was developed. By introducing Hamiltonian paths on 3D topological graphs, the overconstraint reduction strategy for multiloop overconstrained DPMs was proposed based on skew quadrilateral basic units and their sequential arrangements. All Hamiltonian paths on their dual tetrahedron, octahedron and icosahedron were discussed in detail to obtain one simplest tetrahedral mechanism, one simplest cubic mechanism and nineteen dodecahedral mechanisms, respectively. The degree of overconstraint in each simplest DPM is greatly reduced while preserving the original motion behaviour, i.e., one-DOF synchronized radial motion. Moreover, the proposed reduction results are evaluated according to the calculation of the degree of overconstraint combining the Euler formula and the Grübler-Kutzbach formula. The nonsimplest form can be selected and obtained from the proposed approach for specific applications. The proposed construction, analysis and reduction methods provide inspiration for the simplification of known multiloop mechanisms or for the construction of new mechanisms, with potential applications in the fields of manufacturing, architecture and space exploration.

Chapter 4 7*R*-based Archimedean Polyhedrons and Their Symmetric Transformations

4.1 Introduction

Deployable mechanisms have interested researchers over the past decades across various engineering fields as their extraordinary ability to fold a large structure into a compact size. As a special and regular type of 3D deployable mechanisms, deployable polyhedrons and transformable polyhedrons have been developed with various design strategies. Moreover, some interesting polyhedral pairs can be identified through mathematical transformations (details can be found in Section 1.2.3), in which each pair of polyhedrons has the same polyhedral symmetry due to their radial transformation in geometry. Using kinematic strategies to realize such polyhedral transformations obtained in geometry, the proposed S4*R*-based polyhedrons in Chapter 2 present a construction method for a group of transformable polyhedrons. However, their transformable pairs are limited due to the threefold-symmetric construction cell, which can only deal with the folding of hexagon facets of polyhedrons. In this chapter, aiming to realize richer transformations among Archimedean and Platonic polyhedrons, a family of deployable Archimedean polyhedrons are proposed based on spatial 7*R* linkages and their threefold-, fourfold-, fivefold-symmetric loops, all of which perform 1-DOF synchronized radial motion and symmetric transformability.

The outline of this chapter is as follows. By using spatial 7*R* linkages as the construction cells, a family of deployable Archimedean polyhedrons is developed in Section 4.2, in which polyhedral transformations are demonstrated following tetrahedral, octahedral and icosahedral symmetries. Regardless of which transformation, the original symmetry is always preserved in the continuous folding process of 7*R*-based polyhedrons. In Section 4.3, the overconstraint reductions of those 7*R*-based polyhedrons are investigated based on the Hamiltonian-path-based method as a further exploration for the reduction strategy, in which the Hamiltonian paths of all five Platonic polyhedrons are discussed in detail in this section. the nonsimplest 7*R*-based polyhedrons are discussed in Section 4.4. Finally, the conclusions and discussion are given in Section 4.5, which summarizes the main findings in this chapter.

4.2 Construction of 7*R*-based Archimedean Polyhedrons

4.2.1 Polyhedral Construction Based on Symmetric 7*R* Loops

To fold polyhedrons and realize the polyhedral transformation, the first task is to fold polygons on the polyhedral surface. For instance, to transform a truncated tetratetrahedron into a truncated tetrahedron, as illustrated in Fig. 4-1(a), the yellow hexagon facet should be folded into a triangle, and the adjacent cyan squares should vanish (highlighted red line area), while other blue hexagon facets should move synchronously and radially with respect to the polyhedral centroid. For this purpose, as shown in Fig. 4-1 (b), to completely fold the cyan squares, the design strategy of the construction cell originates from a kirigami pattern with nine sheets (p_1 to p_9) when we cut the yellow hexagon facet and add an additional valley crease on each cyan square.

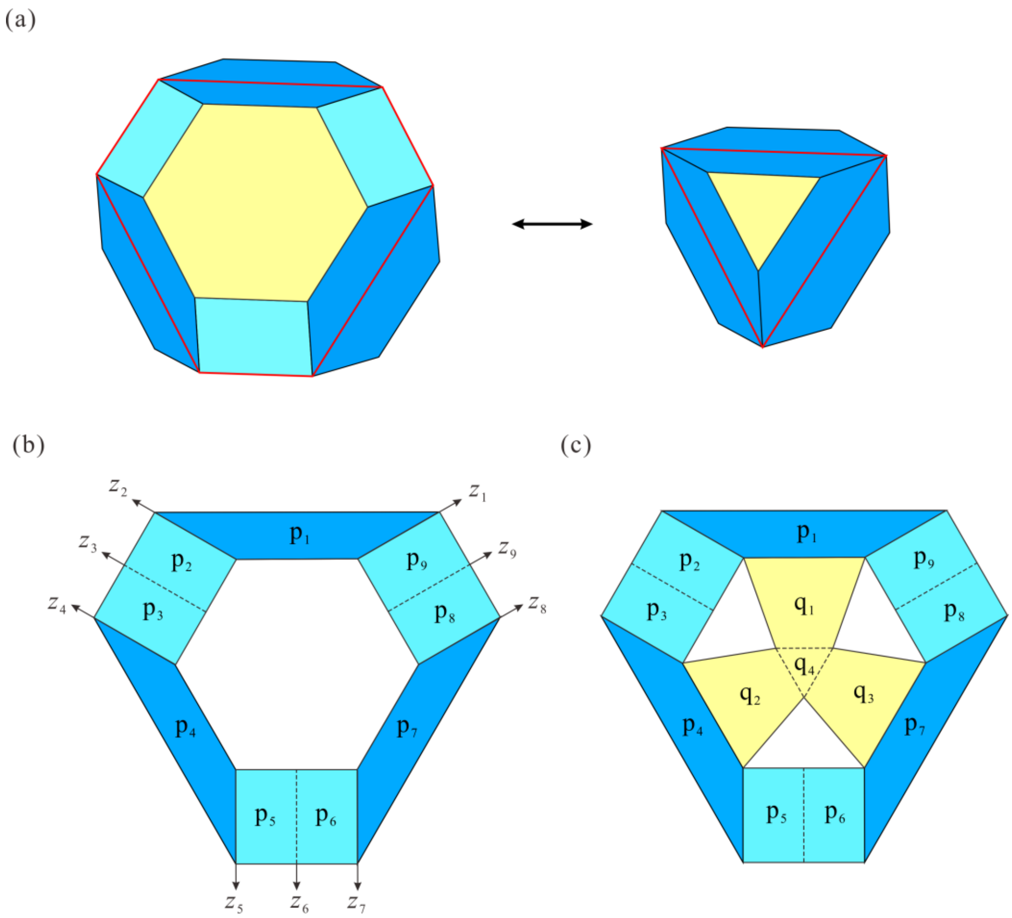

Fig. 4-1 Threefold-symmetric kirigami pattern. (a) Transformation from a truncated tetratetrahedron to a truncated tetrahedron; (b) a spatial 9*R* linkage and (c) a threefold-symmetric 7*R* loop.

This geometry can be kinematically modelled as a threefold-symmetric spatial 9*R* linkage with three sets of parallel revolute joints, i.e., $z_2//z_3//z_4$, $z_5//z_6//z_7$ and $z_8//z_9//z_1$, and other design parameters are dependent on polyhedral geometry, yet it has three DOFs. To obtain 1-DOF folding motion, extra motion constraints need to be introduced into this kirigami pattern. Here, we add four additional yellow sheets (q_1 to q_4) to further associate and constrain the motion of blue platforms (p_1, p_4 and p_7), in which q_1 to q_3 are identical isosceles trapezoids and q_4 is an equilateral triangle to match the threefold symmetry. As a result, a modified kirigami pattern is obtained in Fig. 4-1(c), which can be modelled as a threefold-symmetric 7*R* loop that consists of three 7*R* linkages $p_1p_2p_3p_4q_2q_4q_1$, $p_4p_5p_6p_7q_3q_4q_2$ and $p_7p_8p_9p_1q_1q_4q_3$.

Mobility analysis of the proposed threefold-symmetric 7*R* loop can be investigated and verified using screw theory. The threefold-symmetric 7*R* loop in an arbitrary configuration is given in Fig. 4-2(a) with the local coordinate frame $\{x_i, y_i, z_i\}$, where origin O_i is located at the centre of the yellow equilateral triangle sheet (side length is *b*) and $l=\sqrt{3}a/2-\sqrt{3}b/6$. The motion-screw system can be calculated in the associated local coordinate system, in which

$$\boldsymbol{S}'_{i1}=\begin{bmatrix}1 & 0 & 0 & 0 & l\sin\varphi'_2 & l\cos\varphi'_2-\sqrt{3}b/6\end{bmatrix}^{\mathrm{T}}$$

$$\boldsymbol{S}'_{i2}=\big[-1/2 \quad \sqrt{3}/2 \quad 0 \quad -\sqrt{3}l\sin\varphi'_2/2 \quad -l\sin\varphi'_2/2 \quad l\cos\varphi'_2/4-\sqrt{3}b/24-\sqrt{3}(b/4-\sqrt{3}l\cos\varphi'_2/2)/2\big]^{\mathrm{T}}$$

$$\boldsymbol{S}'_{i3}=\big[-1/2 \quad -\sqrt{3}/2 \quad 0 \quad \sqrt{3}l\sin\varphi'_2/2 \quad -l\sin\varphi'_2/2 \quad l\cos\varphi'_2/4-\sqrt{3}b/24-\sqrt{3}(b/4-\sqrt{3}l\cos\varphi'_2/2)/2\big]^{\mathrm{T}}$$

$$\boldsymbol{S}'_{i4}=\begin{bmatrix}1 & 0 & 0 & 0 & 0 & -\sqrt{3}b/6\end{bmatrix}^{\mathrm{T}}$$

$$\boldsymbol{S}'_{i5}=\begin{bmatrix}-1/2 & \sqrt{3}/2 & 0 & 0 & 0 & -\sqrt{3}b/12\end{bmatrix}^{\mathrm{T}}$$

$$\boldsymbol{S}'_{i6}=\begin{bmatrix}-1/2 & -\sqrt{3}/2 & 0 & 0 & 0 & -\sqrt{3}b/12\end{bmatrix}^{\mathrm{T}}$$

$$\boldsymbol{S}_{i1}=\big[b/2 \quad \sqrt{3}b/6 \quad -\sqrt{6}b/3 \quad -(\sqrt{2}b^2/2-l\cos\varphi')/3-\sqrt{3}bl\sin\varphi'_2/6 \quad bl\sin\varphi'_2/2-\sqrt{6}ab/6 \quad -b(\sqrt{3}b/6-l\cos\varphi')/2+\sqrt{3}ab/12\big]^{\mathrm{T}}$$

$$\boldsymbol{S}_{i2}=\big[-b/2 \quad \sqrt{3}b/6 \quad -\sqrt{6}b/3 \quad -(\sqrt{2}b^2/2-l\cos\varphi')/3-\sqrt{3}bl\sin\varphi_2'/6$$
$$-bl\sin\varphi_2'/2-\sqrt{6}ab/6 \qquad -b(\sqrt{3}b/6-l\cos\varphi')/2-\sqrt{3}ab/12\big]^{\mathrm{T}}$$

$$\boldsymbol{S}_{i3}=\big[-b/2 \quad \sqrt{3}b/6 \quad -\sqrt{6}b/3 \quad -\sqrt{6}b(h/2-\sqrt{3}b/6)/3$$
$$-\sqrt{6}b(b/2+\sqrt{3}h/6)/3 \qquad b(h/2-\sqrt{3}b/6)/2-\sqrt{3}b(b/2+\sqrt{3}h/6)/6\ \big]^{\mathrm{T}}$$

$$\boldsymbol{S}_{i4}=\big[-b/2 \quad \sqrt{3}b/6 \quad -\sqrt{6}b/3 \quad -\sqrt{3}b(\sqrt{3}a/2-\sqrt{3}b/12+l\cos\varphi'/2)/3-\sqrt{3}bl\sin\varphi_2'/6$$
$$-\sqrt{3}b(a/2-b/4-\sqrt{3}l\cos\varphi'/2)/3-bl\sin\varphi_2'/2$$
$$b(\sqrt{3}a/2-\sqrt{3}b/12+l\cos\varphi'/2)/2-\sqrt{3}b(a/2+b/4-\sqrt{3}l\cos\varphi'/2)/6\big]^{\mathrm{T}}$$

$$\boldsymbol{S}_{i5}=\big[0 \quad -\sqrt{3}b/3 \quad -\sqrt{6}b/3 \quad (3\sqrt{2}ab/2+\sqrt{3}b/12+l\cos\varphi'/2)/3+\sqrt{3}bl\sin\varphi_2'/3$$
$$\sqrt{6}b(a/2-b/4+\sqrt{3}l\cos\varphi'/2)/3 \qquad \sqrt{3}b(a/2-b/4+\sqrt{3}l\cos\varphi'/2)/3\big]^{\mathrm{T}}$$

$$\boldsymbol{S}_{i6}=\big[0 \quad -\sqrt{3}b/3 \quad -\sqrt{6}b/3 \quad \sqrt{6}b(h+\sqrt{3}b/3)/3 \quad 0 \quad 0\big]^{\mathrm{T}}$$

$$\boldsymbol{S}_{i7}=\big[0 \quad -\sqrt{3}b/3 \quad -\sqrt{6}b/3 \qquad (3\sqrt{2}ab/2+\sqrt{3}b/12-l\cos\varphi'/2)/3+\sqrt{3}bl\sin\varphi_2'/3$$
$$-\sqrt{6}b(a/2-b/4+\sqrt{3}l\cos\varphi'/2)/3 \qquad \sqrt{3}b(a/2-b/4+\sqrt{3}l\cos\varphi'/2)/3\big]^{\mathrm{T}}$$

$$\boldsymbol{S}_{i8}=\big[b/2 \quad \sqrt{3}b/6 \quad -\sqrt{6}b/3 \quad -\sqrt{6}b(\sqrt{3}a/2-\sqrt{3}b/12+l\cos\varphi'/2)/3-\sqrt{3}bl\sin\varphi_2'/6$$
$$-\sqrt{6}b(a/2-b/4-\sqrt{3}l\cos\varphi'/2)/3+bl\sin\varphi_2'/2$$
$$-b(\sqrt{3}a/2-\sqrt{3}b/12+l\cos\varphi'/2)/2+\sqrt{3}b(a/2+b/4-\sqrt{3}l\cos\varphi'/2)/6\big]^{\mathrm{T}}$$

$$\boldsymbol{S}_{i9}=\big[b/2 \quad \sqrt{3}b/6 \quad -\sqrt{6}b/3 \quad -\sqrt{6}b(h/2+\sqrt{3}b/6)/3$$
$$\sqrt{6}b(b/2+\sqrt{3}h/6)/3 \qquad -b(h/2+\sqrt{3}b/6)/2+\sqrt{3}b(b/2+\sqrt{3}h/2)/6\ \big]^{\mathrm{T}}$$

Then, the associated constraint graph is sketched in Fig. 4-2(b). According to Kirchhoff's circulation law for independent loops shown in the constraint graph, the constraint matrix of the threefold-symmetric $7R$ loop is organized as

$$\boldsymbol{M}_1=\begin{bmatrix} \mathbf{0} & \boldsymbol{S}_{i2} & \boldsymbol{S}_{i3} & \boldsymbol{S}_{i4} & \mathbf{0} & \mathbf{0} & \mathbf{0} & \mathbf{0} & \mathbf{0} & \boldsymbol{S}'_{i1} & \boldsymbol{S}'_{i2} & \mathbf{0} & \boldsymbol{S}'_{i4} & \boldsymbol{S}'_{i5} & \mathbf{0} \\ \mathbf{0} & \mathbf{0} & \mathbf{0} & \mathbf{0} & \boldsymbol{S}_{i5} & \boldsymbol{S}_{i6} & \boldsymbol{S}_{i7} & \mathbf{0} & \mathbf{0} & \mathbf{0} & -\boldsymbol{S}'_{i2} & \boldsymbol{S}'_{i3} & \mathbf{0} & -\boldsymbol{S}'_{i5} & \boldsymbol{S}'_{i6} \\ \boldsymbol{S}_{i1} & \mathbf{0} & \mathbf{0} & \mathbf{0} & \mathbf{0} & \mathbf{0} & \mathbf{0} & \boldsymbol{S}_{i8} & \boldsymbol{S}_{i9} & -\boldsymbol{S}'_{i1} & \mathbf{0} & -\boldsymbol{S}'_{i3} & -\boldsymbol{S}'_{i4} & \mathbf{0} & -\boldsymbol{S}'_{i6} \end{bmatrix} \quad (4\text{-}1)$$

Thus, the rank of this constraint matrix $\boldsymbol{M}_1$ is 14, which indicates that the mobility of the threefold-symmetric $7R$ loop is $m=n-\mathrm{rank}(\boldsymbol{M}_1)=15-14=1$. Moreover, based on the D-H matrix method, the kinematic relationships among the four types of dihedral angles, see Fig. 4-2(a), can be derived as

$$\varphi_2 = 2\varphi_1 - \arccos(1/3)$$
$$\cos\varphi_2' = \sqrt{3}(b - a - 2a\sin(\varphi_2/2))/6l$$
$$\varphi_1' = \varphi_2' - \arccos(1/3) \tag{4-2}$$

in which φ_1 is given as the only kinematic input. Hence, this threefold-symmetric 7*R* loop presents a 1-DOF synchronized radial motion, whose folding sequence is given in Fig. 4-3.

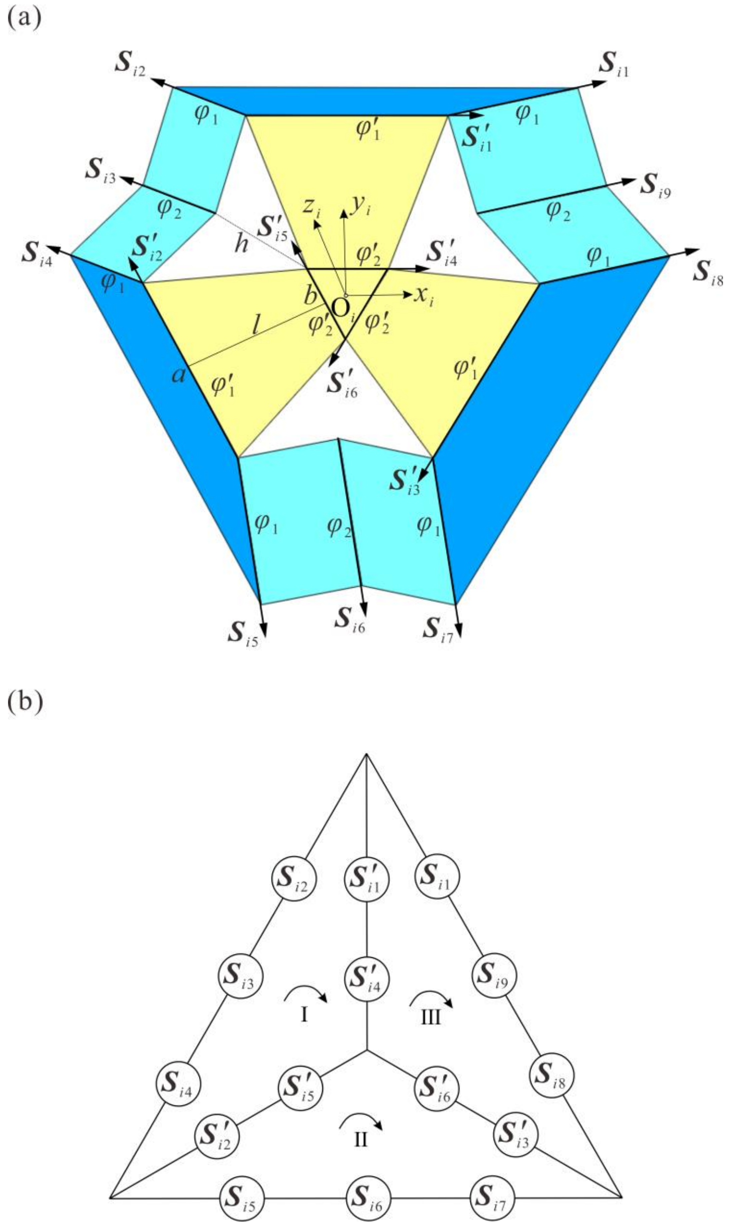

Fig. 4-2 Mobility analysis of the threefold-symmetric 7*R* loop. (a) Coordinate system and (b) constraint graph.

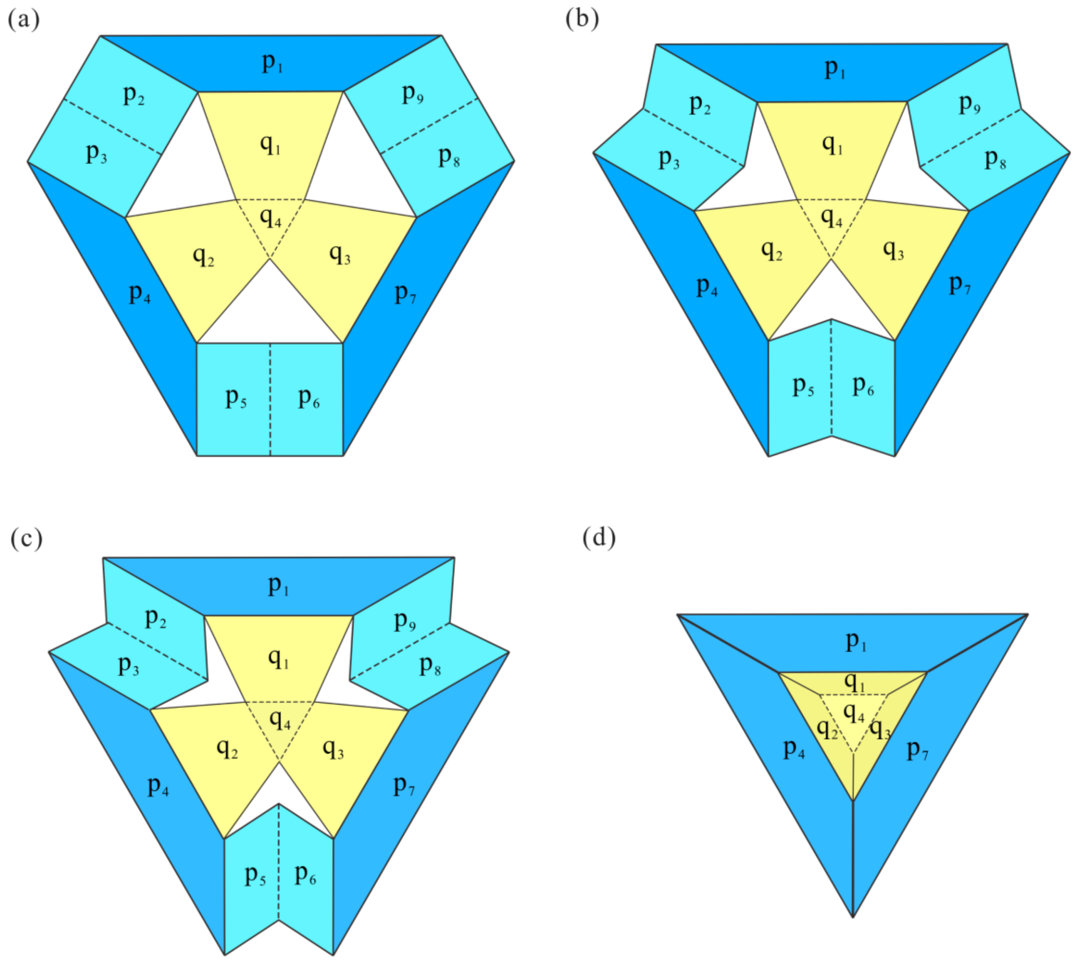

Fig. 4-3 Folding sequence of the threefold-symmetric 7*R* loop.

Regarding a construction cell, see Fig. 4-4(a), the symmetric 7*R* loop can be tessellated with tetrahedral symmetry to synthesize a 7*R*-based truncated tetratetrahedron and realise the transformation as given in Fig. 4-1(a). First, a quarter portion of the entire polyhedral surface is symmetrically highlighted by grey dotted lines according to T_d symmetry. Then, we embed one threefold-symmetric 7*R* loop into this quarter polyhedral surface, referring to the polyhedral geometry. Finally, the 7*R*-based truncated tetratetrahedron is obtained by embedding four 7*R* loops following T_d tessellation. The 1-DOF construction cell and the polyhedral symmetric tessellation guarantee that the 7*R*-based truncated tetratetrahedron also performs a 1-DOF synchronized folding motion, whose cardboard prototype is shown in Fig. 4-4(a). Therefore, the polyhedral transformation from a truncated tetratetrahedron (left) to a truncated tetrahedron (right) is ultimately accomplished during the entire folding process.

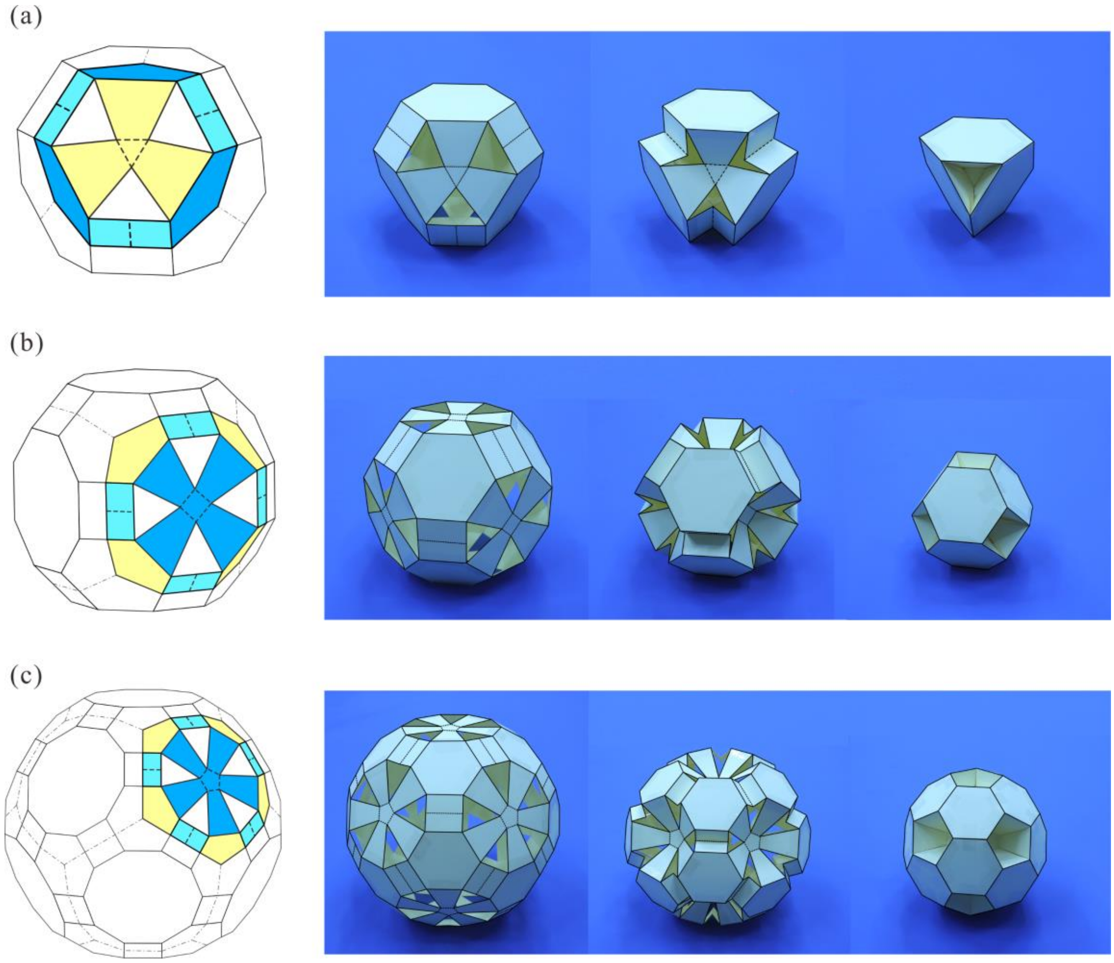

Fig. 4-4 Construction of 7*R*-based deployable polyhedrons with 7*R* loops. (a) 7*R*-based truncated tetratetrahedron constructed by threefold-symmetric 7*R* loops and the transformation sequence from a truncated tetratetrahedron to a truncated tetrahedron; (b) 7*R*-based truncated cuboctahedron constructed by fourfold-symmetric 7*R* loops and the transformation sequence from a truncated cuboctahedron to a truncated octahedron; (c) 7*R*-based truncated icosidodecahedron constructed by fivefold-symmetric 7*R* loops and the transformation sequence from a truncated icosidodecahedron to a truncated icosahedron.

Furthermore, if we fold a truncated cuboctahedron into a truncated octahedron, the corresponding octagons need to be folded into squares, in which the threefold-symmetric 7*R* loop is not applicable. To solve this problem, similar 1-DOF fourfold-symmetric 7*R* loops are introduced, as shown in Fig. 4-4(b), which consists of four spatial 7*R* linkages. One fourfold-symmetric 7*R* loop is embedded into the one-sixth polyhedral surface, and following O_h tessellation, a 7*R*-based truncated cuboctahedron is obtained to fulfil the corresponding polyhedral transformation. Similarly, we can also use the 1-DOF fivefold-symmetric 7*R* loops to address the folding of the decagon and create a 7*R*-based truncated icosidodecahedron following icosahedral symmetry. As illustrated in Fig. 4-4(c), a total of twelve fivefold-symmetric 7*R* loops are involved in this construction, and the transformation from a truncated icosidodecahedron to a truncated icosahedron is revealed.

Considering the truncated tetratetrahedron mechanism as an example to conduct the mobility analysis, the reference coordinate frame $\{x, y, z\}$ in its deployed configuration is established in Fig. 4-5(a), in which its reference origin O is located at the centroid of the truncated tetratetrahedron. Theoretically, the four platforms A, B, C and D are located at the vertices of a virtual dual tetrahedron during the continuous motion process; thus, a dual tetrahedron is introduced in Fig. 4-5(b). in which four local origins O_i (i =1, 2, 3 and 4) are the centres of virtual triangles, i.e., triangles ABC, ACD, ABD and BCD, respectively. The joint screws of a threefold-symmetric 7*R* loop in Fig. 4-2(a) can be transformed to the reference coordinate system with the 3×3 rotation transformation matrix $\boldsymbol{R}_i$ and the skew-symmetric matrix of vector $\boldsymbol{p}_i$. Referring to the polyhedral geometry and $\mathrm{T_d}$ symmetry, $\boldsymbol{R}_i$ and $\boldsymbol{p}_i$ (i =1, 2, …, 6) in the 7*R*-based truncated tetratetrahedron can be obtained as

$$\boldsymbol{R}_1=\begin{bmatrix} 0 & -\sqrt{6}/3 & \sqrt{3}/3 \\ \sqrt{2}/2 & -\sqrt{6}/6 & \sqrt{3}/3 \\ \sqrt{2}/2 & \sqrt{6}/6 & \sqrt{3}/3 \end{bmatrix},\ \boldsymbol{p}_1=d\left[\sqrt{3}/3 \quad -\sqrt{3}/3 \quad \sqrt{3}/3\right]^{\mathrm{T}}$$

$$\boldsymbol{R}_2=\begin{bmatrix} -\sqrt{2}/2 & -\sqrt{6}/6 & -\sqrt{3}/3 \\ 0 & -\sqrt{6}/3 & \sqrt{3}/3 \\ -\sqrt{2}/2 & \sqrt{6}/6 & \sqrt{3}/3 \end{bmatrix},\ \boldsymbol{p}_2=d\left[-\sqrt{3}/3 \quad \sqrt{3}/3 \quad \sqrt{3}/3\right]^{\mathrm{T}}$$

$$\boldsymbol{R}_3=\begin{bmatrix} \sqrt{2}/2 & -\sqrt{6}/6 & -\sqrt{3}/3 \\ -\sqrt{2}/2 & -\sqrt{6}/6 & -\sqrt{3}/3 \\ 0 & \sqrt{6}/3 & -\sqrt{3}/3 \end{bmatrix},\ \boldsymbol{p}_4=d\left[\sqrt{3}/3 \quad \sqrt{3}/3 \quad -\sqrt{3}/3\right]^{\mathrm{T}}$$

$$\boldsymbol{R}_4=\begin{bmatrix} \sqrt{2}/2 & \sqrt{6}/6 & \sqrt{3}/3 \\ 0 & -\sqrt{6}/3 & \sqrt{3}/3 \\ \sqrt{2}/2 & -\sqrt{6}/6 & -\sqrt{3}/3 \end{bmatrix},\ \boldsymbol{p}_4=d\left[\sqrt{3}/3 \quad \sqrt{3}/3 \quad -\sqrt{3}/3\right]^{\mathrm{T}} \tag{4-3}$$

Based on the reference coordinate frame, Fig. 4-5(c) shows the constraint graph with 42 joint screws in the 7*R*-based truncated tetratetrahedron. Thus, the constraint matrix $\boldsymbol{M}_2$ can be expressed as

$$\boldsymbol{M}_2=\begin{bmatrix}\boldsymbol{M}_{11} & \boldsymbol{M}_{12} & \boldsymbol{M}_{13} & \boldsymbol{M}_{14} & \boldsymbol{M}_{15} & \boldsymbol{0}_{6\times6} & \boldsymbol{0}_{6\times6}\\ \boldsymbol{M}_{21} & \boldsymbol{0}_{5\times6} & \boldsymbol{M}_{23} & \boldsymbol{M}_{24} & \boldsymbol{M}_{25} & \boldsymbol{M}_{26} & \boldsymbol{M}_{27}\end{bmatrix} \tag{4-4}$$

where

$$\boldsymbol{M}_{11}=\begin{bmatrix}\boldsymbol{0} & \boldsymbol{S}_{12} & \boldsymbol{S}_{13} & \boldsymbol{S}_{14} & \boldsymbol{0} & \boldsymbol{0}\\ \boldsymbol{S}_{11} & \boldsymbol{0} & \boldsymbol{0} & \boldsymbol{0} & \boldsymbol{0} & \boldsymbol{0}\\ \boldsymbol{0} & \boldsymbol{0} & \boldsymbol{0} & \boldsymbol{0} & \boldsymbol{S}_{15} & \boldsymbol{S}_{16}\\ -\boldsymbol{S}_{11} & \boldsymbol{0} & \boldsymbol{0} & \boldsymbol{0} & \boldsymbol{0} & \boldsymbol{0}\\ \boldsymbol{0} & \boldsymbol{0} & \boldsymbol{0} & \boldsymbol{0} & \boldsymbol{0} & \boldsymbol{0}\\ \boldsymbol{0} & \boldsymbol{0} & \boldsymbol{0} & \boldsymbol{0} & \boldsymbol{0} & \boldsymbol{0}\end{bmatrix},\ \boldsymbol{M}_{12}=\begin{bmatrix}\boldsymbol{0} & \boldsymbol{0} & \boldsymbol{0} & \boldsymbol{S}'_{11} & \boldsymbol{S}'_{12} & \boldsymbol{0}\\ \boldsymbol{0} & \boldsymbol{S}_{18} & \boldsymbol{S}_{19} & -\boldsymbol{S}'_{11} & \boldsymbol{0} & \boldsymbol{S}'_{13}\\ \boldsymbol{S}_{17} & \boldsymbol{0} & \boldsymbol{0} & \boldsymbol{0} & -\boldsymbol{S}'_{12} & -\boldsymbol{S}'_{13}\\ \boldsymbol{0} & -\boldsymbol{S}_{18} & -\boldsymbol{S}_{19} & \boldsymbol{0} & \boldsymbol{0} & \boldsymbol{0}\\ \boldsymbol{0} & \boldsymbol{0} & \boldsymbol{0} & \boldsymbol{0} & \boldsymbol{0} & \boldsymbol{0}\\ \boldsymbol{0} & \boldsymbol{0} & \boldsymbol{0} & \boldsymbol{0} & \boldsymbol{0} & \boldsymbol{0}\end{bmatrix}$$

$$\boldsymbol{M}_{13}=\begin{bmatrix}\boldsymbol{S}'_{14} & \boldsymbol{0} & \boldsymbol{S}'_{16} & \boldsymbol{0} & \boldsymbol{0} & \boldsymbol{0}\\ -\boldsymbol{S}'_{14} & \boldsymbol{S}'_{15} & \boldsymbol{0} & \boldsymbol{0} & \boldsymbol{0} & \boldsymbol{0}\\ \boldsymbol{0} & -\boldsymbol{S}'_{15} & -\boldsymbol{S}'_{16} & \boldsymbol{0} & \boldsymbol{0} & \boldsymbol{0}\\ \boldsymbol{0} & \boldsymbol{0} & \boldsymbol{0} & \boldsymbol{0} & \boldsymbol{0} & \boldsymbol{0}\\ \boldsymbol{0} & \boldsymbol{0} & \boldsymbol{0} & \boldsymbol{0} & \boldsymbol{0} & \boldsymbol{0}\\ \boldsymbol{0} & \boldsymbol{0} & \boldsymbol{0} & \boldsymbol{S}_{25} & \boldsymbol{S}_{26} & \boldsymbol{S}_{27}\end{bmatrix},\ \boldsymbol{M}_{14}=\begin{bmatrix}\boldsymbol{0} & \boldsymbol{0} & \boldsymbol{0} & \boldsymbol{0} & \boldsymbol{0} & \boldsymbol{0}\\ \boldsymbol{0} & \boldsymbol{0} & \boldsymbol{0} & \boldsymbol{0} & \boldsymbol{0} & \boldsymbol{0}\\ \boldsymbol{0} & \boldsymbol{0} & \boldsymbol{0} & \boldsymbol{0} & \boldsymbol{0} & \boldsymbol{0}\\ \boldsymbol{0} & \boldsymbol{0} & \boldsymbol{0} & \boldsymbol{S}'_{21} & \boldsymbol{S}'_{22} & \boldsymbol{0}\\ \boldsymbol{S}_{21} & \boldsymbol{S}_{28} & \boldsymbol{S}_{29} & -\boldsymbol{S}'_{21} & \boldsymbol{0} & \boldsymbol{S}'_{23}\\ \boldsymbol{0} & \boldsymbol{0} & \boldsymbol{0} & \boldsymbol{0} & -\boldsymbol{S}'_{22} & -\boldsymbol{S}'_{23}\end{bmatrix}$$

$$\boldsymbol{M}_{15}=\begin{bmatrix}\boldsymbol{0} & \boldsymbol{0} & \boldsymbol{0} & \boldsymbol{0} & \boldsymbol{0} & \boldsymbol{0}\\ \boldsymbol{0} & \boldsymbol{0} & \boldsymbol{0} & \boldsymbol{0} & \boldsymbol{0} & \boldsymbol{0}\\ \boldsymbol{0} & \boldsymbol{0} & \boldsymbol{0} & \boldsymbol{0} & \boldsymbol{0} & \boldsymbol{0}\\ \boldsymbol{S}'_{24} & \boldsymbol{0} & \boldsymbol{S}'_{26} & \boldsymbol{0} & \boldsymbol{0} & \boldsymbol{0}\\ -\boldsymbol{S}'_{24} & \boldsymbol{S}'_{25} & \boldsymbol{0} & \boldsymbol{0} & \boldsymbol{0} & \boldsymbol{0}\\ \boldsymbol{0} & -\boldsymbol{S}'_{25} & -\boldsymbol{S}'_{26} & \boldsymbol{0} & \boldsymbol{0} & \boldsymbol{0}\end{bmatrix},\ \boldsymbol{M}_{21}=\begin{bmatrix}\boldsymbol{0} & -\boldsymbol{S}_{12} & -\boldsymbol{S}_{13} & -\boldsymbol{S}_{14} & \boldsymbol{0} & \boldsymbol{0}\\ \boldsymbol{0} & \boldsymbol{0} & \boldsymbol{0} & \boldsymbol{0} & \boldsymbol{0} & \boldsymbol{0}\\ \boldsymbol{0} & \boldsymbol{0} & \boldsymbol{0} & \boldsymbol{0} & \boldsymbol{0} & \boldsymbol{0}\\ \boldsymbol{0} & \boldsymbol{0} & \boldsymbol{0} & \boldsymbol{0} & \boldsymbol{0} & \boldsymbol{0}\\ \boldsymbol{0} & \boldsymbol{0} & \boldsymbol{0} & \boldsymbol{0} & \boldsymbol{0} & \boldsymbol{0}\end{bmatrix}$$

$$\boldsymbol{M}_{23}=\begin{bmatrix}\boldsymbol{0} & \boldsymbol{0} & \boldsymbol{0} & \boldsymbol{0} & \boldsymbol{0} & \boldsymbol{0}\\ \boldsymbol{0} & \boldsymbol{0} & \boldsymbol{0} & \boldsymbol{0} & \boldsymbol{0} & \boldsymbol{0}\\ \boldsymbol{0} & \boldsymbol{0} & \boldsymbol{0} & \boldsymbol{0} & \boldsymbol{0} & \boldsymbol{0}\\ \boldsymbol{0} & \boldsymbol{0} & \boldsymbol{0} & \boldsymbol{0} & \boldsymbol{0} & \boldsymbol{0}\\ \boldsymbol{0} & \boldsymbol{0} & \boldsymbol{0} & -\boldsymbol{S}_{25} & -\boldsymbol{S}_{26} & -\boldsymbol{S}_{27}\end{bmatrix},\ \boldsymbol{M}_{24}=\begin{bmatrix}\boldsymbol{0} & \boldsymbol{0} & \boldsymbol{0} & \boldsymbol{0} & \boldsymbol{0} & \boldsymbol{0}\\ -\boldsymbol{S}_{21} & -\boldsymbol{S}_{28} & -\boldsymbol{S}_{29} & \boldsymbol{0} & \boldsymbol{0} & \boldsymbol{0}\\ \boldsymbol{0} & \boldsymbol{0} & \boldsymbol{0} & \boldsymbol{0} & \boldsymbol{0} & \boldsymbol{0}\\ \boldsymbol{0} & \boldsymbol{0} & \boldsymbol{0} & \boldsymbol{0} & \boldsymbol{0} & \boldsymbol{0}\\ \boldsymbol{0} & \boldsymbol{0} & \boldsymbol{0} & \boldsymbol{0} & \boldsymbol{0} & \boldsymbol{0}\end{bmatrix}$$

$$\boldsymbol{M}_{25}=\begin{bmatrix}\boldsymbol{0} & \boldsymbol{0} & \boldsymbol{0} & \boldsymbol{0} & \boldsymbol{0} & \boldsymbol{0}\\ \boldsymbol{0} & \boldsymbol{0} & \boldsymbol{0} & \boldsymbol{0} & \boldsymbol{0} & \boldsymbol{0}\\ \boldsymbol{0} & \boldsymbol{0} & \boldsymbol{0} & \boldsymbol{S}_{35} & \boldsymbol{S}_{36} & \boldsymbol{S}_{37}\\ \boldsymbol{0} & \boldsymbol{0} & \boldsymbol{0} & -\boldsymbol{S}_{35} & -\boldsymbol{S}_{36} & -\boldsymbol{S}_{37}\\ \boldsymbol{0} & \boldsymbol{0} & \boldsymbol{0} & \boldsymbol{0} & \boldsymbol{0} & \boldsymbol{0}\end{bmatrix},\ \boldsymbol{M}_{26}=\begin{bmatrix}\boldsymbol{S}'_{31} & \boldsymbol{0} & \boldsymbol{S}'_{33} & \boldsymbol{S}'_{34} & \boldsymbol{0} & \boldsymbol{S}'_{36}\\ -\boldsymbol{S}'_{31} & \boldsymbol{S}'_{32} & \boldsymbol{0} & -\boldsymbol{S}'_{34} & \boldsymbol{S}'_{35} & \boldsymbol{0}\\ \boldsymbol{0} & -\boldsymbol{S}'_{32} & -\boldsymbol{S}'_{33} & \boldsymbol{0} & -\boldsymbol{S}'_{35} & -\boldsymbol{S}'_{36}\\ \boldsymbol{0} & \boldsymbol{0} & \boldsymbol{0} & \boldsymbol{0} & \boldsymbol{0} & \boldsymbol{0}\\ \boldsymbol{0} & \boldsymbol{0} & \boldsymbol{0} & \boldsymbol{0} & \boldsymbol{0} & \boldsymbol{0}\end{bmatrix}$$

$$\boldsymbol{M}_{27}=\begin{bmatrix} \mathbf{0} & \mathbf{0} & \mathbf{0} & \mathbf{0} & \mathbf{0} & \mathbf{0} \\ \mathbf{0} & \mathbf{0} & \mathbf{0} & \mathbf{0} & \mathbf{0} & \mathbf{0} \\ \mathbf{0} & \mathbf{0} & \mathbf{0} & \mathbf{0} & \mathbf{0} & \mathbf{0} \\ \boldsymbol{S}'_{41} & \boldsymbol{S}'_{42} & \mathbf{0} & \boldsymbol{S}'_{44} & \boldsymbol{S}'_{45} & \mathbf{0} \\ \mathbf{0} & -\boldsymbol{S}'_{42} & \boldsymbol{S}'_{43} & -\boldsymbol{S}'_{44} & \mathbf{0} & \boldsymbol{S}'_{46} \end{bmatrix}, \quad \mathbf{0}_{6\times 6}=\begin{bmatrix} \mathbf{0} & \mathbf{0} & \mathbf{0} & \mathbf{0} & \mathbf{0} & \mathbf{0} \\ \mathbf{0} & \mathbf{0} & \mathbf{0} & \mathbf{0} & \mathbf{0} & \mathbf{0} \\ \mathbf{0} & \mathbf{0} & \mathbf{0} & \mathbf{0} & \mathbf{0} & \mathbf{0} \\ \mathbf{0} & \mathbf{0} & \mathbf{0} & \mathbf{0} & \mathbf{0} & \mathbf{0} \\ \mathbf{0} & \mathbf{0} & \mathbf{0} & \mathbf{0} & \mathbf{0} & \mathbf{0} \\ \mathbf{0} & \mathbf{0} & \mathbf{0} & \mathbf{0} & \mathbf{0} & \mathbf{0} \end{bmatrix}$$

Therefore, the rank of the constraint matrix $\boldsymbol{M}_2$ is 41, which indicates the mobility of the 7*R*-based truncated tetratetrahedron is $m = n - \text{rank}(\boldsymbol{M}_2) = 42 - 41 = 1$.

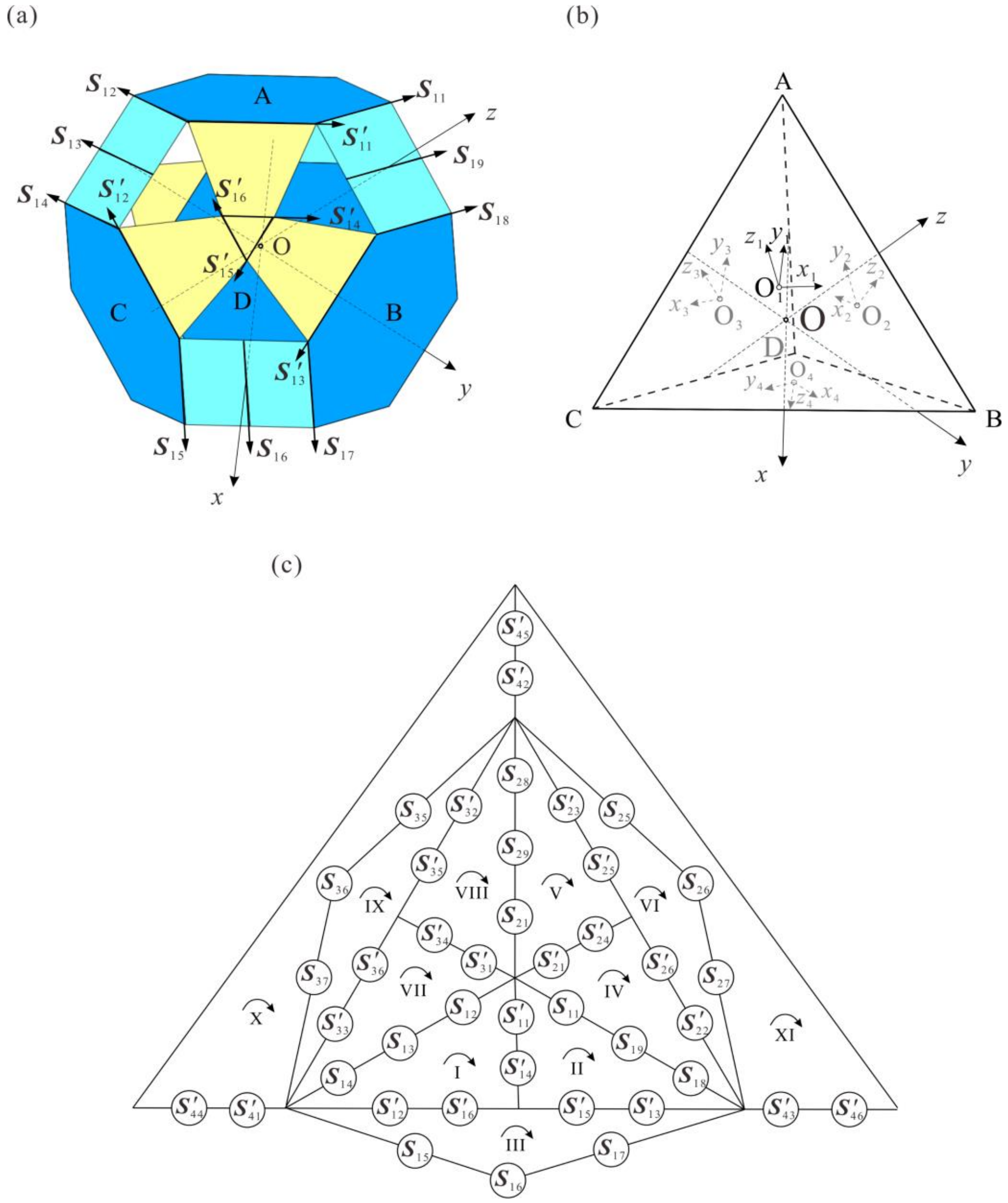

Fig. 4-5 Mobility analysis of the 7*R*-based truncated tetratetrahedron. (a) Coordinate system; (b) constraint graph.

4.2.2 Transformations with T_d Symmetry

Next, considering a truncated tetratetrahedron in Figs. 4-6(a) to (c) as an example in which these types of polygons are illustrated in different colours, we reserve one type and fold the other two, leading to three possible transformations. First, we reserve the blue hexagons as highlighted by the red line in Fig. 4-6(a) and fold the other types by using threefold-symmetric 7*R* loops, whose corresponding kinematic solution has been demonstrated in Fig. 4-4(a). Second, due to the duality of the tetrahedral group, the construction by reserving yellow hexagons in Fig. 4-6(b) also results in the same transformation as given in Fig. 4-6(a). Third, if we reserve cyan squares, then synchronous folding of yellow and blue hexagons can create a different transformation from a truncated tetratetrahedron to a rhombitetratetrahedron, as shown in Fig. 4-6(c). However, we rotate the yellow and blue sheets 60° to ensure connection with the reserved cyan squares, leading to a 1-DOF assembly of spatial 8*R* linkages instead of 7*R* linkages.

Moreover, based on the construction of the 7*R*-based truncated tetratetrahedron in Fig. 4-6(a), we explore the transformation from Archimedean to Platonic polyhedrons. As shown in Fig. 4-6(d), the blue triangles are reserved in the geometric transformation, while the yellow hexagons should be folded. Here, to embed the threefold-symmetric 7*R* loops, we add elongated cyan sheets with a width of *h* along the edges between two adjacent yellow hexagons, in which the original blue triangles are actually inequilateral hexagons and *h* can theoretically be infinitely small. Thus, the 7*R*-based truncated tetrahedron is obtained as is its transformation to a tetratetrahedron. Additionally, we reserve the blue triangles in a rhombitetratetrahedron in Fig. 4-6(e) and fold other facets with threefold-symmetric 7*R* loops to realize the transformation into a tetrahedron. Similarly, we extend three edges with a width of *l* at the vertices of each original triangle to accommodate the embedding of 7*R* loops. Only carrying out the geometric variations, both the 7*R*-based truncated tetrahedron in Fig. 4-6(d) and rhombitetratetrahedron in Fig. 4-6(e) have the same mechanism topology as the 7*R*-based truncated tetratetrahedron in Fig. 4-6(a), i.e., isomorphic assembly of threefold-symmetric 7*R* loops. No matter which transformation is performed in Fig. 4-6, T_d symmetry is always reserved in the continuous folding process of 7*R*-based polyhedrons, as well as the 1-DOF synchronized radial motion.

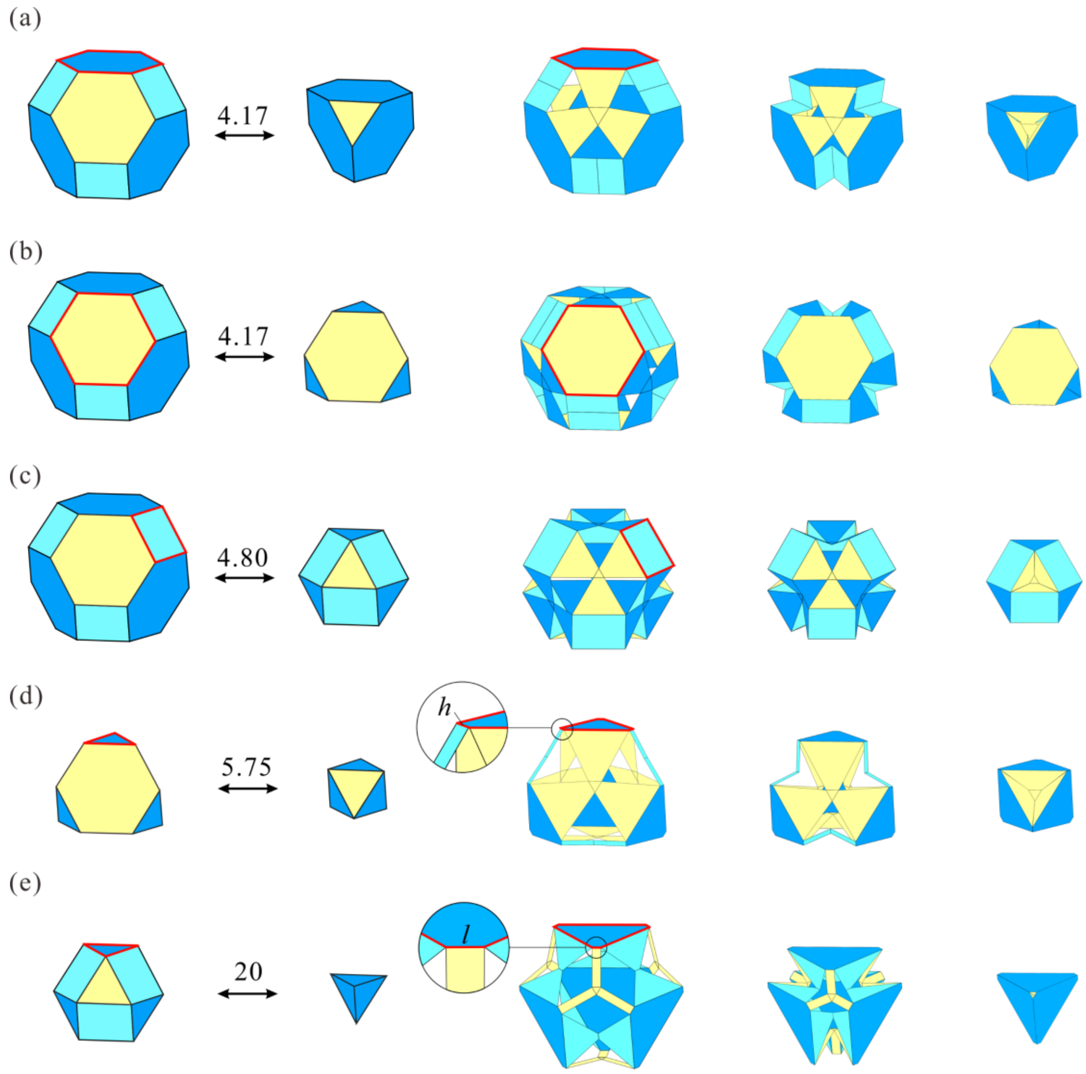

Fig. 4-6 Transformations of 7*R*-based polyhedrons with T_d symmetry. (a) and (b) Transformation from a truncated tetratetrahedron to a truncated tetrahedron; (c) transformation from a truncated tetratetrahedron to a rhombitetratetrahedron; (d) transformation from a truncated tetrahedron to a tetratetrahedron; (e) transformation from a rhombitetratetrahedron to a tetrahedron.

4.2.3 Transformations with O_h and I_h Symmetries

The above construction and transformation methods can also be readily applied to the other Archimedean polyhedrons with O_h and I_h symmetry, respectively. Here, for the transformation of a 7*R*-based truncated cuboctahedron with O_h symmetry, we can obtain three kinematic solutions, as given in Figs. 4-7(a) to (c). Reserving the blue octagon (marked in red line) and using a threefold-symmetric 7*R* loop as the construction cell to fold the yellow hexagons and cyan squares, the transformation from a truncated cuboctahedron to a truncated cube is given in Fig. 4-7(a) based on the O_h

tessellation of a total of eight construction cells. Next, the transformation in Fig. 4-7(b) has been presented by introducing six fourfold-symmetric 7R loops to fold the blue octagons, also see Fig. 4-4(b). Furthermore, by combining the above folding of yellow hexagons and blue octagons while reserving cyan squares, the transformation to rhombicuboctahedron is obtained in Fig. 4-7(c), which results in an assembly of 8R linkages.

Similar to the cases in Figs. 4-6(d) and (e), we obtain more paired transformations among Archimedean and Platonic polyhedrons based on the proposed 7R-based truncated cuboctahedron, see Figs. 4-7(d) to (g). The 7R-based polyhedrons in Figs. 4-7(d) and (e), both transformed into cuboctahedrons, are constructed with threefold- and fourfold-symmetric 7R loops, respectively, in which we introduce elongated cyan sheets along the edge between the facets that need to be folded. The rhombicuboctahedron in Figs. 4-7(f) and (g) can be transformed into a cube and an octahedron, respectively, in which those two 7R-based rhombicuboctahedrons are constructed by embedding threefold- and fourfold-symmetric 7R loops. Thus, the kinematic solutions, as demonstrated in Figs. 4-7(d) and (f), have the same mechanism topology isomorphism as the one in Fig. 4-7(a), as do the cases in Figs. 4-7(e) and (g), as in Fig. 4-7(b). Apparently, the 1-DOF synchronized radial motion with O_h symmetry is presented in each transformation of 7R-based polyhedrons in Fig. 4-7.

Moreover, we readily create a series of 1-DOF 7R-based polyhedrons with I_h symmetry and their corresponding transformations (see Fig. 4-8). Embedding threefold-symmetric 7R loops, fivefold-symmetric 7R loops and their combination in a truncated icosidodecahedron result in the transformations to truncated dodecahedron (Fig. 4-8(a)), truncated icosahedron (Fig. 4-8(b)) and rhombicosidodecahedron (Fig. 4-8(c)), respectively. Implementing a similar construction strategy as shown in Figs. 4-7(d) to (g), the remaining four different 7R-based polyhedrons are obtained in Figs. 4-8(d) to (g), as well as the paired transformations in the icosahedral group. In this way, the folded configurations of the two cases in Figs. 4-8(d) and (e) are identical, as well as the deployed configurations in Figs. 4-8(f) and (g).

Therefore, in addition to two special Archimedean polyhedrons without symmetry, i.e., snub cube and snub dodecahedron, the 1-DOF transformations among the remaining eleven Archimedean and all five Platonic polyhedrons have been presented following T_d, O_h and I_h symmetries.

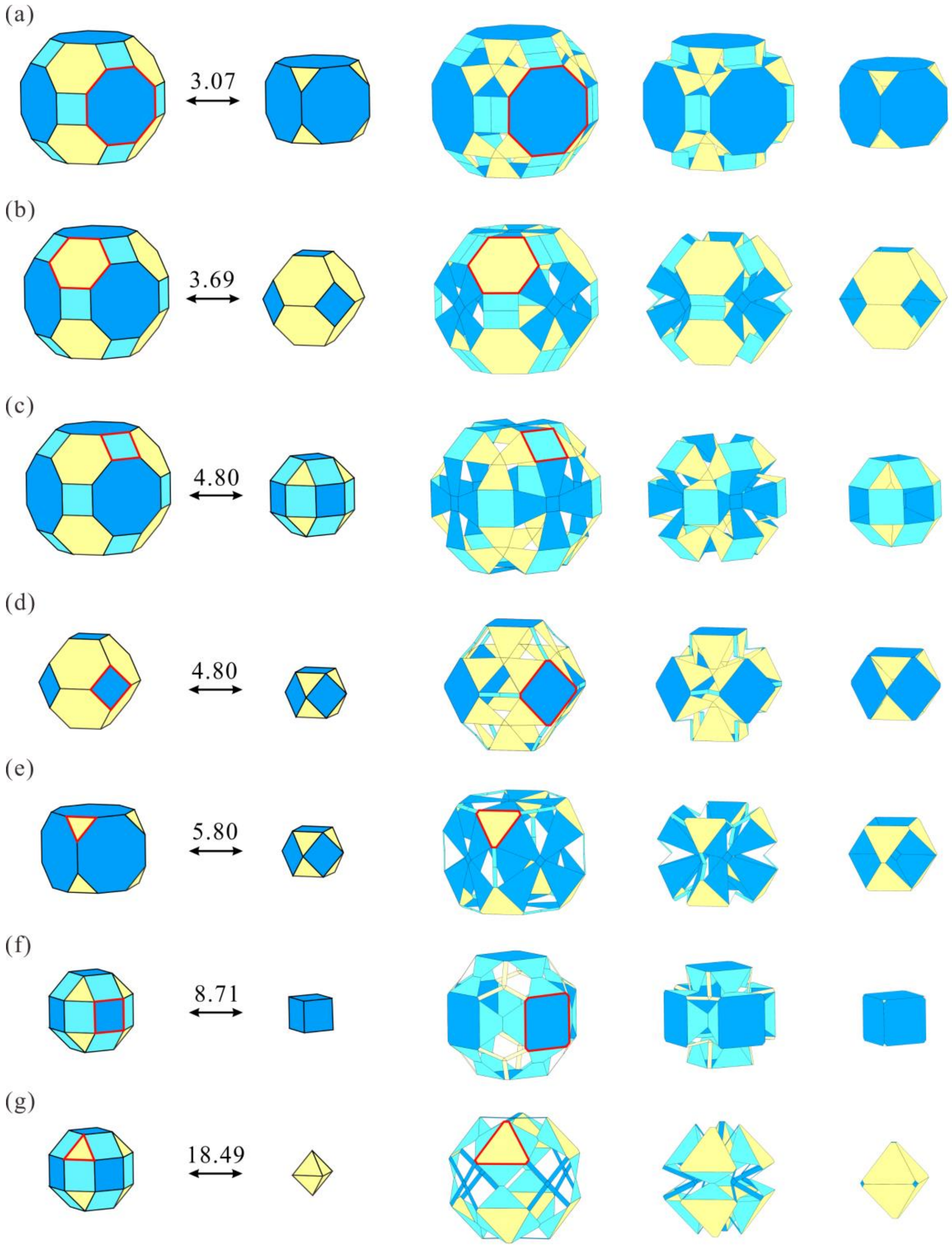

Fig. 4-7 Transformations of 7*R*-based polyhedrons with O_h symmetry. (a) Transformation from a truncated cuboctahedron to a truncated cube; (b) transformation from a truncated cuboctahedron to a truncated octahedron; (c) transformation from a truncated cuboctahedron to a rhombicuboctahedron; (d) transformation from a truncated octahedron to a cuboctahedron; (e) transformation from a truncated cube to a cuboctahedron; (f) transformation from a rhombicuboctahedron to a cube; (g) transformation from a rhombicuboctahedron to an octahedron.

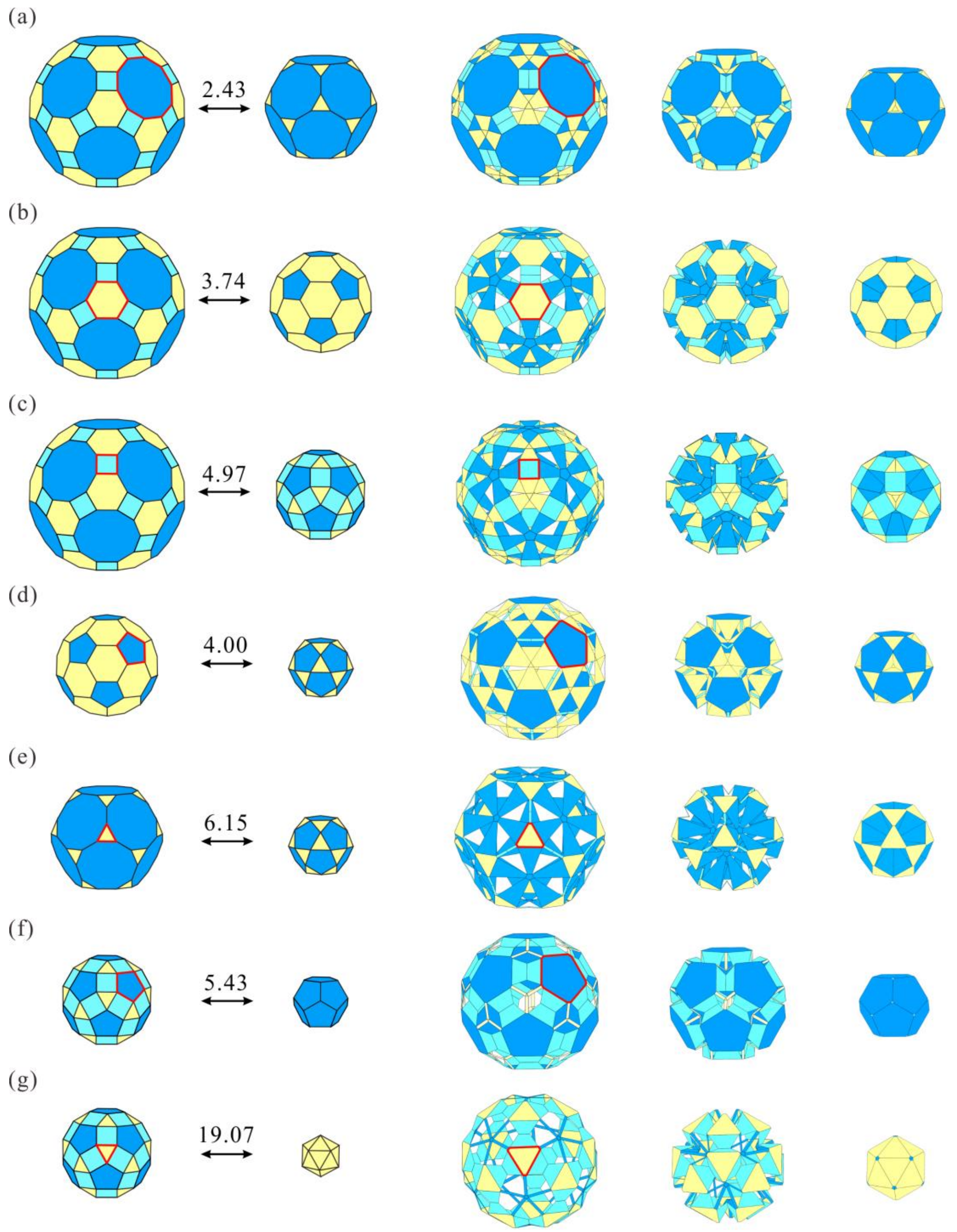

Fig. 4-8 Transformations of 7*R*-based polyhedrons with I_h symmetry. (a) Transformation from a truncated icosidodecahedron to a truncated dodecahedron; (b) transformation from a truncated icosidodecahedron to a truncated icosahedron; (c) transformation from a truncated icosidodecahedron to a rhombicosidodecahedron; (d) transformation from a truncated icosahedron to an icosidodecahedron. (e) Transformation from a truncated dodecahedron to an icosidodecahedron; (f) transformation from a rhombicosidodecahedron to a dodecahedron; (g) transformation from a rhombicosidodecahedron to an icosahedron.

4.3 Overconstraint reduction of 7*R*-based Polyhedrons

4.3.1 Reduction of the 7*R*-based Truncated Tetratetrahedron

The proposed 7*R*-based truncated tetratetrahedron constructed by threefold-symmetric 7*R* loops is illustrated in Fig. 4-9(a), with its corresponding 3D topological graph shown in Fig. 4-9(b), in which the larger blue vertices of a dual tetrahedron stand for the main translational platforms, and smaller dots in corresponding colours denote the involved sheets. To reduce or even eliminate the overconstraint in multiloop 7*R*-based DPMs and find the effective constraint space for polyhedral platforms, we can also present the reduction process by utilizing the topology operation inspired by the Hamiltonian path, which is an extension of the Hamiltonian-path reduction strategy proposed in Chapter 3.

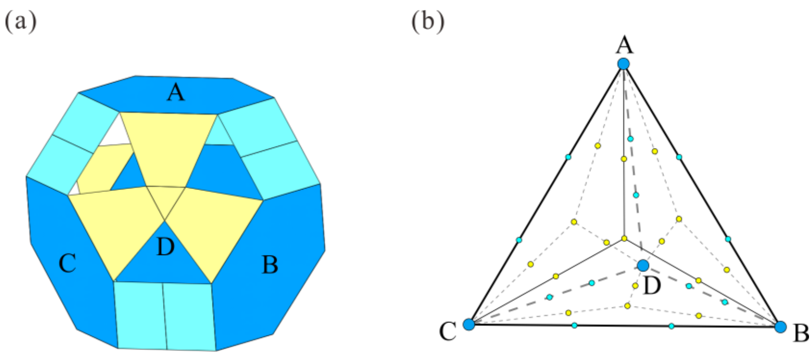

Fig. 4-9 7*R*-based truncated tetratetrahedron. (a) The original mechanism and (b) its corresponding topological graph based on a dual tetrahedron.

Notably, the essential premise of reduction is that each platform requires at least two equivalent prismatic joints to connect it to the entire closed mechanism, i.e., each vertex is related to at least two edges in the topological graph, while the original kinematic properties, including mobility and radial motion, will be preserved among polyhedral platforms.

Thus, we can readily investigate the reduction of 7*R*-based polyhedrons with the assistance of a Hamiltonian path. Considering symmetry, only one 3D Hamiltonian path of the tetrahedron is given in Fig. 4-10(a), as illustrated by the four red lines connecting the four blue vertices. Moreover, referring to the analysis of the degree of overconstraint c as given in Section 3.3, the 32 links and 42 joints in this 7*R*-based mechanism result in overconstraints c=25. Next, this Hamiltonian path splits the tetrahedron into two half shells, as shown in Figs. 4-10(b) and (e). On the one hand, the half shell in Fig. 4-10(b) is an assembly of two 1-DOF equilateral triangular units ABC and BCD, in which each equilateral triangle consists of three isosceles small triangles representing a threefold-symmetric assembly of 1-DOF 7*R* linkages. Next, we can remove edge BC under the mentioned reduction premise without affecting kinematics, where a spatial 8*R* linkage appears at the original edge BC, as shown in Fig. 4-10(c). However, the overconstraints of 7 still exist due to multiloop coupling. Furthermore, we remove edges AB and CD in Fig. 4-10(d), resulting in a 1-DOF 7*R*-8*R*-7*R* assembly, in which the 7*R* linkage can completely constrain the motion of the 8*R* linkage due to two shared joints and three common links. Thus far, the overconstraint has been reduced from the original 25 to 1. Note that if we remove arbitrarily one link or joint, the mobility of this 7*R*-based mechanism will increase; hence, the topological graph in Fig. 4-10(d) can be obtained as the simplest constrained form of the 7*R*-based truncated tetratetrahedron. The mobility and equivalent kinematics can also be obtained with the analysis process as given in Section 4.2.1. However, the other half shell in Fig. 4-10(e) can also lead to the identical simplest constraint form due to tetrahedral symmetry, as shown in Fig. 4-10(g).

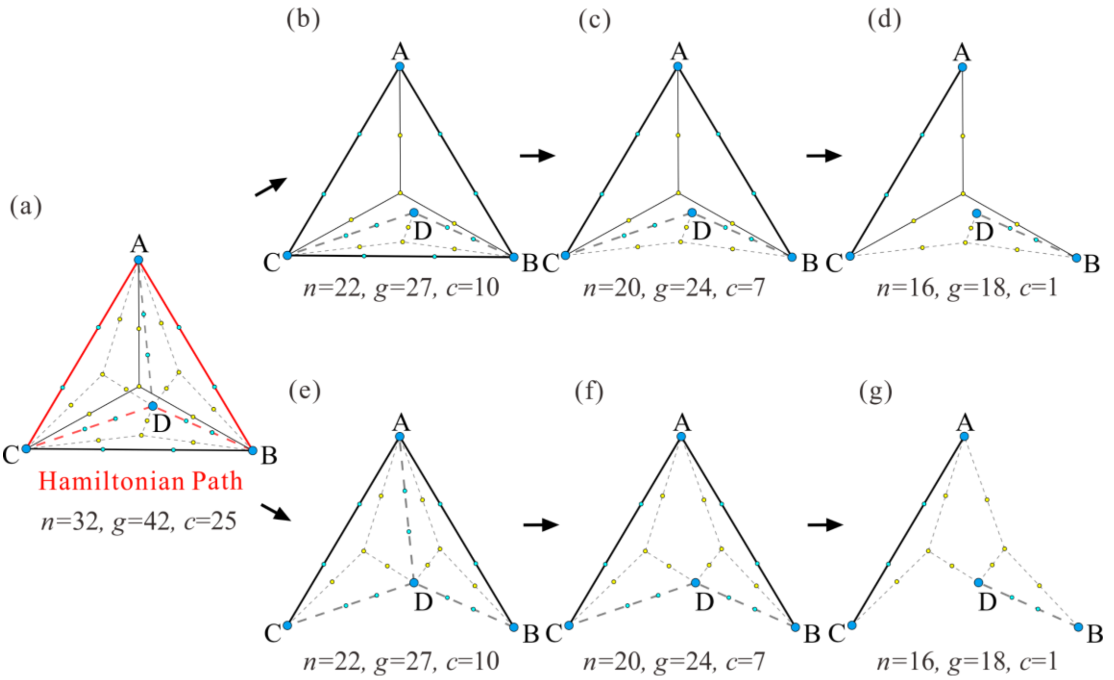

Fig. 4-10 Reduction process of 7*R*-based truncated tetratetrahedron. (a) The only 3D Hamiltonian path (illustrated by the red line). (b)-(d) Reduction process based on one half shell split by the Hamiltonian path. (e)-(g) Reduction process based on the other half shell.

Either edge AB or AC can be selected for removal without affecting the reduction result, as can the edges DB or DC. By mapping the proposed simplest constraint form obtained in Fig. 4-10(d) to the 7*R*-based mechanism, the simplest 7*R*-based truncated tetratetrahedron is demonstrated in Fig. 4-11, in which the 1-DOF synchronized radial motion is preserved. The above reduction remains applicable for the identical 7*R*-based truncated tetratetrahedron obtained in Fig. 4-6(b) due to the duality of the tetrahedron.

Thus, the reduction procedure in this section is the extension of Hamiltonian-path-based method proposed in Section 3.3, which can be summarized as follows: (1) obtain two topology half shells split by the Hamiltonian path; (2) remove redundant constraints inside the path; (3) remove redundant constraints on the contour edge of the path.

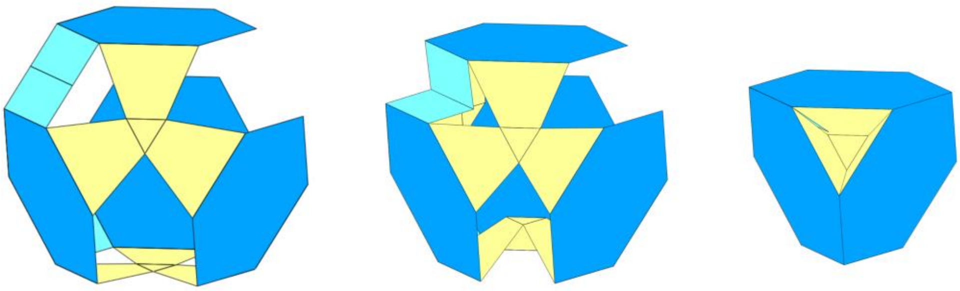

Fig. 4-11 Motion sequence of the simplest 7*R*-based truncated tetratetrahedron constructed by threefold-symmetric 7*R* loops.

4.3.2 Reduction of 7*R*-based Truncated Cuboctahedrons

For the 7*R*-based truncated cuboctahedron constructed by threefold-symmetric 7*R* loops, as shown in Fig. 4-12(a), the corresponding three-dimensional topological graph based on an octahedron is illustrated in Fig. 4-12(b), which has two distinct Hamiltonian paths.

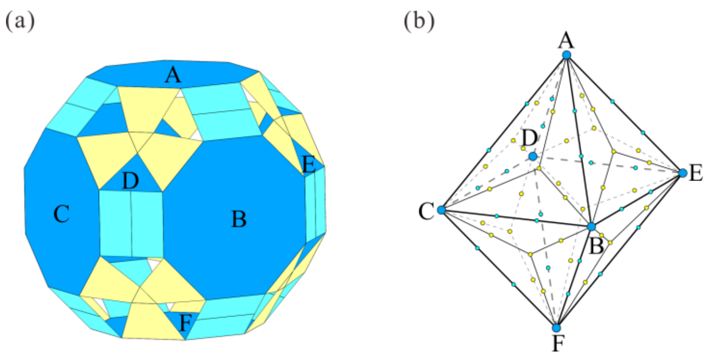

Fig. 4-12 7*R*-based truncated cuboctahedron constructed by threefold-symmetric 7*R* loops. (a) The original mechanism and (b) its corresponding topological graph based on a dual octahedron.

This original 7*R*-based mechanism with 62 links and 84 joints has overconstraints *c*=55, and one Hamiltonian path highlighted in red lines is given in Fig. 4-13(a). One half shell split by path 1 is shown in Fig. 4-13(b); then, the common edges BC, CA and AD among the four equilateral triangles can be sequentially removed (see Fig. 4-13(c)). For further removal, as shown in Fig. 4-13(d), contour edges FC, CD, DE and AB can be removed to construct a 1-DOF 7*R*-8*R*-8*R*-8*R*-7*R* open-loop assembly, in which the overconstraint is reduced from the original 55 to 1. If any link or joint is removed based on Fig. 4-13(d), then the original kinematics among platforms will change, which diverges the reduction premise. To minimize the degree of overconstraint, only two ends of the original Hamiltonian path are reserved in the simplest form. However, due to the octahedral symmetry, the reduction process based on the other half shell, as shown in Figs. 4-13(e) to (g), is the same as the case in Figs. 4-13(b) to (d).

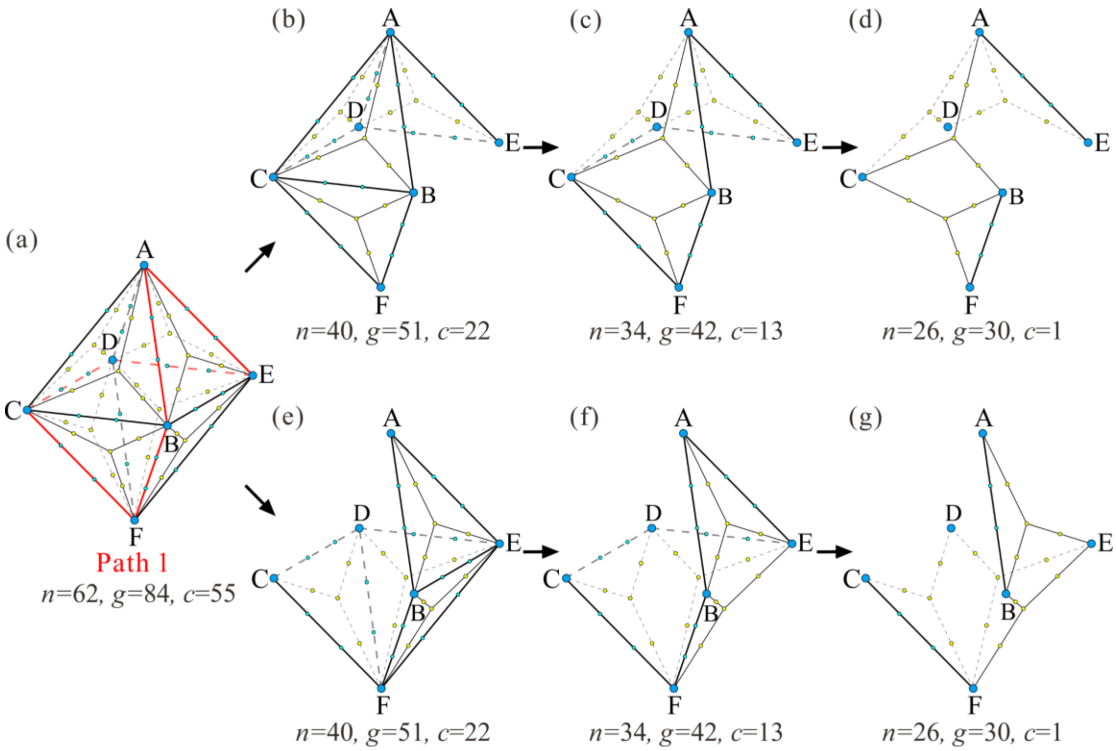

Fig. 4-13 Reduction process of the 7*R*-based truncated cuboctahedron based on path 1. (a) Hamiltonian path 1 of an octahedron (illustrated by the red line). (b)-(d) Reduction process based on one half shell split by path 1. (e)-(g) Reduction process based on the other half shell.

Furthermore, the other Hamiltonian path 2 is shown in Fig. 4-14(a), which also splits this octahedron into two congruent half shells with a threefold zigzag shape due to symmetry (see Figs. 4-14(b) and (e)). Subsequently, we can remove the common edges AB, BC and CA among the four equilateral triangles (see Fig. 4-14(c)). However, because four equilateral triangles are not connected in sequence in Fig. 4-14(b), we cannot obtain a simple open-loop assembly similar to Fig. 4-13(d); thus, we remove edges FC, CD and BE for further reduction. In fact, we can select either edge FB or edge FC in the original triangle BCF in addition to the common edge BC to remove, as can either edge DA or edge DC in the original triangle ACD and edge EA or edge EB in the original triangle ABE. In such a way, its overconstraints are reduced from the original 55 to 4, yet compared with the case in Fig. 4-13(d), this constraint path in Fig. 4-14(d) cannot be treated as the simplest one of this 7*R*-based mechanism, nor can the identical reduction result obtain from Figs. 4-14(e) to (g).

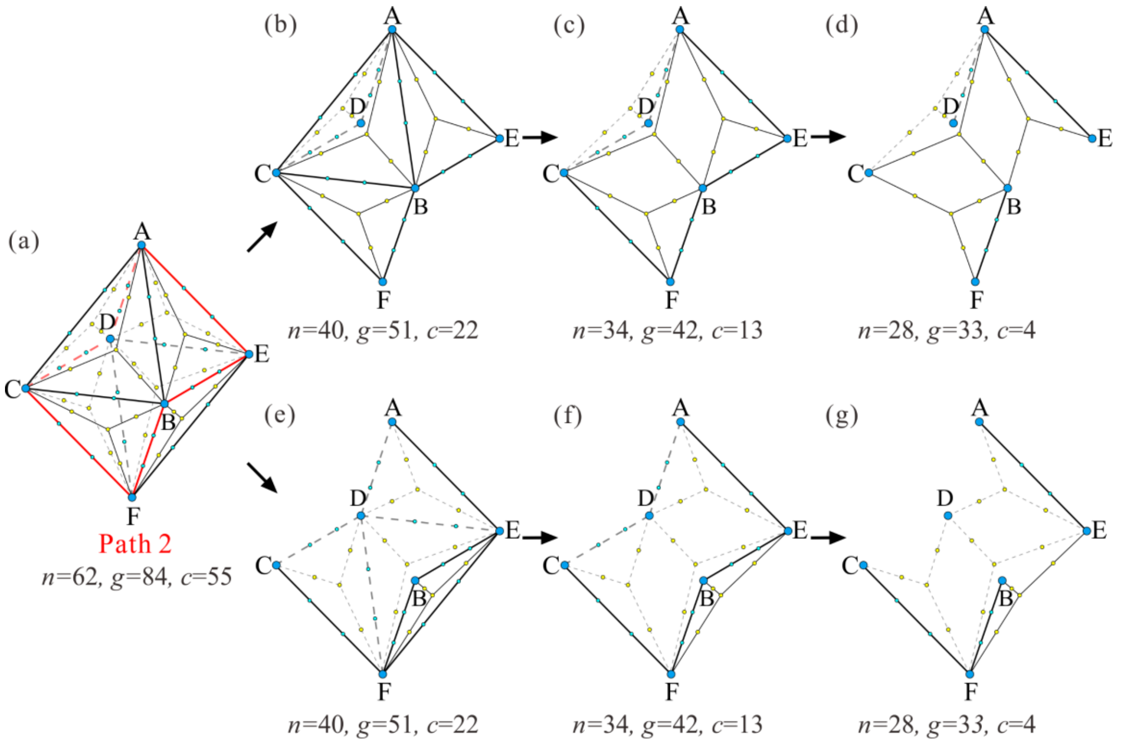

Fig. 4-14 Reduction process of the 7*R*-based truncated cuboctahedron based on path 2. (a) Hamiltonian path 2 of an octahedron (illustrated by the red line). (b)-(d) Reduction process based on one half shell split by path 2. (e)-(g) Reduction process based on the other half shell.

According to the simplest topological graph in Fig. 4-13(d), the simplest constraint form of the 7*R*-based truncated cuboctahedron constructed by threefold-symmetric 7*R* loops is obtained with equivalent kinematics, whose motion sequence is shown in Fig. 4-15. The original radial motion is reserved after the removal of redundant constraints.

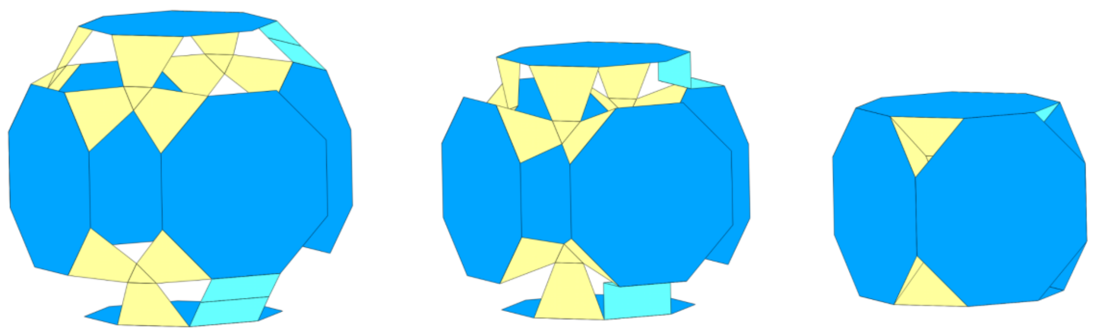

Fig. 4-15 Motion sequence of the simplest 7*R*-based truncated cuboctahedron constructed by threefold-symmetric 7*R* loops.

Moreover, for the 7*R*-based truncated cuboctahedron constructed by fourfold-symmetric 7*R* loops in Fig. 4-16(a), the corresponding 3D topological graph is based on a dual cube, see Fig. 4-16(b), in which each facet of this cube consists of four isosceles right triangles standing for a 1-DOF fourfold-symmetric assembly of 7*R* linkages.

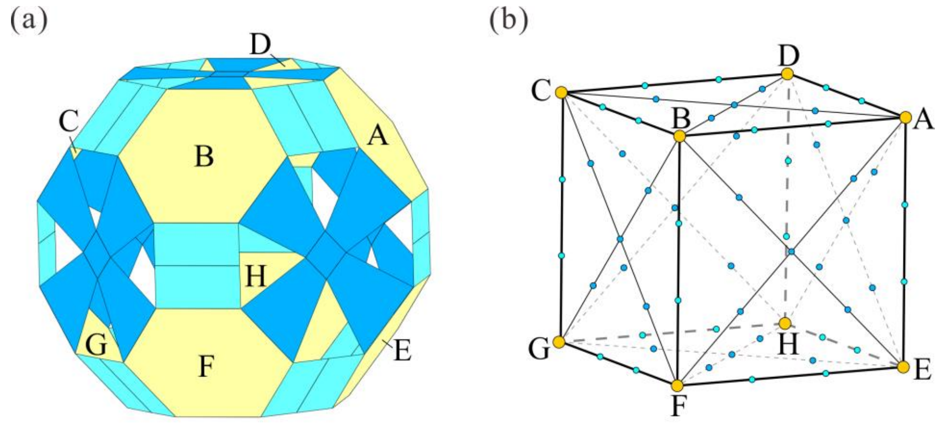

Fig. 4-16 7*R*-based truncated cuboctahedron constructed by fourfold-symmetric 7*R* loops. (a) The original mechanism and (b) its corresponding topological graph based on a dual cube.

This 7*R*-based mechanism constructed by 62 links and 84 joints has overconstraints of 55. Considering symmetry, only one 3D Hamiltonian path of this cube is given in Fig. 4-17(a). Based on one shell split by this Hamiltonian path in Fig.

4-17(b), we can remove the common shared edges BC and AD. Next, to ensure the reduction premise and guarantee the 1-DOF original kinematics, we further remove edges GC, CD and DH to obtain a 7*R*-7*R*-8*R*-7*R*-8*R*-7*R*-7*R* assembly, as shown in Fig. 4-17(d). Due to the fourfold symmetry and to ensure the sequenced connection of each spatial linkage, some 7*R* linkages cannot be reduced, which results in the overconstraint in this simplest constraint form being c=4. In addition, identical reduction results are presented in Figs. 4-17(e) to (g) based on the other shell.

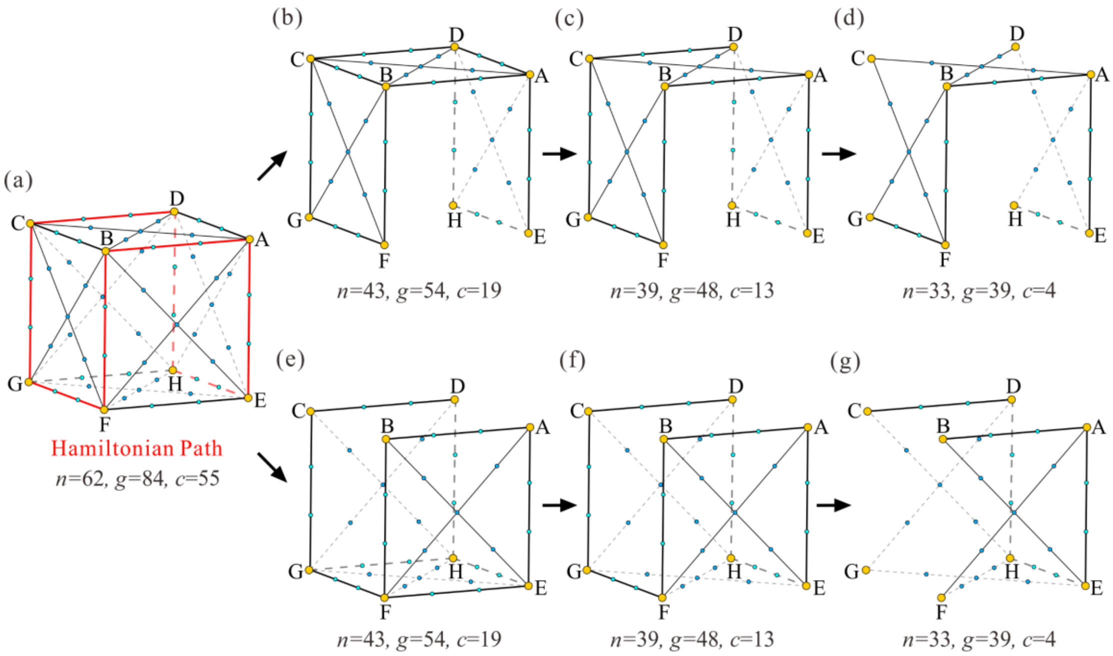

Fig. 4-17 Reduction process of the 7*R*-based truncated cuboctahedron constructed by fourfold-symmetric 7*R* loops. (a) The only Hamiltonian path of a cube (illustrated by the red line). (b)-(d) Reduction process based on one half shell split by the Hamiltonian path. (e)-(g) Reduction process based on the other half shell.

Mapping the simplest topological graph in Figs. 4-17(d) or (g) to the original 7*R*-based mechanism, the simplest constraint form of the ensuing truncated cuboctahedron is shown in Fig. 4-18, which reserves the original 1-DOF radial motion among six yellow platforms.

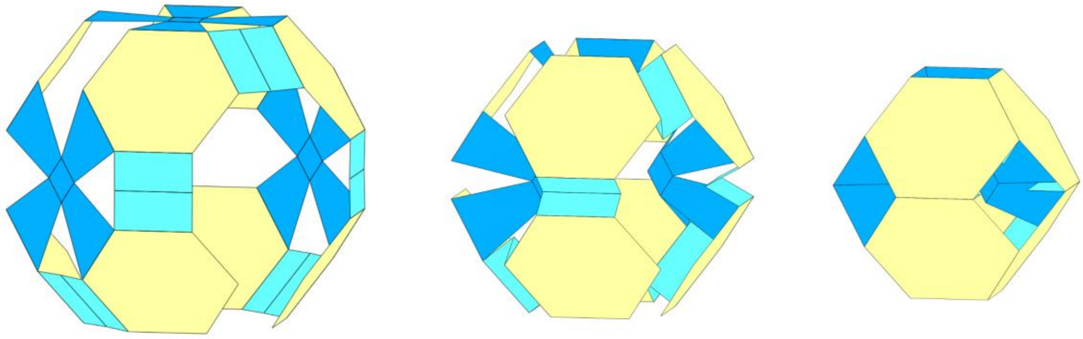

Fig. 4-18 Motion sequence of the simplest 7R-based truncated cuboctahedron constructed by fourfold-symmetric 7R loops.

4.3.3 Reduction of 7*R*-based Truncated Icosidodecahedrons

The proposed 7R-based truncated icosidodecahedron based on threefold-symmetric 7R loops is given in Fig. 4-19(a), together with its corresponding 3D topological graph in Fig. 4-19(b) based on a dual icosahedron. Similar to the Sarrus-based dodecahedral mechanism proposed in Section 3.3, there are 17 distinct Hamiltonian paths on an icosahedron that also bring a major challenge for the reduction of this 7R-based truncated icosidodecahedron.

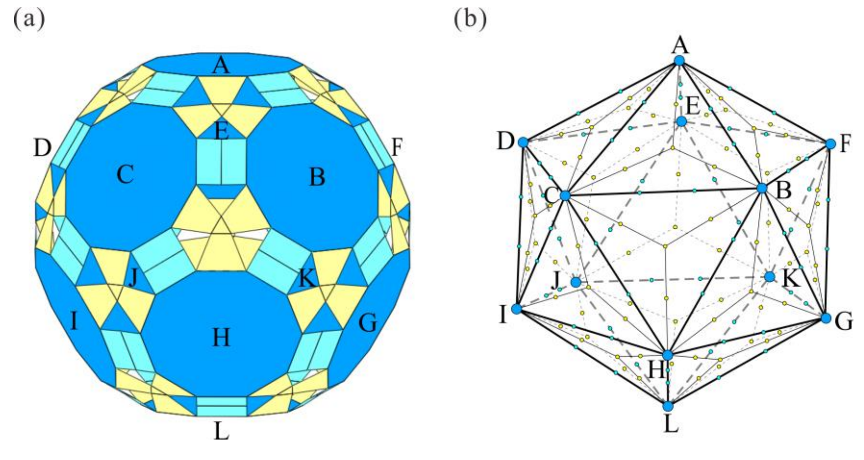

Fig. 4-19 7R-based truncated icosidodecahedron constructed by threefold-symmetric 7R loops. (a) The original mechanism and (b) its corresponding topological graph based on a dual icosahedron.

Nevertheless, the proposed reduction method can still be conducted by taking an arbitrary Hamiltonian path as an example, as shown in Fig. 4-20(a) in red lines. Two distinct half shells split by path 1 are given in Figs. 4-20(b) and (e), respectively. For the first case, the common edges CD, CI, IH, CH, HB, BG, GF, FK and KE are removed in Fig. 4-20(b), and the result is shown in Fig. 4-20(c). Under the reduction premise, several external contour edges of this shell are removed, in which the edges AC, HL and EG of the original path 1 are reserved. However, the overconstraints of this reduction are c=4. On the other hand, the common edges AB, AF, AE, DE, DJ, IJ, JL, KL and GL in Fig. 4-20(e) are removed (see Fig. 4-20(f)). Next, the redundant external contour edges are removed under the reduction premise, and only edges BC and GH are reserved; thus, the simplest constraint form is obtained in Fig. 4-20(g) with overconstraint c=1, in which a 7R-8R-8R-8R-8R-8R-8R-8R-8R-8R-7R assembly is obtained. Therefore, compared with the result in Fig. 4-20(d), the simplest constraint form generated from Hamiltonian path 1 is identified in Fig. 4-20(g), which is also an assembly of spatial 7R and 8R linkages, in which two 7R linkages are respectively set up as two ends of the open-loop assembly.

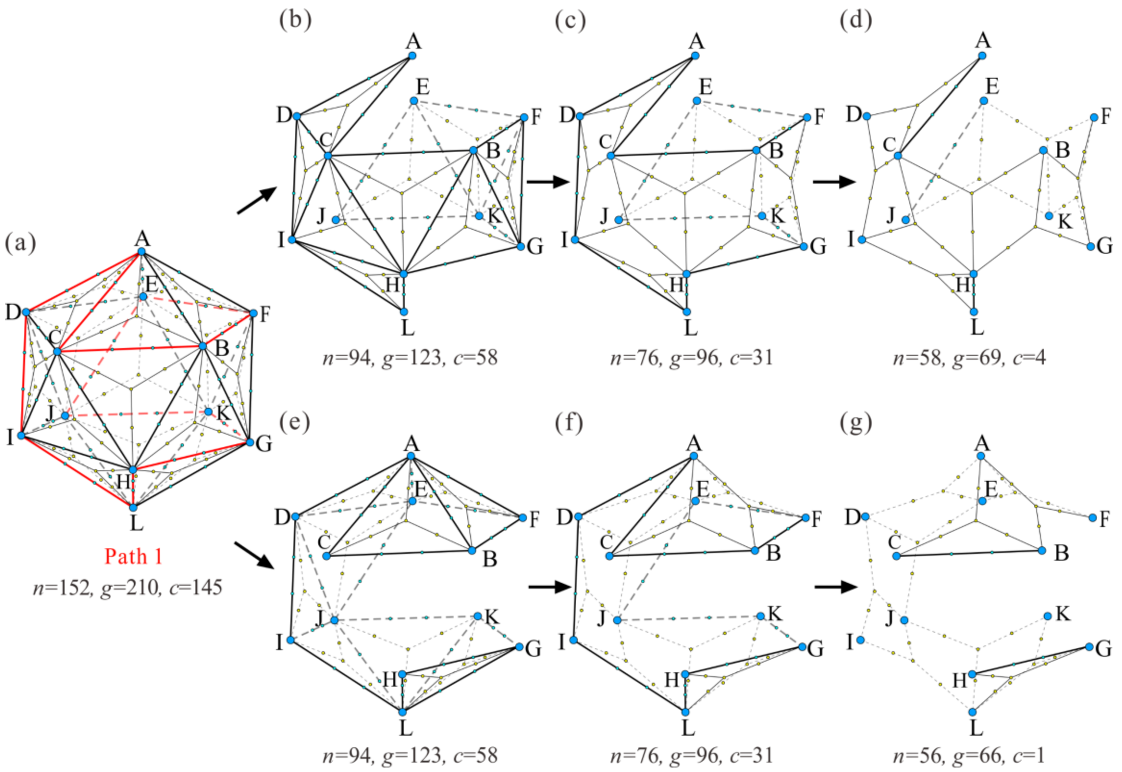

Fig. 4-20 Reduction process of the 7R-based truncated icosidodecahedron constructed by threefold-symmetric 7R loops. (a) Hamiltonian path 1 of an icosahedron (illustrated by the red line). (b)-(d) Reduction process based on one half shell split by path 1. (e)-(g) Reduction process based on the other half shell.

Referring to the simplest topological graph in Figs. 4-20(g), the simplest constraint form of the 7R-based truncated icosidodecahedron constructed by threefold-symmetric 7R loops is obtained without affecting the original kinematics. The mapped 7R-based mechanism is shown in Fig. 4-21, as well as the unchanged synchronized radial motion.

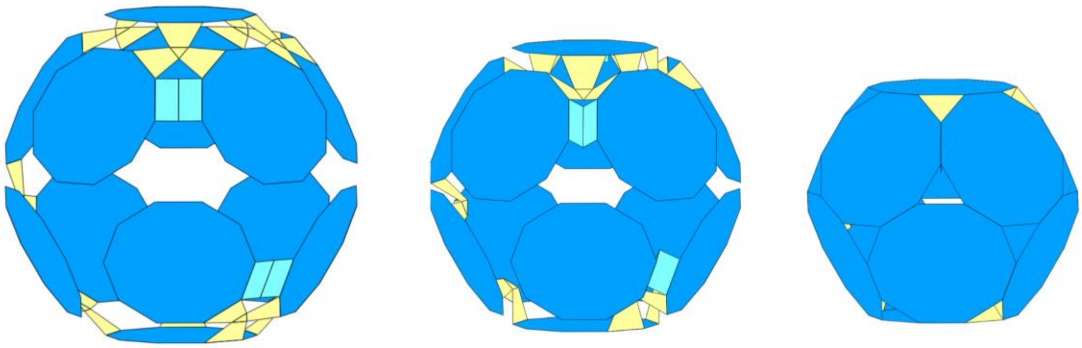

Fig. 4-21 Motion sequence of the simplest 7R-based truncated icosidodecahedron constructed by threefold-symmetric 7R loops.

Due to the complexity of Hamiltonian paths in a dual icosahedron, detailed investigations should be conducted to describe the possible solutions and obtain all the reduction results of this 7R-based truncated icosidodecahedron. Similar to the discussion of reduction for the Sarrus-based dodecahedral mechanism in Section 3.3, under the reduction premise, we can find the other four simplest topological graphs from paths 2 to 5 identified from all 17 Hamiltonian paths (divided into 34 half shells), which are organized and listed in Fig. 4-22. Compared with 145 overconstraints of the original mechanism, each effective reduction result in Fig. 4-22 has one DOF with only one overconstraint after removing the redundant constraints.

Based on these reduction results, the simplest constraint forms of the 7R-based truncated icosidodecahedron are shown in Fig. 4-23, each of which is a 7R-8R-8R-8R-8R-8R-8R-8R-8R-8R-8R-7R spatial assembly. All five simplest constraint forms reserve the original kinematic behaviours among platforms A to L.

Finally, the proposed 7R-based truncated icosidodecahedron based on fivefold-symmetric 7R loops is given in Fig. 4-24(a), as is its corresponding 3D topological graph in Fig. 4-24(b) based on a dual icosahedron. This 7R-based mechanism is constructed by 152 links and 210 joints with overconstraints of 145, in which these numbers are the same as that in the $7R$-based mechanism as given in Fig. 4-18, yet with a distinct mechanism topology.

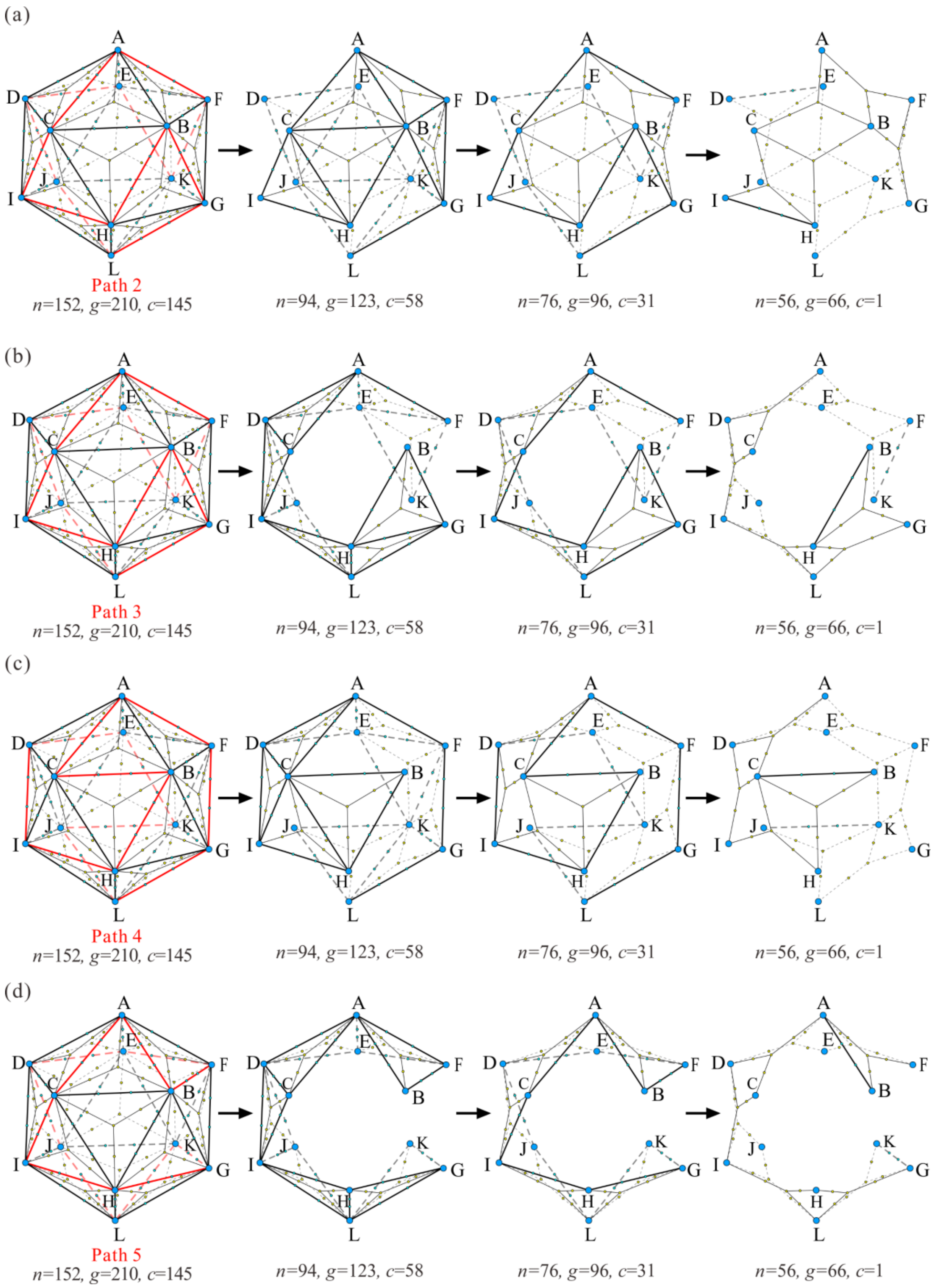

Fig. 4-22 Effective reduction results of this $7R$-based truncated icosidodecahedron based on Hamiltonian paths 2 to 5.

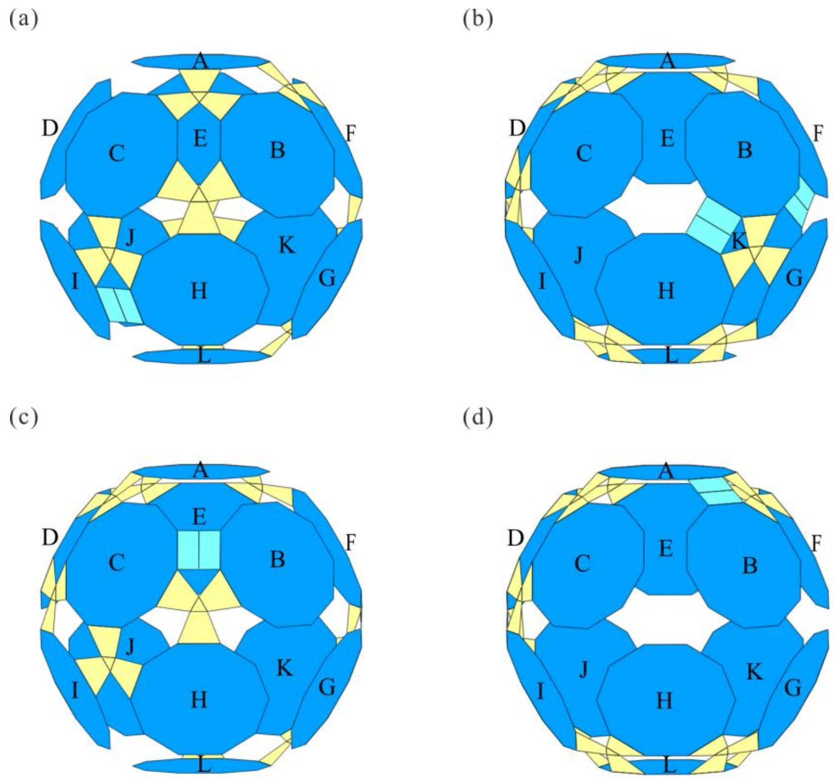

Fig. 4-23 Simplest 7*R*-based truncated icosidodecahedrons based on Hamiltonian paths 2 to 5.

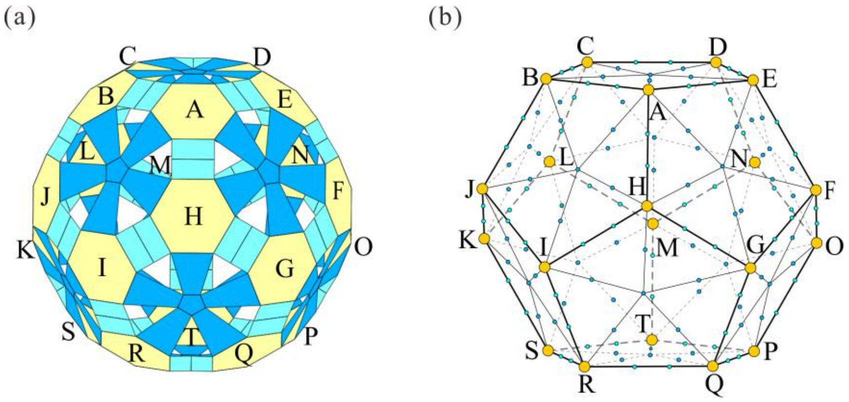

Fig. 4-24 7*R*-based truncated icosidodecahedron constructed by fivefold-symmetric 7*R* loops. (a) The original mechanism and (b) its corresponding topological graph based on a dual dodecahedron.

Referring to I_h symmetry, only one 3D Hamiltonian path (highlighted in red lines) of this dodecahedron is given in Fig. 4-25(a). Then, two identical half shells split by this path are given in Figs. 4-25(b) and (e). Based on one shell spilt by this Hamiltonian path in Fig. 4-25(b), we remove the common edges AE, GF OP, MT and KS among six pentagons, and the result is shown in Fig. 4-25(c). Sequentially, several external contour edges AB, EF, FO, PT, TS and S*R* can be removed under the reduction premise, as indicated in Fig. 4-25(d). However, the overconstraint of this reduction result is c=13 due to the generated 7*R*-7*R*-7*R*-8*R*-7*R*-7*R*-8*R*-7*R*-7*R*-8*R*-7*R*-7*R*-8*R*-7*R*-7*R*-8*R*-7*R*-7*R*-7*R* assembly, in which the remaining external contour edges have to be reversed to guarantee the 1-DOF kinematic equivalence among all platforms. On the other hand, an identical reduction process is illustrated in Figs. 4-25(e) to (g). Mapping the simplest topological graph in Figs. 4-25(d) to the original 7*R*-based mechanism, the simplest constraint form of these 7*R*-based truncated icosidodecahedrons is shown in Fig. 4-26, in which the overconstraints are greatly reduced from 145 to 13.

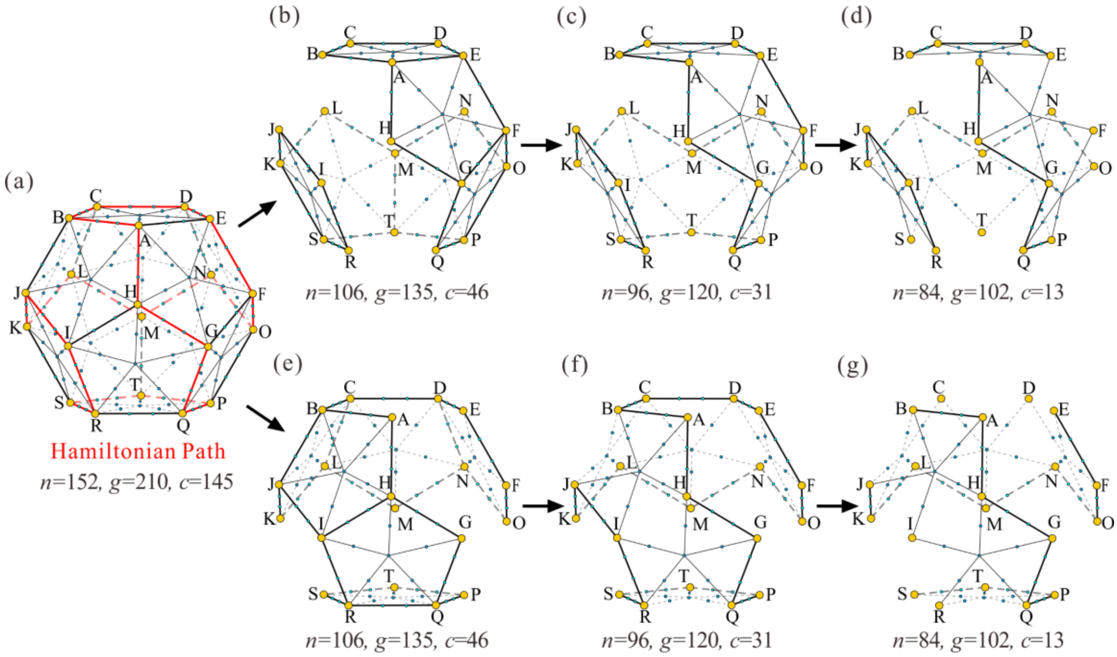

Fig. 4-25 Reduction process of the 7*R*-based truncated icosidodecahedron constructed by fivefold-symmetric 7*R* loops. (a) The only Hamiltonian path of a dodecahedron (illustrated by the red line). (b)-(d) Reduction process based on one half shell split by the Hamiltonian path. (e)-(g) Reduction process based on the other half shell.

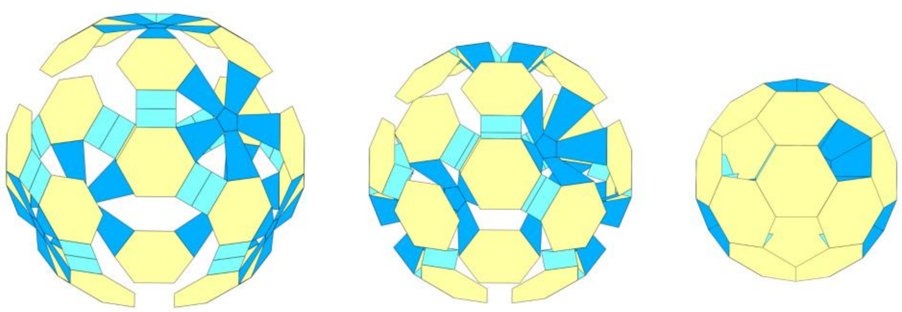

Fig. 4-26 Motion sequence of the simplest 7*R*-based truncated icosidodecahedrons constructed by fivefold-symmetric 7*R* loops.

4.4 Nonsimplest 7*R*-based Polyhedrons with Rotational Symmetries

Similar to the obtained nonsimplest forms of Sarrus-based polyhedral mechanisms, the nonsimplest 7*R*-based polyhedrons can also be explored by means of different rotational symmetries.

Based on the original truncated tetratetrahedron mechanism with c=25 as given in Fig. 4-9, by following C_3 symmetry and combining 7*R* and 8*R* linkages, the 7*R*-8*R* hybrid topological graph is taken as a nonsimplest example of truncated tetratetrahedron mechanism, see Figs. 4-27(a) and (b), in which three 7*R* linkages are arranged on the edges BC, CD and DB, respectively. Based on the screw analysis as given in Section 4.2.1 and the corresponding constraint graph as indicated in Figs. 4-27(c), the constraint matrix of this nonsimplest form can be organized as

$$\boldsymbol{M}_1' = \begin{bmatrix} \boldsymbol{M}_{11} & \boldsymbol{M}_{12} & \boldsymbol{M}_{13} \end{bmatrix} \tag{4-5}$$

with

$$\boldsymbol{M}_{11} = \begin{bmatrix} \mathbf{0} & \mathbf{0} & \mathbf{0} & \mathbf{0} & \mathbf{0} & \mathbf{0} & \mathbf{0} & \mathbf{0} & \mathbf{0} \\ \mathbf{0} & \mathbf{0} & \mathbf{0} & \mathbf{0} & \mathbf{0} & \mathbf{0} & \mathbf{0} & \mathbf{0} & \mathbf{0} \\ \mathbf{0} & \mathbf{0} & \mathbf{0} & \mathbf{0} & \mathbf{0} & \mathbf{0} & \mathbf{0} & \mathbf{0} & \mathbf{0} \\ \mathbf{0} & \mathbf{0} & \mathbf{0} & \mathbf{0} & \mathbf{0} & \mathbf{0} & \boldsymbol{S}_{35} & \boldsymbol{S}_{36} & \boldsymbol{S}_{37} \\ \boldsymbol{S}_{15} & \boldsymbol{S}_{16} & \boldsymbol{S}_{17} & \mathbf{0} & \mathbf{0} & \mathbf{0} & \mathbf{0} & \mathbf{0} & \mathbf{0} \\ \mathbf{0} & \mathbf{0} & \mathbf{0} & \boldsymbol{S}_{25} & \boldsymbol{S}_{26} & \boldsymbol{S}_{27} & \mathbf{0} & \mathbf{0} & \mathbf{0} \end{bmatrix}$$

$$\boldsymbol{M}_{12} = \begin{bmatrix} \boldsymbol{S}_{11}' & \boldsymbol{S}_{12}' & \mathbf{0} & \boldsymbol{S}_{14}' & \mathbf{0} & \boldsymbol{S}_{16}' & \mathbf{0} & \mathbf{0} & \mathbf{0} \\ -\boldsymbol{S}_{11}' & \mathbf{0} & \boldsymbol{S}_{13}' & -\boldsymbol{S}_{14}' & \boldsymbol{S}_{15}' & \mathbf{0} & \boldsymbol{S}_{21}' & \boldsymbol{S}_{22}' & \mathbf{0} \\ \mathbf{0} & \mathbf{0} & \mathbf{0} & \mathbf{0} & \mathbf{0} & \mathbf{0} & -\boldsymbol{S}_{21}' & \mathbf{0} & \boldsymbol{S}_{23}' \\ \mathbf{0} & \mathbf{0} & \mathbf{0} & \mathbf{0} & \mathbf{0} & \mathbf{0} & \mathbf{0} & \mathbf{0} & \mathbf{0} \\ \mathbf{0} & -\boldsymbol{S}_{12}' & -\boldsymbol{S}_{13}' & \mathbf{0} & -\boldsymbol{S}_{15}' & -\boldsymbol{S}_{16}' & \mathbf{0} & \mathbf{0} & \mathbf{0} \\ \mathbf{0} & \mathbf{0} & \mathbf{0} & \mathbf{0} & \mathbf{0} & \mathbf{0} & \mathbf{0} & -\boldsymbol{S}_{22}' & -\boldsymbol{S}_{23}' \end{bmatrix}$$

$$\boldsymbol{M}_{13} = \begin{bmatrix} \mathbf{0} & \mathbf{0} & \mathbf{0} & \boldsymbol{S}_{31}' & \mathbf{0} & \boldsymbol{S}_{33}' & \boldsymbol{S}_{34}' & \mathbf{0} & \boldsymbol{S}_{36}' \\ \boldsymbol{S}_{24}' & \mathbf{0} & \boldsymbol{S}_{26}' & \mathbf{0} & \mathbf{0} & \mathbf{0} & \mathbf{0} & \mathbf{0} & \mathbf{0} \\ -\boldsymbol{S}_{24}' & \boldsymbol{S}_{25}' & \mathbf{0} & -\boldsymbol{S}_{31}' & \boldsymbol{S}_{32}' & \mathbf{0} & -\boldsymbol{S}_{34}' & \boldsymbol{S}_{35}' & \mathbf{0} \\ \mathbf{0} & \mathbf{0} & \mathbf{0} & \mathbf{0} & -\boldsymbol{S}_{32}' & -\boldsymbol{S}_{33}' & \mathbf{0} & -\boldsymbol{S}_{35}' & -\boldsymbol{S}_{36}' \\ \mathbf{0} & \mathbf{0} & \mathbf{0} & \mathbf{0} & \mathbf{0} & \mathbf{0} & \mathbf{0} & \mathbf{0} & \mathbf{0} \\ \mathbf{0} & -\boldsymbol{S}_{25}' & -\boldsymbol{S}_{26}' & \mathbf{0} & \mathbf{0} & \mathbf{0} & \mathbf{0} & \mathbf{0} & \mathbf{0} \end{bmatrix}$$

Therefore, the rank of the constraint matrix $\boldsymbol{M}_1'$ is 26, which indicates the mobility of this nonsimplest mechanism is $m = n - \mathrm{rank}(\boldsymbol{M}_1') = 27 - 26 = 1$. Compared with the simplest truncated tetratetrahedron mechanism with c=1 as given in Fig. 4-11, the overconstraints of this nonsimplest form with C_3 symmetry is c=10.

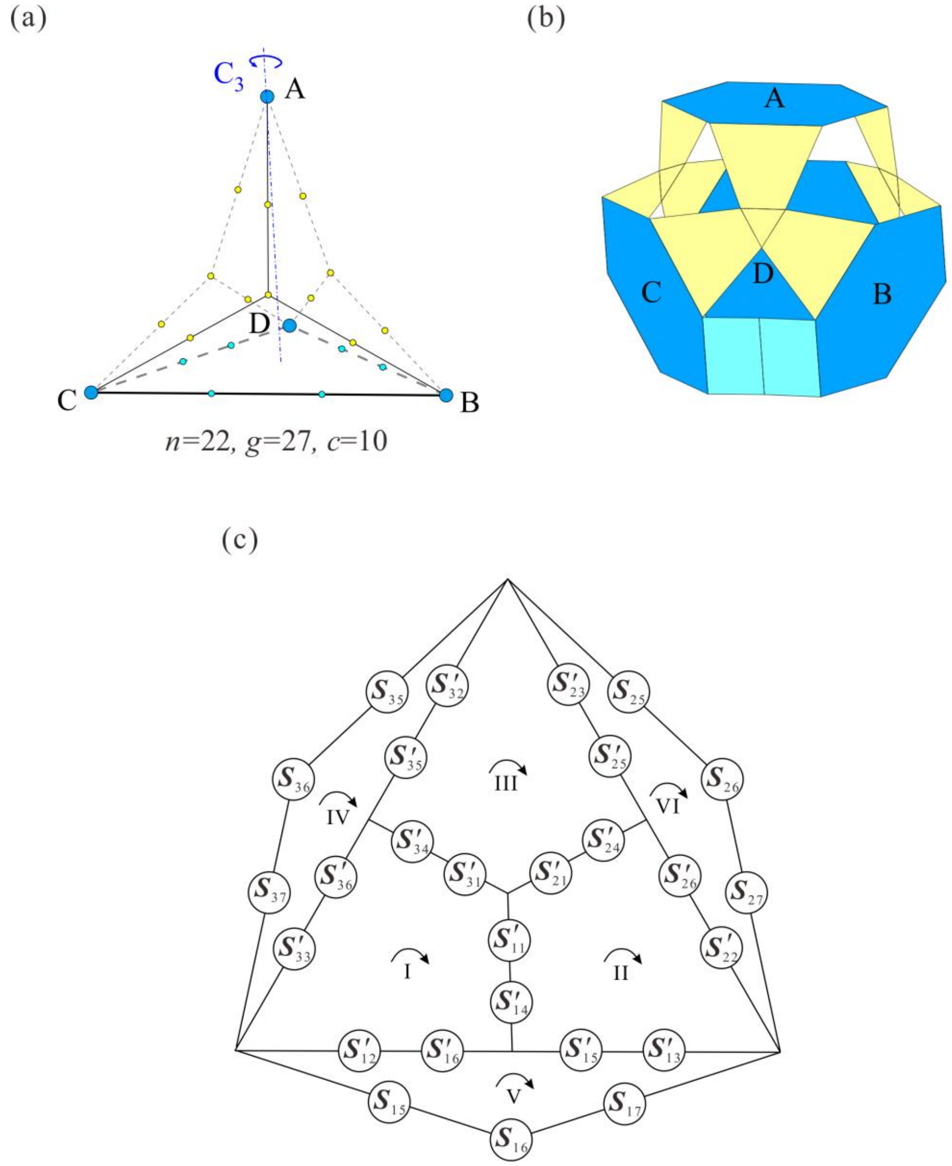

Fig. 4-27 Mobility analysis of the nonsimplest 7R-based truncated tetratetrahedron. (a) nonsimplest topological graph; (b) nonsimplest mechanism form; (c) the corresponding constraint graph.

Next, for the truncated cuboctahedron mechanism constructed by threefold-symmetric 7R loops, as shown in Fig. 4-12, if the cyan small vertices and the related lines in the topological graph are removed following C_4 symmetry, as shown in Fig. 4-

28(a), the reduction result is an assembly of 8*R* loops, and the corresponding 1-DOF mechanism in Fig. 4-28(b) also presents C_4 symmetry. On the other hand, if the yellow small vertices and the related lines are also removed following C_4 symmetry, see Figs. 4-28(c) and (d), yet a 5-DOF assembly of 9*R* loops occurs, which is clearly undesirable under the reduction premise.

By following rotational symmetry and combining 7*R* and 8*R* linkages, the 7*R*-8*R* hybrid topological graph is taken as a nonsimplest example, see Fig. 4-28(e), in which the C_3-axis passes through the centres of triangles ABC and DEF simultaneously. Then, the yellow small vertices in these two triangles together with cyan small vertices in lines AE, EB, BF, FC, CD and DA are removed following C_3 symmetry; thus, a close-loop 7*R*-8*R*-7*R*-8*R*-7*R*-8*R*-7*R*-8*R*-7*R*-8*R*-7*R*-8*R* assembly is obtained, as shown in Fig. 4-28(f), in which the 7*R* linkages are arranged around triangles ABC and DEF to match the C_3 symmetry. Thus, based on the rotational symmetries, the 8*R* assembly with C_4 symmetry and 7*R*-8*R* hybrid assembly can be obtained as two nonsimplest examples of this truncated cuboctahedron mechanism, in which the overconstraints are reduced from the original 55 to 19, instead of the only overconstraint in its simplest form, as given in Fig. 4-13(d). The nonsimplest form is not unique; in addition to the mentioned C_4 and C_3 symmetries, different symmetries can be utilized to construct various nonsimplest forms, such as using C_2 symmetry to obtain a plane-symmetry mechanism.

On the other hand, referring to the truncated cuboctahedron mechanism constructed by fourfold-symmetric 7*R* loops as shown in Fig. 4-16, based on C_4 symmetry, the entire removal of all edges in the cubic topological graph also results in a 1-DOF 8*R* assembly, see Figs. 4-29(a) and (b), in which overconstraints are reduced from the original 55 to 19. Similar to the reduction shown in Figs. 4-28(e) and (f), the reduction following C_4 symmetry can be applied to this mechanism. As shown in Fig. 4-29(c), the blue small vertices in two squares ABCD and EFGH are removed, as well as the cyan blue small vertices in edges AE, BF, CG and DH; thus, a C_4 symmetry topological graph and the corresponding mechanism are indicated in Figs. 4-29(c) and (d), respectively. Thus, the 7*R* linkages are arranged along the reserved edges, and four 8*R* linkages are sequentially arranged between 7*R* linkages to present the C_4 symmetry, which is also a close-loop 7*R*-8*R* hybrid assembly with c=23.

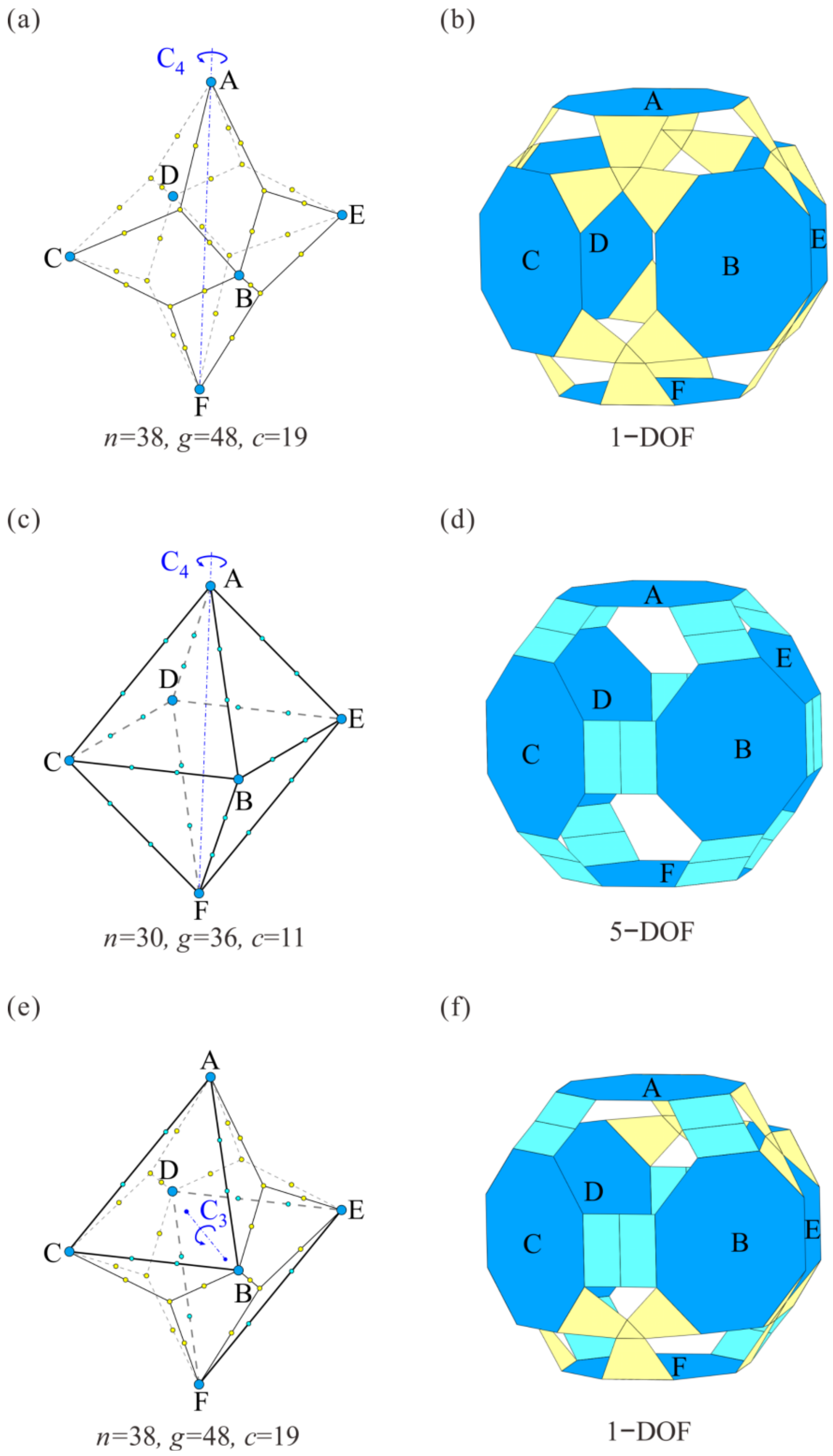

Fig. 4-28 Nonsimplest truncated cuboctahedron mechanisms constructed by threefold-symmetric 7*R* loops. (a) The 8*R* topological graph following C_4 symmetry and (b) the corresponding 1-DOF mechanism; (c) the 9*R* topological graph following C_4 symmetry and (d) the corresponding 5-DOF mechanism; (e) the 7*R*-8*R* hybrid topological graph following C_2 symmetry and (f) the corresponding 1-DOF mechanism.

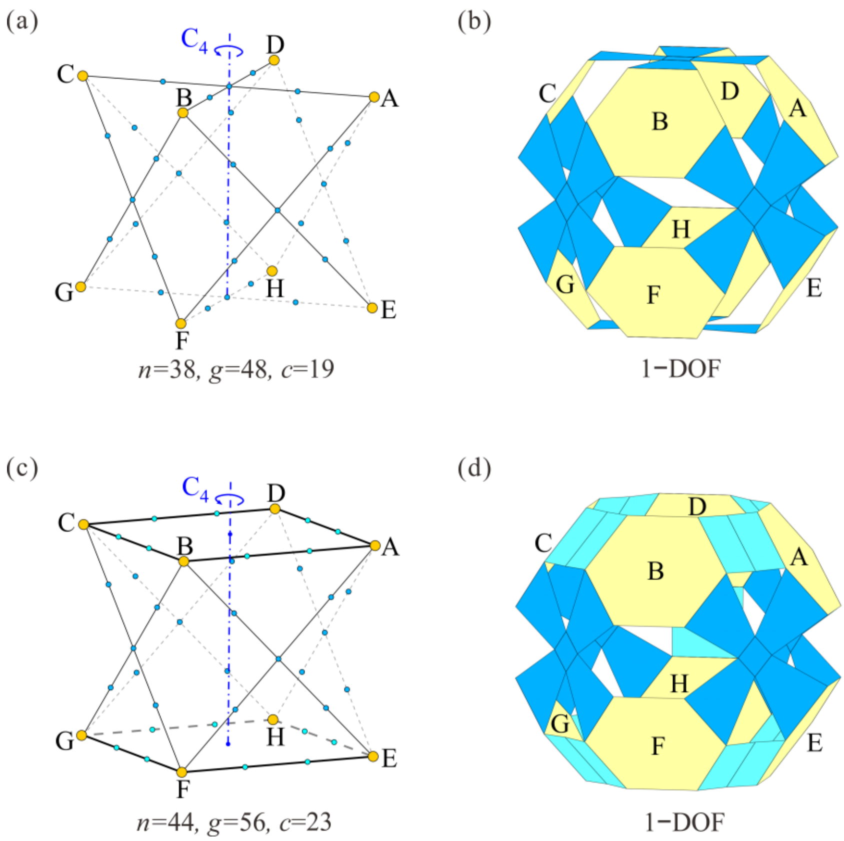

Fig. 4-29 Nonsimplest truncated cuboctahedron mechanisms constructed by fourfold-symmetric 7*R* loops. (a) The 8*R* topological graph following C_4 symmetry and (b) the corresponding 1-DOF mechanism; (c) the 7*R*-8*R* hybrid topological graph following C_4-symmetry and (d) the corresponding 1-DOF mechanism.

Finally, using rotational symmetry, nonsimplest truncated icosidodecahedron mechanisms can also be obtained. For the mechanism constructed by threefold-symmetric 7*R* loops, a 1-DOF 8*R* assembly can also be obtained by removing all edges in its original icosahedral topological graph following C_4 symmetry (see Figs. 4-30(a) and (b)). Then, similar to the nonsimplest topological graph given in Fig. 4-28(c), a 7*R*-8*R* hybrid closed-loop assembly is obtained in Fig. 4-30(c) following C_3 symmetry, i.e., a 1-DOF 7*R*-8*R*-7*R*-8*R*-7*R*-8*R*-7*R*-8*R*-8*R*-7*R*-8*R*-7*R*-8*R*-7*R*-8*R*-7*R*-8*R*-7*R*-8*R*-7*R*-8*R*-7*R*-8*R*-7*R*-8*R* assembly, also showing the corresponding 1-DOF mechanism with C3 symmetry, as given in Fig. 4-30(d).

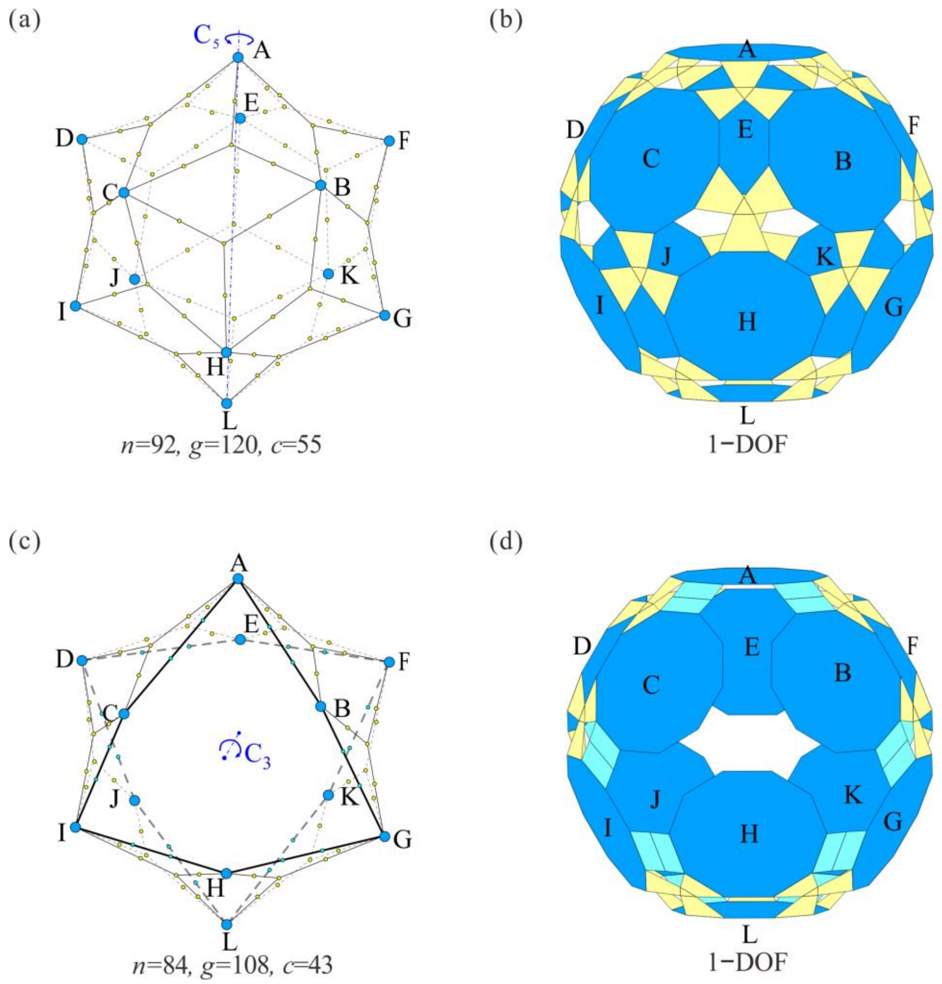

Fig. 4-30 Nonsimplest truncated icosidodecahedron mechanism constructed by threefold-symmetric 7*R* loops. (a) The 8*R* topological graph following C_5 symmetry and (b) the corresponding 1-DOF mechanism; (c) the 7*R*-8*R* hybrid topological graph following C_3 symmetry and (d) the corresponding 1-DOF mechanism.

For the truncated icosidodecahedron mechanism constructed by fivefold-symmetric 7*R* loops, a 1-DOF 8*R* assembly is obtained in Figs. 4-31(a) and (b) by removing all original dodecahedral edges following C_5 symmetry, which results in overconstraints from the original 145 to 55. Additionally, using C_5 symmetry, ten 7*R* linkages are reserved at two pentagons ABCDE and RSTPQ. Then, the remaining elements are all 8*R* linkages arranged with C_5 symmetry. The other nonsimplest form is obtained in Fig. 4-31(c), as well as the corresponding 1-DOF 7*R*-8*R* hybrid mechanism with c=57, as shown in Fig. 4-31(d).

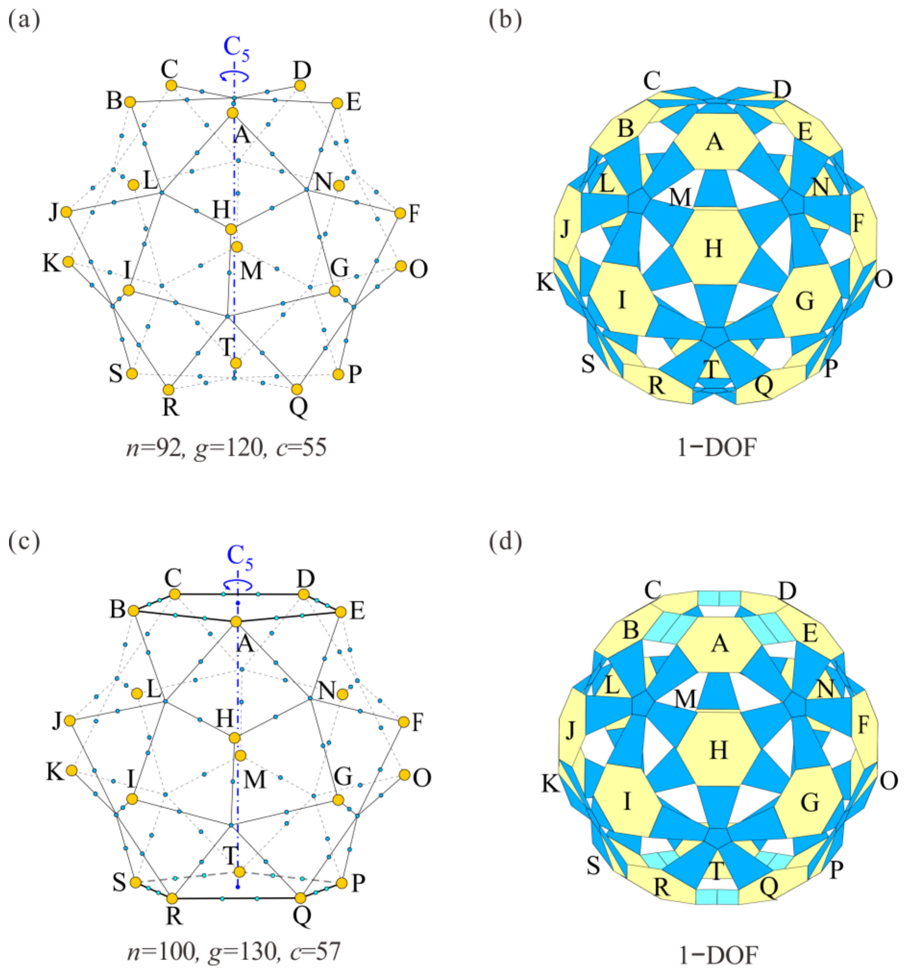

Fig. 4-31 Nonsimplest truncated icosidodecahedron mechanism constructed by fivefold-symmetric 7*R* loops. (a) The 8*R* topological graph following C_5 symmetry and (b) the corresponding 1-DOF mechanism; (c) the 7*R*-8*R* hybrid topological graph following C_3 symmetry and (d) the corresponding 1-DOF mechanism.

4.5 Conclusions and Discussion

In summary, a family of 7*R*-based Archimedean polyhedrons with 1-DOF synchronized radial motion has been designed, as well as paired transformations among Archimedean and Platonic polyhedrons. Moreover, three types of transformable polyhedrons with distinct symmetries, i.e., T_d, O_h and I_h, are constructed, and the corresponding prototypes are fabricated to verify their deployable transformability and kinematic properties. As a further exploration of the reduction strategy, the overconstraint reductions of those 7*R*-based polyhedrons are investigated based on the Hamiltonian-path-based method, in which the Hamiltonian paths of all five Platonic polyhedrons are discussed in detail. Notably, the proposed nonsimplest polyhedrons is considered to possess appropriate stiffness to satisfy practical engineering requirements. Due to the identical threefold-symmetric spatial 9*R* linkage as the outside frame, we can combine the threefold-symmetric 7*R* loop in Fig. 4-1(c) and the S4R-synthesized mechanism in Fig. 2-3(c) when embedding the mechanism units into the polyhedral surface, to obtain the integrated design of DPMs without affecting the kinematics of the polyhedral platforms.

The transformable solutions among eleven Archimedean and all five Platonic polyhedrons, except the snub cube and snub dodecahedron without symmetry, have been investigated in this chapter. This research solves the difficult problem of transformable polyhedrons by means of a kinematic strategy, i.e., multi-symmetric 7*R* loops, thus realizing richer transformable solutions. Future work will explore other possible polyhedral pairs and the corresponding kinematic solutions by considering wider polyhedral symmetry. This work also presents a kinematic strategy to create mechanism-based metamaterial cells, and their tessellation approach and advanced applications in multifunctional and programmable metamaterials should be developed extensively.

Chapter 5 Achievements and Future Works

This dissertation focuses on the mechanism kinematics rather than the dynamics. Its goal is to propose the design method of 1-DOF deployable polyhedral mechanisms with synchronized radial motion by integrating spherical, overconstrained and spatial linkages, reveal the paired polyhedral transformations among Platonic and Archimedean polyhedrons, and present an overconstraint reduction strategy by removing redundant links and joints without affecting the original kinematics. This chapter summarizes the main achievements of this dissertation and highlights opportunities for future work.

5.1 Main Achievements

- **1-DOF Deployable S4*R*-based Polyhedrons**

First, a 1-DOF S4*R*-synchronized mechanism was constructed by embedding three pairs of spherical 4*R* linkages into a spatial 9*R* linkage to provide kinematic constraints. Embedding the proposed S4*R*-synchronized mechanism cells into the surface of Archimedean polyhedrons yielded three 1-DOF transformable S4*R*-based polyhedral mechanisms with distinct symmetries, for which corresponding prototypes have been fabricated to verify their kinematic properties. Referring to the dimensional shortening operations, structural variations of S4*R*-based polyhedrons with mechanism topology isomorphism have been demonstrated to realize all nine polyhedral transformations with different volumetric deployable ratios. The overconstraint reductions of the proposed polyhedrons have been investigated by analysing the constraint conditions and then removing the redundant constraints.

The kinematic model and structural variations of 1-DOF S4*R*-based deployable polyhedrons were presented in Chapter 2. This technique offers a new approach to construct DPMs based on origami mechanisms. The outcomes widen the design concept and structural variations of deployable polyhedral mechanisms.

- **Sarrus-based Deployable Polyhedral Mechanisms**

Second, an innovative and intuitive approach for constructing Sarrus-based deployable polyhedral mechanisms based on three Platonic solids has been demonstrated. Through integrating the Sarrus linkages into a Platonic solid after the expansion operation, deployable tetrahedral, cubic and icosahedral mechanisms have been synthesized and constructed that enable 1-DOF synchronous radial motion, in which three paired polyhedral transformations between Platonic and Archimedean polyhedrons have been revealed. For mobility analysis of Sarrus-based DPMs, an equivalent analysis for multiloop mechanisms was conducted by regarding each Sarrus linkage as an equivalent prismatic joint. Moreover, this dissertation proposes a novel Hamiltonian-path-based method that can greatly reduce the number of overconstraints while maintaining the kinematic properties of Sarrus-based DPMs. The simplest constraint paths of each Sarrus-based DPM have been proposed and identified by introducing the corresponding Hamiltonian path and then removing redundant links and revolute joints.

The construction method, kinematic analysis and overconstraint reduction are presented in Chapter 3. This novel method not only establishes a foundation for further research into deployable polyhedrons but also can inspire a reduction strategy for multiloop overconstrained mechanisms.

- **7*R*-based Archimedean Polyhedrons and Symmetric Transformations**

Finally, a family of 1-DOF 7*R*-based Archimedean polyhedrons with 1-DOF synchronized radial motion was designed, and the paired transformations between Archimedean and Platonic polyhedrons were revealed and identified. Moreover, three types of transformable polyhedrons with T_d, O_h and I_h symmetries have been proposed and fabricated. Regardless of which transformation, the original symmetry is always preserved in the continuous folding process of 7*R*-based polyhedrons. The transformable solutions are applied to eleven Archimedean and all five Platonic polyhedrons (excluding the snub cube and snub dodecahedron without symmetry), having been investigated and discussed in detail. As a further extension of the proposed Hamiltonian-path reduction strategy, the overconstraint reductions of those 7*R*-based polyhedrons have also been investigated with kinematic equivalence, in which the Hamiltonian paths of all five Platonic polyhedrons are discussed in detail.

The approach of design, transformation, control and reduction of the 7*R*-based Archimedean polyhedrons has been presented in Chapter 4. This research provides an opportunity to create deployable and transformable polyhedrons that enhance the development of deployable mechanisms and multifunctional metamaterials.

5.2 Future Works

The research reported in this dissertation establishes a rational design principle of deployable polyhedral mechanisms using different mechanism types as constructed units. To enhance the practical usage of the proposed DPMs, several potential topics can be further explored.

First, in our work on polyhedral construction, we adopted elemental linkages, i.e., spherical $4R$ linkages, Sarrus linkages, and spatial $7R$ and $9R$ linkages, as the mechanism cells to synthesize DPMs. Future studies can explore various types of mechanism cells, such as other spherical linkages and spatial $8R$ linkages. In addition to the deployable Platonic and Archimedean polyhedrons proposed in this dissertation, the 1-DOF mechanism topology can be further investigated to design other deployable mechanisms in various regular and irregular polyhedral groups, such as Johnson solids, prisms and antiprisms, that could facilitate their applications in various engineering fields.

Second, for polyhedral transformations, kinematic solutions with T_d, O_h and I_h symmetries have been proposed. Future work can explore other possible polyhedral pairs and the corresponding kinematic solutions by considering wider polyhedral symmetry. Furthermore, in the kinematics of the polyhedral mechanism, the focus is on the 1-DOF mechanism topology. In addition to the structural variations reported in this dissertation, relative geometric conditions would be properly analysed and adjusted to meet specific engineering requirements.

Third, the degrees of overconstraint have been greatly reduced with the assistance of polyhedral Hamiltonian paths, yet the nonoverconstrained form of the polyhedral mechanism is still a difficult kinematic problem in mechanism, which requires further investigations by means of kinematic and mathematical theory. Referring to the reduction approach, the simplified form (nonsimplest form) of multiloop polyhedral mechanisms can also be selected and obtained for specific applications, such as deployable mechanisms that need appropriate actuation and stiffness without affecting the kinematics. Hence, future studies can explore the dynamics and stiffness analysis to evaluate the reduction effect and motion stability.

Finally, this research also introduces a kinematic strategy to yield three-dimensional metamaterials with enriched properties, such as a large deformation range, Poisson’s ratios of -1 and negative thermal expansion. Furthermore, their tessellation approach and advanced applications in multifunctional and programmable metamaterials can be extensively developed. To achieve functional diversity and tunability of polyhedral metamaterials with a large number of construction cells, actuating materials that can produce deformation responses based on external stimuli such as magnetic, electric, light, or humidity fields can be implanted into the synchronous polyhedral system. Thus, future studies can explore the tessellation strategy, actuating materials and control method of polyhedral metamaterials.

References

[1] Zhang X, Nie R, Chen Y, et al. Deployable structures: structural design and static/dynamic analysis[J]. Journal of Elasticity, 2021: 1-37.

[2] Mira L A, Thrall A P, De Temmerman N. Deployable scissor arch for transitional shelters[J]. Automation in Construction, 2014, 43: 123-131.

[3] Lee T-U, Gattas J M. Geometric design and construction of structurally stabilized accordion shelters[J]. Journal of Mechanisms Robotics, 2016, 8(3): 031009.

[4] Kassabian P, You Z, Pellegrino S. Retractable roof structures[J]. Proceedings of the Institution of Civil Engineers-Structures Buildings, 1999, 134(1): 45-56.

[5] Thrall A P, Adriaenssens S, Paya-Zaforteza I, et al. Linkage-based movable bridges: Design methodology and three novel forms[J]. Engineering Structures, 2012, 37: 214-223.

[6] Lederman G, You Z, Glišić B. A novel deployable tied arch bridge[J]. Engineering Structures, 2014, 70: 1-10.

[7] Stachel H. The heureka-polyhedron[C]. Proceedings of the Proc Conf Intuitive Geometry, Szeged Coll Math Soc J Bolyai, 1991: 447-459.

[8] Hedgepeth J M. Structures for remotely deployable precision antennas[J]. Langley Research Center, Earth Science Geostationary Platform Technology, 1989: 109-128.

[9] Guest S, Pellegrino S. A new concept for solid surface deployable antennas[J]. Acta Astronautica, 1996, 38(2): 103-113.

[10] Cui J, Huang H, Li B, et al. A novel surface deployable antenna structure based on special form of Bricard linkages[C]. Proceedings of the Advances in Reconfigurable Mechanisms and Robots I, London, Springer, 2012: 783-792.

[11] Santiago-Prowald J, Baier H. Advances in deployable structures and surfaces for large apertures in space[J]. CEAS Space Journal, 2013, 5: 89-115.

[12] Xu Y, Guan F-L. Structure–electronic synthesis design of deployable truss antenna[J]. Aerospace Science Technology, 2013, 26(1): 259-267.

[13] Miura K. Triangles and quadrangles in space[C]. Proceedings of the 50th Symposium of the International Association for Shell and Spatial Structures, Editorial Universitat Politècnica de València, 2009: 27-38.

[14] Dufour L, Owen K, Mintchev S, et al. A drone with insect-inspired folding wings[C]. Proceedings of the 2016 IEEE/RSJ International Conference on Intelligent Robots and Systems (IROS), Ieee, 2016: 1576-1581.

[15] Kjærgaard A, Leon G R, Chterev K. Team effectiveness and person-environment adaptation in an analog lunar habitat[J]. Aerospace Medicine Human Performance, 2022, 93(2): 70-78.

[16] Liu S, Lv W, Chen Y, et al. Deployable prismatic structures with rigid origami patterns[J]. Journal of Mechanisms Robotics, 2016, 8(3): 031002.

[17] Hawkes E, An B, Benbernou N M, et al. Programmable matter by folding[J]. Proceedings of the National Academy of Sciences, 2010, 107(28): 12441-12445.

[18] Koh J-S, Cho K-J. Omega-shaped inchworm-inspired crawling robot with large-index-and-pitch (LIP) SMA spring actuators[J]. IEEE/ASME Transactions On Mechatronics, 2012, 18(2): 419-429.

[19] Belke C H, Paik J. Mori: a modular origami robot[J]. IEEE/ASME Transactions on Mechatronics, 2017, 22(5): 2153-2164.

[20] Rus D, Tolley M T. Design, fabrication and control of origami robots[J]. Nature Reviews Materials, 2018, 3(6): 101-112.

[21] Miyashita S, Guitron S, Li S, et al. Robotic metamorphosis by origami exoskeletons[J]. Science Robotics, 2017, 2(10): eaao4369.

[22] Shang H, Wei D, Kang R, et al. Gait analysis and control of a deployable robot[J]. Mechanism and machine theory 2018, 120: 107-119.

[23] Gu Y, Chen Y. Origami cubes with one-DOF rigid and flat foldability[J]. International Journal of Solids Structures, 2020, 207: 250-261.

[24] Kiper G, Söylemez E, Kişisel A Ö. A family of deployable polygons and polyhedra[J]. Mechanism and Machine Theory, 2008, 43(5): 627-640.

[25] Yang F, Chen Y, Kang R, et al. Truss transformation method to obtain the non-overconstrained forms of 3D overconstrained linkages[J]. Mechanism and Machine Theory, 2016, 102: 149-166.

[26] Meng Q, Xie F, Tang R, et al. Deployable polyhedral mechanisms with radially reciprocating motion based on novel basic units and an additive-then-subtractive design strategy[J]. Mechanism and Machine Theory, 2023, 181: 105174.

[27] Yang F. Truss method for kinematic analysis of 3D overconstrained linkages and design of transformable polyhedrons[D]. Tianjin University, 2018.

[28] Wei G. Geometric analysis and theoretical development of deployable polyhedral mechanisms[D]. King's College London, United Kingdom, 2011.

[29] Gu Y, Chen Y. Deployable origami polyhedrons with one-DOF radial motion[J]. Mechanism and Machine Theory, 2023, 184: 105293.

[30] Sarrus P. Note sur la transformation des mouvements rectilignes alternatifs, en mouvements circulaires, et reciproquement[J]. Comptes Rendus, Acad Sci, Paris, 1853, 36: 1036-1038.

[31] Cao W A, Zhang D, Ding H. A novel two-layer and two-loop deployable linkage with accurate vertical straight-line motion[J]. Journal of Mechanical Design, 2020, 142(10): 103301.

[32] Chen Y, Gu Y. Review on origami kinematics[J]. 2022, 52: 154-197.

[33] Wei G, Dai J S. A spatial eight-bar linkage and its association with the deployable platonic mechanisms[J]. Journal of Mechanisms Robotics, 2014, 6(2): 021010.

[34] Wei G, Chen Y, Dai J S. Synthesis, mobility, and multifurcation of deployable polyhedral mechanisms with radially reciprocating motion[J]. Journal of mechanical design, 2014, 136(9): 091003.

[35] Wei G, Dai J. Synthesis and construction of a family of one-dof highly overconstrained deployable polyhedral mechanisms (DPMs)[C]. Proceedings of the International Design Engineering Technical Conferences and Computers and Information in Engineering Conference, American Society of Mechanical Engineers, 2012: 615-626.

[36] Zhang Y, Li M, Chen Y, et al. Thick-panel origami-based parabolic cylindrical antenna[J]. Mechanism and Machine Theory, 2023, 182: 105233.

[37] Liu J, Xu Y, Liu Y, et al. Configuration Design of Single-Loop Non-overconstrained Mechanism with Inactive Joints[J]. Iranian Journal of Science Technology, Transactions of Mechanical Engineering, 2020: 1-9.

[38] Qi J, Gao Y, Yang F. Synthesis of clearance for a kinematic pair to prevent an overconstrained linkage from becoming stuck[J]. Mechanical Sciences, 2023, 14(1): 171-178.

[39] Wojtyra M. Joint reaction forces in multibody systems with redundant constraints[J]. Multibody System Dynamics, 2005, 14: 23-46.

[40] Wojtyra M, Frączek J. Comparison of selected methods of handling redundant constraints in multibody systems simulations[J]. Journal of Computational Nonlinear Dynamics, 2013, 8(2): 021007.

[41] Zhang X. Study on the relationship between mobile assemblies of spatial linkages and rigid origami[D]. Tianjin University, 2018.

[42] Denavit J, Hartenberg R S. A kinematic notation for lower-pair mechanisms based on matrices[J]. ASME Journal of Applied Mechanics, 1955, 22: 215-221.

[43] Hartenberg R, Danavit J. Kinematic synthesis of linkages[M]. New York: McGraw-Hill, 1964.

[44] Beggs J. Advanced Mechanism[M]. Macmillan, 1966.

[45] Altmann S L. Rotations, quaternions, and double groups[M]. Oxford University Press, 1986.

[46] Kuipers J B. Quaternions and rotation sequences: a primer with applications to orbits, aerospace, and virtual reality[M]. Princeton university press, 1999.

[47] Mccarthy J M. Introduction to theoretical kinematics[M]. MIT press, 1990.

[48] Wu W, You Z. Modelling rigid origami with quaternions and dual quaternions[J]. Proceedings of the Royal Society A: Mathematical, physical engineering sciences, 2010, 466(2119): 2155-2174.

[49] Perez A, Mccarthy J M. Dual quaternion synthesis of constrained robotic systems[J]. Journal of Mechanical Design, 2004, 126(3): 425-435.

[50] Gan D, Liao Q, Wei S, et al. Dual quaternion-based inverse kinematics of the general spatial 7R mechanism[J]. Proceedings of the Institution of Mechanical Engineers, Part C: Journal of Mechanical Engineering Science, 2008, 222(8): 1593-1598.

[51] Leclercq G, Lefèvre P, Blohm G. 3D kinematics using dual quaternions: theory and applications in neuroscience[J]. Frontiers in Behavioral Neuroscience, 2013, 7: 7.

[52] Hegedüs G, Schicho J, Schröcker H-P. Bond theory and closed 5R linkages[M]// Latest Advances in Robot Kinematics. Springer. 2012: 221-228.

[53] Hegedüs G, Schicho J, Schröcker H-P. Construction of overconstrained linkages by factorization of rational motions[M]// Latest Advances in Robot Kinematics. Springer. 2012: 213-220.

[54] Hegedüs G, Schicho J, Schröcker H-P. The theory of bonds: A new method for the analysis of linkages[J]. Mechanism and Machine Theory, 2013, 70: 407-424.

[55] Nawratil G. Introducing the theory of bonds for Stewart Gough platforms with self-motions[J]. Journal of Mechanisms Robotics, 2014, 6(1): 011004.

[56] Hegedüs G, Li Z, Schicho J, et al. The theory of bonds II: Closed 6R linkages with maximal genus[J]. Journal of Symbolic Computation, 2015, 68: 167-180.

[57] Ball R S. The theory of screws: A study in the dynamics of a rigid body[M]. Dublin, Hodges, Forster and C, 1876.

[58] Hunt K H. Kinematic geometry of mechanisms[M]. Oxford University Press, 1978.

[59] Varadarajan V S. Lie groups, Lie algebras, and their representations[M]. Springer Science & Business Media, 1974.

[60] Murray R M, Li Z, Sastry S S, et al. A mathematical introduction to robotic manipulation[M]. CRC press, 1994.

[61] Hervé J M. The Lie group of rigid body displacements, a fundamental tool for mechanism design[J]. Mechanism and Machine Theory, 1999, 34(5): 719-730.

[62] Zhang X, López-Custodio P, Dai J S. Compositional submanifolds of prismatic–universal–prismatic and skewed prismatic–revolute–prismatic kinematic chains and their derived parallel mechanisms[J]. Journal of Mechanisms Robotics, 2018, 10(3): 031001.

[63] You Z, Chen Y. Motion structures: deployable structural assemblies of mechanisms[M]. Taylor & Francis, 2012.

[64] Ionescu T G, Antonescu P, Biro I, et al. Terminology for the mechanism and machine science[J]. Mechanism and Machine Theory, 2003, 38: 767-901.

[65] Gogu G. Mobility of mechanisms: a critical review[J]. Mechanism and Machine Theory, 2005, 40(9): 1068-1097.

[66] Chen Y, You Z. Spatial overconstrained linkages—the lost jade[M]//. Springer Netherlands 2012.

[67] Hagiwara I. From Origami to" Origamics"[J]. Japan Journal, 2008, 5(3): 22-25.

[68] Morgan J, Magleby S P, Howell L L. An approach to designing origami-adapted aerospace mechanisms[J]. Journal of Mechanical Design, 2016, 138(5): 052301.

[69] Reis P M, López Jiménez F, Marthelot J. Transforming architectures inspired by origami[J]. Proceedings of the National Academy of Sciences, 2015, 112(40): 12234-12235.

[70] Felton S, Tolley M, Demaine E, et al. A method for building self-folding machines[J]. Science, 2014, 345(6197): 644-646.

[71] Ma J, Zang S, Chen Y, et al. The tessellation rule and properties programming of origami metasheets built with a mixture of rigid and non-rigid square-twist patterns[J]. Engineering, 2022, 17: 82-92.

[72] Chen Y, Peng R, You Z. Origami of thick panels[J]. Science, 2015, 349(6246): 396-400.

[73] Dai J S, Rees Jones J. Mobility in metamorphic mechanisms of foldable/erectable kinds[J]. Journal of Mechanical Design, 1999, 121: 375-382.

[74] Wei G, Dai J S. Origami-inspired integrated planar-spherical overconstrained mechanisms[J]. Journal of Mechanical Design, 2014, 136(5): 051003.

[75] Chen Y, Lv W, Peng R, et al. Mobile assemblies of four-spherical-4R-integrated linkages and the associated four-crease-integrated rigid origami patterns[J]. Mechanism and Machine Theory, 2019, 142: 103613.

[76] Schenk M, Guest S D. Geometry of Miura-folded metamaterials[J]. Proceedings of the National Academy of Sciences, 2013, 110(9): 3276-3281.

[77] Zhang X, Chen Y. Vertex-splitting on a diamond origami pattern[J]. Journal of Mechanisms Robotics, 2019, 11(3): 031014.

[78] Chen Y, Feng H, Ma J, et al. Symmetric waterbomb origami[J]. Proceedings of the Royal Society A: Mathematical, Physical Engineering Sciences, 2016, 472(2190): 20150846.

[79] Tachi T. One-DOF cylindrical deployable structures with rigid quadrilateral panels[C]. Proceedings of the IASS Symposium, Editorial Universitat Politècnica de València, 2010: 2295-2306.

[80] Chen Y, Lv W, Li J, et al. An extended family of rigidly foldable origami tubes[J]. Journal of Mechanisms Robotics, 2017, 9(2): 021002.

[81] Wu W, You Z. A solution for folding rigid tall shopping bags[J]. Proceedings of the Royal Society A: Mathematical, Physical Engineering Sciences, 2011, 467(2133): 2561-2574.

[82] Gu Y, Chen Y. One-DOF origami boxes with rigid and flat foldability[C]. Proceedings of the IFToMM Asian Conference on Mechanism and Machine Science, Springer, 2021: 80-88.

[83] Zhang X, Ma J, Li M, et al. Kirigami-based metastructures with programmable multistability[J]. Proceedings of the National Academy of Sciences, 2022, 119(11): e2117649119.

[84] Bennett G T. A new mechanism[J]. Engineering, 1903, 76: 777-778.

[85] Bricard R. Leçons de cinématique[M]. Gauthier-Villars, 1926.

[86] Chen Y, You Z, Tarnai T. Threefold-symmetric Bricard linkages for deployable structures[J]. International Journal of Solids Structures, 2005, 42(8): 2287-2301.

[87] Wohlhart K. Merging two general Goldberg 5R linkages to obtain a new 6R space mechanism[J]. Mechanism and Machine Theory, 1991, 26(7): 659-668.

[88] Waldron K J. Hybrid overconstrained linkages[J]. Journal of Mechanisms, 1968, 3(2): 73-78.

[89] Zhang X, Chen Y. Mobile assemblies of Bennett linkages from four-crease origami patterns[J]. Proceedings of the Royal Society A: Mathematical, Physical Engineering Sciences, 2018, 474(2210): 20170621.

[90] Qi X Z, Deng Z Q, Ma B Y, et al. Design of large deployable networks constructed by Myard linkages[J]. Key Engineering Materials, 2011, 486: 291-296.

[91] Chen Y. Design of structural mechanisms[D]. Oxford University, UK, 2003.

[92] Zhang X, Chen Y. The diamond thick-panel origami and the corresponding mobile assemblies of plane-symmetric Bricard linkages[J]. Mechanism and Machine Theory, 2018, 130: 585-604.

[93] Huang H, Li B, Zhu J, et al. A new family of Bricard-derived deployable mechanisms[J]. Journal of Mechanisms Robotics, 2016, 8(3): 034503.

[94] Xu Y, Chen Y, Liu W, et al. Degree of freedom and dynamic analysis of the multi-loop coupled passive-input overconstrained deployable tetrahedral mechanisms for truss antennas[J]. Journal of Mechanisms Robotics, 2020, 12(1): 011010.

[95] Guo J, Zhao Y, Xu Y, et al. Mechanics analysis and structural design of a truss deployable antenna mechanism based on 3RR-3URU tetrahedral unit[J]. Mechanism and Machine Theory, 2022, 171: 104749.

[96] Cao W-A, Zhang D, Ding H. A novel two-layer and two-loop deployable linkage with accurate vertical straight-line motion[J]. Journal of Mechanical Design, 2020, 142(10): 103301.

[97] Zhou C, Chen H, Guo W, et al. Novel bundle folding deployable mechanisms to realize polygons and polyhedrons[J]. Mechanism and Machine Theory, 2023, 181: 105210.

[98] Zhang Y, Xu P, Li B. Structure derivative design, network, and kinematic analysis of a class of two-dimensional deployable mechanisms for aerospace platforms[J]. Mechanism and Machine Theory, 2023, 185: 105314.

[99] Kong X, Pfurner M. Type synthesis and reconfiguration analysis of a class of variable-DOF single-loop mechanisms[J]. Mechanism and Machine Theory, 2015, 85: 116-128.

[100] Kong X. A variable-DOF single-loop 7R spatial mechanism with five motion modes[J]. Mechanism and Machine Theory, 2018, 120: 239-249.

[101] Wei G, Dai J S. Reconfigurable and deployable platonic mechanisms with a variable revolute joint[J]. Advances in Robot Kinematics, 2014: 485-495.

[102] Xiu H, Wang K, Wei G, et al. A Sarrus-like overconstrained eight-bar linkage and its associated Fulleroid-like platonic deployable mechanisms[J]. Proceedings of the Institution of Mechanical Engineers, Part C: Journal of Mechanical Engineering Science, 2020, 234(1): 241-262.

[103] Chai X, Zhang C, Dai J S. A single-loop 8R linkage with plane-symmetry and bifurcation property[C]. Proceedings of the 2018 International Conference on Reconfigurable Mechanisms and Robots (ReMAR), IEEE, 2018: 1-8.

[104] Wang R, Song Y, Dai J S. Reconfigurability of the origami-inspired integrated 8R kinematotropic metamorphic mechanism and its evolved 6R and 4R mechanisms[J]. Mechanism and Machine Theory, 2021, 161: 104245.

[105] Cromwell P R. Polyhedra[M]. Cambridge University Press, 1997.

[106] Coxeter H. Regular Polytopes[M]. Ltd., London, 1948.

[107] Verheyen H F. The complete set of Jitterbug transformers and the analysis of their motion[J]. Computers & Mathematics With Applications, 1989, 17: 203-250.

[108] Schwabe C. Eureka and Serendipity: The Rudolf von Laban Icosahedron and Buckminster Fuller's Jitterbug[C]. Proceedings of the Proceedings of Bridges 2010: Mathematics, Music, Art, Architecture, Culture, 2010: 271-278.

[109] Wohlhart K. Kinematics and Dynamics of the Fulleroid[J]. Multibody System Dynamics, 1997, 1: 241-258.

[110] Wohlhart K. New regular polyhedral linkages[M]// Proceedings of the SYROM 2001. . 2001: 239-248.

[111] Kiper G. Fulleroid-like linkages[C]. Proceedings of the Proceedings of EUCOMES 08: The Second European Conference on Mechanism Science, Springer, 2009: 423-430.

[112] Röschel O. A fulleroid-like mechanism based on the cube[J]. Journal for geometry graphics, 2012, 16(1): 19-27.

[113] Kiper G, Söylemez E. Regular polygonal and regular spherical polyhedral linkages comprising Bennett loops[C]. Proceedings of the Computational Kinematics: Proceedings of the 5th International Workshop on Computational Kinematics, Springer, 2009: 249-256.

[114] Wang J, Kong X. Deployable mechanisms constructed by connecting orthogonal Bricard linkages, 8R or 10R single-loop linkages using S joints[J]. Mechanism and Machine Theory, 2018, 120: 178-191.

[115] Wang J, Kong X. Deployable polyhedron mechanisms constructed by connecting spatial single-loop linkages of different types and/or in different sizes using S joints[J]. Mechanism and Machine Theory, 2018, 124: 211-225.

[116] Liu J, Zhao X, Ding H. A class of N-sided antiprism deployable polyhedral mechanisms based on an asymmetric eight-bar linkage[J]. Mechanism and Machine Theory, 2020, 150: 103882.

[117] Cao W-A, Xi S, Ding H, et al. Design and kinematics of a novel double-ring truss deployable antenna mechanism[J]. Journal of Mechanical Design, 2021, 143(12): 124502.

[118] Lu S, Zlatanov D, Ding X, et al. A new family of deployable mechanisms based on the Hoekens linkage[J]. Mechanism and Machine Theory, 2014, 73: 130-153.

[119] Ding X, Yang Y, Dai J S. Design and kinematic analysis of a novel prism deployable mechanism[J]. Mechanism and Machine Theory, 2013, 63: 35-49.

[120] Sun X, Li R, Xun Z, et al. A new Bricard-like mechanism with anti-parallelogram units[J]. Mechanism and Machine Theory, 2020, 147: 103753.

[121] Yang F, You Z, Chen Y. Mobile assembly of two Bennett linkages and its application to transformation between cuboctahedron and octahedron[J]. Mechanism and Machine Theory, 2020, 145: 103698.

[122] Chen Y, Yang F, You Z. Transformation of polyhedrons[J]. International Journal of Solids Structures, 2018, 138: 193-204.

[123] Yang F, Chen Y. One-DOF transformation between tetrahedron and truncated tetrahedron[J]. Mechanism and Machine Theory, 2018, 121: 169-183.

[124] Wohlhart K. Deformable cages[C]. Proceedings of the 10th world congress on the theory of machines and mechanisms, 1999: 683-688.

[125] Kiper G, Söylemez E, Kisisel A U O. Polyhedral linkages synthesized using cardan motion along radial axes[C]. Proceedings of the 12th IFToMM World Congress, 2007: 471-477.

[126] Wohlhart K. Cyclic polyhedra and linkages derived therefrom[J]. Mechanism and Machine Theory, 2017, 108: 142-159.

[127] Wohlhart K. Equally circumscribed cyclic polyhedra generalize Platonic solids[J]. Mechanism and Machine Theory, 2019, 133: 150-163.

[128] Wohlhart K. Twisting towers derived from Archimedean polyhedrons[J]. Mechanism and Machine Theory, 2014, 80: 103-111.

[129] Laliberté T, Gosselin C M. Polyhedra with articulated faces[C]. Proceedings of the Proc of the 12th IFToMM world congress, 2007.

[130] Hoberman C. Reversibly expandable doubly-curved truss structure: U.S. Patents No. 4,942,700. 1990.

[131] Agrawal S K, Kumar S, Yim M. Polyhedral single degree-of-freedom expanding structures: design and prototypes[J]. Journal of Mechanical Design, 2002, 124(3): 473-478.

[132] Gosselin C, Gagnon-Lachance D. Expandable polyhedral mechanisms based on polygonal one-degree-of-freedom faces[J]. Proceedings of the Institution of Mechanical Engineers, Part C: Journal of Mechanical Engineering Science, 2006, 220(7): 1011-1018.

[133] Wohlhart K. Polyhedral zig-zag linkages[C]. Proceedings of the On advances in robot kinematics, Springer, 2004: 351-360.

[134] Li R, Yao Y-A, Kong X. A class of reconfigurable deployable platonic mechanisms[J]. Mechanism and Machine Theory, 2016, 105: 409-427.

[135] Wohlhart K. Double-ring polyhedral linkages[C]. Proceedings of the Interdisciplinary Applications of Kinematics: Proceedings of the International Conference, Lima, Perú, January 9-11, 2008, Springer, 2011: 1-17.

[136] Li R, Yao Y-A, Kong X. Reconfigurable deployable polyhedral mechanism based on extended parallelogram mechanism[J]. Mechanism and Machine Theory, 2017, 116: 467-480.

[137] Xiu H, Wang K, Xu T, et al. Synthesis and analysis of Fulleroid-like deployable Archimedean mechanisms based on an overconstrained eight-bar linkage[J]. Mechanism and Machine Theory, 2019, 137: 476-508.

[138] Song X, Guo H, Li B, et al. Large deployable network constructed by Altmann linkages[J]. 2017, 231(2): 341-355.

[139] Song X, Deng Z, Guo H, et al. Networking of Bennett linkages and its application on deployable parabolic cylindrical antenna[J]. Mechanism and Machine Theory, 2017, 109: 95-125.

[140] Huang Z, Li Q, Ding H. Theory of parallel mechanisms[M]. Springer Science & Business Media, 2012.

[141] Zhang Y, Gu Y, Chen Y, et al. One-DOF rigid and flat-foldable origami polyhedrons with slits[J]. Acta Mechanica Solida Sinica, 2023, 36(4): 479-490.

[142] Milenkovic P, Brown M V. Properties of the Bennett mechanism derived from the RRRS closure ellipse[J]. Journal of Mechanisms Robotics, 2011, 3: 021012.

[143] Lee C-C, Herve J M. Oblique circular torus, Villarceau circles, and four types of Bennett linkages[J]. Proceedings of the Institution of Mechanical Engineers, Part C: Journal of Mechanical Engineering Science, 2014, 228(4): 742-752.

[144] Maxwell J C. L. on the calculation of the equilibrium and stiffness of frames[J]. The London, Edinburgh, Dublin Philosophical Magazine Journal of Science, 1864, 27(182): 294-299.

[145] Brown N C, Ynchausti C, Lytle A, et al. Approaches for minimizing joints in single-degree-of-freedom origami-based mechanisms[J]. Journal of Mechanical Design, 2022, 144(10): 103301.

[146] Bolanos D, Ynchausti C, Brown N, et al. Considering thickness-accommodation, nesting, grounding and deployment in design of Miura-ori based space arrays[J]. Mechanism and Machine Theory, 2022, 174: 104904.

[147] Yang J, Zhang X, Chen Y, et al. Folding arrays of uniform-thickness panels to compact bundles with a single degree of freedom[J]. Proceedings of the Royal Society A: Mathematical, Physical Engineering Sciences, 2022, 478(2261): 20220043.

Appendix

A. Screw analysis of original deployable cubic mechanism

The number of links and revolute joints in the deployable cubic mechanism are 54 and 72, respectively, in which the independent loops of this mechanism are 19. Based on the reference coordinate frame in Fig. 3-9 in Section 3, Fig. A1 shows the original constraint graph with 72 joint screws in the deployable cubic mechanism.

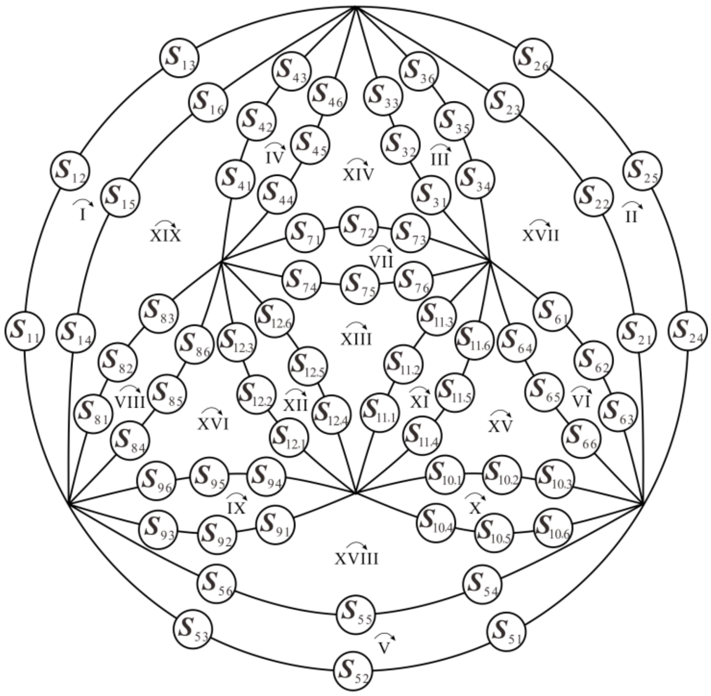

Fig. A1 Original constraint graph of the deployable cubic mechanism.

The details of adjoint transformation matrices are

$$\boldsymbol{R}_1 = \begin{bmatrix} 0 & -\sqrt{2}/2 & \sqrt{2}/2 \\ 1 & 0 & 0 \\ 0 & \sqrt{2}/2 & \sqrt{2}/2 \end{bmatrix},\ \boldsymbol{p}_1 = d_2\begin{bmatrix} 1 & 0 & 1 \end{bmatrix}^{\mathrm{T}}$$

$$\boldsymbol{R}_2 = \begin{bmatrix} -1 & 0 & 0 \\ 0 & -\sqrt{2}/2 & \sqrt{2}/2 \\ 0 & \sqrt{2}/2 & \sqrt{2}/2 \end{bmatrix},\ \boldsymbol{p}_2 = d_2\begin{bmatrix} 0 & 1 & 1 \end{bmatrix}^{\mathrm{T}}$$

$$\boldsymbol{R}_3=\begin{bmatrix}0 & \sqrt{2}/2 & -\sqrt{2}/2\\ -1 & 0 & 0\\ 0 & \sqrt{2}/2 & \sqrt{2}/2\end{bmatrix},\ \boldsymbol{p}_3=d_2\begin{bmatrix}-1 & 0 & 1\end{bmatrix}^{\mathrm{T}}$$

$$\boldsymbol{R}_4=\begin{bmatrix}1 & 0 & 0\\ 0 & \sqrt{2}/2 & -\sqrt{2}/2\\ 0 & \sqrt{2}/2 & \sqrt{2}/2\end{bmatrix},\ \boldsymbol{p}_4=d_2\begin{bmatrix}0 & -1 & 1\end{bmatrix}^{\mathrm{T}}$$

$$\boldsymbol{R}_5=\begin{bmatrix}0 & \sqrt{2}/2 & \sqrt{2}/2\\ 0 & -\sqrt{2}/2 & \sqrt{2}/2\\ 1 & 0 & 0\end{bmatrix},\ \boldsymbol{p}_5=d_2\begin{bmatrix}1 & 0 & 1\end{bmatrix}^{\mathrm{T}}$$

$$\boldsymbol{R}_6=\begin{bmatrix}0 & \sqrt{2}/2 & -\sqrt{2}/2\\ 0 & \sqrt{2}/2 & \sqrt{2}/2\\ 1 & 0 & 0\end{bmatrix},\ \boldsymbol{p}_6=d_2\begin{bmatrix}-1 & 1 & 0\end{bmatrix}^{\mathrm{T}}$$

$$\boldsymbol{R}_7=\begin{bmatrix}0 & -\sqrt{2}/2 & -\sqrt{2}/2\\ 0 & \sqrt{2}/2 & -\sqrt{2}/2\\ 1 & 0 & 0\end{bmatrix},\ \boldsymbol{p}_7=d_2\begin{bmatrix}-1 & -1 & 0\end{bmatrix}^{\mathrm{T}}$$

$$\boldsymbol{R}_8=\begin{bmatrix}0 & -\sqrt{2}/2 & \sqrt{2}/2\\ 0 & -\sqrt{2}/2 & -\sqrt{2}/2\\ 1 & 0 & 0\end{bmatrix},\ \boldsymbol{p}_8=d_2\begin{bmatrix}1 & -1 & 0\end{bmatrix}^{\mathrm{T}}$$

$$\boldsymbol{R}_9=\begin{bmatrix}0 & \sqrt{2}/2 & \sqrt{2}/2\\ 1 & 0 & 0\\ 0 & \sqrt{2}/2 & -\sqrt{2}/2\end{bmatrix},\ \boldsymbol{p}_9=d_2\begin{bmatrix}1 & 0 & -1\end{bmatrix}^{\mathrm{T}}$$

$$\boldsymbol{R}_{10}=\begin{bmatrix}-1 & 0 & 0\\ 0 & \sqrt{2}/2 & \sqrt{2}/2\\ 0 & \sqrt{2}/2 & -\sqrt{2}/2\end{bmatrix},\ \boldsymbol{p}_{10}=d_2\begin{bmatrix}0 & 1 & -1\end{bmatrix}^{\mathrm{T}}$$

$$\boldsymbol{R}_{11}=\begin{bmatrix}0 & -\sqrt{2}/2 & -\sqrt{2}/2\\ -1 & 0 & 0\\ 0 & \sqrt{2}/2 & -\sqrt{2}/2\end{bmatrix},\ \boldsymbol{p}_{11}=d_2\begin{bmatrix}-1 & 0 & -1\end{bmatrix}^{\mathrm{T}}$$

$$\boldsymbol{R}_{12}=\begin{bmatrix}1 & 0 & 0\\ 0 & -\sqrt{2}/2 & -\sqrt{2}/2\\ 0 & \sqrt{2}/2 & -\sqrt{2}/2\end{bmatrix},\ \boldsymbol{p}_{12}=d_2\begin{bmatrix}0 & -1 & -1\end{bmatrix}^{\mathrm{T}} \tag{A1}$$

and the 114×72 original constraint matrix $\boldsymbol{M}_2$ can be expressed as

$$\boldsymbol{M}_2=\begin{bmatrix}\boldsymbol{M}_{11} & \mathbf{0}_{6\times 36}\\ \mathbf{0}_{6\times 36} & \boldsymbol{M}_{22}\\ \boldsymbol{M}_{31} & \boldsymbol{M}_{32}\end{bmatrix} \tag{A2}$$

where

$$\mathbf{0}_{6\times 36}=\begin{bmatrix}\mathbf{0}_6 & \mathbf{0}_6 & \mathbf{0}_6 & \mathbf{0}_6 & \mathbf{0}_6 & \mathbf{0}_6\\ \mathbf{0}_6 & \mathbf{0}_6 & \mathbf{0}_6 & \mathbf{0}_6 & \mathbf{0}_6 & \mathbf{0}_6\\ \mathbf{0}_6 & \mathbf{0}_6 & \mathbf{0}_6 & \mathbf{0}_6 & \mathbf{0}_6 & \mathbf{0}_6\\ \mathbf{0}_6 & \mathbf{0}_6 & \mathbf{0}_6 & \mathbf{0}_6 & \mathbf{0}_6 & \mathbf{0}_6\\ \mathbf{0}_6 & \mathbf{0}_6 & \mathbf{0}_6 & \mathbf{0}_6 & \mathbf{0}_6 & \mathbf{0}_6\\ \mathbf{0}_6 & \mathbf{0}_6 & \mathbf{0}_6 & \mathbf{0}_6 & \mathbf{0}_6 & \mathbf{0}_6\end{bmatrix},\ \boldsymbol{M}_{11}=\begin{bmatrix}\boldsymbol{S}_1 & \mathbf{0}_6 & \mathbf{0}_6 & \mathbf{0}_6 & \mathbf{0}_6 & \mathbf{0}_6\\ \mathbf{0}_6 & \boldsymbol{S}_2 & \mathbf{0}_6 & \mathbf{0}_6 & \mathbf{0}_6 & \mathbf{0}_6\\ \mathbf{0}_6 & \mathbf{0}_6 & \boldsymbol{S}_3 & \mathbf{0}_6 & \mathbf{0}_6 & \mathbf{0}_6\\ \mathbf{0}_6 & \mathbf{0}_6 & \mathbf{0}_6 & \boldsymbol{S}_4 & \mathbf{0}_6 & \mathbf{0}_6\\ \mathbf{0}_6 & \mathbf{0}_6 & \mathbf{0}_6 & \mathbf{0}_6 & \boldsymbol{S}_5 & \mathbf{0}_6\\ \mathbf{0}_6 & \mathbf{0}_6 & \mathbf{0}_6 & \mathbf{0}_6 & \mathbf{0}_6 & \boldsymbol{S}_6\end{bmatrix}$$

$$\boldsymbol{M}_{22}=\begin{bmatrix}\boldsymbol{S}_7 & \mathbf{0}_6 & \mathbf{0}_6 & \mathbf{0}_6 & \mathbf{0}_6 & \mathbf{0}_6\\ \mathbf{0}_6 & \boldsymbol{S}_8 & \mathbf{0}_6 & \mathbf{0}_6 & \mathbf{0}_6 & \mathbf{0}_6\\ \mathbf{0}_6 & \mathbf{0}_6 & \boldsymbol{S}_9 & \mathbf{0}_6 & \mathbf{0}_6 & \mathbf{0}_6\\ \mathbf{0}_6 & \mathbf{0}_6 & \mathbf{0}_6 & \boldsymbol{S}_{10} & \mathbf{0}_6 & \mathbf{0}_6\\ \mathbf{0}_6 & \mathbf{0}_6 & \mathbf{0}_6 & \mathbf{0}_6 & \boldsymbol{S}_{11} & \mathbf{0}_6\\ \mathbf{0}_6 & \mathbf{0}_6 & \mathbf{0}_6 & \mathbf{0}_6 & \mathbf{0}_6 & \boldsymbol{S}_{12}\end{bmatrix},\ \boldsymbol{M}_{31}=\begin{bmatrix}\mathbf{0}_6 & \mathbf{0}_6 & \mathbf{0}_6 & \mathbf{0}_6 & \mathbf{0}_6 & \mathbf{0}_6\\ \mathbf{0}_6 & \mathbf{0}_6 & \mathbf{0}_6 & \mathbf{0}_6 & \mathbf{0}_6 & \mathbf{0}_6\\ \mathbf{0}_6 & \mathbf{0}_6 & -\boldsymbol{S}'_3 & -\boldsymbol{S}''_4 & \mathbf{0}_6 & \mathbf{0}_6\\ \mathbf{0}_6 & \mathbf{0}_6 & \mathbf{0}_6 & \mathbf{0}_6 & \mathbf{0}_6 & -\boldsymbol{S}''_6\\ \mathbf{0}_6 & -\boldsymbol{S}'_2 & -\boldsymbol{S}''_3 & \mathbf{0}_6 & \mathbf{0}_6 & -\boldsymbol{S}'_6\\ \mathbf{0}_6 & \mathbf{0}_6 & \mathbf{0}_6 & \mathbf{0}_6 & -\boldsymbol{S}''_5 & \mathbf{0}_6\\ -\boldsymbol{S}''_1 & \mathbf{0}_6 & \mathbf{0}_6 & -\boldsymbol{S}'_4 & \mathbf{0}_6 & \mathbf{0}_6\end{bmatrix}$$

$$\boldsymbol{M}_{32}=\begin{bmatrix}-\boldsymbol{S}''_7 & \mathbf{0}_6 & \mathbf{0}_6 & \mathbf{0}_6 & -\boldsymbol{S}'_{11} & -\boldsymbol{S}''_{12}\\ \mathbf{0}_6 & -\boldsymbol{S}''_8 & -\boldsymbol{S}''_9 & \mathbf{0}_6 & \mathbf{0}_6 & -\boldsymbol{S}'_{12}\\ -\boldsymbol{S}'_7 & \mathbf{0}_6 & \mathbf{0}_6 & \mathbf{0}_6 & \mathbf{0}_6 & \mathbf{0}_6\\ \mathbf{0}_6 & \mathbf{0}_6 & \mathbf{0}_6 & -\boldsymbol{S}'_{10} & -\boldsymbol{S}''_{11} & \mathbf{0}_6\\ \mathbf{0}_6 & \mathbf{0}_6 & \mathbf{0}_6 & \mathbf{0}_6 & \mathbf{0}_6 & \mathbf{0}_6\\ \mathbf{0}_6 & \mathbf{0}_6 & -\boldsymbol{S}'_9 & -\boldsymbol{S}''_{10} & \mathbf{0}_6 & \mathbf{0}_6\\ \mathbf{0}_6 & -\boldsymbol{S}'_8 & \mathbf{0}_6 & \mathbf{0}_6 & \mathbf{0}_6 & \mathbf{0}_6\end{bmatrix}$$

Thus, the rank of the original constraint matrix $\boldsymbol{M}_2$ is 71, which indicates the mobility of the deployable cubic mechanism as $m=n-\mathrm{rank}(\boldsymbol{M}_2)=72-71=1$.

B. Screw analysis of original deployable dodecahedral mechanism

First, the details of submatrices of $\boldsymbol{M}_{e3}$ can be listed as

$$\boldsymbol{M}_{13}=\begin{bmatrix} \mathbf{0} & \mathbf{0} & \mathbf{0} & \mathbf{0} & \mathbf{0} & \mathbf{0} \\ \mathbf{0} & \mathbf{0} & \mathbf{0} & \mathbf{0} & \mathbf{0} & \boldsymbol{S}_{f18} \\ \mathbf{0} & \mathbf{0} & \mathbf{0} & \mathbf{0} & \mathbf{0} & \mathbf{0} \\ \mathbf{0} & \mathbf{0} & \mathbf{0} & \mathbf{0} & \mathbf{0} & \mathbf{0} \\ \mathbf{0} & \mathbf{0} & \mathbf{0} & \boldsymbol{S}_{f16} & \boldsymbol{S}_{f17} & \mathbf{0} \\ \mathbf{0} & \boldsymbol{S}_{f14} & \boldsymbol{S}_{f15} & \mathbf{0} & \mathbf{0} & \mathbf{0} \end{bmatrix}$$

$$\boldsymbol{M}_{14}=\begin{bmatrix} \mathbf{0} & \mathbf{0} & \mathbf{0} & \mathbf{0} & \mathbf{0} & \boldsymbol{S}_{f24} \\ \boldsymbol{S}_{f19} & \mathbf{0} & \mathbf{0} & \mathbf{0} & \mathbf{0} & -\boldsymbol{S}_{f24} \\ \mathbf{0} & \mathbf{0} & \mathbf{0} & \mathbf{0} & \mathbf{0} & \mathbf{0} \\ \mathbf{0} & \mathbf{0} & \mathbf{0} & \mathbf{0} & \boldsymbol{S}_{f23} & \mathbf{0} \\ \mathbf{0} & \mathbf{0} & \mathbf{0} & \mathbf{0} & -\boldsymbol{S}_{f23} & \mathbf{0} \\ \mathbf{0} & \mathbf{0} & \mathbf{0} & \boldsymbol{S}_{f22} & \mathbf{0} & \mathbf{0} \end{bmatrix}$$

$$\boldsymbol{M}_{15}=\begin{bmatrix} \mathbf{0} & \mathbf{0} & \mathbf{0} & \mathbf{0} & \boldsymbol{S}_{f29} & \boldsymbol{S}_{f30} \\ \mathbf{0} & \mathbf{0} & \mathbf{0} & \mathbf{0} & \mathbf{0} & \mathbf{0} \\ \boldsymbol{S}_{f25} & \boldsymbol{S}_{f26} & \mathbf{0} & \mathbf{0} & \mathbf{0} & -\boldsymbol{S}_{f30} \\ \mathbf{0} & \mathbf{0} & \mathbf{0} & \boldsymbol{S}_{f28} & -\boldsymbol{S}_{f29} & \mathbf{0} \\ \mathbf{0} & \mathbf{0} & \mathbf{0} & \mathbf{0} & \mathbf{0} & \mathbf{0} \\ \mathbf{0} & \mathbf{0} & \mathbf{0} & \mathbf{0} & \mathbf{0} & \mathbf{0} \end{bmatrix}$$

$$\boldsymbol{M}_{22}=\begin{bmatrix} \mathbf{0} & \mathbf{0} & \mathbf{0} & \boldsymbol{S}_{f10} & \mathbf{0} & \mathbf{0} \\ \mathbf{0} & \mathbf{0} & \mathbf{0} & \mathbf{0} & \boldsymbol{S}_{f11} & \mathbf{0} \\ \mathbf{0} & \mathbf{0} & \mathbf{0} & \mathbf{0} & \mathbf{0} & \mathbf{0} \\ \mathbf{0} & \mathbf{0} & \mathbf{0} & \mathbf{0} & \mathbf{0} & \mathbf{0} \\ \mathbf{0} & \mathbf{0} & \boldsymbol{S}_{f9} & \mathbf{0} & \mathbf{0} & \mathbf{0} \\ \mathbf{0} & \mathbf{0} & \mathbf{0} & \mathbf{0} & \mathbf{0} & \boldsymbol{S}_{f12} \end{bmatrix}$$

$$\boldsymbol{M}_{23}=\begin{bmatrix} \mathbf{0} & \mathbf{0} & \mathbf{0} & \mathbf{0} & \mathbf{0} & \mathbf{0} \\ \mathbf{0} & \mathbf{0} & \mathbf{0} & \mathbf{0} & \mathbf{0} & \mathbf{0} \\ \mathbf{0} & \mathbf{0} & \mathbf{0} & \mathbf{0} & \mathbf{0} & \mathbf{0} \\ \mathbf{0} & \mathbf{0} & \mathbf{0} & \mathbf{0} & \mathbf{0} & \mathbf{0} \\ \mathbf{0} & \mathbf{0} & \mathbf{0} & -\boldsymbol{S}_{f17} & -\boldsymbol{S}_{f18} & \mathbf{0} \\ \boldsymbol{S}_{f13} & \mathbf{0} & \mathbf{0} & \mathbf{0} & \mathbf{0} & \mathbf{0} \end{bmatrix}$$

$$\boldsymbol{M}_{24} = \begin{bmatrix} -\boldsymbol{S}_{f19} & \boldsymbol{S}_{f20} & \mathbf{0} & \mathbf{0} & \mathbf{0} & \mathbf{0} \\ \mathbf{0} & -\boldsymbol{S}_{f20} & \mathbf{0} & \mathbf{0} & \mathbf{0} & \mathbf{0} \\ \mathbf{0} & \mathbf{0} & \boldsymbol{S}_{f21} & \mathbf{0} & \mathbf{0} & \mathbf{0} \\ \mathbf{0} & \mathbf{0} & \mathbf{0} & -\boldsymbol{S}_{f22} & \mathbf{0} & \mathbf{0} \\ \mathbf{0} & \mathbf{0} & \mathbf{0} & \mathbf{0} & \mathbf{0} & \mathbf{0} \\ \mathbf{0} & \mathbf{0} & -\boldsymbol{S}_{f21} & \mathbf{0} & \mathbf{0} & \mathbf{0} \end{bmatrix}$$

$$\boldsymbol{M}_{25} = \begin{bmatrix} \mathbf{0} & \mathbf{0} & \mathbf{0} & \mathbf{0} & \mathbf{0} & \mathbf{0} \\ -\boldsymbol{S}_{f25} & \mathbf{0} & \mathbf{0} & \mathbf{0} & \mathbf{0} & \mathbf{0} \\ \mathbf{0} & -\boldsymbol{S}_{f26} & \boldsymbol{S}_{f27} & \mathbf{0} & \mathbf{0} & \mathbf{0} \\ \mathbf{0} & \mathbf{0} & -\boldsymbol{S}_{f27} & -\boldsymbol{S}_{f28} & \mathbf{0} & \mathbf{0} \\ \mathbf{0} & \mathbf{0} & \mathbf{0} & \mathbf{0} & \mathbf{0} & \mathbf{0} \\ \mathbf{0} & \mathbf{0} & \mathbf{0} & \mathbf{0} & \mathbf{0} & \mathbf{0} \end{bmatrix}$$

$$\boldsymbol{M}_{31} = \begin{bmatrix} \mathbf{0} & \mathbf{0} & \boldsymbol{S}_{f3} & \boldsymbol{S}_{f4} & \mathbf{0} & \mathbf{0} \\ \mathbf{0} & \mathbf{0} & \mathbf{0} & -\boldsymbol{S}_{f4} & -\boldsymbol{S}_{f5} & \mathbf{0} \\ \mathbf{0} & \mathbf{0} & \mathbf{0} & \mathbf{0} & \mathbf{0} & \boldsymbol{S}_{f6} \\ \mathbf{0} & \mathbf{0} & \mathbf{0} & \mathbf{0} & \mathbf{0} & \mathbf{0} \\ \mathbf{0} & \mathbf{0} & \mathbf{0} & \mathbf{0} & \mathbf{0} & \mathbf{0} \\ \mathbf{0} & \boldsymbol{S}_{f2} & -\boldsymbol{S}_{f3} & \mathbf{0} & \mathbf{0} & \mathbf{0} \\ \boldsymbol{S}_{f1} & \mathbf{0} & \mathbf{0} & \mathbf{0} & -\boldsymbol{S}_{f5} & -\boldsymbol{S}_{f6} \end{bmatrix}$$

$$\boldsymbol{M}_{32} = \begin{bmatrix} \mathbf{0} & \mathbf{0} & -\boldsymbol{S}_{f9} & \mathbf{0} & \mathbf{0} & \mathbf{0} \\ \mathbf{0} & \mathbf{0} & \mathbf{0} & -\boldsymbol{S}_{f10} & \mathbf{0} & \mathbf{0} \\ \mathbf{0} & \mathbf{0} & \mathbf{0} & \mathbf{0} & -\boldsymbol{S}_{f11} & -\boldsymbol{S}_{f12} \\ \mathbf{0} & \boldsymbol{S}_{f8} & \mathbf{0} & \mathbf{0} & \mathbf{0} & \mathbf{0} \\ \boldsymbol{S}_{f7} & \mathbf{0} & \mathbf{0} & \mathbf{0} & \mathbf{0} & \mathbf{0} \\ \mathbf{0} & -\boldsymbol{S}_{f8} & \mathbf{0} & \mathbf{0} & \mathbf{0} & \mathbf{0} \\ \mathbf{0} & \mathbf{0} & \mathbf{0} & \mathbf{0} & \mathbf{0} & \mathbf{0} \end{bmatrix}$$

$$\boldsymbol{M}_{33} = \begin{bmatrix} \mathbf{0} & \mathbf{0} & \mathbf{0} & \mathbf{0} & \mathbf{0} & \mathbf{0} \\ \mathbf{0} & \mathbf{0} & \mathbf{0} & \mathbf{0} & \mathbf{0} & \mathbf{0} \\ \mathbf{0} & \mathbf{0} & \mathbf{0} & \mathbf{0} & \mathbf{0} & \mathbf{0} \\ \mathbf{0} & \mathbf{0} & -\boldsymbol{S}_{f15} & -\boldsymbol{S}_{f16} & \mathbf{0} & \mathbf{0} \\ -\boldsymbol{S}_{f13} & -\boldsymbol{S}_{f14} & \mathbf{0} & \mathbf{0} & \mathbf{0} & \mathbf{0} \\ \mathbf{0} & \mathbf{0} & \mathbf{0} & \mathbf{0} & \mathbf{0} & \mathbf{0} \\ \mathbf{0} & \mathbf{0} & \mathbf{0} & \mathbf{0} & \mathbf{0} & \mathbf{0} \end{bmatrix}$$

Next, the deployable dodecahedral mechanism consists of 132 links and 180 revolute joints, and the independent loops of this mechanism are 49. Referring to the reference coordinate frame in Fig. 3-11in Section 3, the original constraint graph with 180 joint screws is shown in Fig. B1.

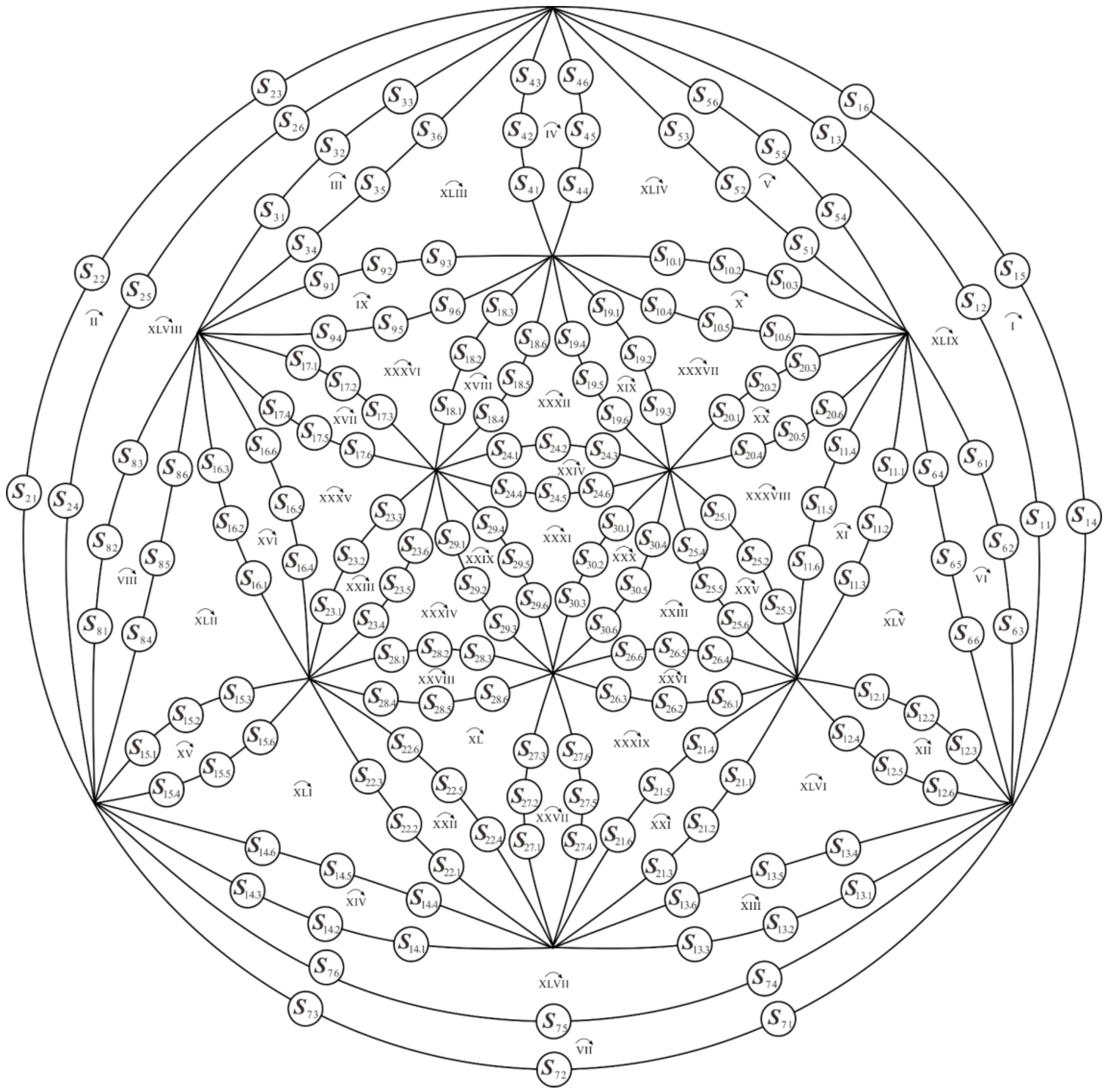

Fig. B1 Original constraint graph of the deployable dodecahedral mechanism.

The details of adjoint transformation matrices in this mechanism are

$$\boldsymbol{R}_1=\begin{bmatrix}-\left(\sqrt{5}+1\right)/4 & -1/2 & -\left(\sqrt{5}-1\right)/4\\ \left(\sqrt{5}-1\right)/4 & -\left(\sqrt{5}+1\right)/4 & 1/2\\ -1/2 & \left(\sqrt{5}-1\right)/4 & \left(\sqrt{5}+1\right)/4\end{bmatrix},\quad \boldsymbol{p}_1=d_3\begin{bmatrix}-\left(\sqrt{5}-1\right)/4\\ 1/2\\ \left(\sqrt{5}+1\right)/4\end{bmatrix}$$

$$\boldsymbol{R}_2=\begin{bmatrix}0 & -1 & 0\\ 1 & 0 & 0\\ 0 & 0 & 1\end{bmatrix},\quad \boldsymbol{p}_2=d_3\begin{bmatrix}0\\ 0\\ 1\end{bmatrix}$$

$$\boldsymbol{R}_3=\begin{bmatrix}\left(\sqrt{5}+1\right)/4 & -1/2 & -\left(\sqrt{5}-1\right)/4\\ \left(\sqrt{5}-1\right)/4 & \left(\sqrt{5}+1\right)/4 & -1/2\\ 1/2 & \left(\sqrt{5}-1\right)/4 & \left(\sqrt{5}+1\right)/4\end{bmatrix},\ \boldsymbol{p}_3=d_3\begin{bmatrix}-\left(\sqrt{5}-1\right)/4\\ -1/2\\ \left(\sqrt{5}+1\right)/4\end{bmatrix}$$

$$\boldsymbol{R}_4=\begin{bmatrix}1/2 & \left(\sqrt{5}-1\right)/4 & -\left(\sqrt{5}+1\right)/4\\ -\left(\sqrt{5}+1\right)/4 & 1/2 & -\left(\sqrt{5}-1\right)/4\\ \left(\sqrt{5}-1\right)/4 & \left(\sqrt{5}+1\right)/4 & 1/2\end{bmatrix},\ \boldsymbol{p}_4=d_3\begin{bmatrix}-\left(\sqrt{5}+1\right)/4\\ -\left(\sqrt{5}-1\right)/4\\ 1/2\end{bmatrix}$$

$$\boldsymbol{R}_5=\begin{bmatrix}-1/2 & \left(\sqrt{5}-1\right)/4 & -\left(\sqrt{5}+1\right)/4\\ -\left(\sqrt{5}+1\right)/4 & -1/2 & \left(\sqrt{5}-1\right)/4\\ -\left(\sqrt{5}-1\right)/4 & \left(\sqrt{5}+1\right)/4 & 1/2\end{bmatrix},\ \boldsymbol{p}_5=d_3\begin{bmatrix}-\left(\sqrt{5}+1\right)/4\\ \left(\sqrt{5}-1\right)/4\\ 1/2\end{bmatrix}$$

$$\boldsymbol{R}_6=\begin{bmatrix}-\left(\sqrt{5}-1\right)/4 & \left(\sqrt{5}+1\right)/4 & -1/2\\ -1/2 & \left(\sqrt{5}-1\right)/4 & \left(\sqrt{5}+1\right)/4\\ \left(\sqrt{5}+1\right)/4 & 1/2 & \left(\sqrt{5}-1\right)/4\end{bmatrix},\ \boldsymbol{p}_6=d_3\begin{bmatrix}-1/2\\ \left(\sqrt{5}+1\right)/4\\ \left(\sqrt{5}-1\right)/4\end{bmatrix}$$

$$\boldsymbol{R}_7=\begin{bmatrix}-\left(\sqrt{5}+1\right)/4 & 1/2 & \left(\sqrt{5}-1\right)/4\\ -\left(\sqrt{5}-1\right)/4 & -\left(\sqrt{5}+1\right)/4 & 1/2\\ 1/2 & \left(\sqrt{5}-1\right)/4 & \left(\sqrt{5}+1\right)/4\end{bmatrix},\ \boldsymbol{p}_7=d_3\begin{bmatrix}\left(\sqrt{5}-1\right)/4\\ 1/2\\ \left(\sqrt{5}+1\right)/4\end{bmatrix}$$

$$\boldsymbol{R}_8=\begin{bmatrix}-\left(\sqrt{5}+1\right)/4 & -1/2 & \left(\sqrt{5}-1\right)/4\\ \left(\sqrt{5}-1\right)/4 & -\left(\sqrt{5}+1\right)/4 & -1/2\\ 1/2 & -\left(\sqrt{5}-1\right)/4 & \left(\sqrt{5}+1\right)/4\end{bmatrix},\ \boldsymbol{p}_8=d_3\begin{bmatrix}\left(\sqrt{5}-1\right)/4\\ -1/2\\ \left(\sqrt{5}+1\right)/4\end{bmatrix}$$

$$\boldsymbol{R}_9=\begin{bmatrix}-\left(\sqrt{5}-1\right)/4 & -\left(\sqrt{5}+1\right)/4 & -1/2\\ 1/2 & \left(\sqrt{5}-1\right)/4 & -\left(\sqrt{5}+1\right)/4\\ \left(\sqrt{5}+1\right)/4 & -1/2 & \left(\sqrt{5}-1\right)/4\end{bmatrix},\ \boldsymbol{p}_9=d_3\begin{bmatrix}-1/2\\ -\left(\sqrt{5}+1\right)/4\\ \left(\sqrt{5}-1\right)/4\end{bmatrix}$$

$$\boldsymbol{R}_{10}=\begin{bmatrix}0 & 0 & -1\\ 0 & 1 & 0\\ 1 & 0 & 0\end{bmatrix},\ \boldsymbol{p}_{10}=d_3\begin{bmatrix}-1\\ 0\\ 0\end{bmatrix}$$

$$\boldsymbol{R}_{11}=\begin{bmatrix}\left(\sqrt{5}-1\right)/4 & \left(\sqrt{5}+1\right)/4 & -1/2\\ 1/2 & \left(\sqrt{5}-1\right)/4 & \left(\sqrt{5}+1\right)/4\\ \left(\sqrt{5}+1\right)/4 & -1/2 & -\left(\sqrt{5}-1\right)/4\end{bmatrix},\ \boldsymbol{p}_{11}=d_3\begin{bmatrix}-1/2\\ \left(\sqrt{5}+1\right)/4\\ -\left(\sqrt{5}-1\right)/4\end{bmatrix}$$

$$\boldsymbol{R}_{12}=\begin{bmatrix}-1&0&0\\0&0&1\\0&1&0\end{bmatrix},\ \ \boldsymbol{p}_{12}=d_3\begin{bmatrix}0\\1\\0\end{bmatrix}$$

$$\boldsymbol{R}_{13}=\begin{bmatrix}\left(\sqrt{5}-1\right)/4&\left(\sqrt{5}+1\right)/4&1/2\\-1/2&-\left(\sqrt{5}-1\right)/4&\left(\sqrt{5}+1\right)/4\\\left(\sqrt{5}+1\right)/4&-1/2&\left(\sqrt{5}-1\right)/4\end{bmatrix},\ \ \boldsymbol{p}_{13}=d_3\begin{bmatrix}1/2\\\left(\sqrt{5}+1\right)/4\\\left(\sqrt{5}-1\right)/4\end{bmatrix}$$

$$\boldsymbol{R}_{14}=\begin{bmatrix}-1/2&-\left(\sqrt{5}-1\right)/4&\left(\sqrt{5}+1\right)/4\\\left(\sqrt{5}+1\right)/4&-1/2&\left(\sqrt{5}-1\right)/4\\\left(\sqrt{5}-1\right)/4&\left(\sqrt{5}+1\right)/4&1/2\end{bmatrix},\ \ \boldsymbol{p}_{14}=d_3\begin{bmatrix}\left(\sqrt{5}+1\right)/4\\\left(\sqrt{5}-1\right)/4\\1/2\end{bmatrix}$$

$$\boldsymbol{R}_{15}=\begin{bmatrix}-1/2&\left(\sqrt{5}-1\right)/4&\left(\sqrt{5}+1\right)/4\\-\left(\sqrt{5}+1\right)/4&-1/2&-\left(\sqrt{5}-1\right)/4\\\left(\sqrt{5}-1\right)/4&-\left(\sqrt{5}+1\right)/4&1/2\end{bmatrix},\ \ \boldsymbol{p}_{15}=d_3\begin{bmatrix}\left(\sqrt{5}+1\right)/4\\-\left(\sqrt{5}-1\right)/4\\1/2\end{bmatrix}$$

$$\boldsymbol{R}_{16}=\begin{bmatrix}\left(\sqrt{5}-1\right)/4&-\left(\sqrt{5}+1\right)/4&1/2\\1/2&-\left(\sqrt{5}-1\right)/4&-\left(\sqrt{5}+1\right)/4\\\left(\sqrt{5}+1\right)/4&-1/2&\left(\sqrt{5}-1\right)/4\end{bmatrix},\ \ \boldsymbol{p}_{16}=d_3\begin{bmatrix}1/2\\-\left(\sqrt{5}+1\right)/4\\\left(\sqrt{5}-1\right)/4\end{bmatrix}$$

$$\boldsymbol{R}_{17}=\begin{bmatrix}-1&0&0\\0&0&-1\\0&-1&0\end{bmatrix},\ \ \boldsymbol{p}_{17}=d_3\begin{bmatrix}0\\-1\\0\end{bmatrix}$$

$$\boldsymbol{R}_{18}=\begin{bmatrix}\left(\sqrt{5}-1\right)/4&-\left(\sqrt{5}+1\right)/4&-1/2\\-1/2&\left(\sqrt{5}-1\right)/4&-\left(\sqrt{5}+1\right)/4\\\left(\sqrt{5}+1\right)/4&1/2&-\left(\sqrt{5}-1\right)/4\end{bmatrix},\ \ \boldsymbol{p}_{18}=d_3\begin{bmatrix}-1/2\\-\left(\sqrt{5}+1\right)/4\\-\left(\sqrt{5}-1\right)/4\end{bmatrix}$$

$$\boldsymbol{R}_{19}=\begin{bmatrix}-1/2&\left(\sqrt{5}-1\right)/4&-\left(\sqrt{5}+1\right)/4\\\left(\sqrt{5}+1\right)/4&1/2&-\left(\sqrt{5}-1\right)/4\\\left(\sqrt{5}-1\right)/4&-\left(\sqrt{5}+1\right)/4&-1/2\end{bmatrix},\ \ \boldsymbol{p}_{19}=d_3\begin{bmatrix}-\left(\sqrt{5}+1\right)/4\\-\left(\sqrt{5}-1\right)/4\\-1/2\end{bmatrix}$$

$$\boldsymbol{R}_{20}=\begin{bmatrix}-1/2&-\left(\sqrt{5}-1\right)/4&-\left(\sqrt{5}+1\right)/4\\-\left(\sqrt{5}+1\right)/4&1/2&\left(\sqrt{5}-1\right)/4\\\left(\sqrt{5}-1\right)/4&\left(\sqrt{5}+1\right)/4&-1/2\end{bmatrix},\ \ \boldsymbol{p}_{20}=d_3\begin{bmatrix}-\left(\sqrt{5}+1\right)/4\\\left(\sqrt{5}-1\right)/4\\-1/2\end{bmatrix}$$

$$\boldsymbol{R}_{21}=\begin{bmatrix}-\left(\sqrt{5}-1\right)/4 & \left(\sqrt{5}+1\right)/4 & 1/2\\ 1/2 & -\left(\sqrt{5}-1\right)/4 & \left(\sqrt{5}+1\right)/4\\ \left(\sqrt{5}+1\right)/4 & 1/2 & -\left(\sqrt{5}-1\right)/4\end{bmatrix},\ \boldsymbol{p}_{21}=d_3\begin{bmatrix}1/2\\ \left(\sqrt{5}+1\right)/4\\ -\left(\sqrt{5}-1\right)/4\end{bmatrix}$$

$$\boldsymbol{R}_{22}=\begin{bmatrix}0 & 0 & 1\\ 0 & -1 & 0\\ 1 & 0 & 0\end{bmatrix},\ \boldsymbol{p}_{22}=d_3\begin{bmatrix}1\\ 0\\ 0\end{bmatrix}$$

$$\boldsymbol{R}_{23}=\begin{bmatrix}-\left(\sqrt{5}-1\right)/4 & -\left(\sqrt{5}+1\right)/4 & 1/2\\ -1/2 & -\left(\sqrt{5}-1\right)/4 & -\left(\sqrt{5}+1\right)/4\\ \left(\sqrt{5}+1\right)/4 & -1/2 & -\left(\sqrt{5}-1\right)/4\end{bmatrix},\ \boldsymbol{p}_{23}=d_3\begin{bmatrix}1/2\\ -\left(\sqrt{5}+1\right)/4\\ -\left(\sqrt{5}-1\right)/4\end{bmatrix}$$

$$\boldsymbol{R}_{24}=\begin{bmatrix}-\left(\sqrt{5}+1\right)/4 & -1/2 & -\left(\sqrt{5}-1\right)/4\\ -\left(\sqrt{5}-1\right)/4 & \left(\sqrt{5}+1\right)/4 & -1/2\\ 1/2 & -\left(\sqrt{5}-1\right)/4 & -\left(\sqrt{5}+1\right)/4\end{bmatrix},\ \boldsymbol{p}_{24}=d_3\begin{bmatrix}-\left(\sqrt{5}-1\right)/4\\ -1/2\\ -\left(\sqrt{5}+1\right)/4\end{bmatrix}$$

$$\boldsymbol{R}_{25}=\begin{bmatrix}-\left(\sqrt{5}+1\right)/4 & 1/2 & -\left(\sqrt{5}-1\right)/4\\ \left(\sqrt{5}-1\right)/4 & \left(\sqrt{5}+1\right)/4 & 1/2\\ 1/2 & \left(\sqrt{5}-1\right)/4 & -\left(\sqrt{5}+1\right)/4\end{bmatrix},\ \boldsymbol{p}_{25}=d_3\begin{bmatrix}-\left(\sqrt{5}-1\right)/4\\ 1/2\\ -\left(\sqrt{5}+1\right)/4\end{bmatrix}$$

$$\boldsymbol{R}_{26}=\begin{bmatrix}\left(\sqrt{5}+1\right)/4 & 1/2 & \left(\sqrt{5}-1\right)/4\\ \left(\sqrt{5}-1\right)/4 & -\left(\sqrt{5}+1\right)/4 & 1/2\\ 1/2 & -\left(\sqrt{5}-1\right)/4 & -\left(\sqrt{5}+1\right)/4\end{bmatrix},\ \boldsymbol{p}_{26}=d_3\begin{bmatrix}\left(\sqrt{5}-1\right)/4\\ 1/2\\ -\left(\sqrt{5}+1\right)/4\end{bmatrix}$$

$$\boldsymbol{R}_{27}=\begin{bmatrix}1/2 & -\left(\sqrt{5}-1\right)/4 & \left(\sqrt{5}+1\right)/4\\ -\left(\sqrt{5}+1\right)/4 & -1/2 & \left(\sqrt{5}-1\right)/4\\ \left(\sqrt{5}-1\right)/4 & -\left(\sqrt{5}+1\right)/4 & -1/2\end{bmatrix},\ \boldsymbol{p}_{27}=d_3\begin{bmatrix}\left(\sqrt{5}+1\right)/4\\ \left(\sqrt{5}-1\right)/4\\ -1/2\end{bmatrix}$$

$$\boldsymbol{R}_{28}=\begin{bmatrix}-1/2 & -\left(\sqrt{5}-1\right)/4 & \left(\sqrt{5}+1\right)/4\\ -\left(\sqrt{5}+1\right)/4 & 1/2 & -\left(\sqrt{5}-1\right)/4\\ -\left(\sqrt{5}-1\right)/4 & -\left(\sqrt{5}+1\right)/4 & -1/2\end{bmatrix},\ \boldsymbol{p}_{28}=d_3\begin{bmatrix}\left(\sqrt{5}+1\right)/4\\ -\left(\sqrt{5}-1\right)/4\\ -1/2\end{bmatrix}$$

$$\boldsymbol{R}_{29}=\begin{bmatrix}-\left(\sqrt{5}+1\right)/4 & 1/2 & \left(\sqrt{5}-1\right)/4\\ \left(\sqrt{5}-1\right)/4 & \left(\sqrt{5}+1\right)/4 & -1/2\\ -1/2 & -\left(\sqrt{5}-1\right)/4 & -\left(\sqrt{5}+1\right)/4\end{bmatrix},\ \boldsymbol{p}_{29}=d_3\begin{bmatrix}\left(\sqrt{5}-1\right)/4\\ -1/2\\ -\left(\sqrt{5}+1\right)/4\end{bmatrix}$$

$$\boldsymbol{R}_{30} = \begin{bmatrix} 0 & 1 & 0 \\ 1 & 0 & 0 \\ 0 & 0 & -1 \end{bmatrix}, \quad \boldsymbol{p}_{30} = d_3 \begin{bmatrix} 0 \\ 0 \\ -1 \end{bmatrix} \tag{B1}$$

Subsequently, referring to the constraint graph in Fig. B1, the 294×180 original constraint matrix $\boldsymbol{M}_3$ can be derived as

$$\boldsymbol{M}_3 = \begin{bmatrix} \boldsymbol{M}_{11} & \mathbf{0}_{6\times36} & \mathbf{0}_{6\times36} & \mathbf{0}_{6\times36} & \mathbf{0}_{6\times36} \\ \mathbf{0}_{6\times36} & \boldsymbol{M}_{22} & \mathbf{0}_{6\times36} & \mathbf{0}_{6\times36} & \mathbf{0}_{6\times36} \\ \mathbf{0}_{6\times36} & \mathbf{0}_{6\times36} & \boldsymbol{M}_{33} & \mathbf{0}_{6\times36} & \mathbf{0}_{6\times36} \\ \mathbf{0}_{6\times36} & \mathbf{0}_{6\times36} & \mathbf{0}_{6\times36} & \boldsymbol{M}_{44} & \mathbf{0}_{6\times36} \\ \mathbf{0}_{6\times36} & \mathbf{0}_{6\times36} & \mathbf{0}_{6\times36} & \mathbf{0}_{6\times36} & \boldsymbol{M}_{55} \\ \mathbf{0}_{6\times36} & \boldsymbol{M}_{62} & \mathbf{0}_{6\times36} & \boldsymbol{M}_{64} & \boldsymbol{M}_{65} \\ \mathbf{0}_{6\times36} & \boldsymbol{M}_{72} & \boldsymbol{M}_{73} & \boldsymbol{M}_{74} & \mathbf{0}_{6\times36} \\ \boldsymbol{M}_{81} & \boldsymbol{M}_{82} & \boldsymbol{M}_{83} & \mathbf{0}_{7\times36} & \mathbf{0}_{7\times36} \end{bmatrix} \tag{B2}$$

and the corresponding submatrices are

$$\boldsymbol{M}_{11} = \begin{bmatrix} \boldsymbol{S}_1 & \mathbf{0}_6 & \mathbf{0}_6 & \mathbf{0}_6 & \mathbf{0}_6 & \mathbf{0}_6 \\ \mathbf{0}_6 & \boldsymbol{S}_2 & \mathbf{0}_6 & \mathbf{0}_6 & \mathbf{0}_6 & \mathbf{0}_6 \\ \mathbf{0}_6 & \mathbf{0}_6 & \boldsymbol{S}_3 & \mathbf{0}_6 & \mathbf{0}_6 & \mathbf{0}_6 \\ \mathbf{0}_6 & \mathbf{0}_6 & \mathbf{0}_6 & \boldsymbol{S}_4 & \mathbf{0}_6 & \mathbf{0}_6 \\ \mathbf{0}_6 & \mathbf{0}_6 & \mathbf{0}_6 & \mathbf{0}_6 & \boldsymbol{S}_5 & \mathbf{0}_6 \\ \mathbf{0}_6 & \mathbf{0}_6 & \mathbf{0}_6 & \mathbf{0}_6 & \mathbf{0}_6 & \boldsymbol{S}_6 \end{bmatrix}, \quad \boldsymbol{M}_{22} = \begin{bmatrix} \boldsymbol{S}_7 & \mathbf{0}_6 & \mathbf{0}_6 & \mathbf{0}_6 & \mathbf{0}_6 & \mathbf{0}_6 \\ \mathbf{0}_6 & \boldsymbol{S}_8 & \mathbf{0}_6 & \mathbf{0}_6 & \mathbf{0}_6 & \mathbf{0}_6 \\ \mathbf{0}_6 & \mathbf{0}_6 & \boldsymbol{S}_9 & \mathbf{0}_6 & \mathbf{0}_6 & \mathbf{0}_6 \\ \mathbf{0}_6 & \mathbf{0}_6 & \mathbf{0}_6 & \boldsymbol{S}_{10} & \mathbf{0}_6 & \mathbf{0}_6 \\ \mathbf{0}_6 & \mathbf{0}_6 & \mathbf{0}_6 & \mathbf{0}_6 & \boldsymbol{S}_{11} & \mathbf{0}_6 \\ \mathbf{0}_6 & \mathbf{0}_6 & \mathbf{0}_6 & \mathbf{0}_6 & \mathbf{0}_6 & \boldsymbol{S}_{12} \end{bmatrix}$$

$$\boldsymbol{M}_{33} = \begin{bmatrix} \boldsymbol{S}_{13} & \mathbf{0}_6 & \mathbf{0}_6 & \mathbf{0}_6 & \mathbf{0}_6 & \mathbf{0}_6 \\ \mathbf{0}_6 & \boldsymbol{S}_{14} & \mathbf{0}_6 & \mathbf{0}_6 & \mathbf{0}_6 & \mathbf{0}_6 \\ \mathbf{0}_6 & \mathbf{0}_6 & \boldsymbol{S}_{15} & \mathbf{0}_6 & \mathbf{0}_6 & \mathbf{0}_6 \\ \mathbf{0}_6 & \mathbf{0}_6 & \mathbf{0}_6 & \boldsymbol{S}_{16} & \mathbf{0}_6 & \mathbf{0}_6 \\ \mathbf{0}_6 & \mathbf{0}_6 & \mathbf{0}_6 & \mathbf{0}_6 & \boldsymbol{S}_{17} & \mathbf{0}_6 \\ \mathbf{0}_6 & \mathbf{0}_6 & \mathbf{0}_6 & \mathbf{0}_6 & \mathbf{0}_6 & \boldsymbol{S}_{18} \end{bmatrix}, \quad \boldsymbol{M}_{44} = \begin{bmatrix} \boldsymbol{S}_{19} & \mathbf{0}_6 & \mathbf{0}_6 & \mathbf{0}_6 & \mathbf{0}_6 & \mathbf{0}_6 \\ \mathbf{0}_6 & \boldsymbol{S}_{20} & \mathbf{0}_6 & \mathbf{0}_6 & \mathbf{0}_6 & \mathbf{0}_6 \\ \mathbf{0}_6 & \mathbf{0}_6 & \boldsymbol{S}_{21} & \mathbf{0}_6 & \mathbf{0}_6 & \mathbf{0}_6 \\ \mathbf{0}_6 & \mathbf{0}_6 & \mathbf{0}_6 & \boldsymbol{S}_{22} & \mathbf{0}_6 & \mathbf{0}_6 \\ \mathbf{0}_6 & \mathbf{0}_6 & \mathbf{0}_6 & \mathbf{0}_6 & \boldsymbol{S}_{23} & \mathbf{0}_6 \\ \mathbf{0}_6 & \mathbf{0}_6 & \mathbf{0}_6 & \mathbf{0}_6 & \mathbf{0}_6 & \boldsymbol{S}_{24} \end{bmatrix}$$

$$\boldsymbol{M}_{44} = \begin{bmatrix} \boldsymbol{S}_{25} & \mathbf{0}_6 & \mathbf{0}_6 & \mathbf{0}_6 & \mathbf{0}_6 & \mathbf{0}_6 \\ \mathbf{0}_6 & \boldsymbol{S}_{26} & \mathbf{0}_6 & \mathbf{0}_6 & \mathbf{0}_6 & \mathbf{0}_6 \\ \mathbf{0}_6 & \mathbf{0}_6 & \boldsymbol{S}_{27} & \mathbf{0}_6 & \mathbf{0}_6 & \mathbf{0}_6 \\ \mathbf{0}_6 & \mathbf{0}_6 & \mathbf{0}_6 & \boldsymbol{S}_{28} & \mathbf{0}_6 & \mathbf{0}_6 \\ \mathbf{0}_6 & \mathbf{0}_6 & \mathbf{0}_6 & \mathbf{0}_6 & \boldsymbol{S}_{29} & \mathbf{0}_6 \\ \mathbf{0}_6 & \mathbf{0}_6 & \mathbf{0}_6 & \mathbf{0}_6 & \mathbf{0}_6 & \boldsymbol{S}_{30} \end{bmatrix}, \boldsymbol{M}_{62} = \begin{bmatrix} \mathbf{0}_6 & \mathbf{0}_6 & \mathbf{0}_6 & \mathbf{0}_6 & \mathbf{0}_6 & \mathbf{0}_6 \\ \mathbf{0}_6 & \mathbf{0}_6 & \mathbf{0}_6 & \mathbf{0}_6 & -\boldsymbol{S}''_{11} & \mathbf{0}_6 \\ \mathbf{0}_6 & \mathbf{0}_6 & \mathbf{0}_6 & \mathbf{0}_6 & \mathbf{0}_6 & \boldsymbol{0}_6 \\ \mathbf{0}_6 & \mathbf{0}_6 & \mathbf{0}_6 & \mathbf{0}_6 & \mathbf{0}_6 & \mathbf{0}_6 \\ \mathbf{0}_6 & \mathbf{0}_6 & \mathbf{0}_6 & \mathbf{0}_6 & \mathbf{0}_6 & \mathbf{0}_6 \\ \mathbf{0}_6 & \mathbf{0}_6 & \mathbf{0}_6 & \mathbf{0}_6 & \mathbf{0}_6 & \mathbf{0}_6 \end{bmatrix}$$

$$\boldsymbol{M}_{64}=\begin{bmatrix} \mathbf{0}_6 & \mathbf{0}_6 & \mathbf{0}_6 & \mathbf{0}_6 & \mathbf{0}_6 & -\boldsymbol{S}''_{24} \\ \mathbf{0}_6 & -\boldsymbol{S}''_{20} & \mathbf{0}_6 & \mathbf{0}_6 & \mathbf{0}_6 & \mathbf{0}_6 \\ \mathbf{0}_6 & \mathbf{0}_6 & \mathbf{0}_6 & \mathbf{0}_6 & \mathbf{0}_6 & \mathbf{0}_6 \\ \mathbf{0}_6 & \mathbf{0}_6 & \mathbf{0}_6 & \mathbf{0}_6 & -\boldsymbol{S}''_{23} & \mathbf{0}_6 \\ \mathbf{0}_6 & \mathbf{0}_6 & -\boldsymbol{S}''_{21} & \mathbf{0}_6 & \mathbf{0}_6 & \mathbf{0}_6 \\ \mathbf{0}_6 & \mathbf{0}_6 & \mathbf{0}_6 & -\boldsymbol{S}''_{22} & \mathbf{0}_6 & \mathbf{0}_6 \end{bmatrix},\ \boldsymbol{M}_{65}=\begin{bmatrix} \mathbf{0}_6 & \mathbf{0}_6 & \mathbf{0}_6 & \mathbf{0}_6 & -\boldsymbol{S}''_{29} & -\boldsymbol{S}'_{30} \\ -\boldsymbol{S}'_{25} & \mathbf{0}_6 & \mathbf{0}_6 & \mathbf{0}_6 & \mathbf{0}_6 & \mathbf{0}_6 \\ -\boldsymbol{S}''_{25} & -\boldsymbol{S}''_{26} & \mathbf{0}_6 & \mathbf{0}_6 & \mathbf{0}_6 & -\boldsymbol{S}''_{30} \\ \mathbf{0}_6 & \mathbf{0}_6 & \mathbf{0}_6 & -\boldsymbol{S}'_{28} & -\boldsymbol{S}'_{29} & \mathbf{0}_6 \\ \mathbf{0}_6 & -\boldsymbol{S}'_{26} & -\boldsymbol{S}''_{27} & \mathbf{0}_6 & \mathbf{0}_6 & \mathbf{0}_6 \\ \mathbf{0}_6 & \mathbf{0}_6 & -\boldsymbol{S}'_{27} & -\boldsymbol{S}''_{28} & \mathbf{0}_6 & \mathbf{0}_6 \end{bmatrix}$$

$$\boldsymbol{M}_{72}=\begin{bmatrix} \mathbf{0}_6 & \mathbf{0}_6 & \mathbf{0}_6 & -\boldsymbol{S}''_{10} & \mathbf{0}_6 & \mathbf{0}_6 \\ \mathbf{0}_6 & \mathbf{0}_6 & \mathbf{0}_6 & \mathbf{0}_6 & \mathbf{0}_6 & \mathbf{0}_6 \\ \mathbf{0}_6 & \mathbf{0}_6 & \mathbf{0}_6 & \mathbf{0}_6 & \mathbf{0}_6 & \mathbf{0}_6 \\ \mathbf{0}_6 & \mathbf{0}_6 & -\boldsymbol{S}''_{9} & \mathbf{0}_6 & \mathbf{0}_6 & \mathbf{0}_6 \\ \mathbf{0}_6 & \mathbf{0}_6 & \mathbf{0}_6 & \mathbf{0}_6 & \mathbf{0}_6 & \mathbf{0}_6 \\ \mathbf{0}_6 & \mathbf{0}_6 & \mathbf{0}_6 & \mathbf{0}_6 & \mathbf{0}_6 & -\boldsymbol{S}''_{12} \end{bmatrix},\ \boldsymbol{M}_{73}=\begin{bmatrix} \mathbf{0}_6 & \mathbf{0}_6 & \mathbf{0}_6 & \mathbf{0}_6 & \mathbf{0}_6 & \mathbf{0}_6 \\ \mathbf{0}_6 & \mathbf{0}_6 & \mathbf{0}_6 & \mathbf{0}_6 & \mathbf{0}_6 & -\boldsymbol{S}''_{18} \\ \mathbf{0}_6 & \mathbf{0}_6 & \mathbf{0}_6 & -\boldsymbol{S}''_{16} & -\boldsymbol{S}''_{17} & \mathbf{0}_6 \\ \mathbf{0}_6 & \mathbf{0}_6 & \mathbf{0}_6 & \mathbf{0}_6 & -\boldsymbol{S}'_{17} & -\boldsymbol{S}'_{18} \\ \mathbf{0}_6 & -\boldsymbol{S}''_{14} & -\boldsymbol{S}''_{15} & \mathbf{0}_6 & \mathbf{0}_6 & \mathbf{0}_6 \\ -\boldsymbol{S}''_{13} & \mathbf{0}_6 & \mathbf{0}_6 & \mathbf{0}_6 & \mathbf{0}_6 & \mathbf{0}_6 \end{bmatrix}$$

$$\boldsymbol{M}_{74}=\begin{bmatrix} -\boldsymbol{S}'_{19} & -\boldsymbol{S}'_{20} & \mathbf{0}_6 & \mathbf{0}_6 & \mathbf{0}_6 & \mathbf{0}_6 \\ -\boldsymbol{S}''_{19} & \mathbf{0}_6 & \mathbf{0}_6 & \mathbf{0}_6 & \mathbf{0}_6 & -\boldsymbol{S}'_{24} \\ \mathbf{0}_6 & \mathbf{0}_6 & \mathbf{0}_6 & \mathbf{0}_6 & -\boldsymbol{S}'_{23} & \mathbf{0}_6 \\ \mathbf{0}_6 & \mathbf{0}_6 & \mathbf{0}_6 & \mathbf{0}_6 & \mathbf{0}_6 & \mathbf{0}_6 \\ \mathbf{0}_6 & \mathbf{0}_6 & \mathbf{0}_6 & -\boldsymbol{S}'_{22} & \mathbf{0}_6 & \mathbf{0}_6 \\ \mathbf{0}_6 & \mathbf{0}_6 & -\boldsymbol{S}'_{21} & \mathbf{0}_6 & \mathbf{0}_6 & \mathbf{0}_6 \end{bmatrix},\ \boldsymbol{M}_{81}=\begin{bmatrix} \mathbf{0}_6 & \mathbf{0}_6 & -\boldsymbol{S}''_{3} & -\boldsymbol{S}'_{4} & \mathbf{0}_6 & \mathbf{0}_6 \\ \mathbf{0}_6 & \mathbf{0}_6 & \mathbf{0}_6 & -\boldsymbol{S}''_{4} & -\boldsymbol{S}'_{5} & \mathbf{0}_6 \\ \mathbf{0}_6 & \mathbf{0}_6 & \mathbf{0}_6 & \mathbf{0}_6 & \mathbf{0}_6 & -\boldsymbol{S}''_{6} \\ \mathbf{0}_6 & \mathbf{0}_6 & \mathbf{0}_6 & \mathbf{0}_6 & \mathbf{0}_6 & \mathbf{0}_6 \\ \mathbf{0}_6 & \mathbf{0}_6 & \mathbf{0}_6 & \mathbf{0}_6 & \mathbf{0}_6 & \mathbf{0}_6 \\ \mathbf{0}_6 & -\boldsymbol{S}''_{2} & -\boldsymbol{S}'_{3} & \mathbf{0}_6 & \mathbf{0}_6 & \mathbf{0}_6 \\ -\boldsymbol{S}'_{1} & \mathbf{0}_6 & \mathbf{0}_6 & \mathbf{0}_6 & -\boldsymbol{S}''_{5} & -\boldsymbol{S}'_{6} \end{bmatrix}$$

$$\boldsymbol{M}_{82}=\begin{bmatrix} \mathbf{0}_6 & \mathbf{0}_6 & -\boldsymbol{S}'_{9} & \mathbf{0}_6 & \mathbf{0}_6 & \mathbf{0}_6 \\ \mathbf{0}_6 & \mathbf{0}_6 & \mathbf{0}_6 & -\boldsymbol{S}'_{10} & \mathbf{0}_6 & \mathbf{0}_6 \\ \mathbf{0}_6 & \mathbf{0}_6 & \mathbf{0}_6 & \mathbf{0}_6 & -\boldsymbol{S}'_{11} & -\boldsymbol{S}'_{12} \\ \mathbf{0}_6 & -\boldsymbol{S}''_{8} & \mathbf{0}_6 & \mathbf{0}_6 & \mathbf{0}_6 & \mathbf{0}_6 \\ -\boldsymbol{S}''_{7} & \mathbf{0}_6 & \mathbf{0}_6 & \mathbf{0}_6 & \mathbf{0}_6 & \mathbf{0}_6 \\ \mathbf{0}_6 & -\boldsymbol{S}'_{8} & \mathbf{0}_6 & \mathbf{0}_6 & \mathbf{0}_6 & \mathbf{0}_6 \\ \mathbf{0}_6 & \mathbf{0}_6 & \mathbf{0}_6 & \mathbf{0}_6 & \mathbf{0}_6 & \mathbf{0}_6 \end{bmatrix},\ \boldsymbol{M}_{83}=\begin{bmatrix} \mathbf{0}_6 & \mathbf{0}_6 & \mathbf{0}_6 & \mathbf{0}_6 & \mathbf{0}_6 & \mathbf{0}_6 \\ \mathbf{0}_6 & \mathbf{0}_6 & \mathbf{0}_6 & \mathbf{0}_6 & \mathbf{0}_6 & \mathbf{0}_6 \\ \mathbf{0}_6 & \mathbf{0}_6 & \mathbf{0}_6 & \mathbf{0}_6 & \mathbf{0}_6 & \mathbf{0}_6 \\ \mathbf{0}_6 & \mathbf{0}_6 & -\boldsymbol{S}'_{15} & -\boldsymbol{S}'_{16} & \mathbf{0}_6 & \mathbf{0}_6 \\ -\boldsymbol{S}'_{13} & -\boldsymbol{S}'_{14} & \mathbf{0}_6 & \mathbf{0}_6 & \mathbf{0}_6 & \mathbf{0}_6 \\ \mathbf{0}_6 & \mathbf{0}_6 & \mathbf{0}_6 & \mathbf{0}_6 & \mathbf{0}_6 & \mathbf{0}_6 \\ \mathbf{0}_6 & \mathbf{0}_6 & \mathbf{0}_6 & \mathbf{0}_6 & \mathbf{0}_6 & \mathbf{0}_6 \end{bmatrix}$$

Finally, the rank of the original constraint matrix $\boldsymbol{M}_3$ is 179, the conclusion that the deployable dodecahedral mechanism has one mobility can be generated as $m=n-\mathrm{rank}(\boldsymbol{M}_3)=180-179=1$.

C. All nonsimplest topology graphs of cubic mechanism.

Without loss of generality, all the reduce solutions of the cubic mechanism are given in Fig. C1, from the removal of 1 line in topological graph to removal of 4 lines, i.e., reserving from 11 to 8 prismatic pairs.

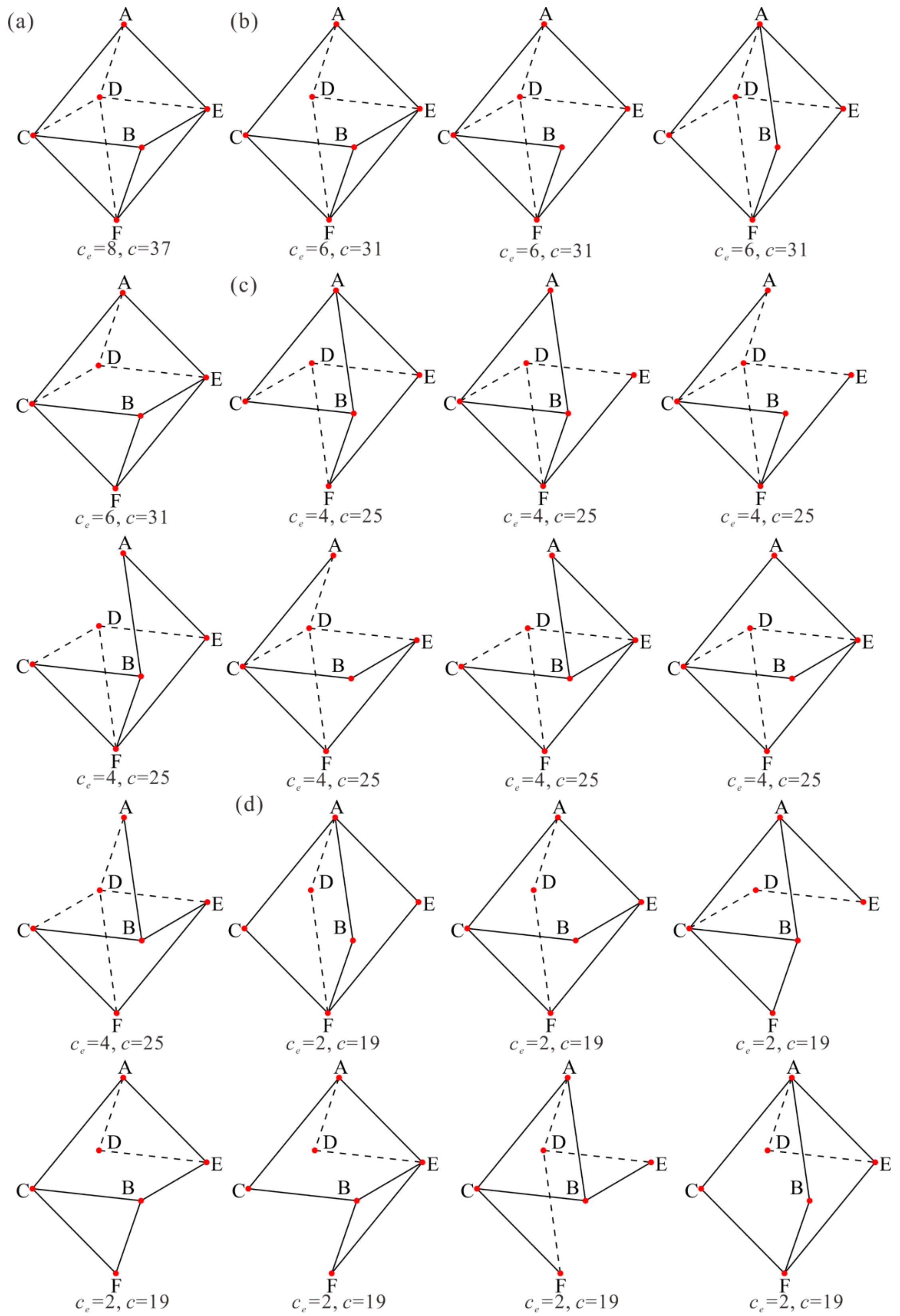

Fig. C1 All other reduced topology graphs of the Sarrus-based cubic mechanism with (a) 11 prismatic pairs, (b) 10 prismatic pairs, (c) 9 prismatic pairs and (d) 8 prismatic pairs, respectively.

中文大摘要

空间折展结构可以实现紧密折叠状态和可控展开状态的相互转变，在实现结构基本承载功能的前提下，能够大尺寸地改变几何形状以满足不同的工况，是实现航天、土木等大型展开结构设计的关键。具有大折展比的三维折展结构较二维结构具有更多优势，如可实现各种不同尺寸的三维形状，并可展开成具有更多功能和更高强度的大型结构。作为一种特殊且形状规则的三维折展结构，折展多面体吸引了来自结构工程师、数学家和科学家等研究人员越来越多的关注。近来，对折展多面体机构的研究工作集中在将连杆及其可动运动链嵌入规则多面体的顶点、面板和棱边处。因此，基本机构单元的设计及其组合方法在折展多面体机构的创新设计中起着至关重要的作用，这意味着新型折展多面体机构的设计需要融合立体几何学和机构运动学的巧妙灵感，以及对于空间对称性的研究探索。

其中，可变换的多面体机构能够在折展过程中实现两种规则多面体的空间构型切换，这则需要基于多面体几何和对称性的独特设计。然而，现有的可变换多面体设计中的配对方案较为单一，如何利用机构运动学策略实现系统且丰富的单自由度多面体变换方案仍是一个巨大挑战。其中，利用对称性原则构建同步径向运动的折展多面体为解决此难题创造了更多的可能。

此外，作为已经被广泛研究和应用的折展结构设计方法，折纸和剪纸技术已经获得了越来越多的关注和研究。通过折纸和剪纸技术可设计出多样的三维空间构型，然而现有研究很少关注到基于折纸和剪纸的折展多面体设计。因此，对折纸机构和剪纸机构在多面体中的探索将为新型折展多面体设计提供全新的思路。与此同时，将具有对称特性的折展多面体视为超材料的胞元，尤其是具有立方体对称性的胞元，利用运动学策略创新其构建方法和组合方式，可形成基于机构运动方式的三维超材料变形模式，为构建多功能、可重构和可编程的多面体超材料提供新的途径。

然而，大多数折展多面体机构都是典型的多环路过约束机构，这是因为机构单元的相互耦合会在这些折展机构中产生大量冗余约束。由于空间折展结构的工作环境恶劣、构件制造中存在误差等原因，其理想的几何约束条件难以得到满足。此时，过约束的存在会产生附加内部载荷，致使折展结构运动不畅甚至不能运动，从而降低了折展结构的可靠性。通过提高制造精度减少误差来保证几何约束条件，会急剧增加制造成本且不能根本上解决问题。在以前的工作中，对于单环路和简单多环路过约束机构的约束消减研究主要集中于铰链类型的更换和边缘冗余铰

链的移除。然而，针对具有复杂拓扑的多环路过约束机构的约束消减，依然是一个具有挑战性的运动学理论难题。所以，借助数学和立体几何学的理论工具，在运动学等价的基础上建立多回路机构的过约束消减准则成为了研究工作的重点和难点，并且其对折展结构的工程化应用具有十分重要的指导意义。

综上所述，系统性构造新型折展多面体机构以及进一步实现其工程应用, 需要完成的工作包括：(1) 构建新型的折展多面体机构单元并创新其单自由度的机构拓扑排布及组合方式；(2) 利用对称性提出新型多面体配对方案，建立目标构型与整体机构拓扑之间的映射关系，构建系列化的折展多面体群；(3) 解析多环路过约束机构的有效约束空间，在包括自由度在内的运动学特性不发生改变的基础上，提出过约束消减方法以大幅降低整体机构的过约束度。

本文聚焦于机构运动学理论，旨在采用不同连杆机构单元来设计新型单自由度同步径向运动的折展多面体机构，实现两个多面体的对称变换，并提出针对多环路过约束多面体机构的过约束消减方法。本文首先构造了一种具有三重对称运动的球面四杆同步机构，以此为构建单元设计了基于球面四杆机构的径向折展多面体，通过几何结构的缩短操作提出了九种多面体的单自由度变换方案。其次，基于 T_d、O_h 和 I_h 对称性，将 Sarrus 机构嵌入至扩展后的柏拉图多面体，设计了一系列基于 Sarrus 机构的单自由度折展多面体，借助旋量理论对构建的多面体机构进行等效的自由度分析，并引入哈密尔顿路径提出了多环路过约束多面体机构的过约束消减方法，在运动等价的基础上大幅降低了机构过约束度。最后，开发了一系列基于空间七杆机构的单自由度径向折展多面体，利用机构学的策略实现了几何中的对称变换，并延伸所提出的哈密尔顿路径消减方法以进一步去除多面体机构的冗余约束。本文主要工作包括以下三部分：

- **基于球面四杆机构的单自由度径向折展多面体**

本文第二章介绍了一类基于球面四杆机构的折展多面体构建方法与运动特性。首先，利用矩阵法对一种三重对称的空间九杆机构进行运动学建模和分析，运动学显式解证明该机构具有三个自由度。为了实现其单自由度的径向运动，额外的运动约束则需要被引入。为此，将三对球面四杆机构嵌入至三自由度的空间九杆机构以提供运动约束，构建出一种基于球面四杆机构的三重对称同步运动机构，其中的每对球面四杆机构共用一个铰链以确保空间九杆机构局部的对称运动。将附加的运动约束条件带入矩阵方程，验证了该折纸同步机构具有单自由度，并且其三个平台在折叠过程中可保持精确的径向直线运动。

对三种具有不同对称特性的多面体进行表面划分，包括具有四面体对称性的大斜方截半四面体、具有立方体对称性的大斜方截半立方体、具有十二面体对称性的大斜方截半立方体十二面体。将提出的单自由度同步机构作为构建胞元并按照相应的对称性嵌入至多面体表面，综合出三种基于球面四杆机构的单自由度多面体机构。每一种多面体机构在同步径向折叠的同时均完成了两种规则多面体之间的变换，且自身对称性时刻保持不变。同时，文中以大斜方截半立方体为例沿着两个路径展示了多边形及其组成的多面体在几何维度的缩短操作，以及将几何缩短映射至多面体机构的结构变化结果，但未改变其机构拓扑。为了进一步探索更多的变换方案，将结构变化方法应用于三种已构建的多面体机构，获得了其余六种单自由度多面体变换方案，其中每组具有相同对称性的结构变化方案都具有相同的机构拓扑，即机构拓扑同构性。至此，第二章共提出了九种多面体的单自由度变换方案，每一种多面体机构都可表现出相对于体心的同步径向折展运动。

基于运动等价，对同步机构单元及整体多面体进行过约束消减以减少机构过约束数。减少其中一对球面四杆机构的约束亦可保证其单自由度径向折展运动。在去除一对球面四杆机构的铰链和杆件后，通过矩阵方程对整体机构的约束条件进行分析，验证了去除冗余约束前后的运动等价特性。此外，如再继续去除其余的铰链和杆件，则会使自由度增加而影响运动等价特性。至此，利用具有立方体对称性的三个多面体展示了整体多面体机构的过约束消减，均保留了原始的单自由度径向运动特性和折展过程中时刻不变的对称特性，并且在此情况下过约束数由原始的 175 降为 119。

引入球面机构及其对称约束为从折纸的角度设计折展多面体机构提供了一种新思路。此外，所提出的基于球面四杆机构的折展多面体及其变换方案为空间折展结构的创新设计提供了新的灵感。

- **基于 Sarrus 机构的单自由度径向折展多面体**

本文第三章基于四面体、立方体和十二面体这三种阿基米德多面体，提出了基于 Sarrus 机构的折展多面体的构建策略、分析方法和过约束消减。首先，将四面体的四个平台进行相对于体心的几何展开操作，此时相邻的两两平台间以直线运动的方式相互远离。为此，选取具有精确直线运动特性的 Sarrus 连杆机构作为折展多面体的基本机构单元。将 Sarrus 连杆机构嵌入至两两平台间以满足几何上的相对直线运动要求，通过综合六个机构单元构建了单自由度四面体机构，以此构建策略还获得了单自由度立方体机构(共需十二个单元)和十二面体机构(共需三十个单元)。

借助旋量理论对多面体机构进行自由度分析，通过求解旋量约束矩阵验证了此类多面体机构的单自由度运动特性。但是，整体多面体机构大量的机构环路数使得约束矩阵的构建和求解异常复杂。针对这一问题，本文将两两平台间的单个 Sarrus 连杆机构等效为一个移动副，则 Sarrus 连杆机构的六个运动旋量可通过两次互易计算等效为一个只表示移动的运动旋量。利用等效后的运动旋量构建旋量约束矩阵，很大程度上简化了多面体机构自由度的计算求解过程，并给出了原始的求解过程以展示自由度等效分析的准确性和便捷性。

大多数折展多面体机构都是多环路的过约束机构，而多环路过约束机构网格的约束消减是一个极具挑战性的机构运动学问题。在移动副等效分析后，上述三种折展多面体均可基于各自的对偶多面体进行拓扑表达，在每一个多面体拓扑图中的点表示多面体的平动平台，两点间的连线表示 Sarrus 连杆机构等效的移动副。同时，机构拓扑消减的前提条件可总结为：(1) 拓扑图中的每个点至少需要两个连线以构成闭环机构；(2) 包括自由度在内的机构运动学特性不发生改变。在此限制条件下，本文引入哈密尔顿路径这一数学概念来指导机构拓扑的消减过程。对于四面体机构，其对偶四面体的拓扑图仅存在一条哈密尔顿路径，通过去除该哈密尔顿路径以外的拓扑元素，获得了其基于空间四边形的单自由度最简约束形式，过约束数由 19 降为 7。对于立方体机构，利用得到的单自由度空间四边形作为基本单元，研究了其对偶八面体的两条哈密尔顿路径，对非最简形式进行排除后只获得了一种最简立方体机构，过约束数由 43 降为 13。对于更为复杂的十二面体机构，详细讨论了其对偶二十面体所具有的十七种不同的哈密尔顿路径，最终获得了十九种最简十二面体机构，过约束数均由 115 降为 31。所提出的三种多面体的最简约束形式在保留原始单自由度径向对称运动特性的同时大幅减少了机构过约束数。

本文第三章所提出的对称构建策略、等效分析方法以及基于哈密尔顿路径的多环路机构网格过约束消减方法，不仅为折展多面体机构的机构学研究奠定强有力的理论基础，也为其实际工程应用的发展提供有效的技术支撑，有望推动折展多面体的创新设计和工程实践。

- **基于空间七杆机构的单自由度径向折展多面体**

本文第四章，基于阿基米德立体几何中可能的多面体变换配对方案，提出了一系列基于空间七杆机构的折展多面体，并用机构学的策略实现了几何中的对称变换。首先，在基于空间九杆机构的剪纸图案内部添加额外的面板和折痕，获得了一种单自由度三重对称的剪纸图案，其运动学模型可视为三重对称的空间七杆

机构网格，同理亦可构建多重对称的空间七杆机构网格。由于空间七杆机构单元的平动特性，此类机构网格均具有单自由度同步运动。将多重对称的机构网格作为构建单元，按照相应的空间对称性嵌入至阿基米德多面体表面，获得了一系列基于空间七杆机构网格的折展多面体机构。

在此基础上，对于组成一个阿基米德多面体表面的三种多边形，通过依次选择保留一种多边形而折叠其余两种的方式，获得了更为丰富的多面体变换方案并按照 T_d、O_h 和 I_h 对称性的顺序分别演示。以具有 O_h 对称性的大斜方截半立方体为例，若保留八边形而折叠六边形和四边形，利用三重对称的空间七杆机构网格可实现大斜方截半立方体与截角立方体之间的变换；若保留六边形，则可利用四重对称的空间七杆机构网格实现大斜方截半立方体与截角八面体之间的变换；若保留四边形并结合上述两种变换方式，则可实现大斜方截半立方体与小斜方截半立方体之间的变换。因此，除了不具有对称性的扭棱立方体和扭棱十二面体，本文在其余十一种阿基米德多面体和五种柏拉图多面体之间，利用多重对称的空间七杆机构网格共实现了五种具有 T_d 对称性的变换方案、七种具有 O_h 对称性的变换方案和七种具有 I_h 对称性的变换方案。

在哈密尔顿路径过约束消减方法基础上，对所提出的多面体机构冗余约束进行进一步的去除。首先利用哈密尔顿路径进行初步消减，其次去除内部相邻单元间共用的冗余约束，最终去除哈密尔顿路径上的边缘冗余约束。在保留原始多面体运动特性的情况下，很大程度上降低了过约束程度，例如基于三重对称构建单元的大斜方截半十二面体的过约束数可由原始的 145 降为 1。本章在阿基米德和柏拉图这两类典型多面体之间提出了丰富的变换方案，丰富了可变换多面体的设计空间，为制造满足各领域实际工程需求的折展多面体提供了理论依据。

- **结论与展望**

本文着眼于机构运动学与立体几何学的交叉融合，建立了基于对称性与不同类型机构单元的折展多面体设计准则，提出了一系列单自由度径向折展多面体的创新设计，获得了丰富的多面体变换方案。同时，本文基于局部简化方法与哈密尔顿路径方法提出了多环路过约束机构的过约束消减方法，在保持运动学等价的同时大幅降低了机构过约束度。因此，本研究结果对同类型研究具有一定的指导意义，不仅为折展多面体机构的创新设计研究奠定强有力的理论基础，也为其实际工程应用的发展提供有效的技术支撑。

此外，本文的研究工作还可以在如下几方面进行进一步的深入研究：

(1) 本文采用了球面四杆机构、Sarrus 过约束机构和空间七杆机构作为机构单元来构造折展多面体，进一步研究可以扩展至其他机构单元类型及其对称与非对称组装，如球面五、六杆机构和空间八杆机构。除了本文提出的可展柏拉图和阿基米德多面体外，后续研究将面向各种规则和不规则多面体群来探索新型空间折展结构的丰富构态，如约翰逊多面体、棱柱和反棱柱等，以促进折展多面体结构的工程化发展。

(2) 本文围绕着 T_d、O_h 和 I_h 对称性分别提出了三类的多面体变换方案，具有更广泛对称性的其他可能变换方案仍需进一步探索。此外，本文主要研究内容为折展多面体的单自由度机构拓扑构建，除文中利用缩短操作实现的整体结构变化外，其他结构变化方式有待于进一步探讨和调整，以满足特殊的工程实践需求。同时，探索折展多面体的空间模块化构建方式将为航天器、太空舱、月面基地等先进装备提供更多可能的方案。

(3) 针对多环路过约束机构的过约束消减这一具有挑战性的理论难题，本文基于哈密尔顿路径这一数学概念提出了运动学的过约束消减方法，虽然过约束程度实现了大幅降低，但整体多面体机构的非过约束形式依然是尚待解决的难题，仍需进一步深入研究。同时，本文提出的消减策略还可应用于各类大型空间过约束机构网格，在折展比和运动特性不变的基础上实现整体机构系统的简化。此外，根据实际工况选择不同程度的约束简化，其中刚度分析和稳定性评估则需要进一步深入研究。

(4) 将折展多面体视为超材料的构建胞元，本文的研究还为构造新型三维超材料提供了一种运动学策略，可赋予其大变形、负泊松比以及负热膨胀等丰富特性。此外，折展多面体胞元的空间组合方法以及在多功能可编程超材料中的先进应用仍需要广泛开发。为了实现具有大量胞元的多面体超材料功能多样性和可编程性，能根据外部刺激(如磁场、电场、光场或湿度场)产生变形响应的驱动材料还需进一步开发。因此，未来研究可以着眼于多面体超材料的组合策略、驱动和控制方法，通过多学科的交叉研究为多面体超材料的变形设计和性能分析提供独特的灵感和新颖的思路。

关键词：机构运动学，折展多面体，多面体变换，对称性，同步径向运动，过约束消减，运动学等价

Publications and Research Projects

Journal Papers:

[1] Gu Y, Chen Y. Origami cubes with 1-DOF rigid and flat foldability[J]. International Journal of Solids and Structures, 2020, 207: 250-261.

[2] Gu Y, Wei G, Chen Y. Thick-panel origami cube[J]. Mechanism and Machine Theory, 2021, 164: 104411.

[3] Sadiq A#, Gu Y#, Luo Y, Chen Y, Ma K. A gain-enhanced reconfigurable radiation array with mechanically driven system and directive elements[J]. Frontiers of Mechanical Engineering, 2022, 17(4): 60. (Jointed first authors)

[4] Ouyang H#, Gu Y#, Gao Z, Hu L, Zhang Z, Ren J, Li B, Sun J, Chen Y, Ding X. Kirigami-inspired thermal regulator[J]. Physical Review Applied, 2023, 19(1): L011001. (Jointed first authors)

[5] Zhang Y#, Gu Y#, Chen Y, Li M, Zhang X. 1-DOF rigid and flat-foldable origami polyhedrons with slits[J]. Acta Mechanica Solida Sinica, 2023, 36(4): 479-490. (Jointed first authors)

[6] Gu Y, Chen Y. Deployable origami polyhedrons with 1-DOF radial motion[J]. Mechanism and Machine Theory, 2023, 184: 105393.

[7] 陈焱，顾元庆. 折纸运动学综述[J]. 力学进展，2023，53(1):154-197. (封面论文，导师一作)

[8] Gu Y, Zhang X, Wei G, Chen Y. Sarrus-inspired deployable polyhedral mechanisms[J]. Mechanism and Machine Theory, 2024, 193: 105564.

[9] Gu Y, Zhang X, Wei G, Chen Y. Hamiltonian-path based constraint reduction for deployable polyhedral mechanisms[J]. Mechanism and Machine Theory, 2024, 193: 105563.

[10] Gu Y, Chen Y. Kirigami Archimedean polyhedrons and their symmetric transformations, Communications Engineering. (Under revision）

Conference Papers:

[1] Gu Y, Chen Y, 1-DOF origami boxes with rigid and flat foldability[C]. Proceedings of 7th IFToMM Asian MMS 2021, Hanoi, Vietnam, December 16-18, 2021: 80-88. (Best Student Paper Silver Award)

[2] 顾元庆, 陈焱. 厚板立方体的运动学等价构建[C]. 第四届可展开空间结构学术会议, 哈尔滨，2020.12.

[3] 顾元庆, 陈焱. Bricard 机构网格的约束简化策略[C]. 第五届可展开空间结构学术会议，西安，2022.12.

Patents:

[1] 顾元庆, 陈焱, 马家耀. 一种单自由度可折展盒子结构[P], CN109353634B, 2021.

[2] 陈焱，顾元庆, 马家耀.一种单自由度双重对称的可折展盒子结构[P], CN109484734B, 2021.

[3] 陈焱，顾元庆, 孙新峰，马家耀.一种单自由度空间可折展多面体结构[P], CN111806725B, 2022.

[4] 王珂，陈焱，赵海峰，顾元庆, 贾晨雪，陈学松，袁林，袁子豪，张璐. 一种可折叠展开的空间实验平台[P], CN112498753B, 2021.

Research Projects Participated in:

[1] 国家自然科学基金杰出青年项目：机构运动学与折展结构，项目编号 51825503.

[2] 国家自然科学基金重点项目：可编程超材料的构建理论与性能调控策略研究，项目编号 52035008.

[3] 国家自然科学基金青年科学基金项目：基于运动等价的空间可展结构过约束数减少策略研究，项目编号 52105032.

Acknowledgments

My gratitude goes first and foremost to Prof. Yan Chen, my supervisor, for her encouragement and guidance throughout my PhD's study. Her constructive suggestions and valuable guidance towards my work have been the driving force to complete my research and life compass to realize my bright future. Furthermore, her patience and generosity with students, her enthusiasm and rigorous attitude with academic research, and her immense knowledge will continue to influence my future work and life.

I wish to express my deepest gratitude to Prof. Guowu Wei from University of Salford for his invaluable discussion and suggestion and the patient guidance. I would also like to thank Prof. Jiayao Ma and Dr. Xiao Zhang for their advices and help on my research, Dr. Fufu Yang, Dr. Shixi Zang, Dr. Weilin Lv, Dr. Huijuan Feng for their kind help. Discussions with them widen my vision and deepen my understanding of the research.

Meanwhile, I would like to thank my colleagues in Motion Structure Laboratory, in particular Mr. Zhenhao Jia, Mr. Yuehao Zhang, Mr. Weiqi Liu, Mr. Mengyue Li, Mr. Zhibo Wei, Mr. Sibo Chai, Miss Kaili Xi, Miss Chenjie Zhao, Miss Can Lu, Mr. Yuxing Song, for their friendly help and contribution to many unforgettable occasions.

Scholarship Fund by China Scholarship Council, the financial support by the National Natural Science Foundation of China (Projects 51825503, 52035008 and 52105032), and the University PhD Scholarship by Tianjin University are also gratefully acknowledged.

Finally, I would like to express my thanks to my parents, my grandparents and my younger brother for their encouragement, support and confidence, and give special thanks to my love Huan for her patience, encouragement and love. All of them give me courage and belief to overcome any difficulty in my study and life.